

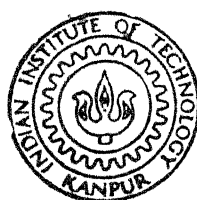
<sup>57</sup>Fe MÖSSBAUER SPECTROSCOPIC STUDIES OF  
Ti - and Sn - SUBSTITUTED Ni - Zn FERRITES

by

RAMESH CHANDRA SRIVASTAVA

PHY  
1989  
D  
SRI  
Mos

771  
phy/1989/D  
Sr 38 f



DEPARTMENT OF PHYSICS

INDIAN INSTITUTE OF TECHNOLOGY, KANPUR

JULY, 1989

<sup>57</sup>Fe MÖSSBAUER SPECTROSCOPIC STUDIES OF  
Ti - and Sn - SUBSTITUTED Ni - Zn FERRITES

*A Thesis Submitted  
In Partial fulfilment of the Requirements  
for the Degree of  
DOCTOR OF PHILOSOPHY*

*by*  
RAMESH CHANDRA SRIVASTAVA

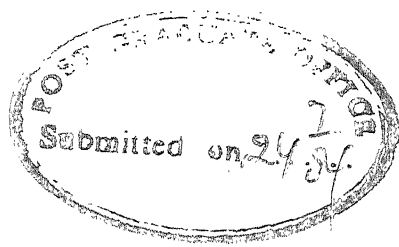
*to the*  
DEPARTMENT OF PHYSICS  
INDIAN INSTITUTE OF TECHNOLOGY, KANPUR  
JULY, 1989

PHY - 1989 - D - 801 - 100

1330

CENTRAL LIBRARY  
Acc. No. A 108277

DEDICATED TO  
MY PARENTS



## CERTIFICATE

This is to certify that the work presented in this thesis entitled "<sup>57</sup>Fe Mössbauer Spectroscopic Studies of Ti- and Sn-Substituted Ni-Zn FERRITES" by Ramesh Chandra Srivastava has been done under our joint supervision and it has not been submitted elsewhere for a degree or diploma.

T.M.Srinivasan

T.M. Srinivasan  
Professor of Physics  
Indian Institute of Technology  
KANPUR-208016, INDIA

D.C.Khan

D.C. Khan  
Professor of Physics  
Indian Institute of Technology  
KANPUR-208016, INDIA

## ACKNOWLEDGEMENT

It is of great pleasure to me to express my profound gratitude to Prof. D.C. Khan for his able guidance, constant help and encouragement in matters both academic and otherwise, throughout the course of my research work. I am equally grateful to Prof. T.M. Srinivasan for his able guidance at every stage of the work.

I am also thankful to Prof. A.R.Das, Department of Metallurgy, for the preparation of ferrite samples in his laboratory.

My sincere thanks are also due to Professors R. Ramachandran, R.M. Singru, R.K. Ray, A.K. Majumdar, Y.R. Waghmare, J.K. Bhattacharjee, V.A. Singh, K. Shahi and D. Saran for their valuable suggestions and keen interest in the progress of my research work.

I am particularly thankful to Prof. N.K. Sanyal and Prof. M. Misra, Department of Physics, University of Gorakhpur, for their inspiration and encouragement.

I express my sincere regards to Mrs. S. Khan for her affection and continuous encouragement through the prolonged and arduous period of my work.

I am also thankful to my colleagues Sumita; friends, Drs. A.K. Agarwal, A. Saxena, R. S. Chauhan, J.K. Misra, O.P. Misra, M. Zulfeqquar and Messrs Himanshu, Ajay, Arun,

Jayanta, Uma Shankar, Sanjay and Paul and many others who helped me in more than one way and made my stay at IIT Kanpur both memorable and exciting.

I am thankful to Mr. H.N. Nigam and his associates of Physics Department, Mr. J.S. Sharma and his associates of Physics Workshop and Mr. S. Singh and his associates of Liquid Nitrogen Plant for being helpful throughout the course of this work.

I am very much thankful to Mr. Ghanshyam Rao Hoshing for excellent typing and Mr. A.K. Ganguly for tracing the figures neatly and clearly.

Finally, I must mention that without the sincere wishes of my brothers and sisters and blessings of my parents my work could hardly be a success.

## LIST OF CONTENTS

	Page No.
CERTIFICATE	i
ACKNOWLEDGEMENT	ii
SYNOPSIS	viii
CHAPTER 1 : FUNDAMENTALS OF MÖSSBAUER SPECTROSCOPY	
1.1 Introduction	1
1.2 The Mössbauer Effect	2
1.3 Hyperfine Interactions	9
1.3.1 Electric Monopole Interaction; The Isomer Shift.	10
1.3.2 The Electric Quadrupole Interaction	13
1.3.3 Sternheimer Anti-Shielding Factor	16
1.3.4 Magnetic Dipole Interaction	19
1.4 Lattice Vibrational Anisotropy (Goldanskii-Karyagin Effect)	20
1.5 Asymmetric Quadrupole Doublet	23
1.6 Mössbauer Spectroscopy vis-a-vis Other Techniques to Investigate Hyperfine Interactions	24
REFERENCES	27
CHAPTER 2 : EXPERIMENTAL METHODS	
2.1 Introduction	29
2.2 Radio Active Mössbauer Source	32
2.3 Mössbauer Spectrometer	33

2.4	Detector and Amplifier	35
2.5	Data Storage (Multichannel Analyser)	37
2.6	Cryostat	38
2.7	Standard Absorbers for Calibration	40
2.8	Sample Preparation	40
2.9	Thickness Optimization of the Absorbers	40
2.10	The Effect of Geometry on Mössbauer Spectra	44
2.11	Curve-Fitting	47
REFERENCES		49
CHAPTER 3 : FERRITES : PREPARATION AND PROPERTIES		51
3.1	Introduction	51
3.2	Structure	52
3.3	Distribution of Cations between A and B sites	53
3.4	Magnetic Properties of Ferrites	57
3.5	Preparation Technique	61
3.6	Origin of the Internal Magnetic Field at the Nucleus	64
REFERENCES		74
CHAPTER 4 : MÖSSBAUER AND MAGNETIC STUDIES OF $Ti^{4+}$ SUBSTITUTED Ni-Zn FERRITES		77
4.1	Introduction	77
4.2	Mössbauer Study of Titanium Substituted $Ni_{1-y}Zn_y Fe_2O_4$ ( $y = 0.0, 0.3, 0.4$ ) Ferrite	82
4.2.1	Titanium Substituted $NiFe_2O_4$ Ferrite	82

4.2.2	Titanium Substituted $\text{Ni}_{0.7}\text{Zn}_{0.3}\text{Fe}_2\text{O}_4$ Ferrite	89
4.2.3	Titanium Substituted $\text{Ni}_{0.6}\text{Zn}_{0.4}\text{Fe}_2\text{O}_4$ Ferrite	97
4.3	Discussion of Results	104
4.3.1	Isomer Shift	104
4.3.2	Quadrupole Splitting	105
4.3.3	Magnetic Hyperfine Splitting	106
4.3.4	Full Width at Half Maximum (FWHM)	109
4.4	Study of Magnetization	110
4.4.1	$\text{Ti}^{4+}$ substituted $\text{NiFe}_2\text{O}_4$	110
4.4.2	$\text{Ti}^{4+}$ substituted $\text{Ni}_{0.7}\text{Zn}_{0.3}\text{Fe}_2\text{O}_4$ Ferrite	119
4.4.3	$\text{Ti}^{4+}$ substituted $\text{Ni}_{0.6}\text{Zn}_{0.4}\text{Fe}_2\text{O}_4$ Ferrite	122
	REFERENCES	133
CHAPTER 5	MÖSSBAUER AND MAGNETIC STUDIES OF $\text{Sn}^{4+}$ SUBSTITUTED Ni-Zn FERRITES	137
5.1	Introduction	137
5.2	$\text{Sn}^{4+}$ Substituted $\text{Ni}_{1-y}\text{Zn}_y\text{Fe}_2\text{O}_4$ ( $y = 0.3, 0.4$ ) Ferrite	138
5.2.1.	Mössbauer Study of $\text{Sn}^{4+}$ Substituted $\text{Ni}_{0.7}\text{Zn}_{0.3}\text{Fe}_2\text{O}_4$ Ferrite	138
5.2.2.	Mössbauer Study of $\text{Sn}^{4+}$ Substituted $\text{Ni}_{0.6}\text{Zn}_{0.4}\text{Fe}_2\text{O}_4$ Ferrite	144

5.3 Discussion of Results	153
5.3.1 Isomer Shift	153
5.3.2 Quadrupole Splitting	154
5.3.3 Magnetic Hyperfine Splitting	154
5.3.4 Full Width at Half Maximum (FWHM)	155
5.4 Study of Magnetization	156
5.4.1 $\text{Sn}^{4+}$ Substituted $\text{Ni}_{0.7}\text{Zn}_{0.3}\text{Fe}_2\text{O}_4$ Ferrite	156
5.4.2. $\text{Sn}^{4+}$ Substituted $\text{Ni}_{0.6}\text{Zn}_{0.4}\text{Fe}_2\text{O}_4$ Ferrite	159
REFERENCES	166
CHAPTER 6 MÖSSBAUER STUDY OF SOME IRON COMPLEXES IN EXTERNAL ELECTRIC FIELD	168
6.1 Introduction	168
6.2 Experimental	168
6.3 Results	169
6.4 Discussion	187
REFERENCES	188
CONCLUSION	190

## SYNOPSIS

<sup>57</sup>Fe MöSSBAUER SPECTROSCOPIC STUDIES OF Ti- and Sn-  
SUBSTITUTED Ni-Zn FERRITES

by

Ramesh Chandra Srivastava  
Department of Physics  
Indian Institute of Technology, Kanpur 208016, India

Mössbauer spectroscopy is a powerful tool for studying the hyperfine interactions of the atomic nucleus with its surroundings. Its basis is the recoilless emission and absorption of gamma-rays. The isomer shift arises due to the Coulomb interaction of the nuclear charge distribution with the s-electron density at the nucleus. The quadrupole splitting results from the interaction of electric quadrupole moment of the nucleus with the electric field gradient (EFG) at the nuclear site. The interaction of the nuclear magnetic dipole moment with the magnetic field at the nucleus gives rise to the magnetic hyperfine interaction.

Khan et al. [1,2] found a very interesting behaviour of saturation magnetization in  $Ti^{4+}$  substituted  $Ni_{0.3}Zn_{0.7}Fe_2O_4$  ferrite. They observed that there is an unexpected dip in the saturation magnetization curve at  $Ti^{4+}$  concentration of 0.03 per formula unit. They

interpreted this as an effect of distribution of  $Ti^{4+}$  ions between A and B sites.  $Ti^{4+}$  ions enter at A site upto the  $Ti^{4+}$  concentration of 0.03 per formula unit and afterwards to the B site also. The corresponding  $Fe^{3+}$  transfer causes an augmentation in the canting angle. Das et al. [3] also observed a similar type of anomalous behaviour in the saturation magnetization curve for a wide range of substituted Ni-Zn ferrites (substituents :  $Ti^{4+}$ ,  $Zr^{4+}$ ,  $Nb^{5+}$  and  $Sn^{4+}$ ; and Zn concentrations: 0.3, 0.5 and 0.7). Contrary to the results of [1-3], the work of other authors [4, 5] show that  $Ti^{4+}$  ions occupy the B site first upto the  $Ti^{4+}$  concentration of 0.3 and beyond this concentration it occupies both A and B sites. Again, their results yield no dip in the saturation magnetization vs.  $Ti^{4+}$  concentration curve. Thus the occupation of higher valency non-magnetic cations and their effect on  $Fe^{3+}$  transfer and B-B interactions remain an open question, particularly for the low concentration of ions.

Khan and Das used magnetization measurements as the basis of their analysis whereas Baijal et al. based their calculations on Mössbauer experimental data. Khan et al. [2] could not analyse their Mössbauer data satisfactorily as the spectra were relaxed. The aim of the present work is to initiate the study of  $Ti^{4+}$  substitution effect in the low Zn concentration zone ( $y = 0.0 - 0.4$ ) of  $Ni_{1-y}Zn_yFe_2O_4$

ferrite by simultaneous Mössbauer and magnetization measurements. In this range the Mössbauer spectra are not relaxed and may be used to get insight into the  $Ti^{4+}$  distribution process as well as microscopic magnetization mechanism.  $Ti^{4+}$  range was chosen to keep the system in the anomalous dip zone of the magnetization experiments of Khan et al. [1, 2]. For further elucidation of the mechanism leading to the anomalous behaviour, we studied  $Sn^{4+}$  substituted Ni-Zn ferrite systems too.

A byproduct of our deep involvement with Mössbauer measurements during our primary aim stated above has been the study of Stark effect in some iron complexes. Previous studies of the influence of an external electric field on the hyperfine structure of Mössbauer spectra were primarily performed on ferroelectrics. Thus the changes in the parameters and shape of Mössbauer spectra with a phase transition in ferroelectrics or reorientation of domains in an electric field were studied. Even though the internal crystal field was expected to be several orders of magnitude more than the applied field, the detection of the effect of external field in a dielectric (i.e. Stark effect) by a high resolution spectrometer was not ruled out. The work of Nair et al. [6] shows that there is no change in the isomer shift and quadrupole splitting of  $Fe(SO_4)_2(NH_4)_2 \cdot 6H_2O$  upto an external field of 50 KV/cm

whereas there is significant increase in these hyperfine parameters in case of  $\text{FeSO}_4 \cdot 7\text{H}_2\text{O}$ . In the present work we present some new findings on the Stark effect in a number of iron complexes.

A brief introduction of Mössbauer spectroscopy is given in Chapter 1. Mössbauer parameters like recoilfree fraction, isomer shift, electric quadrupole interaction and magnetic dipole interaction are incorporated. Other topics such as (a) Goldanskii-Karyagin effect, (b) Sternheimer antishielding effect and, (c) asymmetric quadrupole doublets in Mössbauer spectroscopy are discussed briefly. A short discussion on Mössbauer spectroscopy vis-a-vis other hyperfine techniques is also given in this chapter.

Chapter 2 describes the experimental details. Different aspects of the Mössbauer effect methodology like the radioactive source, Mössbauer spectrometer, cryostat, detector and storage system are discussed in some detail. The optimization of the thickness for best signal to noise ratio is discussed. The computer programme used in the analysis of data is also briefly explained.

Chapter 3 is a review of the structural characteristics and the basic physical properties of ferrites. The normal, inverse and the intermediate spinel structures are presented. The basic criterion of cation

distribution between A and B sites are discussed. The Néel theory of magnetic properties is briefly given. An outline of the preparation of samples is presented. A review of the origin of hyperfine fields in magnetic materials is also introduced in this chapter.

Chapter 4 deals with the study of  $Ti^{4+}$  substituted  $Ni_{1-y}Zn_yFe_2O_4$  ferrite for  $y = 0.0, 0.3$  and  $0.4$ . The Mössbauer spectra at both  $295$  and  $77^0K$  consisted of two overlapping sextets, yielding the hyperfine magnetic field at the two sublattice sites A (tetrahedral) and B (octahedral). The field  $H_{eff}(A)$  at A site decreases with the increase of  $Ti^{4+}$  concentration. The change in the hyperfine field with  $Ti^{4+}$  concentration is explained as due to the change in supertransferred hyperfine field ( $H_{STHF}$ ). It is found that the hyperfine field  $H_{eff}(B)$  at B site remains almost constant. This is attributed to the fact that all the  $Ti^{4+}$  ions enter at B site only.

The variation of magnetization, obtained from VSM measurements, and the net effective hyperfine magnetic field  $|H_{eff}(B) - H_{eff}(A)|$ , with  $Ti^{4+}$  concentration, when plotted on comparable scales, follow the same trend. If Néel type of magnetic ordering is considered then a linear decrease of magnetization with  $Ti^{4+}$  concentration is expected, as the Mössbauer spectroscopy reveals that  $Ti^{4+}$  ions enter only at B site. But in all the three systems a

deviation from this type of behaviour of magnetization is observed. This is explained by the presence of canted spin structure of the Yafet-Kittel type. Evidently, the positional readjustment of the ions due to electrostatic forces after the entry of non-magnetic tetravalent ions in the lattice causes the readjustment of the values of exchange constants,

$$J_{Fe^{3+}(A)-Ni^{2+}(B)}, J_{Fe^{3+}(A)-Fe^{3+}(B)}, J_{Ni^{2+}(B)-Ni^{2+}(B)},$$

$$J_{Fe^{3+}(B)-Fe^{3+}(B)}, J_{Fe^{3+}(B)-Ni^{2+}(B)} \text{ and } J_{Fe^{3+}(A)-Fe^{3+}(A)}$$

A plot of these exchange constants against  $Ti^{4+}$  concentration clearly shows that all the constants remain almost unchanged except  $J_{Ni^{2+}(B)-Ni^{2+}(B)}$ . The change in this exchange constant reflects exactly the change in the lattice parameter. It is then evident that the overlap of the wavefunctions of the  $Ni^{2+}$  ions (through  $O^{2-}$  ions) and its change with the ion separation are basically responsible for the change in the canting of spins and consequently the anomalous magnetization of these ferrites.

Chapter 5 contains the studies of  $Sn^{4+}$  substituted  $Ni_{1-y}Zn_yFe_2O_4$  ferrite for  $y = 0.3$  and  $0.4$ . As in  $Ti^{4+}$  substituted  $Ni_{1-y}Zn_yFe_2O_4$  ferrites, in these systems too,  $H_{eff}(B)$  remains almost constant whereas  $H_{eff}(A)$  decreases with the increase of  $Sn^{4+}$  concentration. As discussed in Chapter 4, the variation in  $H_{eff}(A)$  with  $Sn^{4+}$  concentration

is explained as due to the change in  $H_{STHF}$ . Unlike the  $Ti^{4+}$  case, we observed that here the magnetization falls suddenly by the minimal entry of  $Sn^{4+}$ , followed by a very slow decrease. This is again explained by the presence of canted spin structure. The changes in the canting angle with the increase of  $Sn^{4+}$  concentration is found to be due to the change in  $J_{Ni^{2+}(B)-Ni^{2+}(B)}$ . In this case the lattice parameter increases monotonically with the increase of  $Sn^{4+}$  concentration. For the  $Sn^{4+}$  concentration of greater than 0.004 the exchange integrals reflect the change in the lattice parameter. However, for the concentration less than 0.004, the change of ionic separation and exchange constant ( $J_{Ni^{2+}(B)-Ni^{2+}(B)}$ ) show contradictory trends. One would suspect that the outermost 4d electrons of  $Sn^{4+}$  contribute to this trend. However, a satisfactory elucidation of this problem can be achieved by  $^{119}Sn$  Mössbauer spectroscopy of the system.

In Chapter 6 we present some new findings in few iron complexes like ferrous ammonium sulphate hexahydrate, sodium nitorprusside, potassium ferricyanide, red and black Roussin salts. The induced Stark effect was observed in all the systems by a high resolution Mössbauer spectrometer.

In the end we have summarized the entire work. A few problems are proposed for the future study. It is hoped

that the present work has contributed to our knowledge of the hyperfine interactions of substituted Ni-Zn ferrite and the induced Stark effect in iron complexes, leading to a knowledge of their microscopic structure and bonding characteristics.

## REFERENCES

1. D.C. Khan, M. Misra and A.R. Das, J. Appl. Phys. 53, 2722 (1982).
2. D.C. Khan and M. Misra, Bull. Mater. Sci., 17, 253 (1985).
3. A.R. Das, V.S. Ananthan and D.C. Khan, J. Appl. Phys. 57, 4189 (1985).
4. C. Prakash and J.S. Baijal, Sol. State. Commun. 50, 557 (1984).
5. J.S. Baijal and C. Prakash, Proc. of the Forth International Conf. on Ferrites, Part II, San Francisco, California, Oct. 31-Nov 2, 1984, p-187.
6. N.V. Nair and D.C. Khan, Phys. Rev. B, 24, 5417 (1981).

## CHAPTER 1

### FUNDAMENTALS OF MÖSSBAUER SPECTROSCOPY

#### 1.1 *Introduction* :

Mössbauer effect [1] was discovered by R.L. Mössbauer, a German Physicist, in 1958. This discovery ushered in a very powerful technique in the field of hyperfine interactions. The unlimited potentialities of this discovery led to its rapid development into a scientific discipline and its immense application in the fields of physics, chemistry, metallurgy, biophysics, biochemistry, earthscience, and many other areas. The words of R.L. Mössbauer which he cited in his Nobel Laureate speech of Dec. 1961 have proved to be prophetic :

"We may therefore hope that this young branch of physics stands only at its threshold, and that it will be developed in the future, not only to extend the applications of existing knowledge but to make possible new advances in the existing world of unknown phenomenon and effects."

The field of hyperfine interaction with special reference to Mössbauer spectroscopy is treated in a number of books, reviews and monographs [2-13] in detail. We, therefore, give here a brief discription of the subject.

Mössbauer effect is sometimes referred to as the resonance fluorescence of  $\gamma$ -rays or the recoilless emission and absorption of  $\gamma$ -rays or as the zero phonon emission and absorption of  $\gamma$ -rays when the emitting nuclei are embedded in a solid. These names describe the physics of the phenomenon.

### 1.2 The Mössbauer Effect :

Let a nucleus of mass  $M$  which is at rest radiate a gamma ray photon of energy  $E_\gamma^s$  in decaying from excited state  $E_{ex}$  to the ground state  $E_{gr}$ . The recoil energy  $E_R$  imparted to the emitting nucleus may be obtained by the application of the law of conservation of linear momentum. The recoil energy is given by

$$E_R = \frac{(E_\gamma^s)^2}{2MC^2} \approx \frac{E_\gamma^2}{2MC^2} \quad (1.1)$$

(since  $E_R \ll MC^2$ )

here  $C$  is the velocity of light. The conservation of energy yields

$$E_o = E_{ex} - E_{gr} = E_\gamma^s + E_R$$

or  $E_\gamma^s = E_o - E_R \quad (1.2)$

In the same way we can consider the excitation of the system from the ground state  $E_{gr}$  to the excited state  $E_{ex}$  by absorption of a gamma photon and realise that the energy

$E_{\gamma}^a$  of the incident photon must provide an extra amount of recoil energy  $E_R$  over and above the excitation energy  $E_o$  for the process to occur. Hence,

$$E_{\gamma}^a = E_o + E_R \quad (1.3)$$

It is well known that the excited state  $E_{ex}$  of the nucleus does not possess a single energy but is characterised by a spectral line shape  $\omega(E)$  centred around  $E_o$  such that

$$\omega(E) = [1 + 4(E - E_o^2)/\Gamma^2]^{-1} \quad (1.4)$$

here  $\Gamma$ , the natural linewidth, is related to the mean life time,  $\tau$ , by Heisenberg's uncertainty relation

$$\Gamma \cdot \tau = \hbar \quad (1.5)$$

The energy of the stable ground state,  $E_{gr}$ , is very sharp because it is characterised by  $\Gamma \rightarrow 0$  and  $\tau \rightarrow \infty$ . Thus in the transition from the excited state to the ground state, the photon displays a lineshape similar to the eq. (1.4) but centred around  $E_{\gamma}^s$ . Similarly, the energy of photon which can induce a transition from the ground state to the excited state also displays the same distribution given by eq. (1.4) but centred around  $E_{\gamma}^a$ . The resonant absorption or emission of  $\gamma$ -rays takes place ideally for  $E_{\gamma}^a = E_{\gamma}^s$ , but will also occur as long as the following two distribution function overlap considerably :

$$\omega_s(E) = \left[ 1 + \frac{4(E-E_s^s)^2}{\Gamma^2} \right]^{-1} \quad (1.6a)$$

$$\omega_a(E) = \left[ 1 + \frac{4(E-E_a^s)^2}{\Gamma^2} \right]^{-1} \quad (1.6b)$$

In fig (1.1) we have shown the nature of this overlap in two cases : (a) the atomic system (emission of an optical photon) where  $E_R \ll \Gamma$  and, therefore, the emission and absorption lines overlap almost completely; (b) the nuclear system (the emission of a gamma-ray photon) where  $E_R \gg \Gamma$  (e.g., in case of  $^{57}\text{Fe}$  nucleus  $E_R = 1.957 \times 10^{-3}$  eV and  $\Gamma = 4.55 \times 10^{-9}$  eV) and, therefore, the overlap of emission and absorption lines is not possible. Thus we see that nuclear resonance absorption is not possible in isolated atoms.

The unsatisfactory situation with respect to nuclear resonance absorption first changed in 1950 with Moon's [14] experiment. The fundamental idea behind his experiment was the compensation of the recoil energy loss of the gamma ray photon. The radio active source was moved at a suitably high velocity towards the absorber. The displacement of the emission spectrum towards higher energies achieved in this way through the Doppler effect was able to produce a measurable nuclear fluorescence effect.

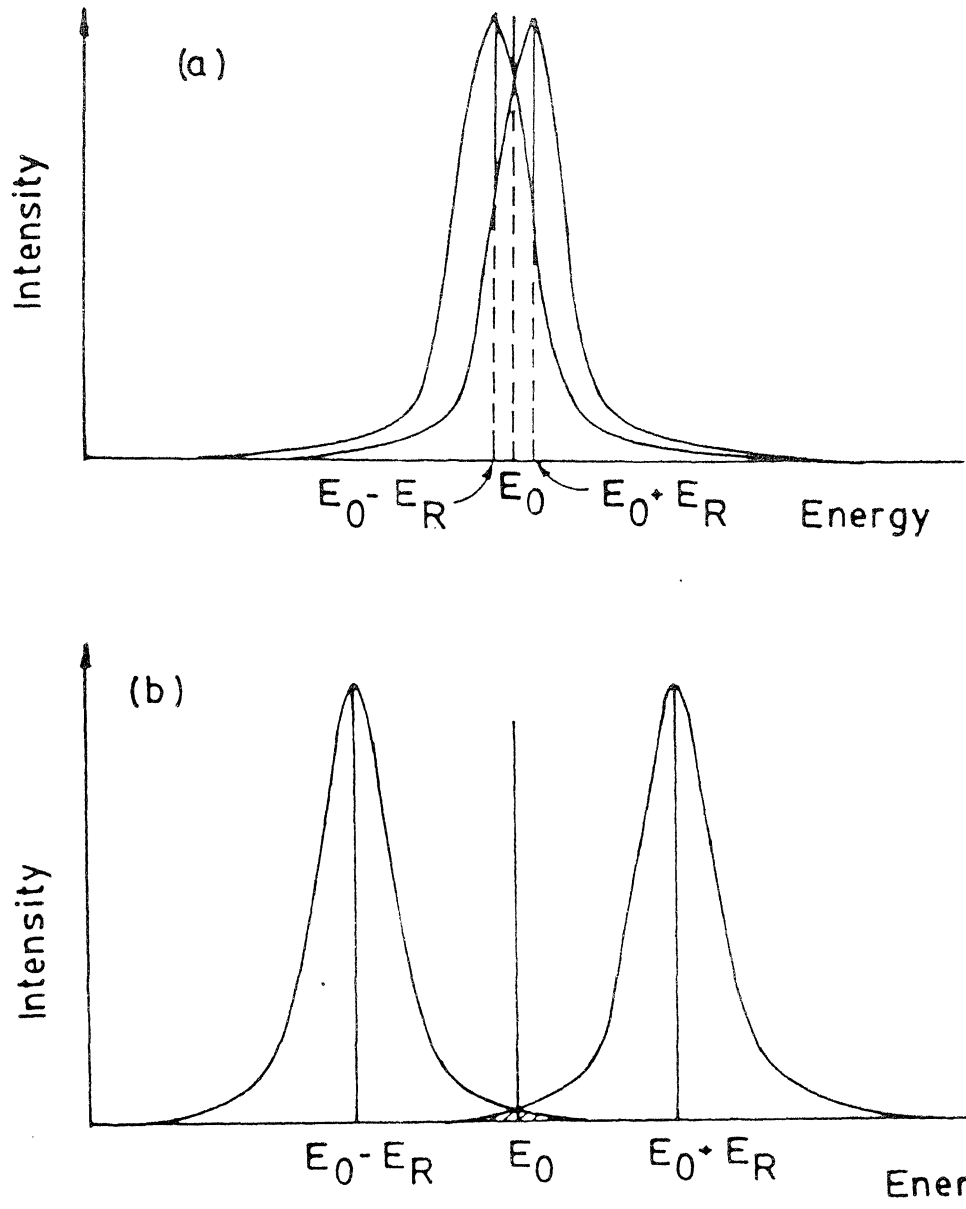


FIG. 1.1 Overlap of the emission and absorption lines showing the relation between  $E_0$ ,  $E_{\gamma}^s$ ,  $E_{\gamma}^a$  and for two cases : (a) Optical case , (b) Nuclear case .

In the solid state a Mössbauer active atom under consideration is bound to the lattice. If a  $\gamma$ -ray is emitted from the excited Mössbauer nucleus, the concomitant recoil energy may be assumed to be consisted of two parts

$$E_R = E_{tr} + E_{vib} \quad (1.7)$$

$E_{tr}$  is the translational energy transferred through linear momentum to the crystallite as a whole, which accomodates the Mössbauer nucleus under consideration.  $E_{tr}$  can be calculated by using the eq. (1.1) in which M stands now for the mass of the whole crystallite. Since the mass of the crystallite is very large as compared to the mass of a single nucleus,  $E_{tr}$  turns out to be many orders of magnitude smaller than  $\Gamma$  and can therefore be neglected.

Most of the recoil energy  $E_R$  is, thus, converted into mean lattice vibrational energy  $E_{vib}$ . If recoil energy  $E_R$  is larger than the characteristic lattice vibration (phonon) energy but smaller than the displacement energy ( $\sim 25$  eV) then the decaying Mössbauer atom will remain in its lattice position and will dissipate  $E_{vib}$  by heating the surrounding lattice. In case, however,  $E_R$  is smaller than the characteristic phonon energy ( $\sim 10^{-2}$  eV for solids),  $E_{vib}$  causes a change in the vibrational energy of the oscillators by the integral multiples of the phonon energy

$h\nu_E$  ( $\nu_E$  represents the Einstein frequency). There is a certain probability  $f$  that no lattice excitation (zero phonon process) takes place during the gamma emission or absorption process.  $f$  is called the recoil free fraction and denotes the fraction of nuclear transitions which occur without recoil. A general expression for the probability of recoilless emission or absorption of the  $\gamma$ -rays is given by

$$f = \exp [-k^2 \langle x^2 \rangle] \quad (1.8)$$

where  $k$  is the wave vector and  $\langle x^2 \rangle$  is the mean square displacement of the nucleus from its equilibrium position. In the Debye model of solids, the recoilfree fraction  $f$  is given by the following expression,

$$f = \exp \left[ -\frac{3E_R}{2k_B\theta_D} \left\{ 1 + 4 \left( \frac{T}{\theta_D} \right)^2 \int_0^{\theta_D/T} \frac{x}{e^x - 1} dx \right\} \right] \quad (1.9)$$

where the symbols have their usual meaning.

In the limit of low and high temperature the above equation reduces to

$$f = \exp \left[ -\frac{3E_R}{2k_B\theta_D} \right] ; \text{ if } T \ll \theta_D \quad (1.10a)$$

and

$$f = \exp \left[ -\frac{6E_R T}{k_B\theta_D^2} \right] ; \text{ if } T > \theta_D \quad (1.10b)$$

To observe resonance fluorescence the probability of recoilless transition,  $f$ , should be large and this suggests that  $E_R \ll k_B \theta_D$ . Since  $E_R \propto E_0^2$ , we should choose low energy Mössbauer nuclide. However, for very low energy,  $\gamma$ -rays will have a poor emission yield and we would need very thin absorbers. Depending on  $\theta_D$  values, the nuclear resonance fluorescence has been mostly observed for  $10 \text{ KeV} < E_0 < 150 \text{ KeV}$ .

The real breakthrough in nuclear resonance absorption of gamma rays came with Mössbauer's experiment at Heidelberg. He intended to measure the lifetime of the  $129 \text{ KeV}$  state in  $^{191}\text{Ir}$ . Nuclear resonance absorption was planned to be achieved by making the emission line and the absorption line partially overlap each other through thermal broadening. By lowering the temperature it was generally expected that the transition lines would sharpen up because of less Doppler broadening and consequently smaller degree of overlap. However, the opposite was observed by Mössbauer. This was explained by him as the increase in the probability of recoilfree transition of the  $\gamma$ -photons, and henceforth resonance fluorescence of  $\gamma$ -rays came to be known as Mössbauer effect.

Mössbauer effect has provided us with an extremely precise method for measuring the small energy shifts of the nuclear energy levels. In Mössbauer experiment either the

soure or the absorber is subjected to a velocity programme to give an appropriate Doppler energy shifts to the  $\gamma$ -rays so that one may obtain the resonance intensity as a function of energy.

### 1.3 Hyperfine Interaction :

In the previous section (1.2) we dealt with transitions between unperturbed energy levels of "bare" nuclei and have called the transition energy  $E_0$ . In reality, we deal with atoms and molecules in a solid. Nuclei are, therefore, generally affected by electric and magnetic fields, which may be created by shell electrons and the charges in the near neighbourhood. The nuclei may also possess various kinds of nuclear moments. These generally interact with the electric and magnetic fields in the nuclear region and perturb the nuclear energy levels. This perturbation, called nuclear hyperfine interaction, may be such that it only shifts the nuclear energy levels, as is the case in electric monopole interaction, or it splits degenerate nuclear levels into sublevels without shifting the centroid of the multiplet, as are observed in electric quadrupole interaction and magnetic dipole interaction. Only these three kinds of interactions have to be considered in Mössbauer spectroscopy. A Mössbauer spectrum, in general, reflects the nature and strength of the hyperfine interaction.

### 1.3.1 Electric Monopole Interaction; The Isomer Shift :

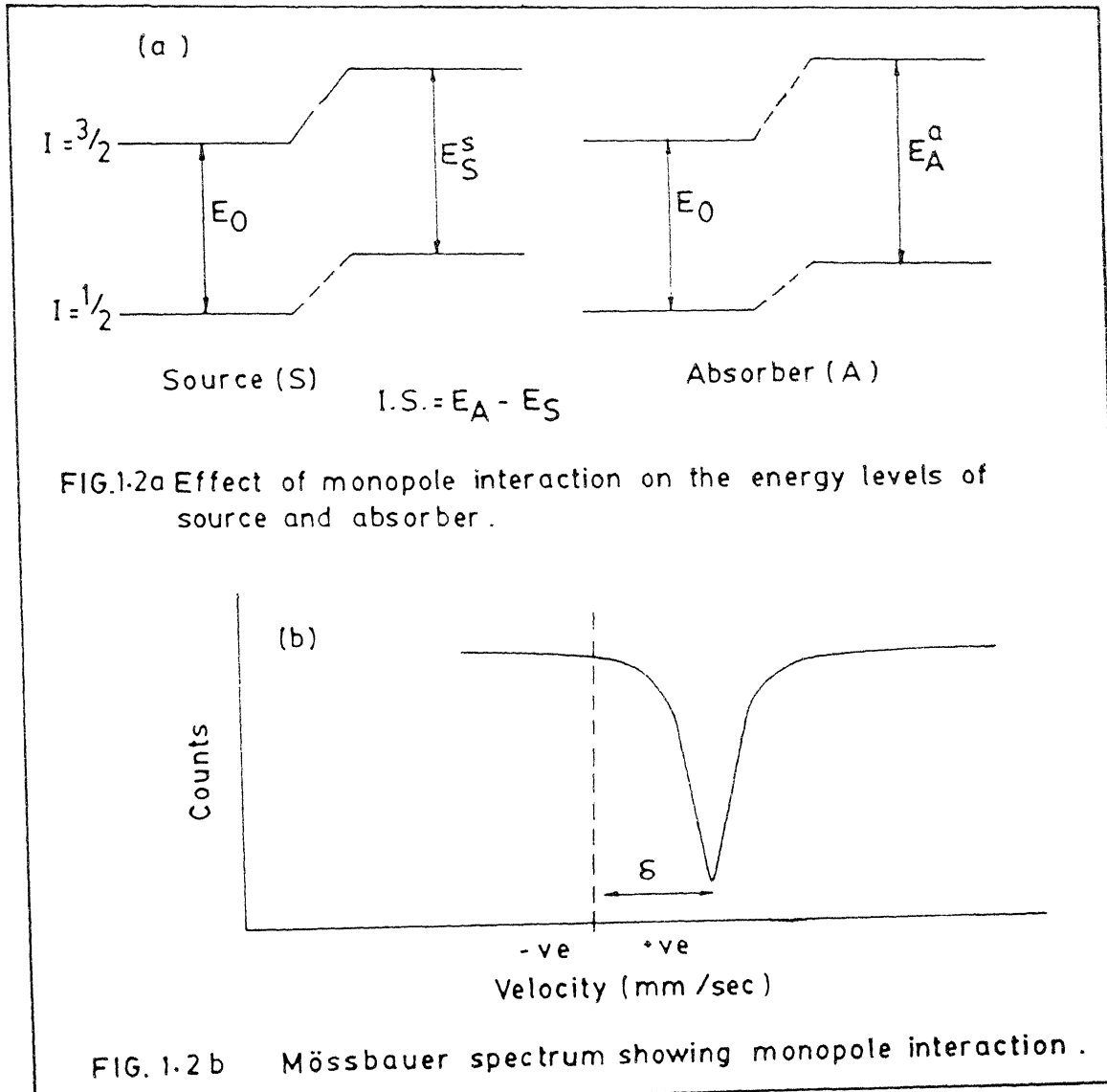
The isomer shift  $\delta$  is the result of electric monopole interaction of the nuclear charge distribution (because of the finite size of the nucleus) with the electron charge density at the nucleus (s-electrons). The fact that the environment of the source and absorber nuclei are different, the amount of interaction between s-electron density at the nucleus and the nuclear charge is different in the source and the absorber. This is schematically shown in fig. (1.2a) and the corresponding Mössbauer spectrum is shown in fig. (1.2b).

In the non-relativistic approximation, the isomer shift is expressed as

$$\delta = \left( \frac{2\pi}{5} \right) Z e^2 \left[ R_e^z - R_g^z \right] \left[ |\psi(0)|_A^2 - |\psi(0)|_S^2 \right] \quad (1.11)$$

here  $Z$  is the atomic number;  $e$ , the electronic charge;  $R_e$  and  $R_g$ , the radius of the nucleus in the excited and ground state respectively and;  $|\psi(0)|_A^2$  and  $|\psi(0)|_S^2$  are the density of the s-electrons at the nucleus of absorber and source respectively.

In heavy elements the wavefunction  $\psi$  is subject to modification by relativistic effects. Therefore, the electron density at the nucleus will be modified as well and eq. (1.11) require a relativistic correction. Using



Dirac wave function and first order perturbation theory, it has been shown that this correction simply consists of a dimensionless factor  $S(Z)$ , which is introduced into the above expression for  $\delta$ .

$$\delta = \left( \frac{2\pi}{5} \right) Ze^2 S(Z) \left[ R_e^2 - R_g^2 \right] \left[ |\psi(0)|_A^2 - |\psi(0)|_S^2 \right] \quad (1.12)$$

The values of the relativity factor  $S(Z)$  for  $Z = 1$  to 96 are given in [15].  $S(Z) = 1.32$  for iron ( $Z = 26$ ). In Mössbauer effect studies, where one compares compounds of a given Mössbauer nuclide, the problem of relativistic correction does not arise because the relativity factor  $S(Z)$  is constant for all compounds of a given Mössbauer nuclide. Moreover, if one uses a particular Mössbauer source (e.g.  $^{57}\text{Co-in-Rh}$ ) and looks at various absorbers of a given Mössbauer nuclide then  $|\psi(0)|_S^2$  in eq. (1.11) is constant for all the absorbers. The term  $\left( \frac{2\pi}{5} \right) Ze^2 (R_e^2 - R_g^2)$  in eq. (1.11) is also constant for a particular nuclear transition. Therefore, the isomer shift  $\delta$  is a linear function of the charge density  $|\psi(0)|_A^2$  in the absorber.

The isomer shift data are commonly used to study the chemical structure, oxidation state, bonding etc. in compounds. The isomer shift values of the same element in different systems are related to changes in the electron densities and are, therefore, used to find the structure and phase of the system.

### 1.3.2 The Electric Quadrupole Interaction :

In the discussion of electric monopole interaction it is assumed that the nuclear charge distribution is spherically symmetric and uniform. But this is an ideal condition and the nuclear charge distribution deviates from spherical symmetry. This deviation may be different in different nuclear states. The nuclei in the state  $I = 0, \frac{1}{2}$  do not possess an observable quadrupole moment. Any nucleus in the state  $I > \frac{1}{2}$  has a non-zero quadrupole moment. The quadrupole moment is a tensor quantity with elements

$$Q_{ij} = \int \rho_n(\vec{r}) x_i x_j d^3x \quad (1.13)$$

where  $\rho_n(\vec{r})$  is the nuclear charge and  $x_i, x_j$  are the cartesian components of the position vector  $\vec{r}$ .

A non-zero electric quadrupole moment interacts with the electric field gradient (EFG) present at the site of the Mössbauer nuclide. The Hamiltonian of the interaction is given by

$$\mathcal{H}(e2) = \hat{Q} \cdot (\hat{\nabla} \hat{E}) \quad (1.14)$$

Here  $\hat{Q}$  denotes the operator of the nuclear electric quadrupole moment and  $(\hat{\nabla} \hat{E})$  represents the EFG tensor operator.

A point charge  $q$  at a distance  $r = (x^2 + y^2 + z^2)^{1/2}$  from the nucleus produces a potential  $V(r) = q/r$  at the nucleus. The gradient of the electric field at the nucleus is

$$EFG = \nabla \vec{E} = -\nabla \nabla V = - \begin{bmatrix} V_{xx} & V_{xy} & V_{xz} \\ V_{yz} & V_{yy} & V_{yz} \\ V_{zx} & V_{zy} & V_{zz} \end{bmatrix}$$

where

$$V_{ij} = \frac{\partial^2 V}{\partial i \partial j} \quad (i, j = x, y, z) \quad (1.15)$$

The electric field gradient is a (3x3) second-rank tensor. Only five of the nine components are independent parameters. Three of the off diagonal elements are dependent because of the symmetric form of the EFG tensor, i.e.  $V_{xy} = V_{yx}$ ,  $V_{xz} = V_{zx}$ ,  $V_{yz} = V_{zy}$ . The Laplace's equation for the potential requires that the EFG be a traceless tensor

$$V_{xx} + V_{yy} + V_{zz} = 0 \quad (1.16)$$

Hence only two of the diagonal elements are independent. To avoid complexity, a unique axis system called the "principal axes of the EFG tensor" is defined such that the off-diagonal elements of EFG tensor vanish and the diagonal elements are ordered as

$$|V_{zz}| \geq |V_{yy}| \geq |V_{xx}| \quad (1.17)$$

Another parameter usually known as asymmetry parameter,  $\eta$ , is defined such that

$$\eta = \frac{V_{xx} - V_{yy}}{V_{zz}} \quad (1.18)$$

and

$$0 \leq \eta \leq 1$$

Finally, the interaction between the  $z$  component of EFG and electric quadrupole moment gives the Hamiltonian as

$$\mathcal{H}(e2) = \frac{eQV_{zz}}{4I(2I-1)} \left[ 3\hat{I}_z^2 + \hat{I}_z + \eta \left( \hat{I}_+^2 + \hat{I}_-^2 \right) / 2 \right] \quad (1.19)$$

Here  $I$  is the nuclear spin quantum number,  $\hat{I}$  is the nuclear spin operator,  $\hat{I}_{\pm} = \hat{I}_x \pm i\hat{I}_y$  are ladder operators, and  $\hat{I}_x, \hat{I}_y, \hat{I}_z$  are the nuclear spin component operators along  $x, y, z$  axes respectively. Since the separation of nuclear energy levels is usually much larger than the magnitude of the Hamiltonian  $\mathcal{H}(e2)$ , therefore, the first order perturbation theory gives the energy correction as

$$E_Q = \frac{eQV_{zz}}{4I(2I-1)} \left[ 3m_I^2 - I(I+1) \right] \left( 1 + \frac{\eta}{3} \right)^{1/2} \quad (1.20)$$

Here  $m_I = I, I-1, I-2, \dots, -I$  is the nuclear magnetic spin quantum number. The effect of the electric quadrupole interaction in a Mössbauer nuclide with  $I = 3/2$  as the excited state and  $I = 1/2$  as the ground state is shown in fig. (1.3a). The excited state ( $I=3/2$ ) is split into two doubly degenerate substates  $\left| \frac{3}{2}, \pm \frac{3}{2} \right\rangle$  and  $\left| \frac{3}{2}, \pm \frac{1}{2} \right\rangle$ .

There is no splitting in the nuclear ground state ( $I = \frac{1}{2}$ ), because  $Q = 0$ . For an axially symmetric EFG, i.e.,  $\eta = 0$  we obtain the shift in substates as follows

$$E_Q (\pm \frac{3}{2}) = \frac{eQV_{zz}}{4} ; \quad \text{for the state } \left| \frac{3}{2}, \pm \frac{3}{2} \right\rangle$$

and

$$E_Q (\pm \frac{1}{2}) = - \frac{eQV_{zz}}{4} ; \quad \text{for the state } \left| \frac{3}{2}, \pm \frac{1}{2} \right\rangle$$

The difference in energy  $\Delta E_Q$  between the two substates is

$$\Delta E_Q = E_Q (\pm \frac{3}{2}) - E_Q (\pm \frac{1}{2})$$

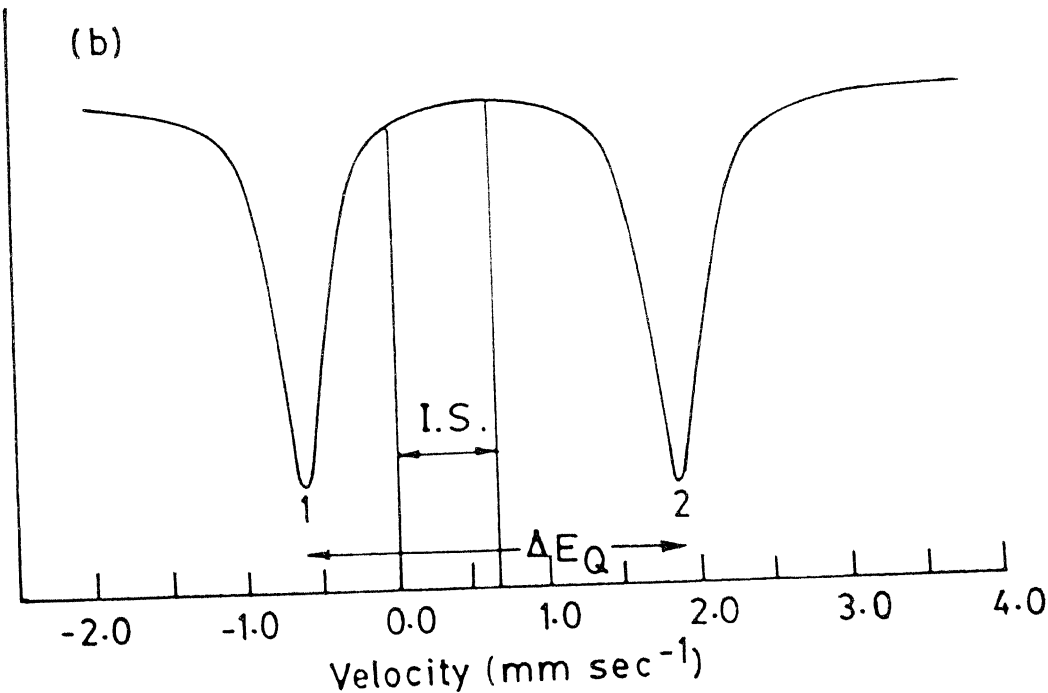
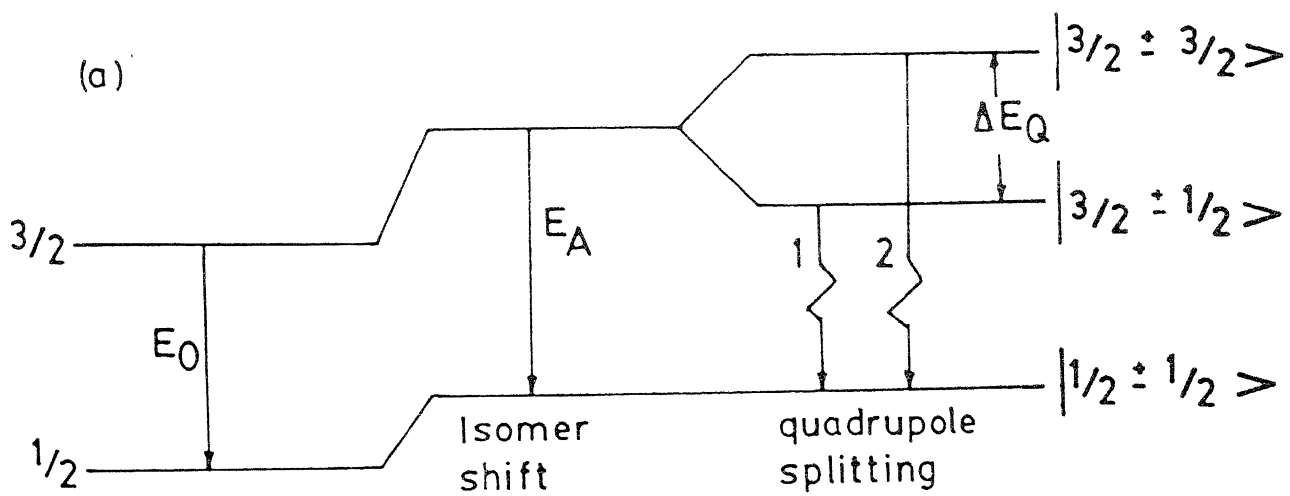
or

$$\Delta E_Q = \frac{eQV_{zz}}{2}$$

The resultant Mössbauer spectrum in case of quadrupole splitting is shown in fig. (1.3b). The isomer shift is also shown in this picture, because the electric monopole interaction is always present due to the difference in the density of s-electron wavefunctions at the site of the nucleus in the source and the absorber.

### 1.3.3 Sternheimer Anti-Shielding Factor :

In general there are two fundamental sources of EFG:  
 (i) charges on distant atoms or ions, surrounding the



1.3 Effect of the quadrupole interaction on the nuclear energy levels of absorber (a), and the resulting Mössbauer spectrum showing the quadrupole splitting and isomer shift.(b).

Mössbauer atom in non-cubic symmetry, usually called the lattice or ligand contribution; (ii) non-cubic electron distribution in partially filled valence orbitals of the Mössbauer atom, usually called the valence electron contribution. The strength of the quadrupole interaction at the nuclear site gets considerably modified, as shown by Sternheimer [16-18], due to the presence of atomic electrons. The shell of a Mössbauer atom gets distorted in the presence of a non-cubic charge distribution in the surrounding crystal lattice in such a way that the lattice contribution to EFG is greatly enhanced. The effective EFG at nuclear site can be written as

$$V_{zz} = (1 - \gamma_{\infty}) V_{zz}^{\text{latt}} + (1 - R) V_{zz}^{\text{local}} \quad (1.21)$$

where  $V_{zz}^{\text{latt}}$  is the EFG at nuclear site due to the ions of the lattice in absence of atomic electrons. An additional EFG  $- \gamma_{\infty} V_{zz}^{\text{latt}}$  appears at the nuclear site due to the polarization of electron cloud. This phenomenon is known as "Sternheimer anti-shielding" and the factor  $\gamma_{\infty}$  is called the anti-shielding factor. The values of  $(1 - \gamma_{\infty})$  for medium and heavy ions lie in the range of 10 to 80. For iron compounds it is estimated of the order of 10. The factor R in eq. (1.21) correspond to atomic shielding of EFG at the nucleus due to the unfilled orbitals ( $V_{zz}^{\text{local}}$ ). The factor R has been estimated to be 0.2 - 0.3 for iron

and tin. The above picture is not exactly valid for metals and alloys because of the presence of conduction electrons. The EFG at nuclear site in these cases cannot be wholly as due to lattice and valence electron contributions, as the significant contribution from conduction electrons is also well established.

#### 1.3.4 Magnetic Dipole Interaction :

A nucleus with spin  $I > 0$  has a magnetic dipole moment  $\vec{\mu}$ , and if there is a magnetic field  $\vec{H}$  at the nucleus then the magnetic dipole moment interacts with the magnetic field and the corresponding Hamiltonian is

$$\mathcal{H} (m_1) = -\vec{\mu} \cdot \vec{H} = -g_N \beta_N \vec{I} \cdot \vec{H} \quad (1.22)$$

here  $g_N$  is the nuclear Landé splitting factor and  $\beta_N$  is the nuclear Bohr magneton. Using the first order perturbation theory the energy correction due to magnetic dipole interactions is

$$E_m (m_1) = -g_N \beta_N \hbar m_1 \quad (1.23)$$

where

$$m_1 = +I, I-1, \dots, -I$$

Thus we see that the magnetic dipole interaction splits a nuclear state  $|I\rangle$  into  $2I+1$  equally spaced substates. Each of the substates is characterised by the nuclear magnetic spin quantum number  $m_1$ . The allowed  $\gamma$ -transitions are for

$\Delta I = 1$  and  $\Delta m_I = 0, \pm 1$ . In case of  $^{57}\text{Fe}$ , the six allowed transitions are shown in fig. (1.4), giving rise to six finger pattern. In practice, however, pure nuclear magnetic dipole interactions are rarely encountered. We, therefore, observe that a nuclear state is simultaneously perturbed by both magnetic dipole and electric quadrupole interactions. In this situation, the substates of  $I = 3/2$  state (in case of  $^{57}\text{Fe}$ ) are no longer equally spaced. If  $\mathcal{K}(e2) \ll \mathcal{K}(m1)$  and assuming EFG tensor to be axially symmetric whose principal axis makes an angle  $\theta$  with the axis of magnetic field then the first order perturbation theory yields the general expression of energy correction as

$$E = -g_N \beta_N H m_I + (-1)^{|m_I| + \frac{1}{2}} \left( \frac{eQV_{zz}}{8} \right) (3 \cos^2 \theta - 1) \quad (1.24)$$

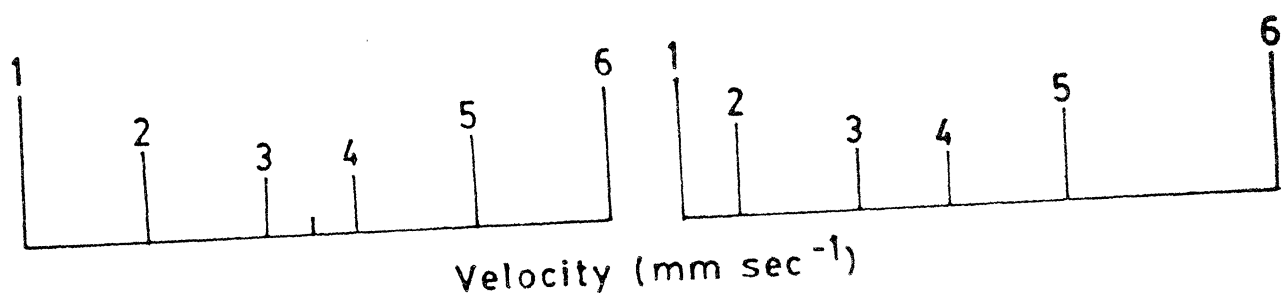
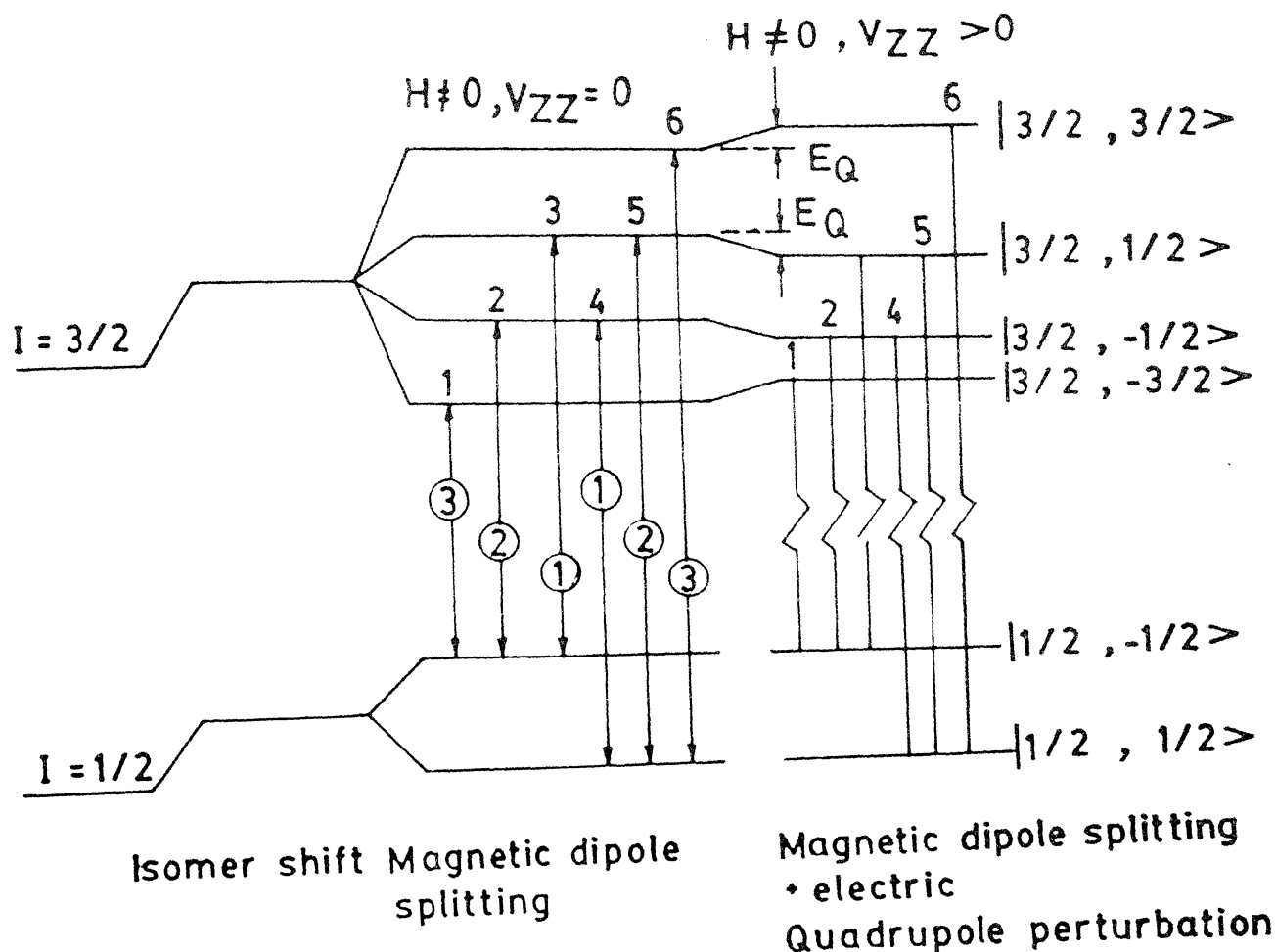
#### 1.4 Lattice Vibrational Anisotropy (Goldanskii-Karyagin Effect) :

The intensity of the Mössbauer absorption peak depends on the recoil-free factor

$$f = \exp [-\langle (\vec{k} \cdot \vec{x})^2 \rangle]$$

If the gamma ray direction  $\vec{k}$  is expressed in polar coordinates  $\theta$  and  $\Phi$  with respect to EFG axis, we can write

$$\langle (\vec{k} \cdot \vec{x})^2 \rangle = k^2 [\{\langle x_x^2 \rangle \cos^2 \phi + \langle x_y^2 \rangle \sin^2 \phi\} \sin^2 \theta + \langle x_z^2 \rangle \cos^2 \theta]$$



3.1.4 Effect of the magnetic hyperfine interaction on the nuclear energy levels of the absorber.

If the amplitudes of vibration are not equal in all the directions then the recoil-free fraction becomes a function of  $\theta$  and  $\phi$ . For  $^{57}\text{Fe}$  quadrupole doublet for a polycrystalline sample the intensity ratio of the two lines is given by

$$\frac{M_\pi}{M_\sigma} = \frac{\int_0^{2\pi} \int_0^\pi f(\theta, \phi) (1 + \cos^2 \theta) \sin \theta d\theta d\phi}{\int_0^{2\pi} \int_0^\pi f(\theta, \phi) \left(\frac{5}{3} - \cos^2 \theta\right) \sin \theta d\theta d\phi}$$

for axially symmetric vibrations

$$\langle x_x^2 \rangle = \langle x_y^2 \rangle = \langle x_\perp^2 \rangle \neq \langle x_z^2 \rangle = \langle x_{||}^2 \rangle$$

and

$$f(\theta, \phi) = \exp [-k^2 \langle x_\perp^2 \rangle] \exp [k^2 (\langle x_\perp^2 \rangle - \langle x_{||}^2 \rangle) \cos^2 \theta]$$

resulting in

$$\frac{M_\pi}{M_\sigma} = \frac{\int_0^\pi \exp [-k^2 (\langle x_{||}^2 \rangle - \langle x_\perp^2 \rangle) \cos^2 \theta] (1 + \cos^2 \theta) \sin \theta d\theta}{\int_0^\pi \exp [-k^2 (\langle x_{||}^2 \rangle - \langle x_\perp^2 \rangle) \cos^2 \theta] \left(\frac{5}{3} - \cos^2 \theta\right) \sin \theta d\theta}$$

Thus we see that even for random orientation of crystallites, the intensities of the two lines may be different. The intensities of the magnetically split lines are also modified for the same reasons, i.e. the anisotropy of the recoil-free fraction. This effect is known as Goldanskii-Karyagin effect. As the vibrational anisotropy is an increasing function of temperature the asymmetry in

intensities related to this effect also increases with temperature.

### 1.5 Asymmetric Quadrupole Doublet :

The observed quadrupole doublet may be asymmetric due to the following three reasons :

- (i) Lack of randomness of crystallites (texture effect);
- (ii) Anisotropy of Debye-Waller factor;
- (iii) Relaxation effect.

The first one has the distinct property that the ratio of intensities strongly depends upon the angle between the gamma-ray direction and the sample surface. The second and third effects are independent of sample orientation but depends very much on temperature. The intensity ratio due to anisotropy of the Debye-Waller factor is approximately 1 at low temperature and increases with increasing temperature. In polycrystalline materials, it is often difficult to differentiate between the Goldanskii-Karyagin effect and the texture effect. However, most metals and alloys have cubic or almost cubic crystallographic structures, thus the recoil-free fraction can be regarded as isotropic and the Goldanskii-Karyagin effect can be neglected. On the other hand, the texture or preferred orientations of the crystallites in certain directions might be very pronounced. For the third case,

the asymmetry ratio will strongly depend on the relaxation mechanism. If the fluctuations in the internal magnetic field are due to spin-lattice relaxation we expect relaxation time to decrease with increasing temperature. This means that raising the temperature will decrease the asymmetry, an effect opposite to temperature dependence of Goldanskii-Karyagin effect. On the other hand, if the fluctuations in the magnetic field are due to spin-spin relaxation, the asymmetry will depend on the paramagnetic ions.

#### *1.6 Mössbauer Spectroscopy vis-a-vis other Techniques to Investigate Hyperfine Interactions :*

Many other techniques such as NMR, EPR and PAC have been developed to study the hyperfine interactions. In this section we will bring out the relative advantages and disadvantages of these techniques vis-a-vis Mössbauer spectroscopy.

In Mössbauer spectroscopy, the line width of the resonance line is limited by the life time of the nucleus in the excited state. This corresponds to  $10^4$  -  $10^5$  gauss, which is quite broad as compared to the NMR line widths. This has both merits as well as demerits. This means that the precision of NMR measurement is much higher but it is difficult to detect the NMR lines. In such cases, the two

techniques can be used together. Mössbauer spectroscopy could be used to locate the lines and then the NMR could be used to accurately measure the splittings. In the presence of strong spin-spin interactions between neighbouring ions, the NMR lines may be broadened so much that it cannot be observed at all. Similar situation may also arise in the presence of local inhomogeneous surroundings such as in alloys. Indeed, in alloys, it is very difficult to measure hyperfine interaction by NMR except in very dilute cases. Mössbauer spectroscopy does not suffer from such drawbacks.

Another limitation of both NMR and EPR, particularly in metals, arises because of skin effect. As a result, the measurements can be limited to only small particles. In contrast, in Mössbauer spectroscopy, one can use large crystals. In NMR techniques, one is essentially concerned with the splitting of the nuclear ground state and if the nuclear ground state has zero angular momentum, which is the case for even-even nuclei, then conventional resonance methods cannot measure hyperfine interactions. In contrast, in Mössbauer spectroscopy, one deals with a transition between two nuclear states and the above limitation therefore does not arise. Moreover, EPR is generally limited to atoms or ions where the electronic ground state is degenerate. The degeneracy is lifted by the application of magnetic field and transitions are then

observed between the resulting levels. It is unusual that electronic levels in the absence of magnetic field have a splitting which lies within the relatively fixed limits of the microwave frequency range. This is a drawback which does not exist for Mössbauer spectroscopy or the NMR.

PAC involves the measurement of the rotation and attenuation of the correlation pattern which implies that the unperturbed correlation pattern is already known. This is not always possible. Another drawback of PAC is that it is not easy to separate the electric quadrupole and magnetic hyperfine interactions. This is, however, comparatively easy in Mössbauer spectroscopy. Another distinct advantage of Mössbauer spectroscopy is the possibility of the measurement of monopole interaction leading to chemical shift. However, unlike to Mössbauer spectroscopy, PAC is not limited to low energies.

In the present thesis we study of microscopic structure and properties of  $Ti^{4+}$  and  $Sn^{4+}$  substituted nickel-zinc ferrites by determining the hyperfine parameters by Mössbauer experiment and analyzing them.

## REFERENCES

1. R.L. Mössbauer, *Z. Physik*, 151, 124 (1958).
2. Mössbauer Spectroscopy (Ed. by U. Gonser), Springer Verlag, Berlin (1975).
3. Mössbauer Effect and its Applications by V.G. Bhide, Tata McGraw-Hill Pub., New Delhi (1973).
4. Chemical Applications of Mössbauer Spectroscopy (Ed. by V.I. Goldanskii and R.H. Herber), Academic Press, New York (1968).
5. Mössbauer Isomer Shifts (Ed. by G.K. Shenoy and F.W. Wagner), North-Holland Pub. Co., Amsterdam (1978).
6. N.N. Greenwood and T.C. Gibb, "Mössbauer Spectroscopy", Chapman and Hall Ltd., London (1971).
7. G.M. Bancroft, "Mössbauer Spectroscopy, an Introduction for Inorganic Chemists and Geochemists", Mc-Graw-Hill, London (1973).
8. Mössbauer Effect (Ed. by L.S. Kothari, J.S. Baijal and S.P. Tewari), Academic Press, New Delhi (1984).
9. Applications of Mössbauer Spectroscopy, Volume I, (Ed. by R.L. Cohen) Academic Press, New York (1976).
10. An Introduction to Mössbauer Spectroscopy (Ed. by L. May) Plenum Press, New York-London (1971).
11. Mössbauer Spectroscopy and Transition Metal Chemistry by Philipp Gütlich, Rainer Link and Alfred Trautwein, Springer-Verlag (1978).

12. Mössbauer Effect : Principles and Applications by G.K. Wertheim, Academic Press, New York (1964).
13. The Mössbauer Effect by H. Frauenfelder, Benjamin, New York (1962).
14. P.B. Moon, Proc. Phys. Soc. London, 64, 76 (1951).
15. D.A. Shirley, Rev. Mod. Phys., 36, 339 (1964).
16. R.M. Sternheimer, Phys. Rev., 80, 102 (1950).
17. R.M. Sternheimer, Phys. Rev., 84, 244 (1951).
18. R.M. Sternheimer, Phys. Rev., 130, 1423 (1963).

## CHAPTER 2

## EXPERIMENTAL METHODS

2.1 *Introduction* :

The following instruments form the basic units of a Mössbauer Spectroscopy experimental arrangement :

- (i) Radioactive source which emits gamma-ray, e.g., 14.4 KeV gamma-ray emitted in the electron capture decay of  $^{57}\text{Co}$  to  $^{57}\text{Fe}$  nucleus [fig.(2.1)].
- (ii) Sample containing  $^{57}\text{Fe}$  nuclei (in case of  $^{57}\text{Fe}$  Mössbauer Spectroscopy) as an absorber.
- (iii) Mössbauer spectrometer having an electromechanical transducer for providing relative velocity between the source and the absorber.
- (iv) The dewar and the furnace for keeping the absorber at the required temperature.
- (v) A radiation detector for counting the gamma-rays (proportional counter in case of  $^{57}\text{Fe}$  Mössbauer spectroscopy).
- (vi) A storage device (the multichannel analyser) which stores the data as a function of relative velocity between the source and the absorber.

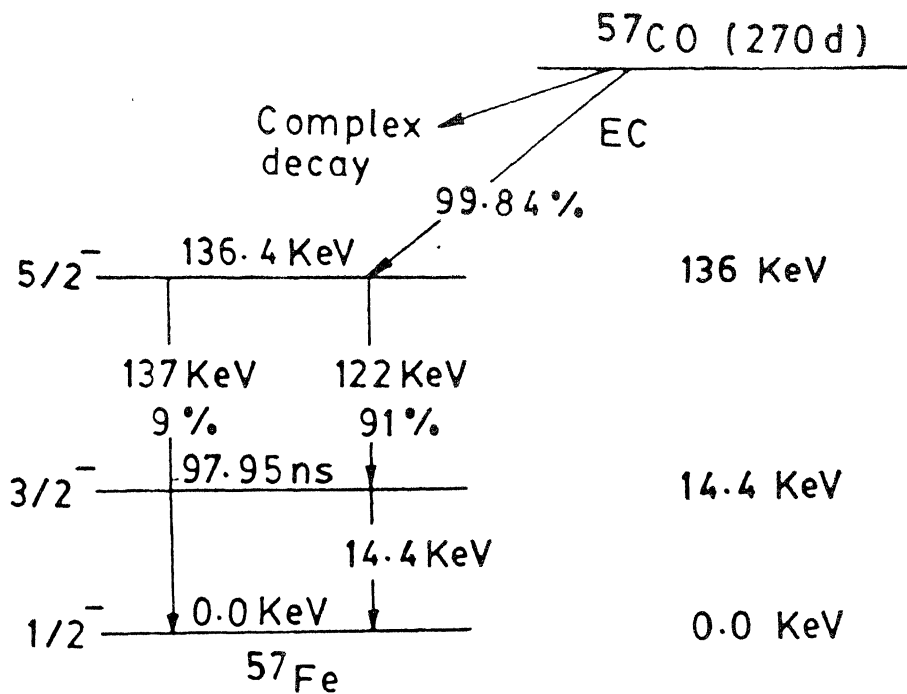


FIG. 2.1 RADIOACTIVE DECAY SCHEME OF  $^{57}\text{Co}$

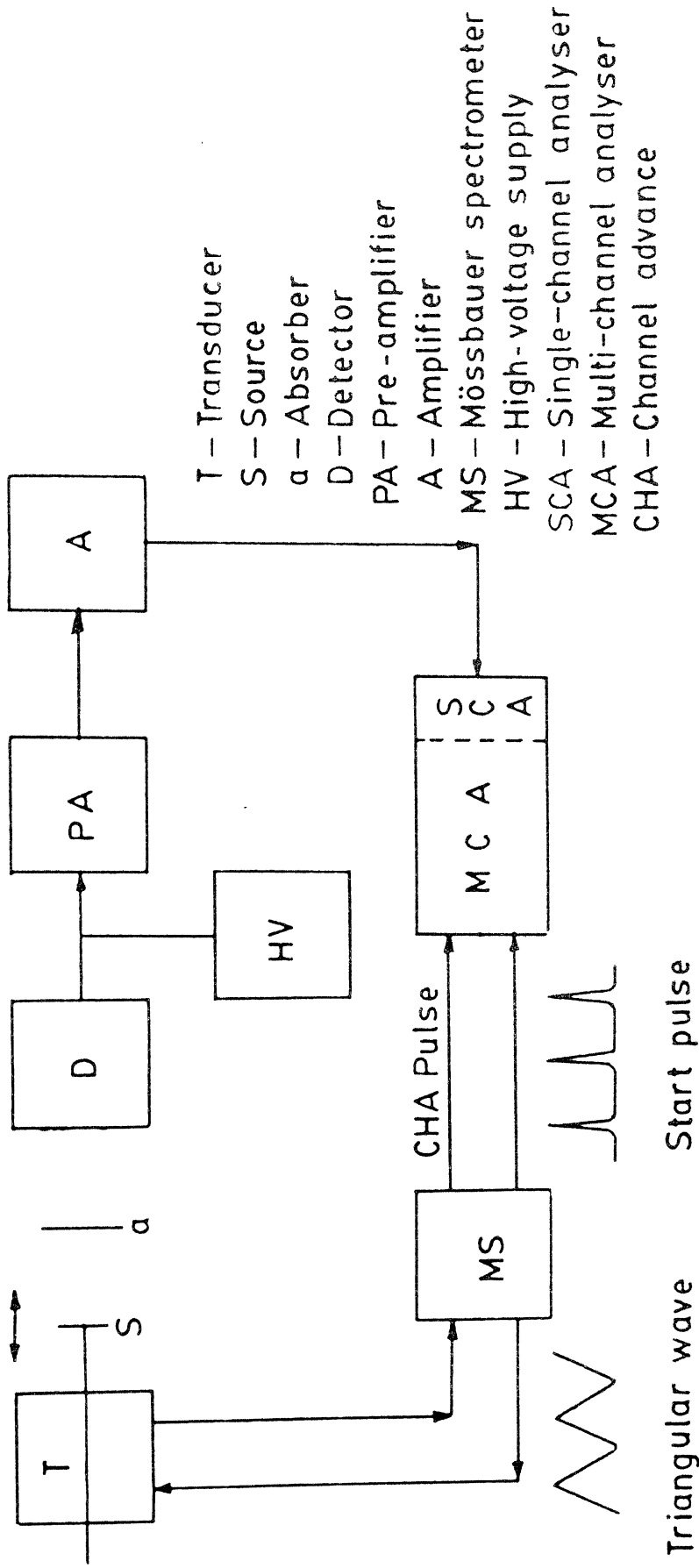


Fig. 2.2 Schematic diagram of various instruments involved in a Mössbauer effect experiment.

In this chapter we shall give brief description of the apparatus used in the present experimental work. Details of the general experimental methodology of Mössbauer spectroscopy have been reported in the literature [1-8] and, therefore, will not be reproduced here. A schematic block diagram of various instruments used in Mössbauer spectroscopy is shown in fig.(2.2).

## 2.2 Radioactive Mössbauer Source :

The radioactive source used in Mössbauer spectroscopy should have the following properties :

- (i) The source material should be deposited in a host matrix which is chemically stable.
- (ii) The emitted gamma-ray should have a single line (in the energy spectrum). In other words, there should be no electric field gradient or internal magnetic field at the site of the  $^{57}\text{Fe}$  nuclei in the Mössbauer source.
- (iii) Recoil-free fraction in the host matrix should be large.
- (iv) Line broadening caused by self-absorption, thickness etc. should be minimum.
- (v) The radiations which are not contributing to the Mössbauer effect such as the characteristic X-rays

and gamma-rays, should have low intensity. Moreover, the 'interfering' radiation should be such that they could be clearly separated from the resonant gamma-ray (14.4 KeV) in the energy spectrum.

In our experiments we used 25-mCi  $^{57}\text{Co}$  Mössbauer source deposited in Rhodium matrix. The source was procured from M/s E.I. duPont, U.S.A. The recoil-free fraction as specified by the supplier was 0.76. The characteristic X-ray of Rh have energies in the range 22-23.2 KeV, which is quite high in comparison with 14.4 KeV, the energy of the gamma-ray responsible for Mössbauer effect, and so could be filtered out easily. The source gave a single line Mössbauer absorption peak using potassium ferrocyanide as absorber with full-width-at-half-maximum (FWMH) of  $0.224 \pm 0.002\text{mm/sec}$  at  $295^\circ\text{K}$ . At room temperature, the FWHM with sodium nitroprusside as absorber was found to be  $0.220 \pm 0.002\text{mm/sec}$ .

### 2.3 Mössbauer Spectrometer :

The Mössbauer spectrometer used in the present work was obtained from M/s Wissel, West Germany. It consists of a Digital Function Generator (Model DFG-1200), a Mössbauer Drive Unit (model MR-360), and a Velocity Transducer (Model MA-260).

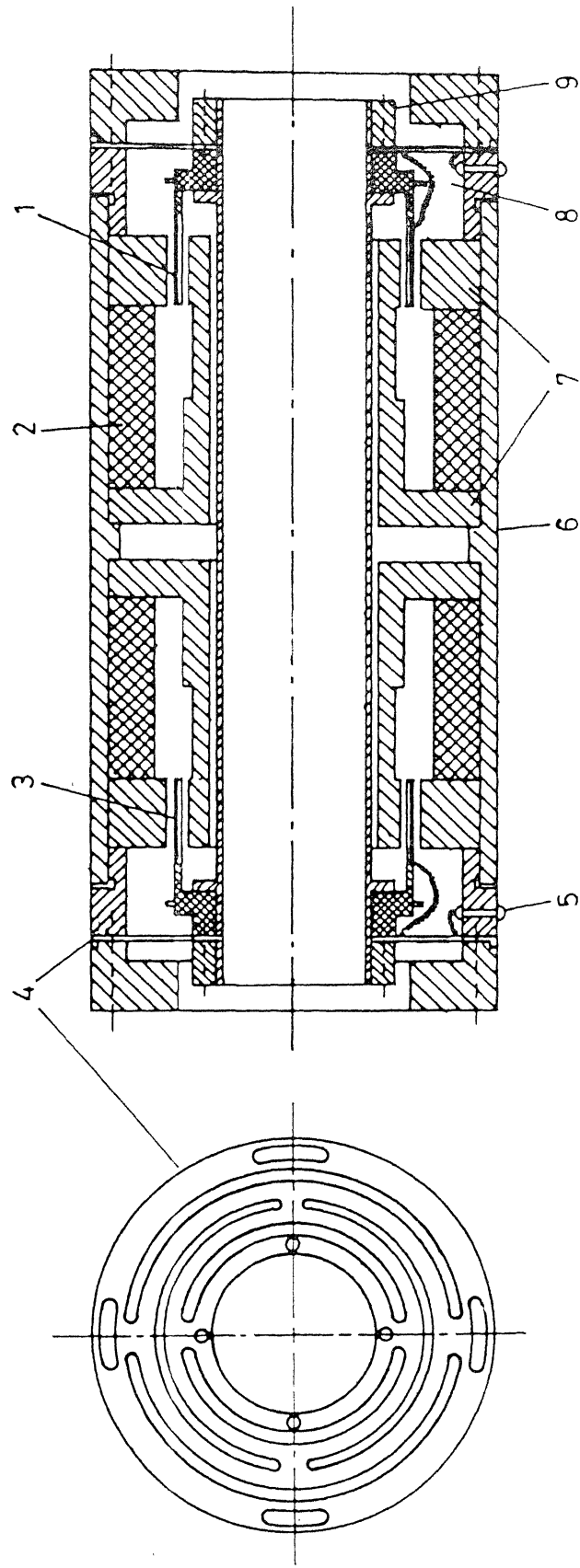
The Digital Function Generator, DFG-1200, is used to provide a reference signal to the Mössbauer driving system which determines the waveform of the source motion. It has two basic functions - sine and triangle (constant acceleration). Throughout our experiments we have run the spectrometer in constant acceleration mode. The driving system consists of the electromagnetic Mössbauer velocity transducer, MA-260, and the Mössbauer Driving Unit, MR-360. It provides a relative velocity between the source and the absorber during the Mössbauer effect measurement. For this purpose, the driving unit feeds the velocity transducer with an electronically controlled voltage. The velocity transducer and the driving unit form together a feedback loop, which minimises the deviation of the source motion from its correct value. A high precision of the source motion is achieved with this driving system not only at the resonance frequency of the transducer, but in the entire frequency range (1-100 Hz).

The Mössbauer velocity transducer, MA-260, is based on the principle of two mechanically coupled loudspeakers. The driving coil causes the motion of the transducing element. The pickup coil, which is rigidly connected with the driving coil through the common connecting tube, gives the information of the value of the velocity back to the driving unit. The resonance frequency of the transducer is

approximately 23 Hz. The large diameter of the connecting tube and the improved design of the guide springs result in an excellent frequency response of the source motion. A schematic representation of the velocity transducer is shown in fig. (2.3).

#### 2.4 Detector and Amplifier:

Most of the Mössbauer sources are not monochromatic and emit radiations of higher and lower energy than the Mössbauer gamma-ray. The detection system must have high efficiency for the Mössbauer radiation (14.4 KeV in case of  $^{57}\text{Fe}$  Mössbauer spectroscopy). The proportional counter is generally used for the energy range from 1 to 20 KeV. So this type of counter is used extensively for  $^{57}\text{Fe}$  Mössbauer spectroscopy. The counter consists of an outer cylinder at ground potential and a central wire at high positive potential, working as anode. The counter is filled with inert gas. A gamma-ray entering the counter ionizes the gas and forms ion pairs. The electrons will accelerate to the anode and form other ion pairs by collision with gas atoms. To prevent a continuous electrical discharge in the counter, a quenching gas such as  $\text{CH}_4$  or  $\text{CO}_2$  is added with the inert gas. During the recoilless absorption of gamma-ray a large number of X-rays are also produced and their energies may be close to the energy of the gamma-ray (14.4 KeV) responsible for Mössbauer effect. This causes undesired background in the spectrum. Proper resolution of



1 - Pickup coil, 2 - Permanent magnet, 3 - Drive coil, 4 - Guide spring,  
5 - Electrical feed through, 6 - Connecting tube, 7 - Magnet yokes, 8 -Coil shell,  
9 - Flange for mounting source.

Fig. 2.3 Electromechanical Transducer.

these X-rays with the Mössbauer energy is an important feature of the detection system. In our proportional counter this requirement was satisfactorily met since the FWHM of the 14.4 KeV gamma-ray is 2 KeV. We used an argon-filled proportional counter with aluminized myler window which was obtained from the Technical Physics Division, BARC, Trombay, Bombay. The counter was run at a high DC voltage of +1500V using a high voltage power supply (model Harrison 6522A, Hawlett Packard). It was connected to the preamplifier (model 401, Mech-Tronics Nuclear) and a linear amplifier (model 512, Mech-Tronics Nuclear). The output of the amplifier is fed to the ND-62 multichannel analyser.

## 2.5 Data Storage (Multichannel Analyser) :

The ND-62 microprocessor based 2048 (2K) channel analyser was used in PHA mode for selecting the 14.4 KeV gamma-ray and the storage of data. The multichannel analyser is operated in multi-scaling mode. Multichannel scaling is comparable to counting in a series of scalers, each being put into operation for a preset time, called the dwell time per channel. The sweep is triggered by the start pulse from the spectrometer and the address register in the ND-62 is advanced by the channel advance pulse from the spectrometer with minimum dead time. The data acquired in each subsequent sweep is added to the data stored in the

previous sweep. The data can be printed out in a line printer (teletype) or can be plotted in a Hawlett Packard Model 7015A X-Y recorder.

## 2.6 Cryostat:

A liquid nitrogen cryostat was designed and fabricated in our laboratory. This can be used in the range  $77^{\circ}\text{K}$  to  $300^{\circ}\text{K}$ . The cryostat is shown in fig. (2.4). There are two concentric cylindrical brass vessels connected by thin walled stainless steel tube. This tube is used for pouring the liquid nitrogen in the inner vessel. A copper rod of 3 cm. dia is attached to the inner vessel. This rod, called the cold finger, can be demounted whenever desired. The thermal insulation between the two vessels is provided by evacuating the space between them. The absorber can be kept pressed to the cold finger by a flat thick copper plate. This gives a better uniformity of temperature over the sample zone. Nichrome wire is wounded on the cold finger near the sample zone with mica insulation for heating the sample. The temperature of the sample is measured by means of a copper-constantan thermocouple. The leads of the thermocouple and that of the heater are taken out through glass to metal seals fixed at the outer vessel. Myler windows are provided on the outer vessel assembly for admitting gamma-rays. The bottom flange can be easily opened to change the samples. All

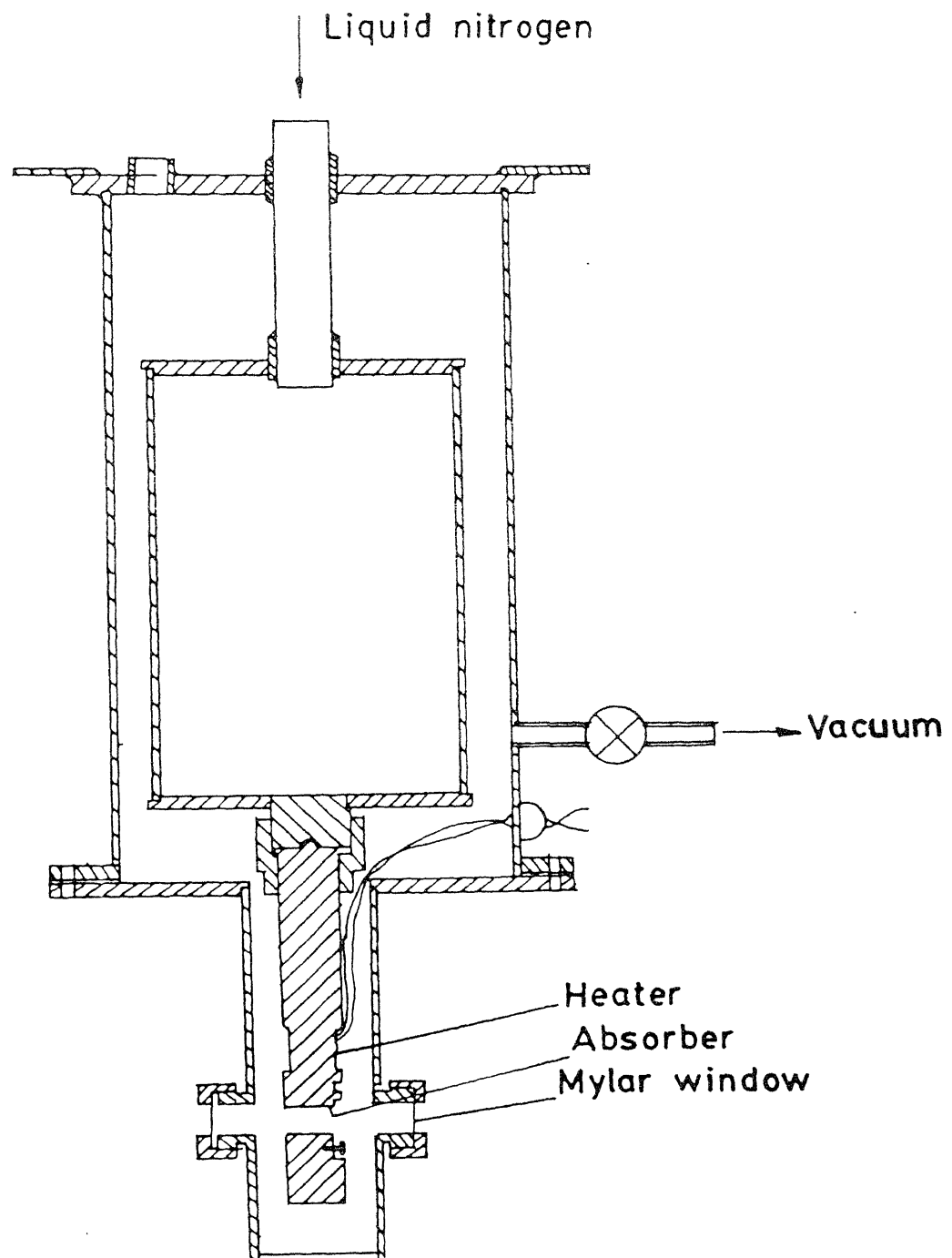


Fig.2.4 Design of the cryostat used in the Mössbauer experiments carried out in the temperature range 80 - 300 K.

parts of the dewar are nickel electroplated to prevent heating by radiation.

#### 2.7 Standard Absorbers for Calibration:

A natural iron foil (0.0005" thick), 310 stainless steel, Sodium Nitroprusside, and Potassium Ferrocyanide (supplied by NEN Products, USA), were used for the calibration purpose.

#### 2.8 Sample Preparation:

The method of preparation of absorbers differ from sample to sample. Hence, it will be discussed in detail with the study of each sample. X-ray diffraction was used to verify the crystal structure.

#### 2.9 Thickness Optimisation of the Absorbers :

It is well known that the area and width of Mössbauer spectral lines are substantially modified by saturation (thickness) effects, unless the absorber is very thin. This is, of course, a property of absorption spectra in general [9]. The line broadening of the Mössbauer spectra due to thick absorbers has been analyzed in detail by several authors [10-13]. The integrated area  $A$ , of a Mössbauer absorption peak is given by the saturation function  $L(t)$  for a Lorentzian line shape as

$$A = \frac{\pi}{2} f_s \Gamma L(t) \quad (2.1)$$

where  $f_s$  is the recoilfree fraction of gamma-ray source,  $\Gamma$  is the natural line width of the absorption spectrum and,  $t$  is the effective absorber thickness which is given by

$$t = \sigma n f_a \quad (2.2)$$

where  $\sigma$  is the resonance cross-section of the absorbing nuclei,  $n$  is the number of absorbing nuclei/cm<sup>2</sup> in the path of gamma-rays and,  $f_a$  is the recoilfree fraction of the absorber.

In order to increase the resonance absorption and reduce the non-resonance absorption, as far as possible, the thickness of the absorber should be optimized.

The number of transmitted gamma-rays at the resonance dip as a function of absorber thickness is given by the equation [14]

$$N(t, V_o) = (1-f)N + f N \exp(-t/2) J_0(it/2) \quad (2.3)$$

here  $t$  is the thickness parameter,  $V_o$  is the Doppler velocity and,  $N$  is the number of gamma-rays incident corresponding to the particular transition in the absorber.

The amplitude of the Mössbauer line is then

$$N - N(t, V_o) = fN[1 - \exp(-t/2) J_0(it/2)] \quad (2.4)$$

$J_0\left(\frac{it}{2}\right)$  is the zero order Bessel function of imaginary argument. This expression suggests that the resonance absorption amplitude increases with thickness mono-

tonically. As the number of active nuclei in the path of gamma-ray photon increases the absorption will be more. If, however, the absorber is too thick the non-resonant damping of all gamma-rays will increase and the background noise will also increase resulting in masking of the spectrum. On the other hand, if the absorber is too thin, the resonance effect would be reduced because of fewer active nuclei ( $^{57}\text{Fe}$ ) in the path of the gamma-ray. Thus there must be an optimum thickness, which for a given number of incident photons, will give a larger absorption peak. When the non-resonant absorption is also taken into account [13], the amplitude becomes

$$N-N(d, V_o) = fN \left[ 1 - \exp(-\mu_r d/2) J_o \left( i \frac{\mu_r d}{2} \right) \exp(-\mu_a d) \right] \quad (2.5)$$

where  $\mu_r$  and  $\mu_a$  are the maximum resonant and non-resonant absorption coefficients. The relation between  $\mu_r$  and  $\sigma$  is

$$\mu_r = \left[ \frac{n}{d} \right] \sigma f_a \quad (2.6)$$

here  $d$  is the actual thickness of the sample and  $n/d$  is the density of the active nuclei. Shimony [15] maximized this with respect to  $d$  to get the highest peak for a given  $N$ . The optimum thickness in that case is given by the equation

$$\frac{\mu_r}{2\mu_a} = \frac{\exp(\mu_r d_o / 2) - J_o(i \mu_r d_o / 2)}{J_o(i \mu_r d_o / 2) + J_s(i \mu_r d_o / 2)} \quad (2.7)$$

using the identity  $\frac{d(J_0(x))}{dx} = -J_1(x)$

If we concentrate on a good spectrum with minimum statistical uncertainty a better parameter for that is

$$\alpha = \frac{\text{Amplitude of the absorption dip}}{\text{Statistical uncertainty in the counts}}$$

At velocities far away from  $V_0$  the counts are

$$N(d, \infty) = N \exp(-\mu_a d) \quad (2.8)$$

If the absorption is not too large then the statistical uncertainty is given by

$$\begin{aligned} \Delta N &= [N(d, \infty)]^{1/2} \\ &= [N \exp(-\mu_a d)]^{1/2} \end{aligned}$$

Therefore,

$$\alpha(d) = \frac{f\sqrt{N} [1 - \exp(-\mu_r d/2)] J_0\left(\frac{i\mu_r d}{2}\right)}{\exp(-\frac{\mu_a d}{2})} \quad \dots (2.9)$$

Equating the derivative of  $\alpha(d)$  with respect to  $d$  to zero, we get,

$$\frac{\mu_r}{\mu_a} = \frac{\exp(\mu_r d_0/2) - J_0(i\mu_r d_0/2)}{J_0(i\mu_r d_0/2) + J_1(i\mu_r d_0/2)} \quad (2.10)$$

From this equation, we can find  $d_0$  in terms of  $\mu_r$  and  $\mu_a$ .

## 2.10 The Effect of Geometry on Mössbauer Spectra :

The effect of geometry on Mössbauer experiments are predominantly of two types. Firstly, as the source moves, the distance between the source and the detector changes. The count rate, which depends on the distance between the source and the detector, changes in a manner consistent with  $1/r^2$  dependence and one gets a non-flat baseline in the Mössbauer spectrum. Throughout our experiments, the source moves in constant acceleration mode. The velocity of the source can be written as

$$v(t) = -v_o + \frac{4v_o}{T} t \quad \text{for } 0 \leq t \leq T/2 \quad (2.11)$$

$$v(t) = 3v_o - \frac{4v_o}{T} t \quad \text{for } \frac{T}{2} \leq t \leq T$$

here  $v_o$  is the amplitude of velocity and  $T$ , its time period. The distance between the source and the detector can be obtained by integrating equation (2.11) and is given by

$$x(t) = -v_o t + \frac{2v_o}{T} t^2 + x_o \quad 0 \leq t \leq T/2 \quad (2.12)$$

$$x(t) = 3v_o t - \frac{2v_o}{T} t^2 + x_o \quad T/2 \leq t \leq T$$

here  $x_o$  is the distance between the source and the detector at time  $t = 0$ . The distances between the source and the

detector given by equation (2.12) should match at  $t = T/2$ . This gives  $X_o = x_o - v_o T$ . Writing  $x(t) = X_o + \Delta x(t)$ , we get

$$x(t) = -v_o t + \frac{2v_o}{T} t^2 \quad 0 \leq t \leq T/2 \quad (2.13)$$

$$= 2v_o t - \frac{2v_o}{T} t^2 \quad T/2 \leq t \leq T$$

The count rate in the absence of any absorber can be expressed as

$$C(t) = \frac{K}{[X_o + \Delta x(t)]^2} \quad (2.14)$$

here  $K$  is a constant.

The maximum value of  $|\Delta x|$  is at  $t = T/4$  and  $3T/4$  where velocity of the source is zero

$$|\Delta x|_{\max} = \frac{v_o T}{8} \quad (2.15)$$

If the dwell time is 100  $\mu\text{s}$  and the spectrum is recorded in 512 channels then

$$T = 100 \mu\text{s} \times 512 = 51.2 \text{ ms}$$

$$\text{If } v_o \approx 10 \text{ mm/sec, } \frac{v_o T}{8} \approx 0.05 \text{ mm}$$

$$\text{For } x_o = 5 \text{ cm, } \frac{\Delta x}{X} \approx 0.001$$

If we expand equation (2.14) using the binomial theorem then we find that the first-order shift in baseline is  $\simeq 0.1\%$  at the maximum. This may be neglected if the resonance absorption is much larger. But one should be very careful if the resonant absorption is small.

The simplest way to nullify the effect due to first-order shift in baseline is to 'fold' the data about the maximum velocity. Since  $V(t) = V(T-t)$ , it is justified to add the counts in channels corresponding to time  $t$  and  $T-t$ . This will eliminate the effect due to the changes in count rate in the first order and will also improve the statistics of the experiment. This procedure can be followed only if the linearity of the velocity cycle is extremely good in both halves of the velocity cycle and there is no significant phase shift between the advance pulse of the address scaler and the velocity waveform. Otherwise, folding the spectrum would result in bad quality and poor resolution.

The second effect, known as 'cosine smearing effect' is caused by the finite size of the source and the absorber. The gamma-rays reaching the detector have different angles with respect to the direction of motion of the source. If this angle is  $\theta$ , then the energy of the gamma-rays as seen by the absorber will be given by

$$E'_\gamma = E_\gamma \left( 1 - \frac{V \cos\theta}{C} \right)$$

Here  $V$  is the velocity of the source and  $C$  is the velocity of light. Thus, a large solid angle in the counting geometry will cause a distortion in the shape of the Mössbauer absorption line. This difficulty can be overcome by maintaining an adequate separation between the source and the detector.

### 2.11 Curve-Fitting :

If the relaxation effects are small then the Mössbauer lines can be approximated by a Lorentzian curve. The basic method of curve-fitting is to choose some functional form of the absorption peak, e.g., Lorentzian. The main purpose of these curve fittings are to find the values of the adjustable parameters, which provide the closest agreement between experimental data and the data simulated by the assumed function.

Our computer programme is based upon the method developed by Law and Bailey [16, 17]. Let  $\phi_i = \phi_i(B_1, B_2, \dots, B_m)$  be the functional form chosen for the experimental points  $Y$ . We want to find a set of parameters  $B_K$  such that

$$S^2 = \sum_{i=1}^N S_i^2 = \sum_{i=1}^N (Y_i - \phi_i)^2 \quad (2.16)$$

is minimised. Here  $N$  is the number of data points. If  $\phi$  is expanded in Taylor series about the parameters  $B_K$ , the

following is obtained by truncating all but the linear terms :

$$\begin{aligned}\phi^{(i+1)} = \phi^{(i)} + \left[ \frac{\partial \phi}{\partial B_1} \right]^{(i)} \Delta B_1 + \left[ \frac{\partial \phi}{\partial B_2} \right]^{(i)} \Delta B_2 + \\ \dots + \left[ \frac{\partial \phi}{\partial B_m} \right]^{(i)} \Delta B_m \quad \dots \quad (2.17)\end{aligned}$$

The superscript refers to iteration  $i$ . If this is substituted in equation (2.16) and the condition of minimum ( $\frac{\partial S^2}{\partial B_k} = 0$ ) is imposed, a set of  $m$  simultaneous equations is obtained. These equations are solved to get the corrections  $\Delta B_k$  and the new values of the parameters  $B_k^{i+1} = B_k^i + \Delta B_k$  are obtained. To ensure that the new values are better,  $\Delta B_k$  is changed in small steps at the point of convergence so that  $S^2$  is minimum.

The function of  $\phi$  and its derivatives are calculated in a separate subroutine. A change in function form can be accommodated by making changes only in this subroutine. The programme also gives the error matrix [18] from which the standard error in the fitted parameter  $B_m$  can be calculated. All the computations are done in DEC-1090 computer at I.I.T. Kanpur.

## REFERENCES

1. U. Gonser "Mössbauer Spectroscopy" edited by U. Gonser, Springer-verlag, Berlin-Heidelberg, New York (1975).
2. N.N. Greenwood and T.C. Gibb "Mössbauer Spectroscopy", Chapman and Hall Ltd., London (1971).
3. N. Benczer-Koller and R.H. Herber in "Chemical Applications of Mössbauer Spectroscopy" edited by V.I. Goldanskii and R.H. Herber, Academic Press, New York (1968).
4. G.M. Bancroft "Mössbauer Spectroscopy, An Introduction for Inorganic Chemists and Geochemists", McGraw-Hill, London (1973).
5. V.G. Bhide "Mössbauer Effect and its Applications", Tata McGraw-Hill Publishing Company Ltd., New Delhi (1973).
6. "Mössbauer Effect Methodology, Vol. 1-9 edited by I.J. Gruverman, Plenum Press, New York (1965-74).
7. J.J. Spijkerman in "An Introduction to Mössbauer Spectroscopy" edited by L. May, Plenum Press, New York (1971).

8. A. Vertes, L. Korecz and K. Burger "Mössbauer Spectroscopy", Elsevier Scientific Publishing Co., Amsterdam (1979).
9. E.U. Condon and G.H. Shortley, "The Theory of Atomic Spectra", Cambridge University Press, London, 1935, p.-111.
10. S. Margulies and J.R. Ehrman, Nucl. Instr. and Meth. 12, 131 (1961).
11. D.A. Shirley, M. Kaplan and P. Avel, Phys. Rev.. 123, 816 (1961).
12. D.A. O'Connor, Nucl. Instr. and Meth., 21, 318 (1963).
13. A.J. Stone, Nucl. Instr. and Meth. 107, 285 (1973).
14. R.M. Housley, N.E. Ericson and J.G. Dash, Nucl. Instr. and Meth., 27, 29 (1964).
15. U. Shimony, Nucl. Instr. and Method 37, 348 (1965).
16. V.J. Law and R.V. Bailey, Chem. Eng. Sc. 18, 183 (1963).
17. H.C. Verma, Ph.D. Thesis, Indian Institute of Technology, Kanpur, India (1980) (unpublished).

## CHAPTER 3

## FERRITES : PREPARATION AND PROPERTIES

3.1 *Introduction :*

The story of ferrite began with the search for ferromagnetic core materials of very high resistivity to obtain reasonably low eddy current losses. Indeed, this requirement is imperative at microwave frequencies (GHz) as the eddy current power loss is proportional to the square of the frequency for ordinary ferromagnetic materials. Ferrites, having a resistivity of the order of  $10^7$  ohm-meter as compared to  $10^{-7}$  ohm-meter for iron, reduce the eddy current losses in them to negligible values even at microwave frequencies. The magnetostrictive property of ferrites makes it suitable for transducer applications. The square loop ferrites have their applications in storage and switching devices. The gyromagnetic property has its use at microwave frequencies.

Ni-Zn ferrites have gained great importance in the last two decades for they have higher values of saturation magnetic moment and Curie temperature than that of Mn-Zn ferrites. They are more suitable for high power applications [1, 2] and can also be used as microwave resonance isolators [3]. Guillaud [4] and Pauthenet [5] studied their  $\sigma$ -T curves. Gorter [6] studied the changes in

CENTRAL LIBRARY  
IIT KANPUR

Acc. No. A.108477

these curves caused by the introduction of the non-magnetic tetravalent  $Ti^{4+}$  ions.

In this chapter we shall give a brief introduction to the structure and magnetic properties of ferrites so as to form the basis of the analysis of our experimental results.

### 3.2 Structure :

Ferrites are oxides with a formula  $MeO \cdot Fe_2O_3$  or  $Me^{2+}Fe_2^{3+}O_4^{2-}$ . In the above formula Me represents divalent Mn, Fe, Co, Ni, Cu, Zn, Cd, Mg, ( $0.5 Li^+ + 0.5 Fe^{3+}$ ), or two or more of these in mixed crystals. All these materials have more or less the same crystal structure as the mineral spinel. Spinel structure is a cubic, approximately close-packed arrangement of oxygen anions ( $r \sim 1.32 \text{ \AA}^\circ$ ), with metal cations having radii  $0.4 - 1.0 \text{ \AA}^\circ$  distributed amongst two kinds of interstices A (tetrahedral) and B (octahedral), coordinated by four and six oxygen anions respectively. The magnetic moment per formula unit, obtained by saturation magnetization measurements at low temperature, is not the sum of the atomic moments, but much lower. Néel explained this on the basic assumption that a preponderant negative exchange interaction (AB) between the magnetic moments of the A and B sublattices causes these to have antiparallel orientation, so that the resultant moment equals the

difference between the moments of the sublattices A and B.

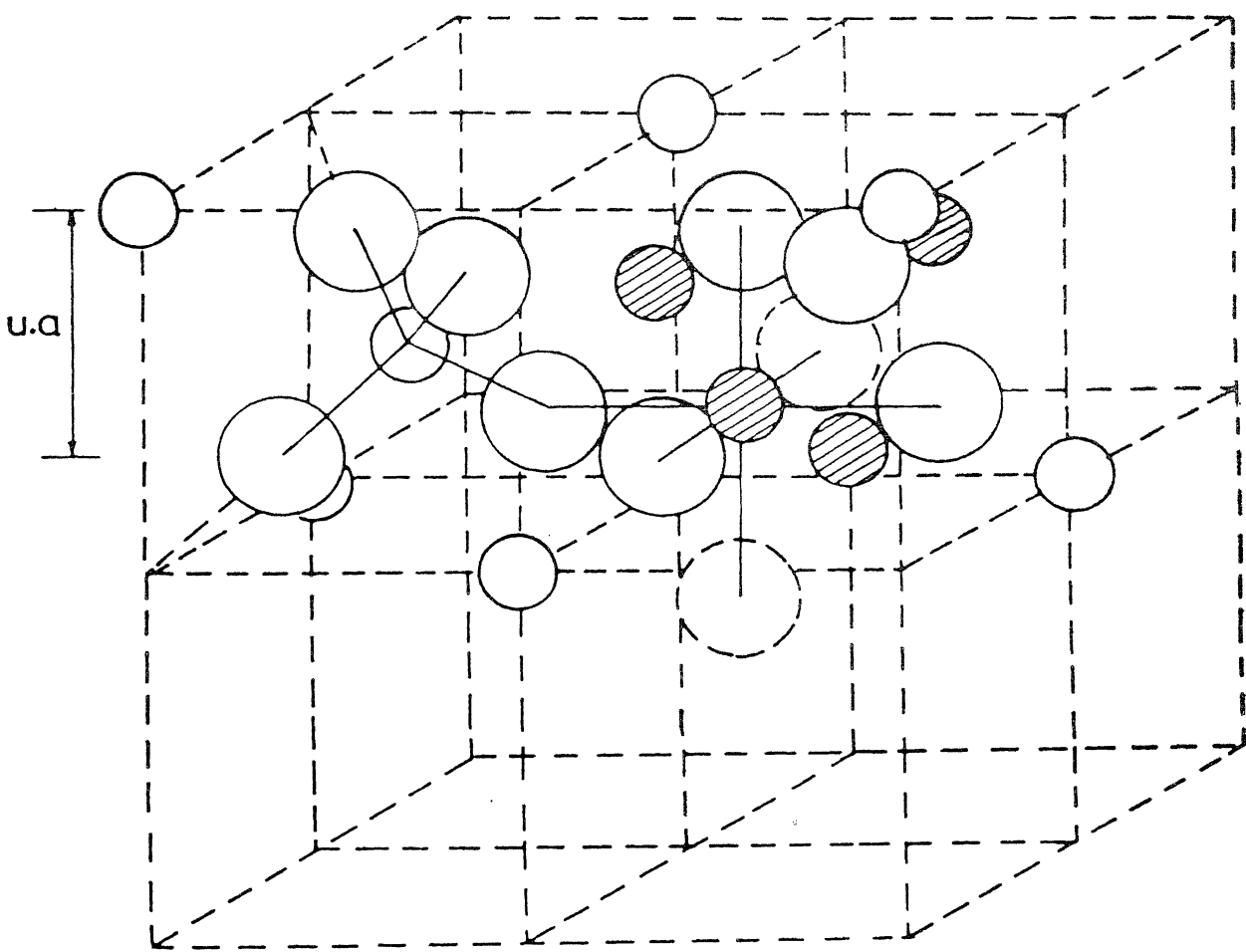
This happens if AA and BB exchange interactions are positive and are very small in magnitude compared to the negative AB exchange interaction. This uncompensated antiferromagnetism is called ferrimagnetism. This spinel structure is shown in fig (3.1).

The unit cell of the spinel lattice that has cubic symmetry contains eight molecules of  $\text{MeFe}_2\text{O}_4$ . The relatively large oxygen ions form an f.c.c. lattice. The distribution of cations in the ferrites may be one of the following three types :

- (i) Normal Spinel Structure :  $8 \text{Me}^{2+}$  ions are at the tetrahedral A site and  $16 \text{Fe}^{3+}$  ions at the octahedral B site.
- (ii) Inverse Spinel Structure :  $8\text{Fe}^{3+}$  ions are at the tetrahedral A position and  $8 \text{Fe}^{3+} + 8 \text{Me}^{2+}$  ions at the octahedral B position.
- (iii) Intermediate Structure :  $\text{Fe}_{1-x}^{3+} \text{Me}_x^{2+}$  at the tetrahedral A position and  $\text{Fe}_{1+x}^{3+} \text{Me}_{1-x}^{2+}$  at the octahedral B position.

### 3.3 Distribution of Cations Between A and B sites :

To a first approximation, the chemical bond in ferrites is assumed to be purely ionic, so that the main



THE POSITION OF IONS IN ONLY TWO OCTANTS IS SHOWN.

The dashed circles belong to the other octant. The drawn lines indicate the 4-fold and 6-fold co-ordination of the metal-ions position. Large circles : Oxygen ions ; Small hatched circles : Metal-ions at octahedral sites ; Small un-hatched circles : Metal-ions at tetrahedral sites ; ( $u = 3/8$ )

FIG. 3.1 UNIT CELL OF SPINEL STRUCTURE .

part of the lattice energy is formed by the Coulomb energy and the Born repulsive energy. Other contributing factors are : polarization, individual preference of certain ions for four fold or six fold coordination and magnetic interaction. These energies depend on the lattice parameter,  $a$ ; oxygen parameter,  $u$ ; and the cation distribution. In principle, the energy minimization should give the equilibrium values of each one of these parameters.

The analysis of the Coulomb energy problem [7] leads to the inference that a cation which has a low charge and is large with respect to the other cations will prefer tetrahedral position. The difference in the electronic configuration of the cations lead to another set of preference criteria for tetrahedral and octahedral sites :

- (i) the ions with filled 3d shell, like  $Zn^{2+}$  and  $Cd^{2+}$  have a tendency to form covalent bonds with  $sp^3$  orbitals. They, therefore, occupy the tetrahedral sites in spinels;
- (ii) the ions with noble-gas structure show no preference for either tetrahedral or octahedral sites and;
- (iii) for half-filled 3d-shell with spherical symmetry, no individual preference is shown for either position. Here the preference will be determined by

the influence of crystalline electric field originating from the neighbouring ions on the average energy levels and the spatial distribution of the 3d charges. Over and above these, the magnetic superexchange interaction energy is strongly dependent on the distribution of the magnetic ions amongst the crystallographic positions. The magnitude of this energy is, however, comparatively small.

For the cases where both types of cations ( $Me^{2+}$  and  $Fe^{3+}$ ) occupy a particular type of site, tetrahedral or octahedral, as in inverse spinels or intermediate structure, the distribution of different cations in any sublattice, A or B, is random.

For a spinel ferrite of the composition, e.g.  $(Me_x^{2+}Fe_{1-x}^{3+})_A[Me_{1-x}^{2+}Fe_{1+x}^{3+}]B_4O_4^{2-}$ , the equilibrium distribution is determined by a Boltzmann expression given by Néel [8] :

$$\frac{x(x+1)}{(1-x)^2} = \exp(-E/kT) \quad (3.1)$$

in which E is the energy involved in the interchange of a  $Me^{2+}$  ion in the octahedral position and a  $Fe^{3+}$  ion in the tetrahedral position. An accurate determination of x from X-ray diffraction is usually impossible. Pauthanet and Bochirol [9] have determined x and thus E from magnetic

saturation data for  $MgFe_2O_4$  and  $CuFe_2O_4$ .

### 3.4 Magnetic Properties of Ferrites :

Néel [10] assumed that a ferrimagnetic crystal lattice could be devided into two sublattices such as would be formed by the A and B sites in the spinel structure. He considered only a single kind of magnetic ion with  $\lambda$  and  $\mu$  the fractions of magnetic ions on A and B sites respectively. The interactions between magnetic ions may be classed as A-A, B-B, A-B, and B-A. In the Néel's theory it is assumed that the A-B and B-A interactions are identical; they predominate over A-A and B-B interactions, and are such as to favour the alignment of the magnetic moment of each A ion antiparallel with the moment of B ion. The magnetic interactions are limited to the nearest neighbours only. With  $n$  representing the molecular field coefficient between the nearest neighbour A-B interaction,  $\alpha n$  the A-A interaction coefficient and  $\beta n$  the B-B interaction coefficient, the molecular fields at the A and B sites are

$$H_A = n (\alpha \lambda M_A - \mu M_B) \quad (3.2)$$

$$H_B = n (\beta \mu M_B - \lambda M_A) \quad (3.3)$$

here the minus sign shows that we are considering only the case of antiferromagnetic interactions. Néel has shown that in this case the high temperature susceptibility can be expressed in the form

$$\frac{1}{\chi} = \frac{T-\Theta}{C} - \frac{\xi}{T-\Theta}, \quad (3.4)$$

where

$$\Theta = -nC (2\lambda\mu - \lambda^2\alpha - \mu^2\beta)$$

$$\xi = n^2C \lambda\mu [\lambda(1+\alpha) - \mu(1+\beta)]^2$$

$$\Theta' = nC\lambda\mu (2 + \alpha + \beta)$$

$$\text{and } C = \frac{Ng^2 \mu_B^2 J(J+1)}{3k}$$

where the terms have their usual meanings.

The above equation represents a hyperbola, with an asymptotic Curie point  $\Theta$  and the paramagnetic Curie point

$$T_C = \frac{nC}{2} [\lambda\alpha + \mu\beta + \sqrt{(\lambda\alpha - \mu\beta)^2 + 4\lambda\mu}] \quad (3.5)$$

The predicted susceptibility curve of a ferrimagnetic material is shown in fig (3.2).

At the temperature below the paramagnetic Curie point,  $T_C$ , the magnetization of each sublattice follows a Brillouin function :

$$M_A = M_A(0) B_J \left[ \frac{\mu H_A}{kT} \right] \quad (3.6a)$$

$$M_B = M_B(0) B_J \left[ \frac{\mu H_B}{kT} \right] \quad (3.6b)$$

Since  $H_A \neq H_B$ ,  $M_A$  and  $M_B$  will, in general, have different temperature dependence.

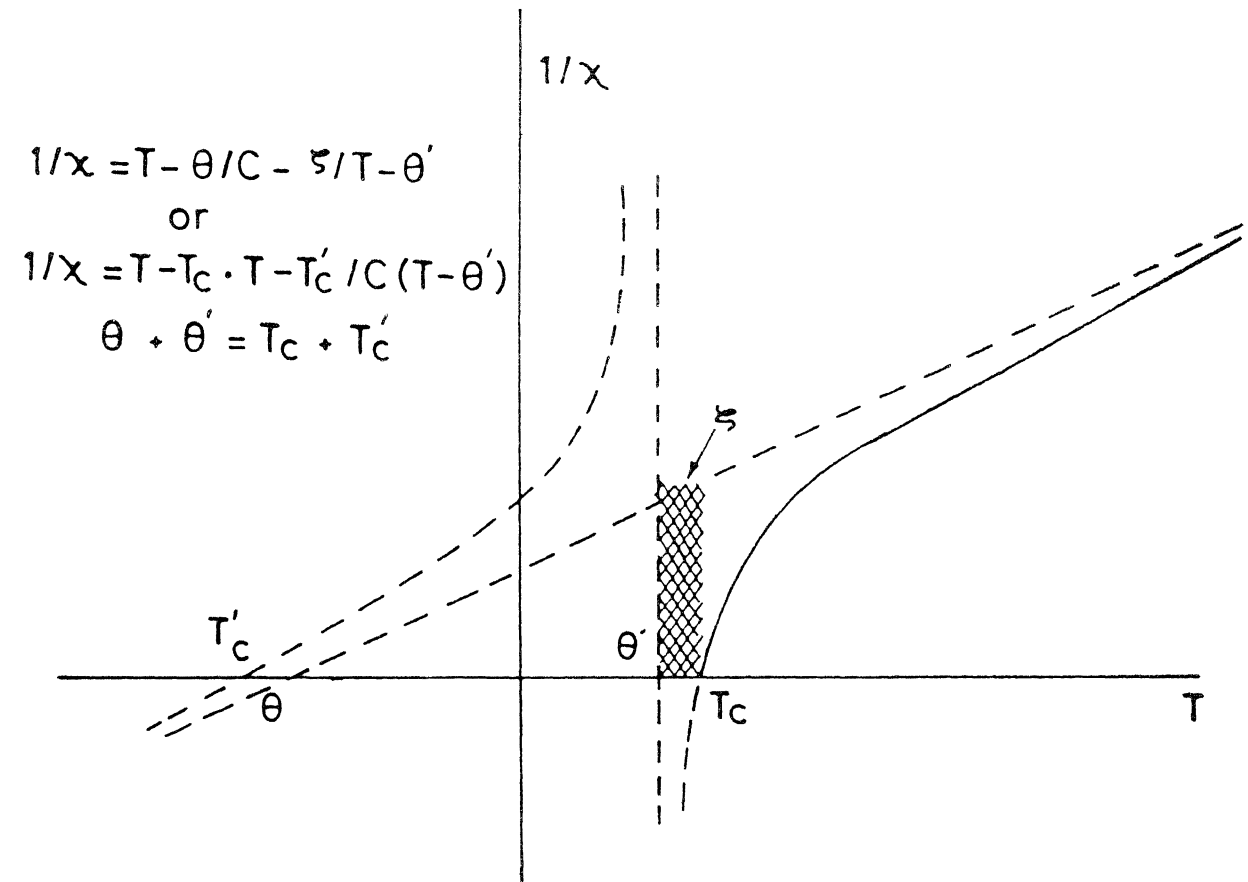


FIG. 3.2 THE NÉEL HYPERBOLA. THE EXPERIMENTALLY OBSERVED SUSCEPTIBILITY IS SHOWN BY THE SOLID SEGMENT OF THE HYPERBOLA.

Yafet and Kittel [11] modified the Néel's theory of ferrimagnetism of single A and single B sublattices, and introduced A, A'; B, B' sublattices. They proposed that a large antiferromagnetic B-B interaction leads to canting of spins at B and B' sublattices and similarly large antiferromagnetic A-A interaction leads to canting of spins at A and A' sublattices. This model was experimentally verified for a number of materials, e.g.,  $\text{CuCr}_2\text{O}_4$  [12] and  $\text{MnCr}_2\text{S}_4$  [13].

The Ni-ferrite has an inverted spinel structure and consequently, its magnetization is due to the  $\text{Ni}^{2+}$  ions only. The substitution of  $\text{Zn}^{2+}$  ions, which occupy the A-site upsets the ferric balance. Firstly, the non-magnetic  $\text{Zn}^{2+}$  displaces an  $\text{Fe}^{3+}$  ion of A-site to the B-site so that there is no longer a complete cancellation of the  $\text{Fe}^{3+}$  moments in the two sublattices. Secondly, the displaced  $\text{Fe}^{3+}$  ion which has gone to B-site takes the place of the newly removed  $\text{Ni}^{2+}$  ion. Since the  $\text{Fe}^{3+}$  ion has a large mangetic moment, this would increase the saturation magnetization. However, as the concentration of  $\text{Zn}^{2+}$  ions increases, the reduced number of  $\text{Fe}^{3+}$  ions on the A-site are less able to maintain the alignement of the B-sublattice moments against B-B interaction. Thus the canting of moments start at the B site. With the increase of  $\text{Zn}^{2+}$  concentration at the A-site canting angle also increases and hence the net saturation magnetization

decreases.  $T_c$  decreases with the increase of Zn-concentration [4, 6].

The arguments of this section are based on the molecular field approach of Néel. Because of the complexities of the structure and the problem introduced by the non-equivalent sublattices not much advanced level of work has been done beyond the generalization of Néel's theory to three sublattice case [14, 15].

### 3.5 Preparation Technique :

Polycrystalline ferrites are usually formed by solid-state reactions. For example, the stoichiometric nickel ferrite may be written as  $\text{NiO}$ ,  $\text{Fe}_2\text{O}_3$  and the reaction forming this from the solid constituent oxides is



In order to produce such a reaction in a reasonable time, an intimate mixture of the two oxides must be raised to a high temperature, of the order of  $1400^\circ\text{C}$ . It is of utmost importance to make materials of known composition and properties in a reproducible manner. Both the initial and final firing conditions play an important role in this standardization. For example, with given materials the final chemical composition may not be unique without proper firing conditions. In particular, the valence state of the metal ions present and the amount of oxygen taken into the

lattice may vary. In a ferrite, many ions can occur in different valence states; iron, for example, can occur as a divalent or a trivalent ion. If either the gas atmosphere during firing is not sufficiently oxidizing, or the ratio of the quantities of metal in the starting material is not correct, the desired concentration of a given valence state ion cannot be obtained. Where the deviations are considerable a second phase segregates from the ferrite. This can have an adverse effect on the magnetic properties of the ferrite.

A sintered polycrystalline ferrite is not truly a 'solid' but contains many pores. The quantity, size and shape, and distribution of these pores throughout the solid will vary with different forming techniques, firing temperatures and firing time. Evidently, the distribution and size of the pores will affect the physical properties too.

The basic steps in the preparation of ferrites are :  
(i) preparation of materials to form an intimate mixture with the metal ions in the ratio which they will have in the final product; (ii) heating this mixture to form the ferrite; (iii) powdering the prepared material and pressing into the required shape and; (iv) sintering to form the final product. All these steps are not necessarily distinct steps.

To avoid the lengthy milling process involved in dry mixing and to improve the homogeneity, the samples for present work were made by the solution route technique. The calculated amount of the dried salt mixtures of the metallic ions were used. The dried salt mixtures were taken into an alumina crucible. They were heated in an electric furnace at  $800^{\circ}\text{C}$  for three hours. The salts decompose to respective metal oxides at this temperature. The loss of weight in the sample confirmed the decomposition. The mixture was ground to fine powder. The decomposed sample in the form of fine powder was again ground to bring about thorough mixing. Polyvinyl alcohol (PVA) was added to the mixture as binder and was pressed into cylindrical pellets. The pellets were fired at  $900^{\circ}\text{C}$  for about 10 hours in alumina crucible. After slow cooling, the pellets were again ground to fine powder. Cylindrical pellets were made using PVA binder. The pellets were packed with packing material of similar base composition in alumina crucible. The samples were finally sintered at  $1200^{\circ}\text{C}$  for about 7 hours under oxidizing atmosphere. The packing material around the fired sample was carefully removed. The purpose of packing powder is to prevent the evaporation of Zn. X-ray diffraction was done on a Siefert X-ray unit with Cu as target. The X-ray diffraction pattern confirmed the presence of a single spinel phase in all the samples.

### 3.6 Origin of the Internal Magnetic Field at the Nucleus :

The Mössbauer [16] and NMR [17-21] measurements have been made on a great variety of magnetic solids, revealing the presence of large internal magnetic field acting on the nuclei of these materials. These internal magnetic fields also affect specific heat [22, 23] and EPR [24, 25] results. These fields can give important information about the distribution of the cations and may yield valuable insight into the mechanism responsible for the magnetic behaviour of solids. Apart from the external, demagnetizing and Lorentzian magnetic fields, there is an effective magnetic hyperfine field on the nucleus. This field is the sum of various contributions which are intimately related to the electronic structure of the magnetic solid. Marshall [26, 27] and Watson and Freeman [28, 29] have built the foundations of a theoretical understanding of these contributions. The magnetic interaction, in one electron approximation, was first treated by Fermi [30] using the relativistic quantum mechanics. The Hamiltonian of this interaction may be expressed as

$$\mathcal{H} = g \epsilon_n \mu_e \mu_n \left[ \frac{8\pi}{3} \delta(r) \hat{S} \cdot \hat{I} + \frac{(\hat{L} - \hat{S}) \cdot \hat{I}}{r^3} + \frac{3(\hat{S} \cdot \hat{r})(\hat{I} \cdot \hat{r})}{r^5} \right]$$

where  $\hat{L}$ ,  $\hat{S}$  and  $\hat{I}$  represent, respectively, electron-orbital, electron-spin, and nuclear-spin angular momentum

operators;  $\mu_e$  and  $\mu_n$  are the Bohr and nuclear magnetons;  $g$  and  $g_n$  are the electronic and nuclear spectroscopic splitting factors. The first term of the above equation is referred to as the Fermi contact term. This term contains the delta function which describes the s-electron density at the nucleus. The second term describes the interaction between the nuclear dipole and the orbital angular momentum of the electrons. The last term is the dipole-dipole interaction. The fermi contact term, is non-zero only for the s-electrons. However, for s-electrons, the other terms are zero.

The Hamiltonian when expressed as  $-\hat{\mu} \cdot \hat{H}_{\text{eff}}$  gives the concept of effective magnetic field at the nucleus. For the Fermi contact part of the Hamiltonian, the field could be expressed as

$$H_C = \frac{8\pi}{3} g\mu_e S |\psi(0)|^2$$

here  $|\psi(0)|^2$  is the s-electron density at the nucleus and  $S$ , the electron spin.

The Fermi contact term has been generally accepted as providing the explanation for the origin of the hyperfine fields observed in free atomic spectra, molecular beam measurements and the Knight shifts in metals. In all these systems, the density at the nucleus of an outer unpaired s-electron is considered to be responsible for the observed

effective magnetic field. For systems such as  $Mn^{2+}$ ,  $Fe^{3+}$  with no unpaired s-electron but with a net spin no hyperfine field is expected to exist. The origin of large hyperfine field actually observed for these cases remained a puzzle until Sternheimer [31] suggested that the polarization of the core electrons by the spin of outer electrons would produce a net spin density at the nucleus and hence  $H_c$  via Fermi contact interaction. Wood and Pratt [32] and Heine [33], in independent investigations, estimated the magnitude of the effect and showed that the reasonable agreement with experiments could be achieved by this method.

Theoretical calculation, based on one-electron approximation, of the magnetic hyperfine interactions were made for many atoms. However, when these calculations were compared with experimental values of the hyperfine fields in solids, it was found that the one electron approximation is totally inadequate in most of the cases. To cite one example, the EPR measurement of hyperfine constant for  $Mn^{2+}$  ion [34] indicated a field of 550 KOe. The ion has a configuration  $3d^5$  with  $^6S_{5/2}$  as its spectroscopic state. Because of the spherical symmetry of the charge distribution around the nucleus the dipolar term is zero. The Fermi contact term is also zero in one electron approximation.

Another difficulty in one electron approximation is

about the sign of the field. The field at the nucleus, in one-electron approximation, is expected to be parallel to the direction of atomic magnetization. But in many experiments [35, 36] it has been observed that the hyperfine field at the nucleus is opposite to the atomic magnetization.

Watson and Freeman [28] treated the problem of origin of effective field in magnetic materials in great detail. Their calculations are based on Hartree-Fock method. In the usual application of the Hartree-Fock method, one assumes a single Slater's determinant with one electron function. This is solved for variationally by following a self-consistent field procedure which minimises the total energy of the system with respect to small variations of the one-electron functions [37, 38]. There are several restrictions which are associated with the conventional application of the method. The one that concerns us involves the requirement that electron in the same atomic shell but differing in spin have the same radial wavefunctions. For the system with the net spin (say  $\uparrow$ ), this restriction is no longer valid since the electrons with up ( $\uparrow$ ) spin experiences different exchange interactions than do electrons with down ( $\downarrow$ ) spin. Relaxation of the restriction of the common radial wavefunction in H-F calculations, leads to different charge distributions for the orbitals in the same shell but

differing in spin and hence to a net spin density  $[|\psi(o)|_{\uparrow}^2 - |\psi(o)|_{\downarrow}^2]$ . This difference is the origin of non-zero Fermi contact interaction for paired s-electrons and a convenient measure of this is given by

$$\kappa = \frac{4\pi}{S} \sum_n [|\psi(o)|_{\uparrow}^2 - |\psi(o)|_{\downarrow}^2] \quad (3.7)$$

here S denotes the number of unpaired (spin up or down) electrons and  $\kappa$  is expressed in atomic units. With  $\kappa$  in atomic units, hyperfine field is found in gauss by using the conversion factor 1 a.u. of  $\kappa = 4.21 \times 10^4$  gauss.

Qualitatively, the situation of core polarization is somewhat like that shown in fig.(3.3). The core-radial wavefunction densities are shown for H-F and unrestricted H-F approximations. The heavy arrow indicates roughly the position of the maximum in the 3d spin density. In H-F calculations, it is assumed that core electrons of up and down spins have the same radial distributions. When we relax this assumption, we get a change in the radial distribution for spin up and spin down core-electrons. Exchange polarization thus produces unpairing of core-electrons and hence a net spin density at the nucleus.

Another contribution to the hyperfine field is the dipolar field  $H_D$  produced by the surrounding magnetic ions. It arises out of the dipolar interaction between the nuclear dipole and the electronic dipole and could be

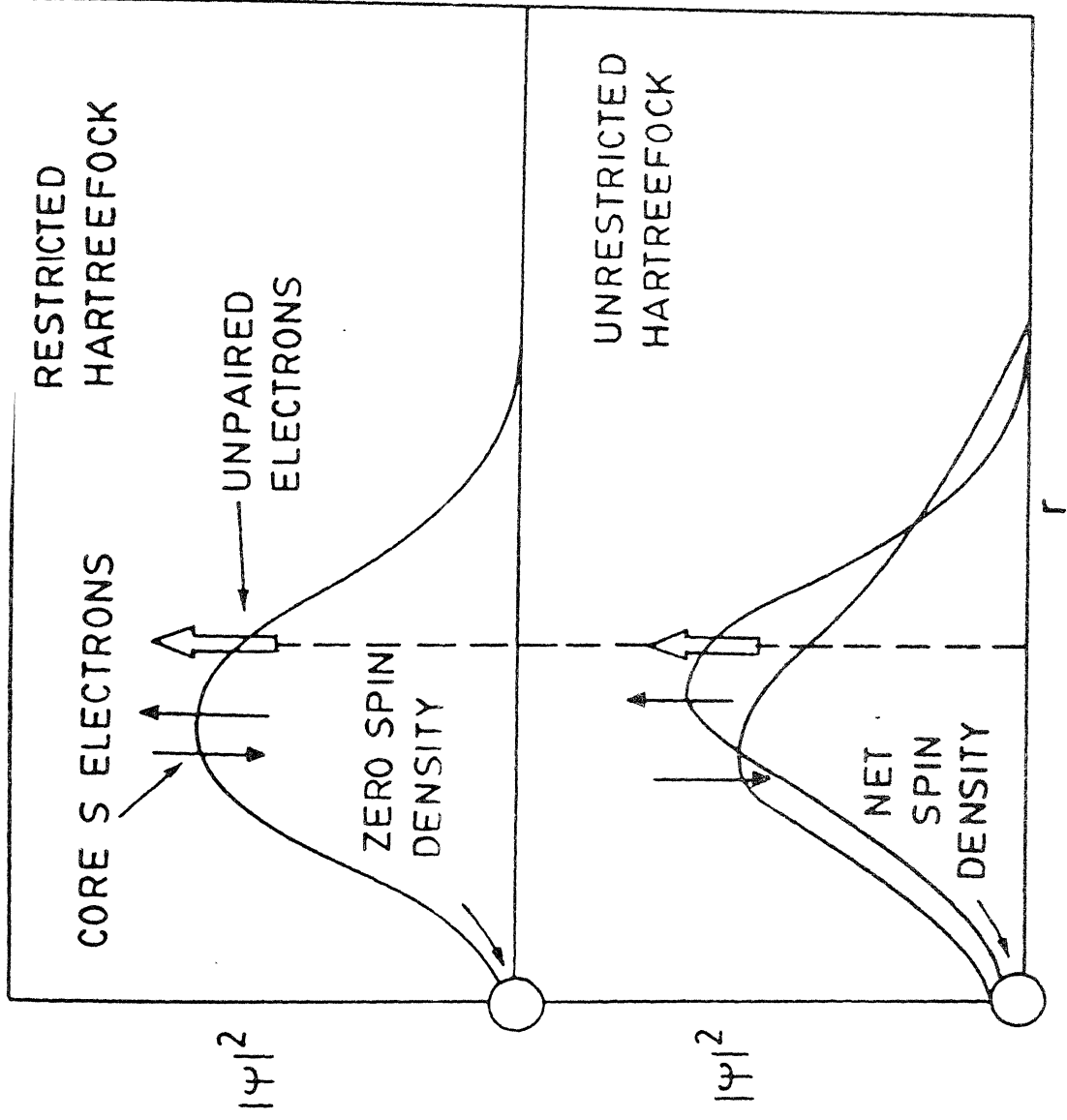


FIG. 3.3 BECAUSE OF THE CORE POLARIZATION THERE IS A NET SPIN DENSITY AT THE NUCLEUS GIVING RISE TO  $H_c$

expressed as

$$H_D = 2\mu_B \langle r^{-3} \rangle \langle 3\cos^2\theta - 1 \rangle \langle s \rangle$$

In case of cubic symmetry  $H_D$  is zero.

Yet another contribution to the hyperfine field is the orbital current field,  $H_O$ . This is produced due to the unquenched orbital moment of the atom and is given by

$$H_O = 2\mu_B \langle r^{-3} \rangle \langle L_Z \rangle$$

In case of orbital singlet, such as  $d^3$ ,  $d^4$ ,  $d^5$ ,  $d^8$  and  $d^9$  configurations, the orbital moment is quenched and  $L_Z$  is zero.

Lastly, the most important contribution to the hyperfine field, which will be discussed in later chapters is the supertransferred hyperfine field  $H_{STHF}$ . It is called super- transferred because the spin-density here is transferred from a distant cation to the central cation via an intermediate anion in a similar process as that proposed for superexchange. The super- transferred hyperfine field has been extensively discussed by Simanek et al. [39] and Sawatzky et al. [40, 41]. They studied clusters composed of a central ferric high-spin ion in an octahedron of six  $O^{2-}$  ions which in turn were surrounded by six ferric high spin iron ions.  $H_{STHF}$  at  $Fe^{3+}$  ion at A site is due to the spin

transfer from the d-orbitals of the nearest-neighbour cations (i.e., belonging to the B sublattice) through the ligand anions to the s-orbitals of the  $\text{Fe}^{3+}$  ion under consideration. The direction of  $H_{\text{STHF}}(\text{A})$  is parallel to  $M_S(\text{B})$  and thus parallel to  $H_C(\text{A})$  if the magnetic moments of the ions at A and B sites are antiferromagnetically coupled.

Huang et al. [42] gave two mechanism that can produce supertransferred hyperfine field. These mechanism are shown in figs (3.4a) and (3.4b).

In the first mechanism, fig. (3.4a) the  $2p_z$  orbital on the ligand contains a certain fraction of unpaired spin density which has been transferred from a  $d_z^2$  orbital on  $\text{Mn}^{2+}(1)$ . This unpaired spin on the ligand orbital can be partly transferred to the s-orbital on  $\text{Mn}^{2+}(2)$  by orthogonalization, giving an unpaired spin density in the occupied ns orbital. The net effect of  $\text{Mn}^{2+}(1)$ , is, therefore, the creation of unpaired s-electron spin density at  $\text{Mn}^{2+}(2)$  which has the same spin direction as the  $d_z^2$  orbital of  $\text{Mn}^{2+}(1)$ , i.e., opposite to the spin direction of  $d_z^2$  ( $\text{Mn}^{2+}(2)$ ). Since, by negative core polarization we mean that the hyperfine field produced by the d-electrons is opposite to that which would be produced by the s-electrons with the same spin direction as the d-electrons. The effect of this covalent transfer is to increase the absolute value of the hyperfine field.

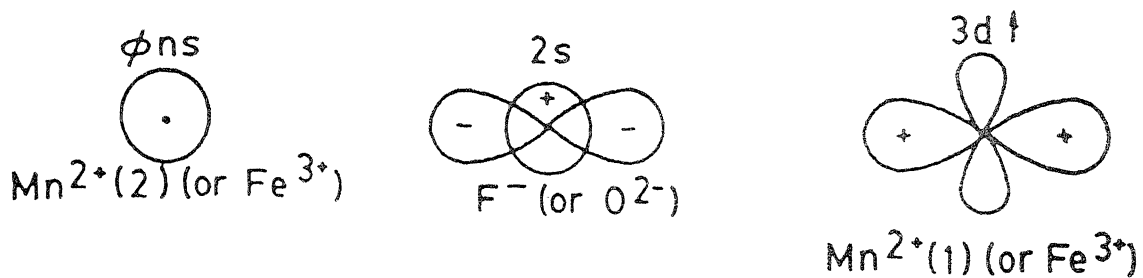


Fig. 3.4 (a)

Atomic orbitals involved in constructing the antibonding molecular orbitals at Mn (1) involving the ligand and Mn (2) orbitals.

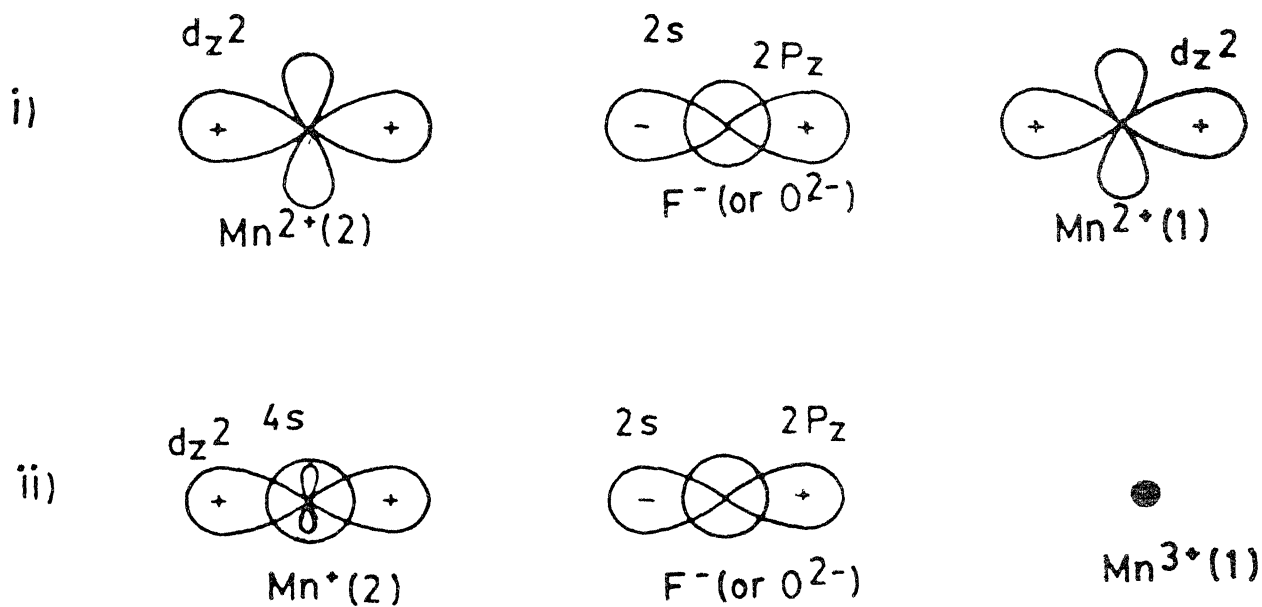


Fig. 3.4 (b)

(i) Ground configuration of Mn(1)-ligand-Mn(2).

(ii) Excited configuration where an electron has been transferred from the d-orbital of Mn(1) to the unoccupied 4s-orbital of Mn(2).

In the second mechanism, fig (3.4b), an electron is transferred directly from the  $3d_{z^2}$  of  $Mn^{2+}(1)$ , leaving it as  $Mn^{3+}$ , to an unoccupied 4s-orbital on  $Mn^{2+}(2)$ . The charge transfer Hamiltonian being spin independent, the spin of the electron transferred to the 4s-orbital on  $Mn^{2+}(2)$  is the same as that on  $Mn^{2+}(1)$  or opposite to the spin of the d-orbitals on  $Mn^{2+}(2)$ . Just as for the first mechanism, this again leads to an increase in the absolute value of the hyperfine field.

The Mössbauer hyperfine field  $H_{\text{eff}}$  in the ferrites consists of both the 1s, 2s, 3s core polarization contact term (eqn. 3.7) and the supertransferred term described above and hence can be written as

$$H_{\text{eff}} = \alpha \vec{M}_A + \beta \vec{M}_B \quad (3.8)$$

This equation forms the basis of the analysis of our Mössbauer data on the substituted Ni-Zn ferrites.

## REFERENCES

1. W. Six, Philips Tech. Rev. 13, 301, (1952).
2. F.G. Brockman, H. Van der Heide and, M.W. Louwerce, Philips Tech. Rev. 30, 312 (1969).
3. R.A. Waldron, "Ferrites - An Introduction to Microwave Engineers", D. Van Nostrand Co. Ltd., London, p-223.
4. C. Guillaud, J. Phys. Rad. 12, 239, (1951).
5. R. Pauthenet, Ann. Phys. 7, 710, (1950).
6. E.W. Gorter, Philips Res. Rep. 9, 295 (1954).
7. E.J.W. Verwey, P.W. Haayman and F.C. Romeijn, J. Chem. Phys. 15, 181 (1947).
8. L. Néel, C.R. Acad. Sci. Paris, 230, 190 (1950).
9. R. Pauthenet and L. Rochirol, J. Phys. Rad. 12, 249 (1951).
10. L. Néel, Ann. Phys. 3, 137 (1948).
11. Y. Yafet and C. Kittel, Phys. Rev. 87, 290 (1952).
12. E. Prince, Acta Cryst. 10, 554 (1957).
13. R. Plumier, Compt. Rend. Aca. Sci. 268, 1549 (1969).
14. C.M. Srivastava et al., Phys. Rev. 14, 2032 (1976).
15. C.M. Srivastava et al., Phys. Rev. 19, 499 (1979).
16. R.L. Mössbauer, Z. Physik 151, 124 (1958).
17. A.C. Gossard and A.M. Portis, Phys. Rev. Lett. 3, 164 (1959).
18. A.C. Gossard and A.M. Portis, J. Appl. Phys. 31, 2055 (1960).
19. J.I. Budnick, L.J. Brunner, E.L. Boyd, and R.M. Blume, Bull. Am. Phys. Soc. 5, 491 (1960).

20. Y. Koi, A. Tsujimura and Y. Yukimoto, J. Phys. Soc. Japan, 15, 1342 (1960).
21. Y. Koi, A. Tsujimura and T. Kushida, J. Phys. Soc. Japan 15, 2100 (1960).
22. C.V. Heer and R.A. Erikson, Phys. Rev. 108, 896 (1957).
23. V. Arp, D. Edmunds and R. Petersen, Phys. Rev. Lett. 3, 212 (1959).
24. A. Abragam, J. Horowitz and M.H.L. Pryce, Proc. Roy. Soc. (London) A230, 169 (1955).
25. W. Low "Paramagnetic Resonance in Solids", (Acad. Press Inc., New York, 1960).
26. W. Marshall, Phys. Rev. 110, 1280 (1958).
27. W. Marshall and C.E. Johnson, J. de Phys. Radium 23, 733 (1962).
28. R.E. Watson and A.J. Freeman, Phys. Rev. 123, 2027 (1961).
29. R.E. Watson and A.J. Freeman, in Magnetism IIA, ed. G.T. Rado and H. Shul (Acad. Press, New York, 1965) p.147.
30. E. Fermi, Z. Phys. 60, 320 (1930).
31. R.M. Sternheimer, Phys. Rev. 86, 316 (1952).
32. J.H. Wood and G.W. Pratt, Phys. Rev. 107, 995 (1957).
33. V. Heine, Phys. Rev. 107, 1002 (1957).
34. J.S. Van Wieringen, Disc. Faraday Soc. 19, 118 (1955).
35. A.J.F. Boyle, D. St. P. Bunbury and C. Edwards, Phys. Rev. Lett. 5, 553 (1960).

36. R.S. Preston, S.S. Hanna and J. Hewberle, Phys. Rev. 128, 2207 (1962).
37. R.E. Watson, Phys. Rev. 118, 1036 (1960).
38. R.E. Watson, Phys. Rev. 119, 1934 (1960).
39. E. Simanek, N.L. Huang and R. Orbach, J. Appl. Phys. 38, 1072 (1967).
40. F. Van der Woude and G.A. Sawatzky, Phys. Rev. B, 4, 3159 (1971).
41. G.A. Sawatzky and F. Van der Woude, J. de Physique 12, C6-47 (1974).
42. N.L. Huang, R. Orbach and E. Simanek, Phys. Rev. Lett. 17, 134 (1966).

## CHAPTER 4

MÖSSBAUER AND MAGNETIC STUDIES OF  $Ti^{4+}$  SUBSTITUTED  
Ni-Zn FERRITE

4.1 *Introduction* :

Ni-Zn ferrites of general composition  $Ni_{1-y}Zn_yFe_2O_4$  ( $y = 0.0-1.0$ ) have been widely studied [1-6]. The most interesting physical properties of this system, both from fundamental and applied points of view, are the properties related to its magnetic structure.

In Ni-Zn ferrite the saturation magnetization attains a maximum value at concentration  $y = 0.5$  [7,8] and then decreases up to  $y = 1.0$ . The Néel's theory [9], which is able to account for the initial increase, is, however, unable to account for the subsequent decrease. Over the past years, several theories have been proposed to elucidate the magnetic properties of Ni-Zn ferrite system, the two most prominent being the Yafet-Kittel model [10] and the Gilleo model [11]. In the Yafet-Kittel model, a canted spin structure is assumed whereas in the Gilleo model superparamagnetic clusters are assumed to be present.

Previous investigations of Ni-Zn ferrite system have produced a considerable body of contradictory results. The neutron diffraction study of Wilson and Casper [12] indicated that for  $y = 0.5$  in the  $Ni_{1-y}Zn_yFe_2O_4$  ferrite the

magnetic intensities of the diffraction pattern could be best fitted if a non-canting configuration was assumed for the  $Fe^{3+}$  spins and a random orientation of  $Ni^{2+}$  spins. Ishikawa [13] investigated the macroscopic magnetic properties of Ni-Zn ferrite at high Zn concentration and concluded that superparamagnetic clusters rather than canted spin structures were present. The neutron diffraction study of Ni-Zn ferrite system by Satya Murthy et al. [14] supports the existence of canted spin structure for  $y > 0.25$ .

The first investigation of the hyperfine magnetic field at the iron nucleus in Ni-Zn ferrite system, in the region of low Zn content was performed by NMR spectroscopy by Abe et al. [15]. They reported the existence of two hyperfine fields, one at the tetrahedral (or A) site and the other at the octahedral (or B) site. They also found that the octahedral field decreases more rapidly with the increasing zinc concentration, while the tetrahedral field showed very little change.

In the first systematic investigation of Ni-Zn ferrite system by Mössbauer spectroscopy, Goldanskii et al. [2] reported the existence of two hyperfine fields corresponding to the two sublattice sites, but contrary to the NMR investigations, they reported that the tetrahedral

field decreased more rapidly with Zn content than the octahedral field. But later on, this was again contradicted by Daniels and Rosencwaig [3]. Again, Goldanskii et al. did not find any evidence of superparamagnetic clusters as suggested by Gillo and by Ishikawa's experiments. No attempt, however, was made to test the presence of canted spin structure as proposed by Yafet and Kittel. Daniels et.al. [3] found that the Mössbauer spectra of  $\text{Ni}_{1-y}\text{Zn}_y\text{Fe}_2\text{O}_4$  ferrite system at room temperature consist of two separate six-line Zeeman patterns, one due to  $\text{Fe}^{3+}$  ions at the A site and the other due to  $\text{Fe}^{3+}$  ions at the B site for  $y = 0.0, 0.25$  and  $0.40$ . For  $y = 0.62$  the Mössbauer spectrum is a relaxed one whereas for  $y \geq 0.7$  the spectra are very similar to paramagnetic spectrum consisting of an intense octahedral doublet and a weak tetrahedral singlet.

Raj and Kulshreshtha [4] studied  $\text{Ni}_{1-y}\text{Zn}_y\text{Fe}_2\text{O}_4$  ferrite for  $y = 0.5$  and  $0.75$  at various temperatures and found that with the increase in temperature the hyperfine field decreased more rapidly than that was expected from the decrease in sublattice magnetization. They tried to explain this by assuming the existence of collective spin flipping as in the case of superparamagnetic relaxation. Neutron diffraction studies [14] and Mössbauer studies

[3,5] discarded the hypothesis of existence of paramagnetic centres. Ferromagnetic resonance studies of Srivastava and Patni [16] also showed that superparamagnetic clusters do not exist.

An important aspect of the study of Ni-Zn ferrites is the consideration of the mechanism and the physical consequences of the process of the transfer of  $Fe^{3+}$  ions from the tetrahedral to the octahedral sites induced by the presence of non-magnetic  $Zn^{2+}$  ions. If, however, one starts with a given concentration of Ni and Zn in Ni-Zn ferrite and introduces a non-magnetic ion of higher valency (e.g.,  $Ti^{4+}$ ,  $Sn^{4+}$  etc.), the requirement of charge balance will initiate  $Fe^{3+}$  transfer through a different kind of process. The partial pressure of oxygen at the time of sintering and cooling also plays a major role.

$Ti^{4+}$  substituted Ni-Zn ferrite system were studied by a number of workers [17-22]. Khan et al. [17, 18] found a very interesting behaviour of saturation magnetization in  $Ti^{4+}$  substituted  $Ni_{0.3}Zn_{0.7}Fe_2O_4$  ferrite. They observed that there is an unexpected dip in the saturation magnetization curve at  $Ti^{4+}$  concentration of 0.03 per formula unit. They interpreted this as an effect of distribution of  $Ti^{4+}$  ions between A and B sites.  $Ti^{4+}$  ions enter A site upto  $Ti^{4+}$  concentration of 0.03 per formula

unit and afterwards to the B site also. This transfer process causes an augmentation in the canting angle from  $51^\circ$  at zero concentration of  $Ti^{4+}$  to  $60^\circ$  at the  $Ti^{4+}$  concentration of 0.03. This is followed by a subsequent decrease in the canting angle by  $5^\circ$  upto the  $Ti^{4+}$  concentration of 0.146 and then becomes almost constant upto the  $Ti^{4+}$  concentration of 0.285. This type of anomalous behaviour in Ni-Zn ferrite system was also corroborated by the experiments of Das et al. [19] for a wide range of substituted Ni-Zn ferrites (substitutents:  $Ti^{4+}$ ,  $Zr^{4+}$ ,  $Nb^{5+}$  and  $Sn^{4+}$ ; and Zn concentrations : 0.3, 0.5 and 0.7).

Baijal et al. [20,21] studied  $Zn_{0.25}Ni_{0.75+x}Ti_xFe_{2-2x}O_4$  ( $x = 0.0$  to  $0.5$  in the steps of  $0.1$ ) ferrite and Puri et al. [22] studied  $Zn_yNi_{1+x-y}Ti_xFe_{2-2x}O_4$  ( $y = 0.1$  and  $0.5$ ;  $x = 0.1$  to  $0.9$  in the steps of  $0.2$ ) ferrite. Their work did not yield any anomalous dip in the saturation magnetization curve as observed by Khan et al. [17, 18]. Contrary to the results of Khan et al. [17,18] and Das et al. [19], the results of Baijal et al. [20,21] and Puri et al. [22] show that  $Ti^{4+}$  ions occupy the B site first upto the  $Ti^{4+}$  concentration of  $0.3$  and beyond this concentration it occupies both A and B sites. Thus the occupation of tetravalent non-magnetic cations particularly at low

concentrations, remains an open question. Khan et al. [18] could not analyse the Mössbauer data satisfactorily as the spectra were relaxed.

The present work is undertaken to initiate the study of  $Ti^{4+}$  substitution effect in the non-canting zone ( $y = 0.0 - 0.4$  in  $Ni_{1-y}Zn_yFe_2O_4$  ferrite) in a systematic way. In this range, the Mössbauer spectra are not relaxed and, therefore, may be used to get an insight into the  $Ti^{4+}$  distribution process as well as microscopic magnetization mechanism.  $Ti^{4+}$  range was chosen to keep the system in the anomalous dip zone of the experiments of Khan et al. [17,18].

In this Chapter we will discuss the Mössbauer and magnetic results of  $Ti^{4+}$  substituted  $Ni_{1-y}Zn_yFe_2O_4$  ferrite for  $y = 0.0, 0.3$  and  $0.4$ . For further elucidation of the mechanism leading to the anomalous behaviour, we will discuss the results of  $Sn^{4+}$  substituted Ni-Zn ferrite system in the next chapter.

#### 4.2 Mössbauer Study of Titanium Substituted $Ni_{1-y}Zn_yFe_2O_4$ ( $y = 0.0, 0.3, 0.4$ ) Ferrite :

##### 4.2.1 Titanium Substituted $Fe_2O_4$ Ferrite :

The nickel ferrite system is completely inverse spinel, with the unit cell consisting of eight formula

units of the form  $(\text{Fe}^{3+}) [\text{Ni}^{2+} \text{Fe}^{3+}] \text{O}_4^{2-}$ . The 32 oxygen anions per unit cell form a face centred cubic lattice with the metallic cations occupying the interstices. The cations enclosed by ( ) occupy the tetrahedral sites or A sites and the cations enclosed by [ ] occupy the octahedral sites or B sites.  $\text{Ni}^{2+}$  ions have preference for octahedral sites because their charge distribution fits into the crystal field of octahedral sites [23].

Mössbauer spectra of samples were recorded at room temperature and liquid nitrogen temperature. They show a well defined Zeeman pattern consisting of two separate sextets due to  $\text{Fe}^{3+}$  ions at A and B sites. Mössbauer spectra of  $\text{Ni}_{1+x} \text{Ti}_x \text{Fe}_{2-2x} \text{O}_4$ ,  $0 \leq x \leq 0.1$  at  $295^\circ\text{K}$  and  $77^\circ\text{K}$  are shown in figs. (4.1) and (4.2) respectively.

The isomer shift of  $\text{Fe}^{3+}$  ions (with respect to sodium nitroprusside) at tetrahedral site, I.S.(A), and at octahedral site, I.S.(B) show no significant change with  $\text{Ti}^{4+}$  substitution at  $295^\circ\text{K}$  and  $77^\circ\text{K}$  [fig. (4.3)]. The weighted average value of isomer shift at A and B sites of  $\text{Ni}_{1+x} \text{Ti}_x \text{Fe}_{2-2x} \text{O}_4$  ferrite at  $295^\circ\text{K}$  are  $0.536 \pm 0.002$  and  $0.645 \pm 0.002$  mm/sec respectively. At  $77^\circ\text{K}$ , the weighted average value of isomer shift at A and B sites are  $0.721 \pm 0.002$  and  $0.873 \pm 0.002$  mm/sec respectively.

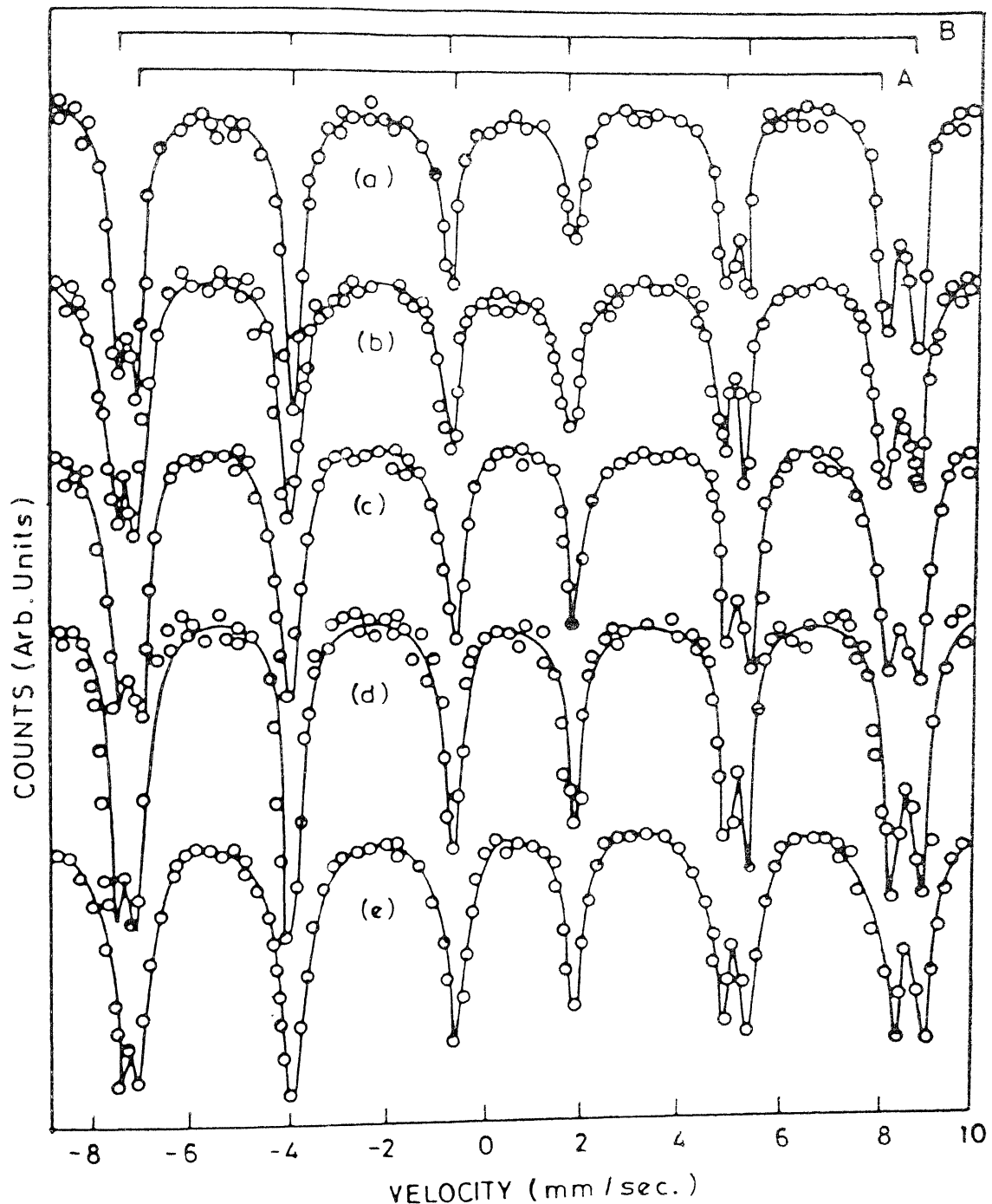


Fig. 4.1 Mössbauer spectra of  $\text{Ni}_{1+x}\text{Ti}_x\text{Fe}_{2-2x}\text{O}_4$  at 295°K (a)  $x = 0.005$ , (b)  $x = 0.015$ , (c)  $x = 0.03$ , (d)  $x = 0.05$ , (e)  $x = 0.1$ .

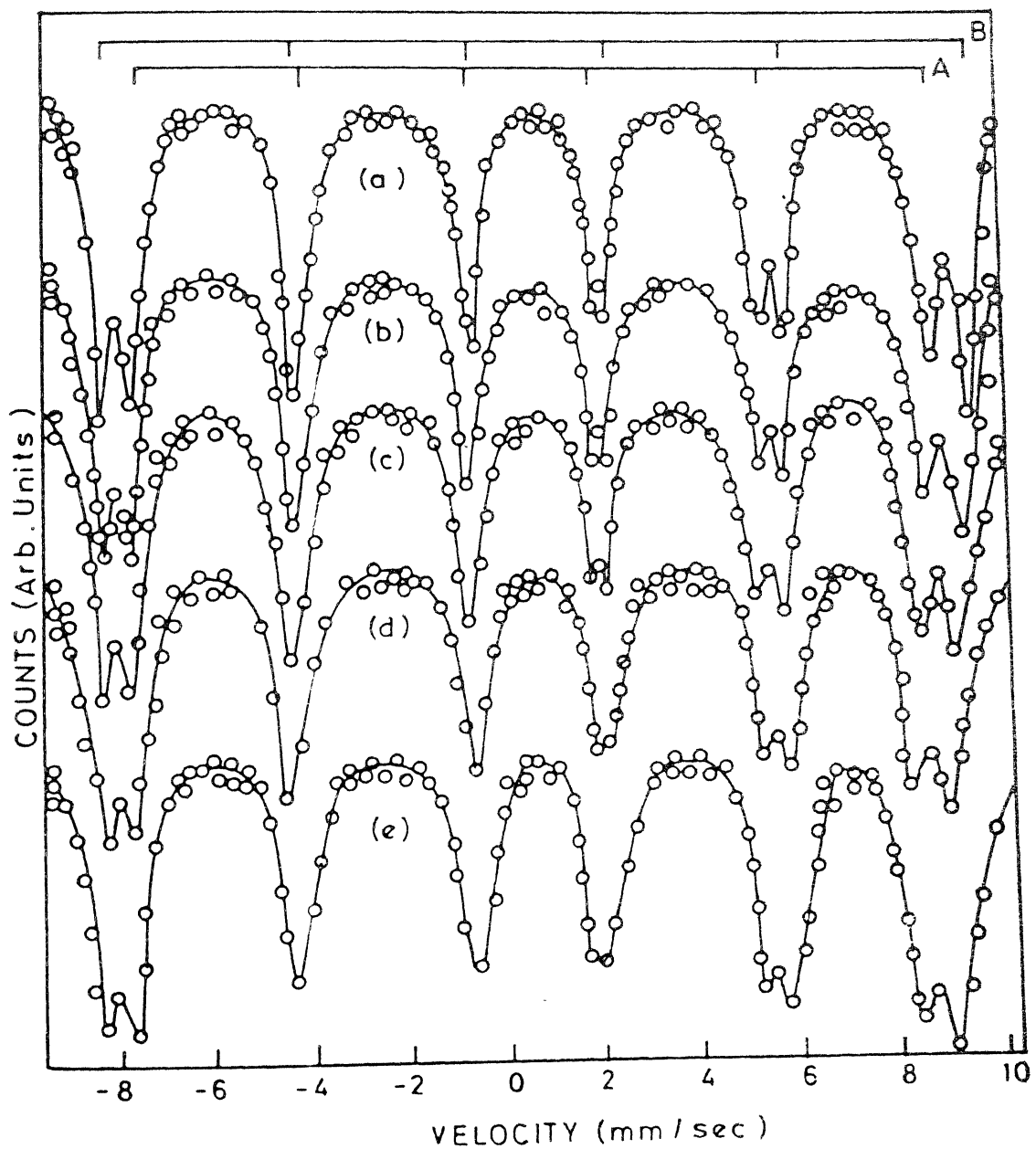


Fig. 4.2 Mössbauer spectra of  $\text{Ni}_{1+x}\text{Ti}_x\text{Fe}_{2-2x}\text{O}_4$  at 77°K  
(a)  $x = 0.005$ , (b)  $x = 0.015$ , (c)  $x = 0.03$ , (d)  $x = 0.05$ ,  
(e)  $x = 0.1$ .

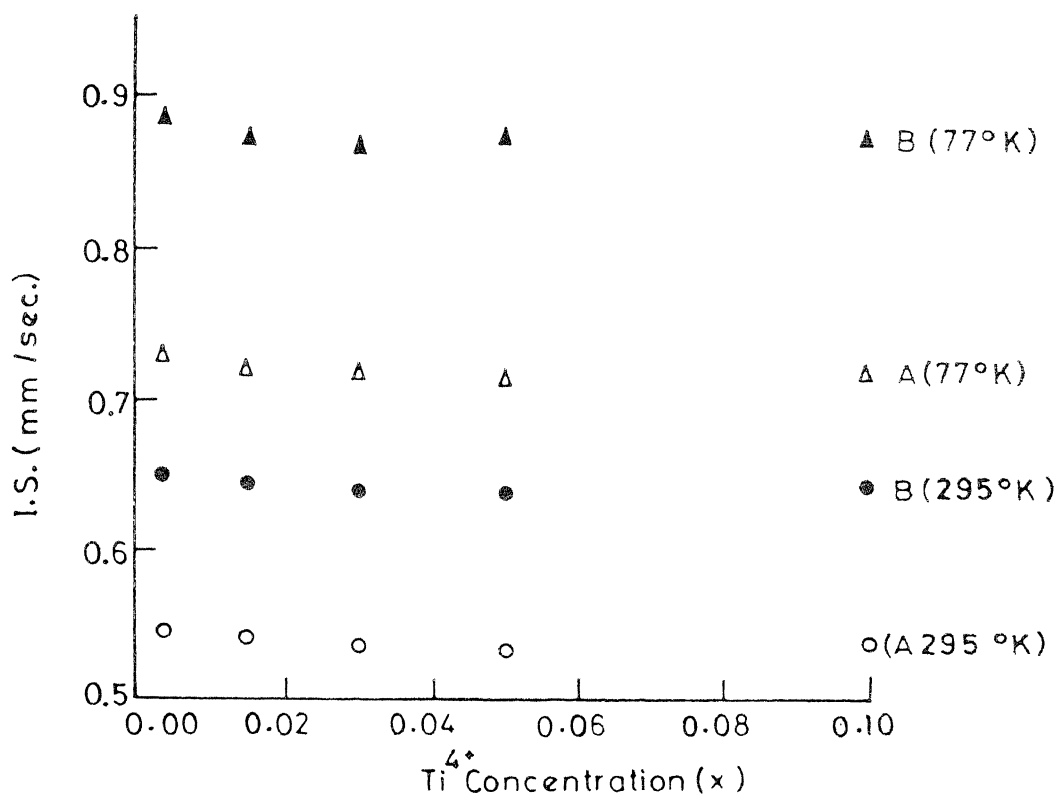


Fig. 4.3 Variation of Isomer shift with Ti<sup>4+</sup> concentration in  $\text{Ni}_{1+x} \text{Ti}_x \text{Fe}_{2-2x} \text{O}_4$ .

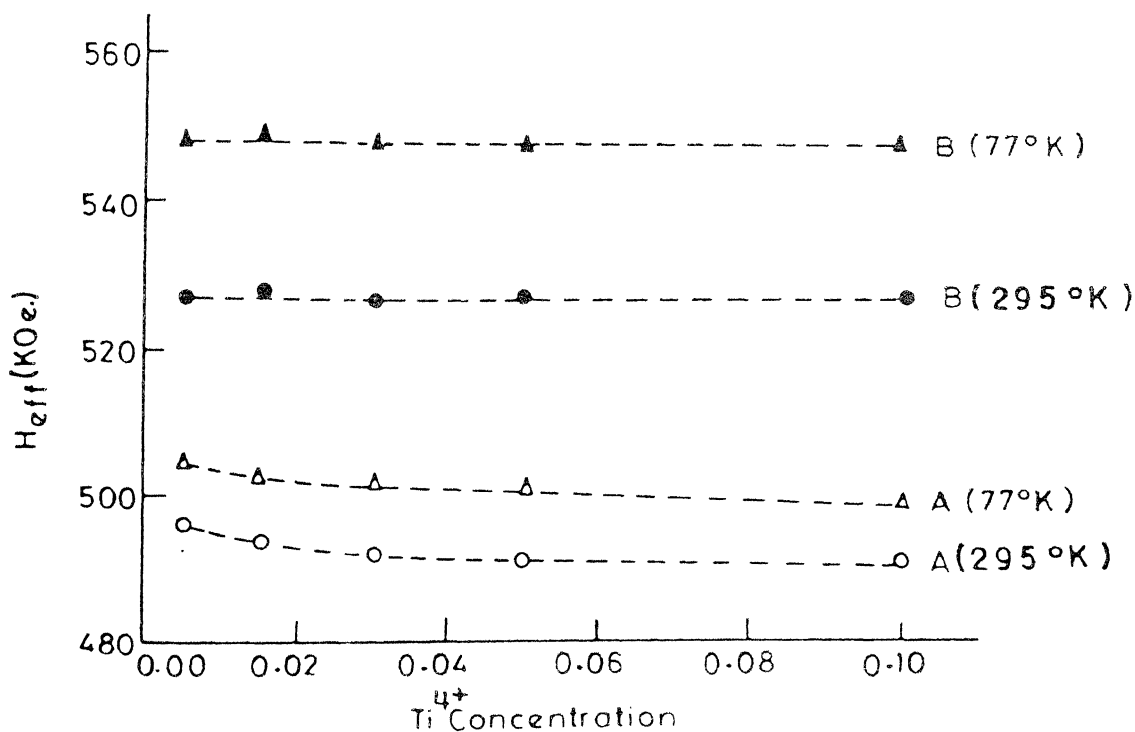


Fig. 4.4 Variation of effective magnetic field with Ti<sup>4+</sup> concentration in  $\text{Ni}_{1+x} \text{Ti}_x \text{Fe}_{2-2x} \text{O}_4$ .

In all the samples exhibiting Zeeman hyperfine pattern, no quadrupole splitting was observed within the experimental error for both A and B sites. Mössbauer spectra of  $\text{NiFe}_2\text{O}_4$  obtained by other investigators [24, 25] also showed zero quadrupole splitting.

At room temperature the variation of effective magnetic field,  $H_{\text{eff}}$ , at A and B sites with  $\text{Ti}^{4+}$  concentration is shown in fig. (4.4). It is observed that there is no significant change in the  $H_{\text{eff}}$  at B site, and it remains almost constant at a value of  $527 \pm 1$  KOe. But there is a decrease in the  $H_{\text{eff}}$  at A site from  $496 \pm 1$  KOe to  $491 \pm 1$  KOe as the concentration of  $\text{Ti}^{4+}$  increases from  $x = 0.005$  to  $x = 0.1$ . A similar behaviour of  $H_{\text{eff}}$  at the two sublattices is observed at liquid nitrogen temperature [fig. (4.4)].  $H_{\text{eff}}(A)$  decreases from  $505 \pm 1$  KOe to  $498 \pm 1$  KOe whereas  $H_{\text{eff}}(B)$  remains almost constant at a value of  $548 \pm 1$  KOe as the concentration of  $\text{Ti}^{4+}$  increases from  $x = 0.005$  to  $x = 0.1$ . The value of  $H_{\text{eff}}$  at the two sublattices at  $295$  and  $77^\circ\text{K}$  for  $x = 0.1$  concentration of  $\text{Ti}^{4+}$  are in good agreement with the values reported by other workers [26].

In fig. (4.5) we have shown the variation of linewidth of the Mössbauer absorption peak with  $\text{Ti}^{4+}$  concentration. It is observed that at  $295^\circ\text{K}$  the linewidth

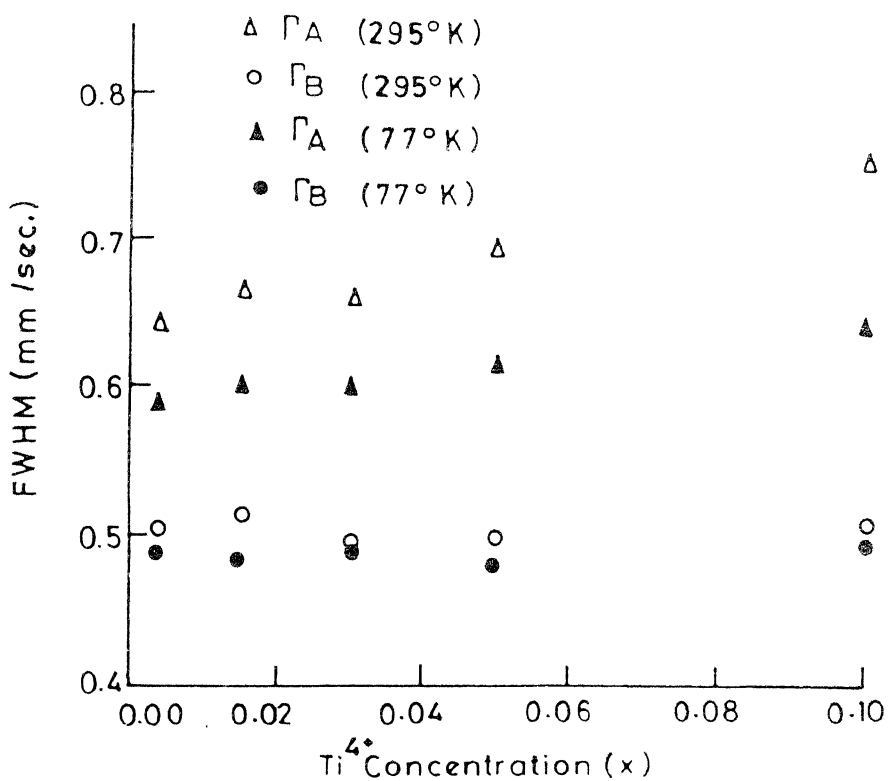


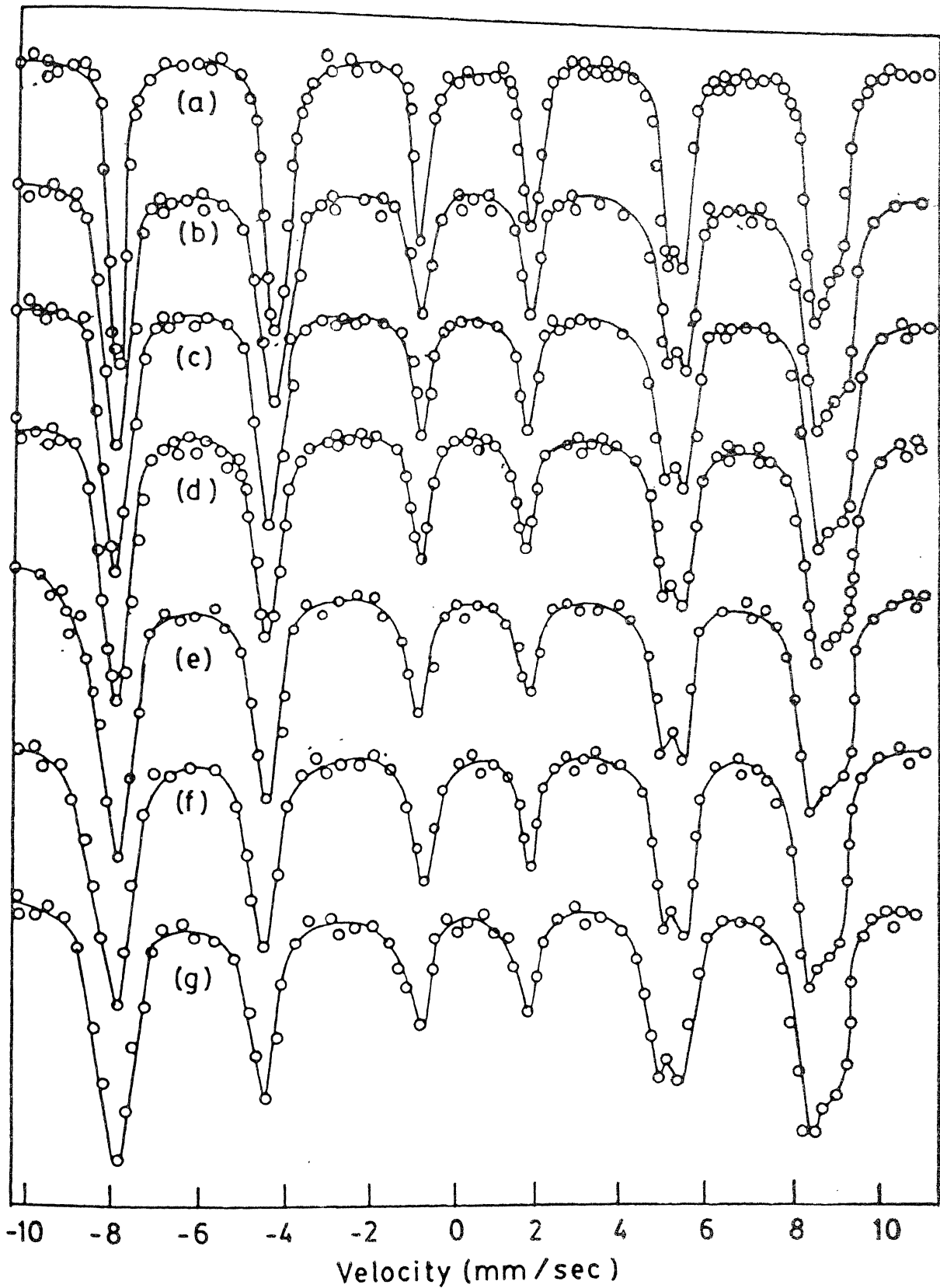
Fig. 4.5 Variation of full width at half maximum with Ti<sup>4+</sup> concentration in  $\text{Ni}_{1+x} \text{Ti}_x \text{Fe}_{2-2x} \text{O}_4$ .

of the octahedral component of spectrum,  $\Gamma_B$ , remains almost constant at a value of  $0.505 \pm 0.002$  mm/sec whereas the linewidth of the tetrahedral component of spectrum,  $\Gamma_A$ , increases from  $0.645 \pm 0.003$  mm/sec to  $0.760 \pm 0.003$  mm/sec as the concentration of  $Ti^{4+}$  increases from  $x = 0.005$  to  $x = 0.1$ . There is a little decrease in the value of  $\Gamma_B$  from  $0.505 \pm 0.002$  mm/sec at  $300^\circ K$  to  $0.490 \pm 0.003$  mm/sec at  $77^\circ K$  and it remains almost constant at this value if  $Ti^{4+}$  concentration increases from  $x = 0.005$  to  $x = 0.1$ .  $\Gamma_A$  decreases from  $0.645 \pm 0.003$  mm/sec at  $295^\circ K$  to  $0.590 \pm 0.002$  mm/sec at  $77^\circ K$ . At  $77^\circ K$ ,  $\Gamma_A$  increases from  $0.590 \pm 0.002$  to  $0.690 \pm 0.002$  mm/sec as the concentration of  $Ti^{4+}$  increases from  $x = 0.005$  to  $x = 0.1$ .

#### 4.2.2 Titanium Substituted $Ni_{0.7}Zn_{0.3}Fe_2O_4$ Ferrite :

Mössbauer spectra of  $Ni_{0.7+x}Zn_{0.3}Ti_xFe_{2-2x}O_4$  ( $0 \leq x \leq 0.1$ ) at  $295$  and  $77^\circ K$  are shown in figs. (4.6) and (4.7) respectively. These spectra show a well defined Zeeman pattern consisting of two separate sextets; one due to  $Fe^{3+}$  ions at A site and the other due to  $Fe^{3+}$  ions at B site.

The isomer shift of  $Fe^{3+}$  ions (with respect to SNP) at tetrahedral site, I.S.(A), and at octahedral site, I.S.(B), show no significant change with  $Ti^{4+}$  concentration. The values of isomer shift at  $295$  and  $77^\circ K$  with different concentration of  $Ti^{4+}$  ions are shown in fig.



4.6 Mössbauer spectra of  $\text{Ni}_{0.7+x} \text{Zn}_{0.3} \text{Ti}_x \text{Fe}_{2-2x} \text{O}_4$  at room temperature (a)  $x = 0.00$ , (b)  $x = 0.002$ , (c)  $x = 0.01$ , (d)  $x = 0.016$ , (e)  $x = 0.032$ , (f)  $x = 0.05$ , (g)  $x = 0.08$ .

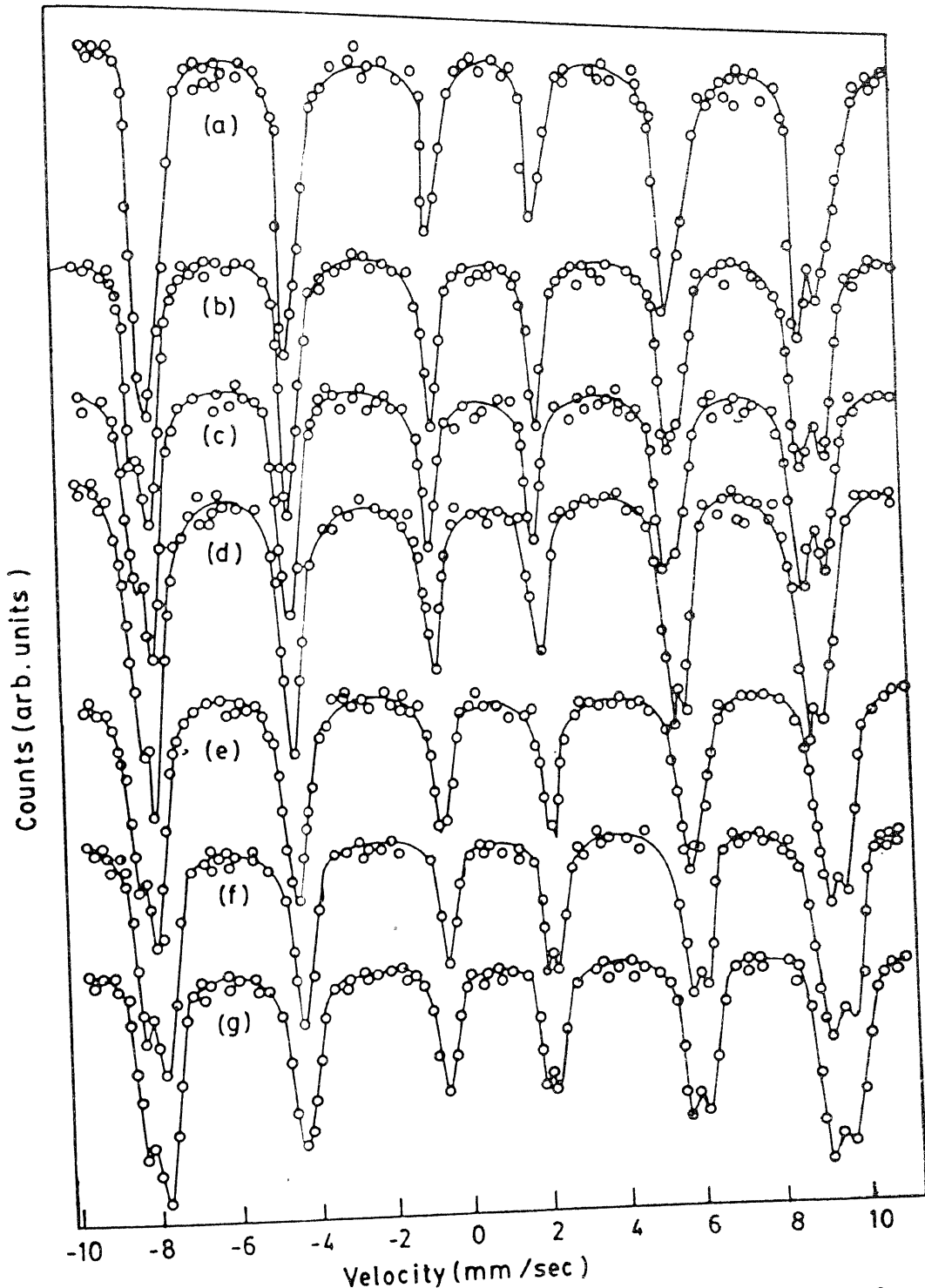


Fig. 4.7 Mössbauer spectra of  $\text{Ni}_{0.7+x} \text{Zn}_{0.3} \text{Ti}_x \text{Fe}_{2-2x} \text{O}_4$  at  $77^\circ\text{K}$  (a)  $x = 0.00$ , (b)  $x = 0.002$ , (c)  $x = 0.01$ , (d)  $x = 0.016$ , (e)  $x = 0.032$ , (f)  $x = 0.05$ , (g)  $x = 0.08$ .

(4.8). The weighted average value of isomer shift at A and B sites of  $\text{Ni}_{0.7+x}\text{Zn}_{0.3}\text{Ti}_x\text{Fe}_{2-2x}\text{O}_4$  ( $0 \leq x \leq 0.1$ ) at  $295^\circ\text{K}$  are  $0.533 \pm 0.002$  and  $0.615 \pm 0.002$  mm/sec respectively. At  $77^\circ\text{K}$ , the weighted average value of isomer shift with respect to SNP at A and B sites are  $0.719 \pm 0.002$  and  $0.840 \pm 0.002$  mm/sec respectively.

In these systems too, no quadrupole splitting was observed within the experimental error for both A and B sites.

At room temperature, the variation of  $H_{\text{eff}}$  at A and B sites with  $\text{Ti}^{4+}$  concentration are shown in fig. (4.9). From the graph it is clear that there is no significant change in  $H_{\text{eff}}(\text{B})$ , and it remains almost constant at a value of  $495 \pm 1$  KOe.  $H_{\text{eff}}(\text{A})$ , on the other hand, decreases from  $487 \pm 1$  KOe to  $483 \pm 1$  KOe as the concentration of  $\text{Ti}^{4+}$  increases from  $x = 0.00$  to  $x = 0.08$ . A similar behaviour of  $H_{\text{eff}}(\text{A})$  and  $H_{\text{eff}}(\text{B})$  with  $\text{Ti}^{4+}$  concentration are observed at  $77^\circ\text{K}$  also [fig. (4.9)]. Here  $H_{\text{eff}}(\text{B})$  remains constant at  $519 \pm 1$  KOe whereas  $H_{\text{eff}}(\text{A})$  decreases from  $492 \pm 1$  KOe to  $486 \pm 1$  KOe as the concentration of  $\text{Ti}^{4+}$  increases from  $x = 0.00$  to  $x = 0.08$ . For zero concentration of  $\text{Ti}^{4+}$  the values of  $H_{\text{eff}}$  at the two sublattices at  $295$  and  $77^\circ\text{K}$  are in excellent agreement with the values reported in the literature [3].

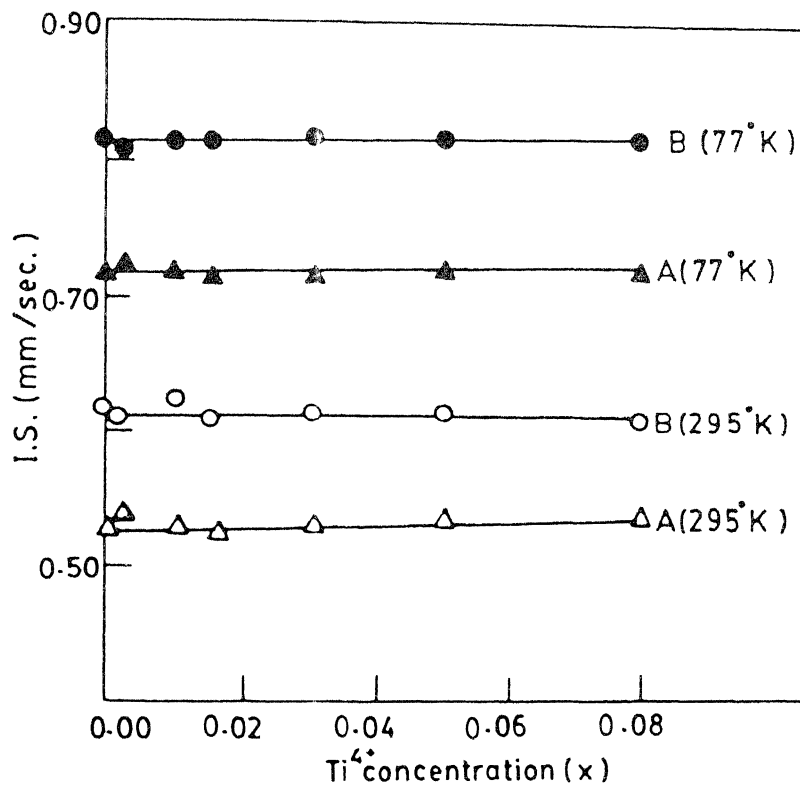


FIG. 4.8 Variation of isomer shift with  $Ti^{4+}$  concentration in  $Ni_{0.7-x}Zn_{0.3}Ti_xFe_{2-2x}O_4$  ferrite.

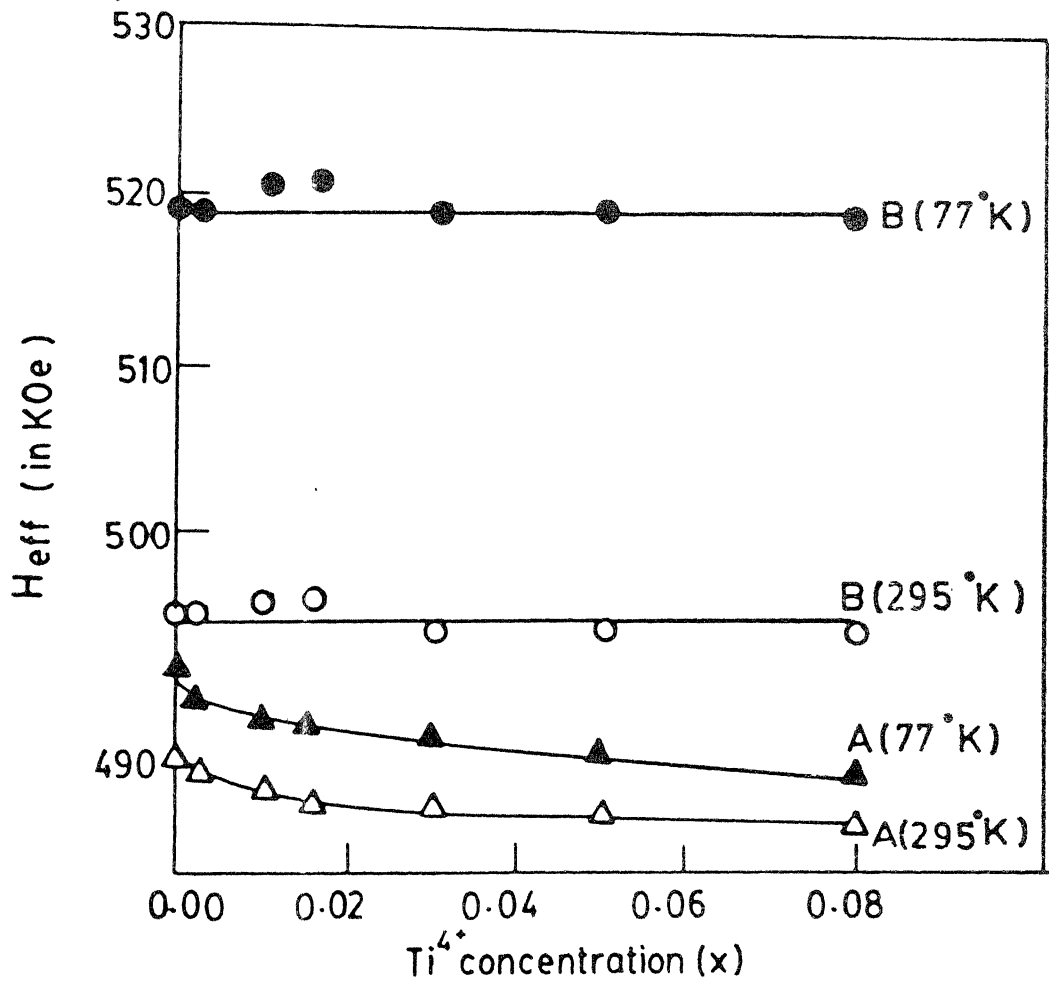


FIG. 4.9 Variation of effective magnetic field with Ti<sup>4+</sup> concentration in  $\text{Ni}_{0.7+x}\text{Zn}_{0.3}\text{Ti}_x\text{Fe}_{2-2x}\text{O}_4$  ferrite.

In fig.(4.10) we have shown the variation of full width at half maximum (FWHM) of the Mössbauer absorption peak with  $Ti^{4+}$  concentration. We found that there is no significant change in the values of  $\Gamma_B$  at 295 and 77°K with  $Ti^{4+}$  concentration. At 295°K,  $\Gamma_B$  remains almost constant at a value of  $0.775 \pm 0.003$  mm/sec whereas at 77°K it drops to  $0.610 \pm 0.004$  mm/sec and remains almost constant at that value as the concentration of  $Ti^{4+}$  increases from  $x = 0.00$  to  $x = 0.08$ . The FWHM of the tetrahedral component of spectrum,  $\Gamma_A$ , at 295°K, increases from  $0.561 \pm 0.004$  mm/sec to  $0.675 \pm 0.004$  mm/sec as the concentration of  $Ti^{4+}$  increases from  $x = 0.00$  to  $x = 0.08$ .  $\Gamma_A$  at 77°K is  $0.492 \pm 0.004$  mm/sec for the zero concentration of  $Ti^{4+}$  and it increases upto  $0.550 \pm 0.003$  mm/sec for  $x = 0.08$ . Daniels et al. [3] reported that at 294°K the octahedral linewidth,  $\Gamma_B$ , of  $Ni_{1-y}Zn_yFe_2O_4$  ferrite increases continuously with increasing  $y$  upto 0.62 whereas for the tetrahedral linewidth,  $\Gamma_A$ , a minima occurs at  $y = 0.2$ . At 77°K,  $\Gamma_B$  increases slowly as  $y$  increases from  $y = 0.0$  to  $y = 0.4$  followed by a sharp increase in  $\Gamma_B$  as  $y$  increases from  $y = 0.4$  to  $y = 0.7$ . On the other hand,  $\Gamma_A$  decreases slowly as  $y$  varies from 0.0 to 0.4 and then increases as  $y$  increases from  $y = 0.4$  to  $y = 0.7$ . The values of  $\Gamma_A$  and  $\Gamma_B$  at 295 and 77°K of our sample with zero concentration of  $Ti^{4+}$  are consistent with the values reported by Daniels et al.[3].

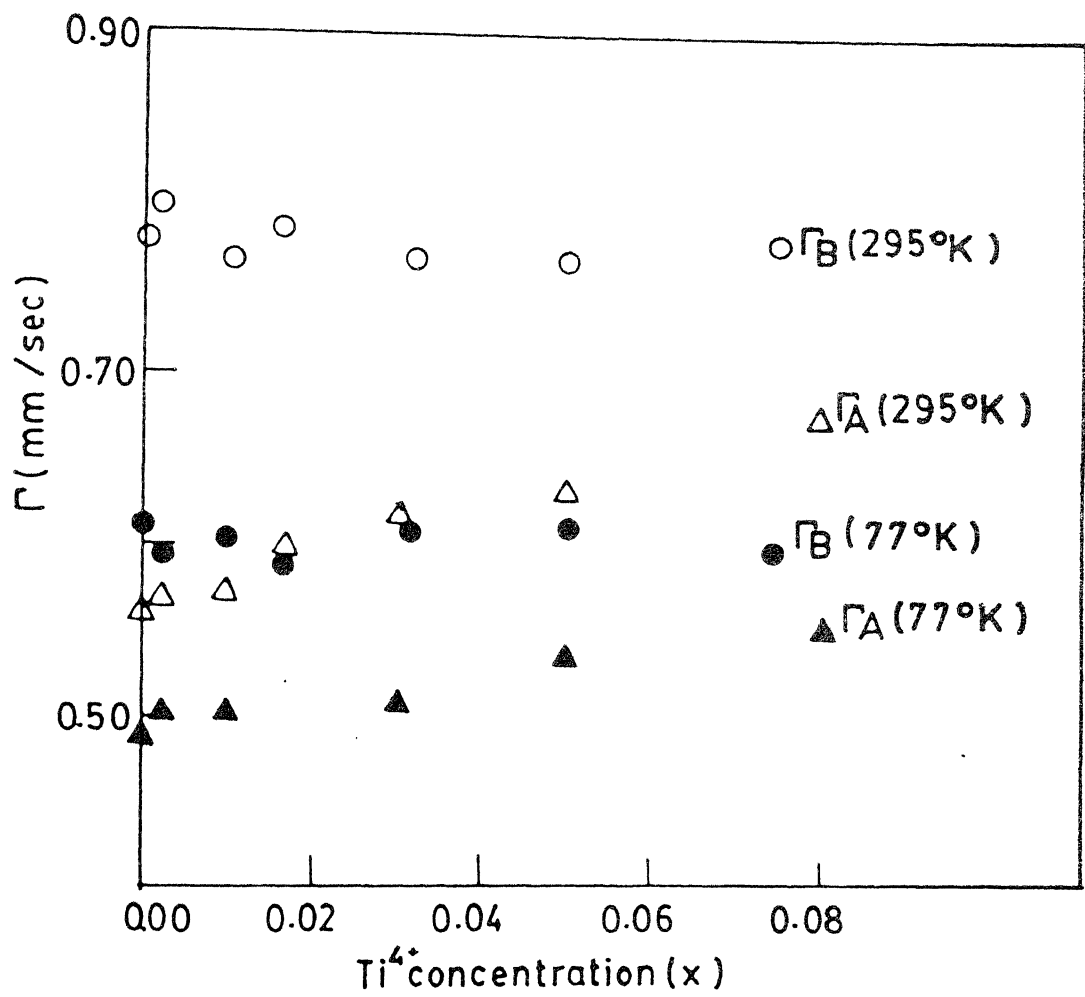


FIG. 4.10 Variation of FWHM with Ti<sup>4+</sup> concentration in  $\text{Ni}_{0.7+x} \text{Zn}_{0.3} \text{Ti}_{4+} \text{Fe}_{2-2x} \text{O}_4$  ferrite.

#### 4.2.3 Titanium Substituted $Ni_{0.6}Zn_{0.4}Fe_2O_4$ Ferrite :

Mössbauer spectra of the samples were recorded at both 295 and 77°K. They showed a well defined Zeeman pattern consisting of two separate sextets. One is due to  $Fe^{3+}$  ions at A site and the other due to  $Fe^{3+}$  ions at B site. Mössbauer spectra of  $Ni_{0.6+x}Zn_{0.4}Ti_xFe_{2-2x}O_4$  ( $0 \leq x \leq 0.1$ ) at 295 and 77°K are shown in figs. (4.11) and (4.12) respectively.

The isomer shift of  $Fe^{3+}$  ions at tetrahedral site, I.S.(A), and at octahedral site, I.S.(B) do not show any significant change with  $Ti^{4+}$  concentration. The values of isomer shift at 295 and 77°K with different concentration of  $Ti^{4+}$  are shown in fig. (4.13). The weighted average value of I.S.(A) and I.S.(B) (with respect to SNP) at 295°K are  $0.542 \pm 0.003$  and  $0.642 \pm 0.003$  mm/sec respectively. The weighted average value of isomer shift with respect to SNP at 77°K at A and B sites are  $0.734 \pm 0.003$  and  $0.872 \pm 0.003$  mm/sec respectively.

In these systems too no quadrupole splitting was observed within the limit of experimental error for both A and B sites.

The variation of  $H_{eff}$  at A and B sites with  $Ti^{4+}$  concentration are shown in fig. (4.14). It is evident from the graph that there is no significant change in  $H_{eff}(B)$

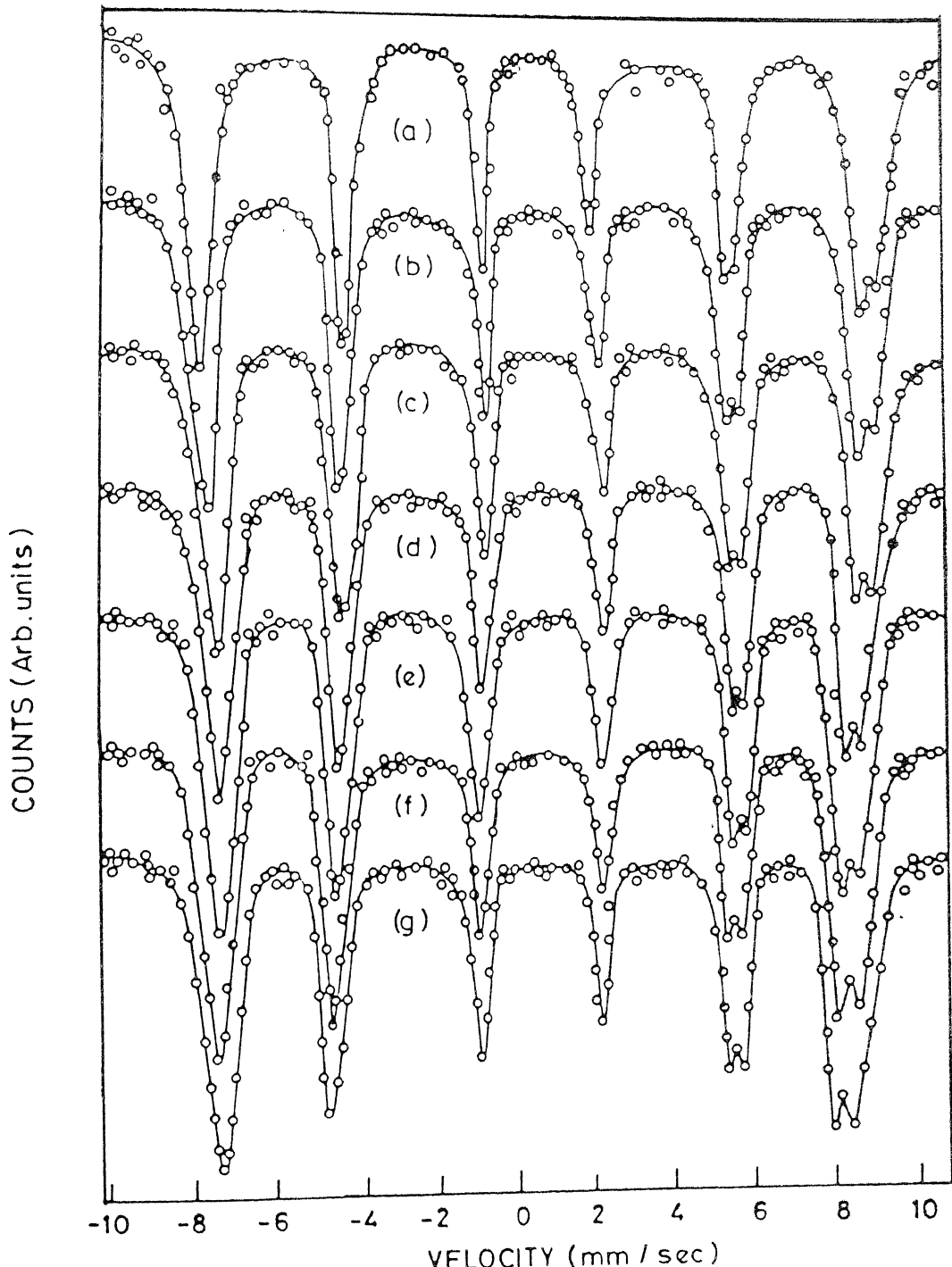


Fig. 4.11 Mössbauer spectra of  $\text{Ni}_{0.6+x} \text{Zn}_{0.4} \text{Ti}_x \text{Fe}_{2-2x} \text{O}_4$  at 295 K (a)  $x = 0.00$ , (b)  $x = 0.002$ , (c)  $x = 0.004$ , (d)  $x = 0.015$ , (e)  $x = 0.02$ , (f)  $x = 0.05$ , (g)  $x = 0.08$

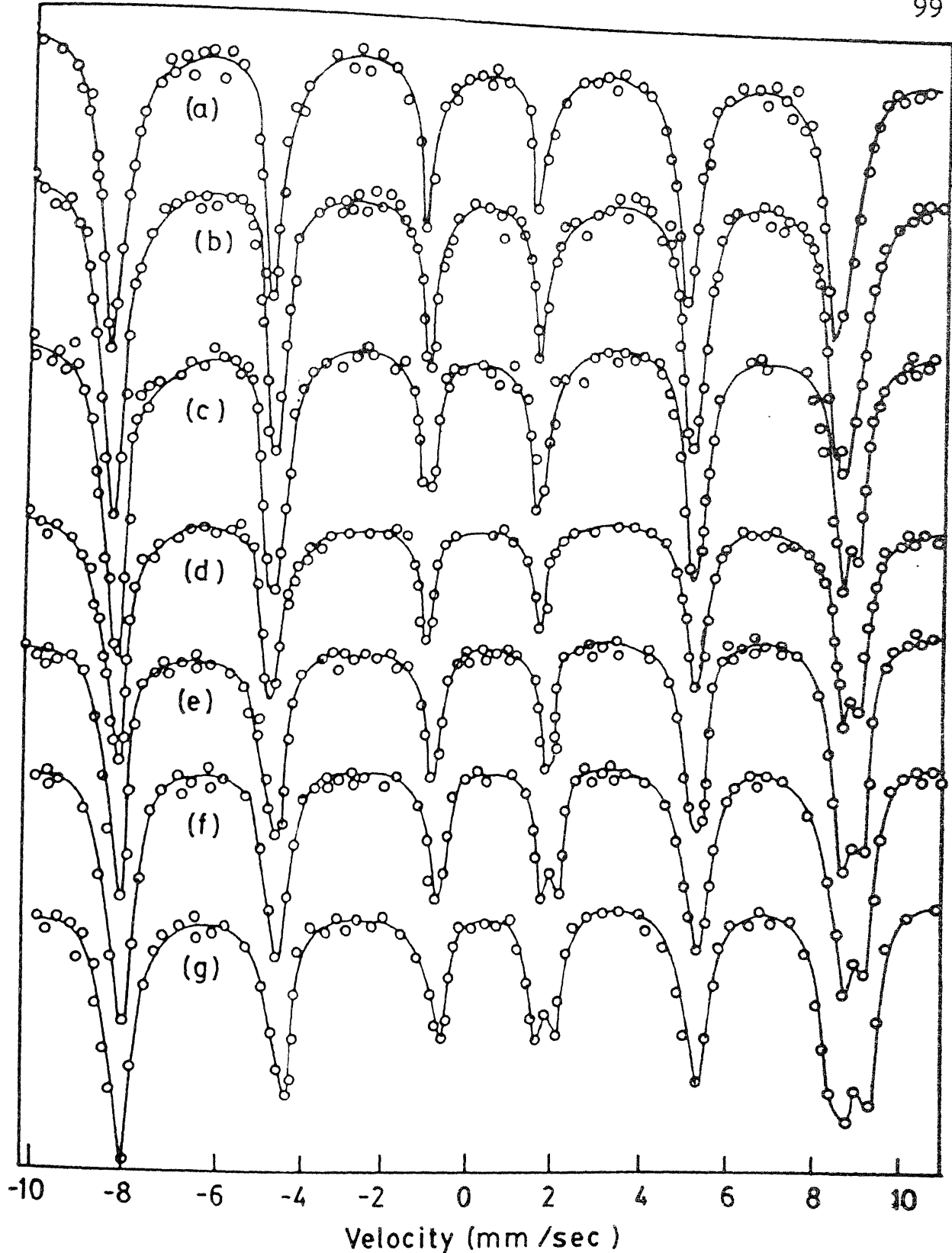


Fig. 4.12 Mössbauer spectra of  $\text{Ni}_{0.6+x} \text{Zn}_{0.4} \text{Ti}_x \text{Fe}_{2-2x} \text{O}_4$   
 at  $77^\circ\text{K}$  (a)  $x = 0.00$ , (b)  $x = 0.002$ , (c)  $x = 0.004$ ,  
 (d)  $x = 0.015$ , (e)  $x = 0.02$ , (f)  $x = 0.05$ , (g)  $x = 0.08$ .

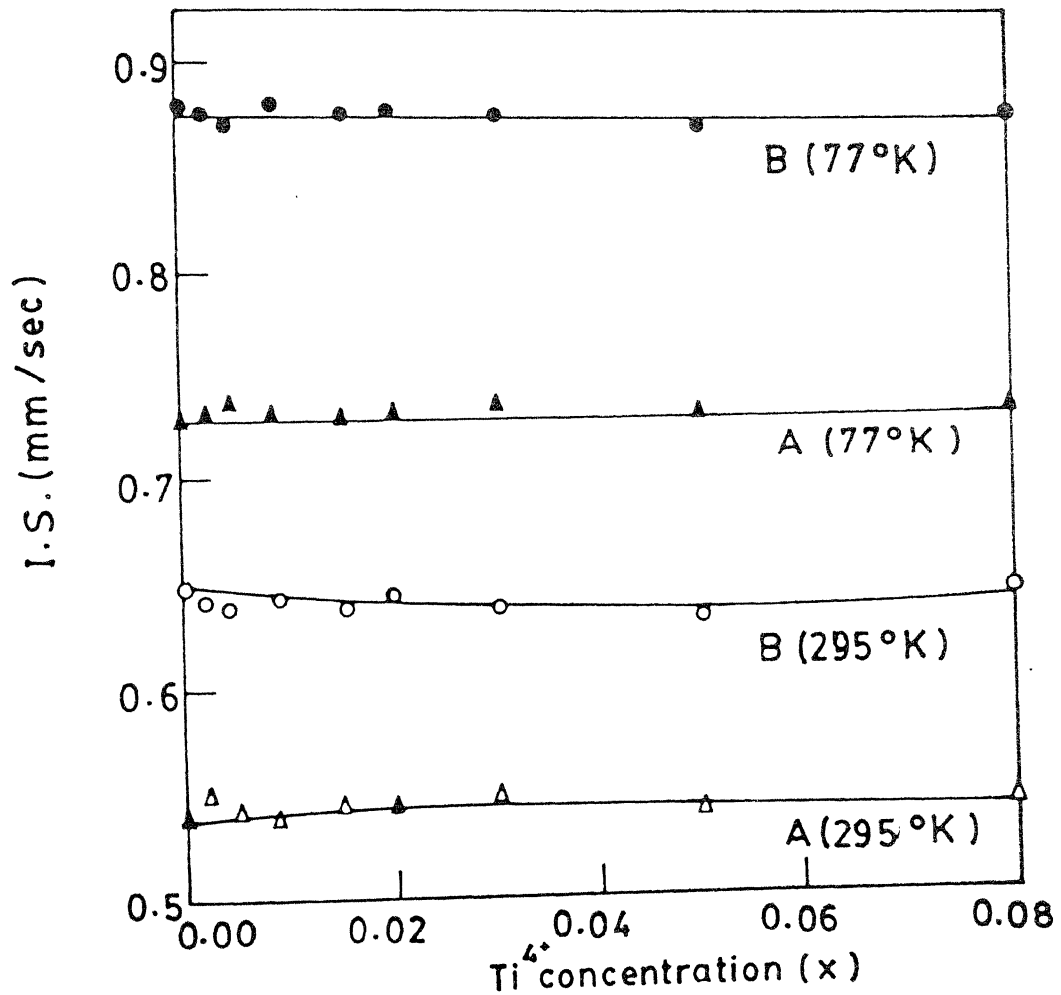


FIG. 4.13 Variation of isomer shift with  $Ti^{4+}$  concentration in  $Ni_{0.6+x}Zn_{0.4}Ti_xFe_{2-2x}O_4$  ferrite.

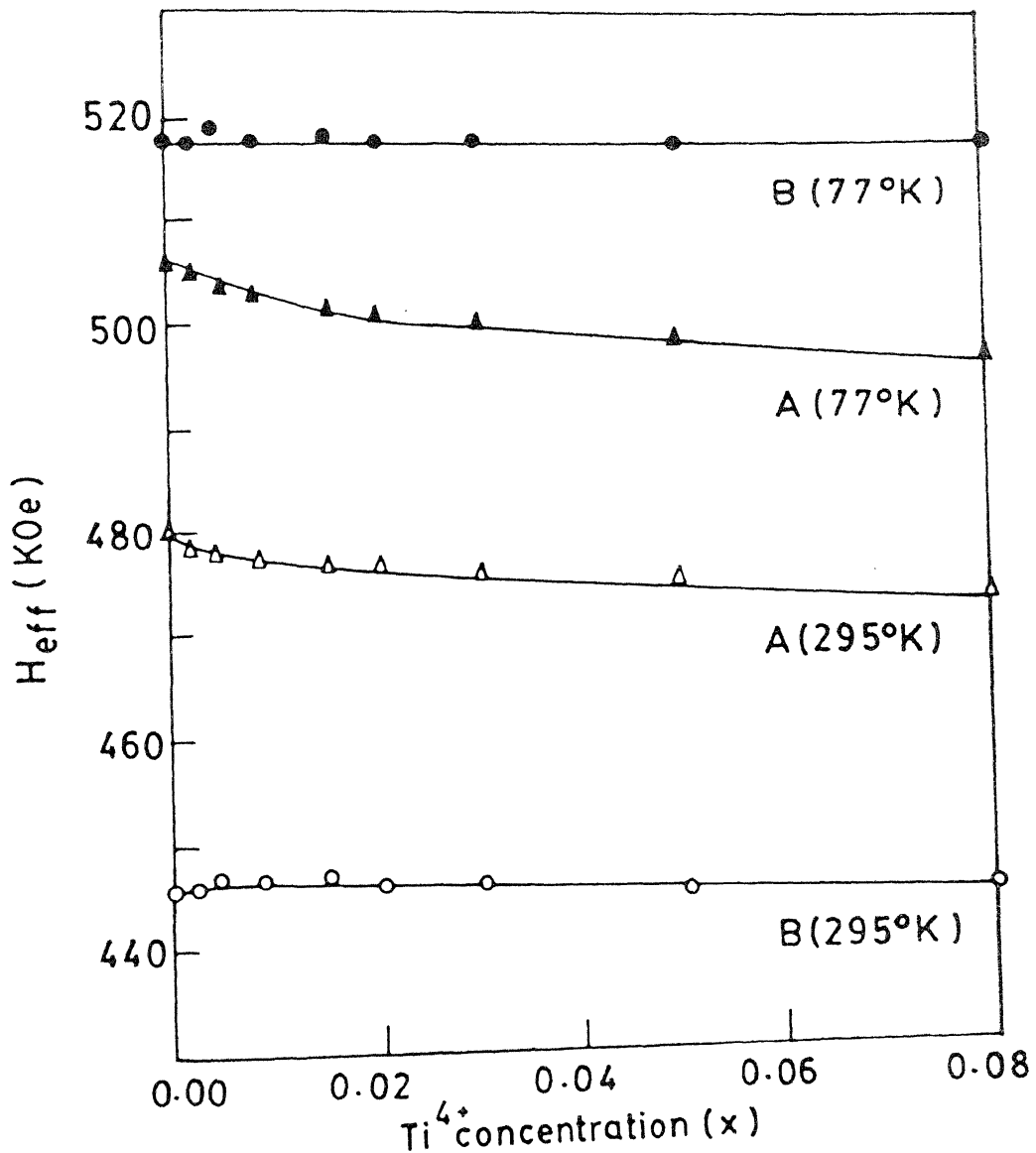


FIG. 4.14 Variation of hyperfine magnetic field with  $\text{Ti}^{4+}$  concentration in  $\text{Ni}_{0.6+x}\text{Zn}_{0.4}\text{Ti}_x\text{Fe}_{2-2x}\text{O}_4$  ferrite.

and it remains almost constant at a value of  $446 \pm 1$  KOe.  $H_{eff}(A)$ , on the other hand, decreases from  $480 \pm 1$  KOe to  $474 \pm 1$  KOe as the concentration of  $Ti^{4+}$  increases from  $x = 0.00$  to  $x = 0.08$ . A similar behaviour of  $H_{eff}(A)$  and  $H_{eff}(B)$  with  $Ti^{4+}$  concentration are observed at  $77^\circ K$  also [fig. (4.14)]. At  $77^\circ K$ ,  $H_{eff}(B)$  remains constant at a value of  $518 \pm 1$  KOe whereas  $H_{eff}(A)$  decreases from  $506 \pm 1$  KOe to  $497 \pm 1$  KOe. For the zero concentration of Ti, the values of  $H_{eff}(A)$  and  $H_{eff}(B)$  at  $295$  and  $77^\circ K$  are in excellent agreement with the values reported in the literature [3].

We have shown the variation of  $\Gamma_A$  and  $\Gamma_B$  of the Mössbauer absorption peaks with  $Ti^{4+}$  concentration in fig. (4.15). We found that there is no significant change in the values of  $\Gamma_B$  at  $295$  and  $77^\circ K$  with  $Ti^{4+}$  concentration. At  $295^\circ K$ ,  $\Gamma_B$  remains almost constant at a value of  $1.150 \pm 0.004$  mm/sec. as the concentration of  $Ti^{4+}$  increases from  $x = 0.00$  to  $x = 0.08$ . This value of  $\Gamma_B$  is a little less than the value ( $\Gamma_B = 1.2$  mm/sec) reported by Daniels et al. [3] of  $Ni_{0.6}Zn_{0.4}Fe_2O_4$  ferrite.  $\Gamma_B$  drops to  $0.650 \pm 0.003$  mm/sec at  $77^\circ K$  and it remains almost constant at this value as the concentration of Ti increases from  $x = 0.00$  to  $x = 0.08$ . At  $295^\circ K$ ,  $\Gamma_A$  increases from  $0.801 \pm 0.004$  mm/sec to  $0.955 \pm 0.004$  mm/sec whereas at  $77^\circ K$  it increases from  $0.556 \pm 0.004$  to  $0.691 \pm 0.004$

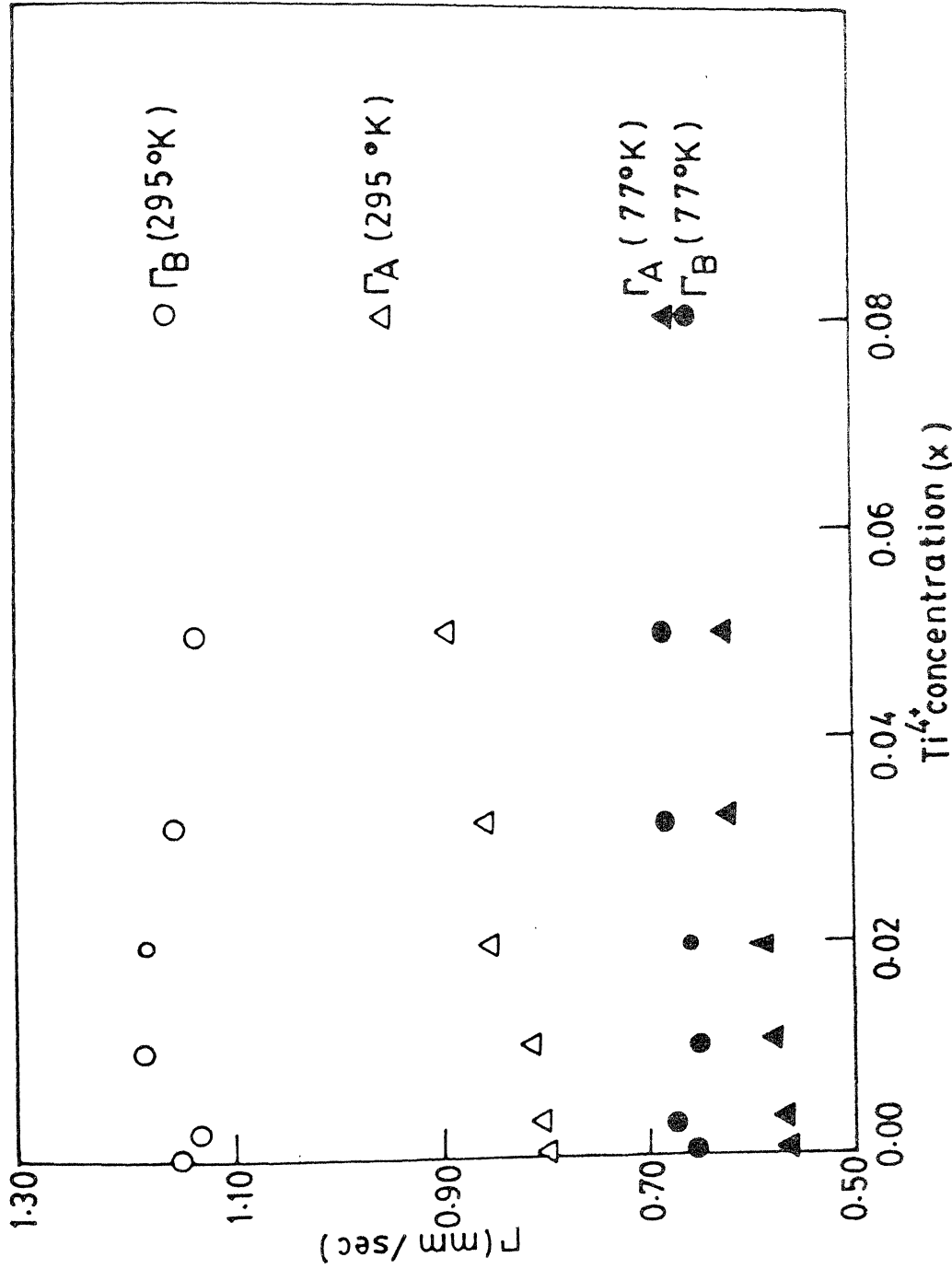


FIG. 4.15 Variation of FWHM with Ti concentration in  $\text{Ni}_{0.6+x}\text{Zn}_{0.4-x}\text{Ti}_x\text{Fe}_{2-2x}\text{O}_4$  ferrite.

mm/sec as the concentration of  $Ti^{4+}$  increases from  $x = 0.00$  to  $x = 0.08$ .

#### 4.3 Discussion of Results :

##### 4.3.1 Isomer Shift :

It is observed that in all the three systems i.e.,  $Ti^{4+}$  substituted  $Ni_{1-y}Zn_yFe_2O_4$  ( $y = 0.0, 0.3$  and  $0.4$ ) ferrite, the isomer shift of  $Fe^{3+}$  ions at both A and B sites remain almost unchanged with  $Ti^{4+}$  concentration. Since the isomer shift, for a particular nuclear transition of the Mössbauer source, is dependent only on the s-electron charge density of the absorber,  $|\psi(0)|_A^2$ , our results indicate that the s-electron density at the  $Fe^{3+}$  nucleus is not affected by  $Ti^{4+}$  substitution. The values of isomer shift at A and B sites show that iron is in  $Fe^{3+}$  high spin state [27, 28]. The result I.S.(A) < I.S.(B) is in agreement with the results of other workers [29, 30]. This is interpreted as due to the large bond separation  $Fe^{3+}-O^{2-}$  for octahedral ions as compared to that of tetrahedral ions. Due to smaller overlapping of orbitals of  $Fe^{3+}$  and  $O^{2-}$  ions, the covalency effect is small, and hence the isomer shift is large at the octahedral sites. It is also found that the isomer shift at  $77^\circ K$  is larger than its value at room temperature. This increased value of isomer shift at  $77^\circ K$  is due to the thermal red shift between the

source at room temperature and the absorber at 77°K [31, 32].

#### 4.3.2 Quadrupole Splitting :

In all the samples exhibiting Zeeman hyperfine pattern, no quadrupole splitting was observed within the experimental error for both A and B sites. Mössbauer spectra of  $\text{NiFe}_2\text{O}_4$  obtained by other investigators [33, 34] also confirmed zero quadrupole splitting. This lack of an observable quadrupole splitting in ferrites has been mistakenly interpreted as signifying the absence of an EFG. That such is not the case is clearly shown by the spectra which no longer display a Zeeman pattern (Mössbauer spectra of  $\text{Ni}_{1-y}\text{Zn}_y\text{Fe}_2\text{O}_4$ ,  $0.7 \leq y < 1.0$  by Daniels et al. [3]). The zero quadrupole splitting in such ferrites may be explained as due to the presence of chemical disorder. The chemical disorder will produce a distribution of electric field gradient of varying magnitude, direction, sign and symmetry. The resulting distribution of the quadrupole shift, as given by Eq.(4.1) (Matthias et al. [35])

$$|\Delta E_Q| = \frac{1}{2} |\Delta E_{Q0}| (3 \cos^2 \theta - 1) \quad (4.1)$$

where  $|\Delta E_{Q0}|$  is the magnitude of the shift when the magnetic interaction tends to zero and  $\theta$  is the angle between the axially symmetric EFG and the magnetic field direction, will produce a noticeable broadening (quadrupole

broadening) of the individual lines of Zeeman pattern. Because of the overall cubic symmetry of the spinel ferrites and the randomness of chemical disorders Eq. (4.1) will give rise to approximately equal probability for quadrupole splitting of opposite sign. Hence the centres of the Zeeman lines will not change. This will then result in no net observable quadrupole splitting.

#### 4.3.3 Magnetic Hyperfine Splitting :

The variation of magnetic hyperfine field at the two sublattices could be understood on the basis of Néel's molecular field theory [9] and the supertransferred hyperfine field,  $H_{\text{STHF}}$  [36-38]. The  $H_{\text{eff}}$  at a lattice site is primarily due to core polarization of its site ion. But its variation is due to that of the supertransferred hyperfine field. We analyse our result in terms of  $H_{\text{STHF}}$ . In all the three systems it is found that  $H_{\text{eff}}(B)$  remains almost constant whereas  $H_{\text{eff}}(A)$  decreases with the increase of  $\text{Ti}^{4+}$  concentration. We attribute these to the fact that all the  $\text{Ti}^{4+}$  ions occupy the B site and the consequent reduction of the magnetization  $M_B$ . We give below our arguments in favour of these conclusions.

In the present series of ferrites,  $\text{Ni}_{1-y+x}\text{Zn}_y\text{Ti}_x\text{Fe}_{2-2x}\text{O}_4$ , let  $x\text{Ti}^{4+}$  ions are distributed over A and B sites in such a way that  $z\text{Ti}^{4+}$  ions replace  $z\text{Fe}^{3+}$

ions at the A site;  $(x-z)Ti^{4+}$  ions and  $xNi^{2+}$  ions replace  $(2x-z)Fe^{3+}$  ions at the B site. According to this, the ionic distribution follows the structural formula  $(Zn_y^{2+}Fe_{1-y-z}^{3+}Ti_z^{4+}) [Ni_{1-y+x}^{2+}Fe_{1+y-2x+z}^{3+}Ti_{x-z}^{4+}]O_4^{2-}$ . According to the assumptions of Néel's Molecular field theory, the A-B superexchange interaction are stronger than the A-A or the B-B superexchange interaction.  $Zn^{2+}$  and  $Ti^{4+}$  ions, being diamagnetic, do not participate in the magnetic superexchange interaction. Since  $Fe_A^{3+}-O^{2-}-Fe_B^{3+}$  superexchange interaction is stronger than  $Fe_A^{3+}-O^{2-}-Ni_B^{3+}$  superexchange interaction [39], the effective magnetic field is primarily due to average  $Fe_A^{3+}-O^{2-}-Fe_B^{3+}$  magnetic bonds per  $Fe^{3+}$  ion. According to the above ionic distribution, the tetrahedral  $Fe^{3+}$  ions have, on the average,  $(1+y-2x+z)/2$  of their intersublattice magnetic bonds with  $Fe^{3+}$  ions at the octahedral site and  $(1-y+x)/2$  of their intersublattice magnetic bonds with  $Ni^{2+}$  ions. On the other hand, the octahedral  $Fe^{3+}$  ions have, on the average,  $(1-y-z)$  of their intersublattice magnetic bonds with  $Fe^{3+}$  ions at the A site. Since for a particular concentration of Zn (i.e.  $y$  is constant) there is no appreciable change in  $H_{eff}$  at the B site with  $Ti^{4+}$  addition, we conclude that  $Z$  is zero and all the  $Ti^{4+}$  ions occupy the B site. This in turn, reduces the number of intersublattice magnetic bonds which the  $Fe_A^{3+}$  ions

experience. Hence the value of  $H_{\text{eff}}(A)$  is found to decrease with the increase of  $\text{Ti}^{4+}$  ions at B site. From the cation distribution it is seen that there is no change in the concentration of  $\text{Fe}^{3+}$  ions at A site since  $z$  is zero. Hence the tetrahedral environment of  $\text{Fe}_B^{3+}$  ion does not change and, therefore, the number of magnetic bonds which  $\text{Fe}_B^{3+}$  ion experience, remains unchanged. This explains the constant value of  $H_{\text{eff}}(B)$ .

The observed variation of  $H_{\text{eff}}$  with  $\text{Ti}^{4+}$  concentration can also be understood to arise from the change in supertransfer hyperfine field. The super transferred hyperfine field at the  $\text{Fe}^{3+}$  ion at A site is due to the spin transfer from the d-orbitals of the nearest neighbour cations (i.e. belonging to B sublattice) through the ligand anions to the 4s-orbitals of the  $\text{Fe}^{3+}$  ions under consideration. Thus the supertransferred field at A site will depend on the magnetic moment of the B site. Hence we attribute the decrease in  $H_{\text{eff}}(A)$  to the fact that all the non-magnetic  $\text{Ti}^{4+}$  ions occupy the B site and thereby reducing the magnetization  $M_B$ ; this in turn, reduces the supertransferred hyperfine field at A site. Similarly it can be argued that the supertransferred hyperfine field at B site should remain constant as the magnetization  $M_A$  does not change, since the  $\text{Ti}^{4+}$  ions enter only at B site.

#### 4.3.4 Full Width at Half Maximum (FWHM) :

Apart from the quadrupole broadening discussed in Sec. 4.3.2 there is another contribution to the line broadening of the Mössbauer absorption peaks. If two or more cations are present in one or both the sublattices then there will be a distribution of the values of  $\langle S_z \rangle$  which results in a distribution of the values of the hyperfine magnetic field at the nucleus. This causes the broadening of the individual lines of the Mössbauer Zeeman pattern. For the sake of convenience we can call this effect as magnetic broadening.

It is found that in all the three systems the FWHM at A site,  $\Gamma_A$  increases with  $Ti^{4+}$  concentration whereas  $\Gamma_B$ , the FWHM at B site remain almost constant. As we have seen that the change in  $H_{eff}(A)$  is mainly because of the change in the contribution of supertransferred hyperfine field at A site which, in turn, is owing to the change in  $\langle S_z \rangle$  at B site. The increase in the value of  $\Gamma_A$  with  $Ti^{4+}$  concentration shows that the width of the distribution of  $\langle S_z \rangle$  values at B site increases as all the  $Ti^{4+}$  ions enter at the octahedral B site. On the other hand,  $\Gamma_B$  remains almost constant with the  $Ti^{4+}$  concentration. This is because of the fact that the distribution of  $\langle S_z \rangle$  at A site is unaffected by the substitution of  $Ti^{4+}$  ions at B site.

site. With the decrease in temperature, the distribution of  $\langle S_z \rangle$  is narrowed and hence a decrease in the line broadening is expected. This is evidenced by the decrease in  $\Gamma_A$  and  $\Gamma_B$  at  $77^\circ\text{K}$ .

#### 4.4 Study of Magnetization :

##### 4.4.1 $\text{Ti}^{4+}$ Substituted $\text{NiFe}_2\text{O}_4$ Ferrite :

The variation of magnetization with  $\text{Ti}^{4+}$  concentration is shown in fig. (4.16). In this fig. we have also shown the variation of  $|\text{H}_{\text{eff}}(\text{B}) - \text{H}_{\text{eff}}(\text{A})|$  with  $\text{Ti}^{4+}$  concentration on comparable scales. For a better visual aid in comparison, an inverted scale has been chosen for the net effective magnetic field,  $|\text{H}_{\text{eff}}(\text{B}) - \text{H}_{\text{eff}}(\text{A})|$ . It is clear from the graph that the net effective magnetic field follows the same trend as that of the magnetization. Mössbauer spectroscopy reveals that in  $\text{Ni}_{1+x}\text{Ti}_x\text{Fe}_{2-2x}\text{O}_4$  ( $x = 0.0-0.1$ ) ferrite the  $\text{Ti}^{4+}$  ions occupy the B site. This information when put in the Néel type of magnetic ordering model leads to a linear decrease of magnetization with  $\text{Ti}^{4+}$  concentration. But the magnetization shows a sudden fall followed by a slow decrease as the concentration of  $\text{Ti}^{4+}$  ions increases [fig. (4.16)]. Hence we conclude that the change of magnetization is not only due to the simple replacement of magnetic ions at B site by non-magnetic  $\text{Ti}^{4+}$ .

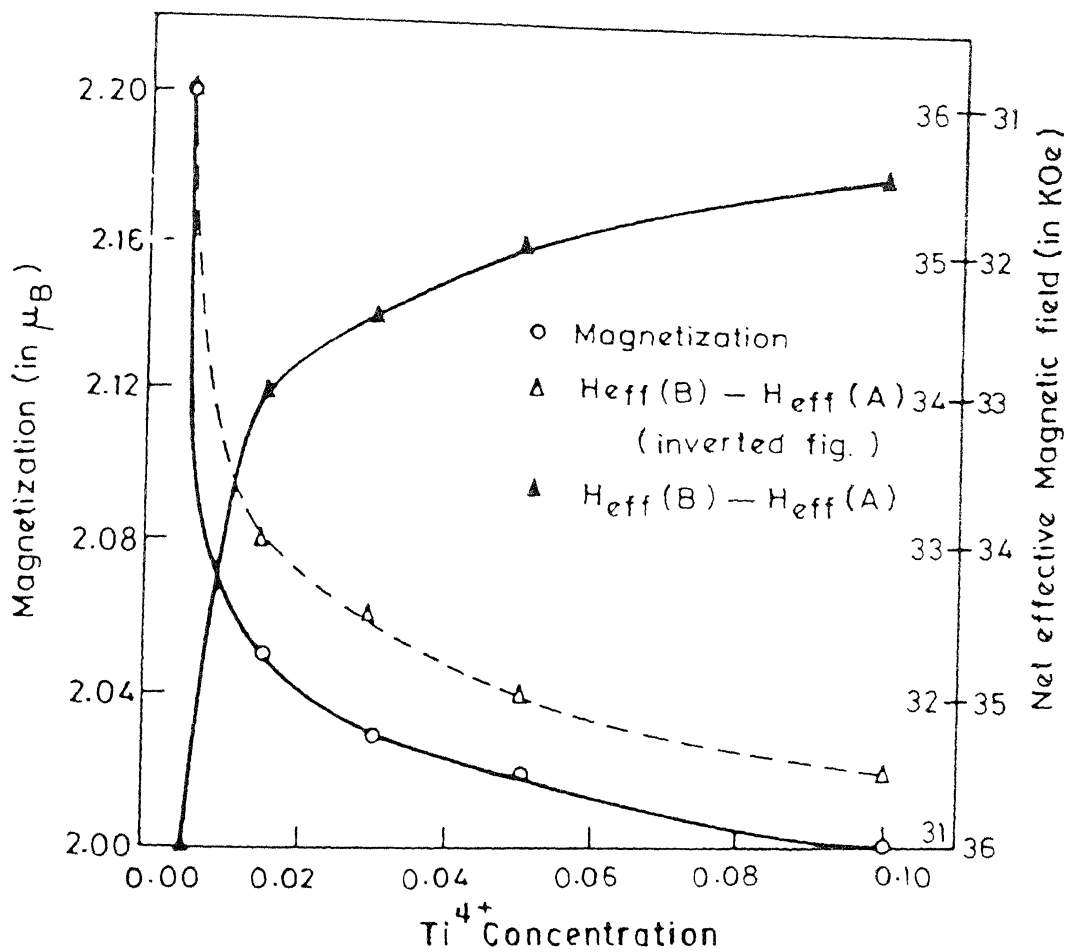


Fig. 4.16 Variation of magnetization and the net effective magnetic field with  $Ti^{4+}$  concentration. The outer scale on the right is for  $\Delta$  (inverted fig.) and the inner scale is for  $\blacktriangle$ .

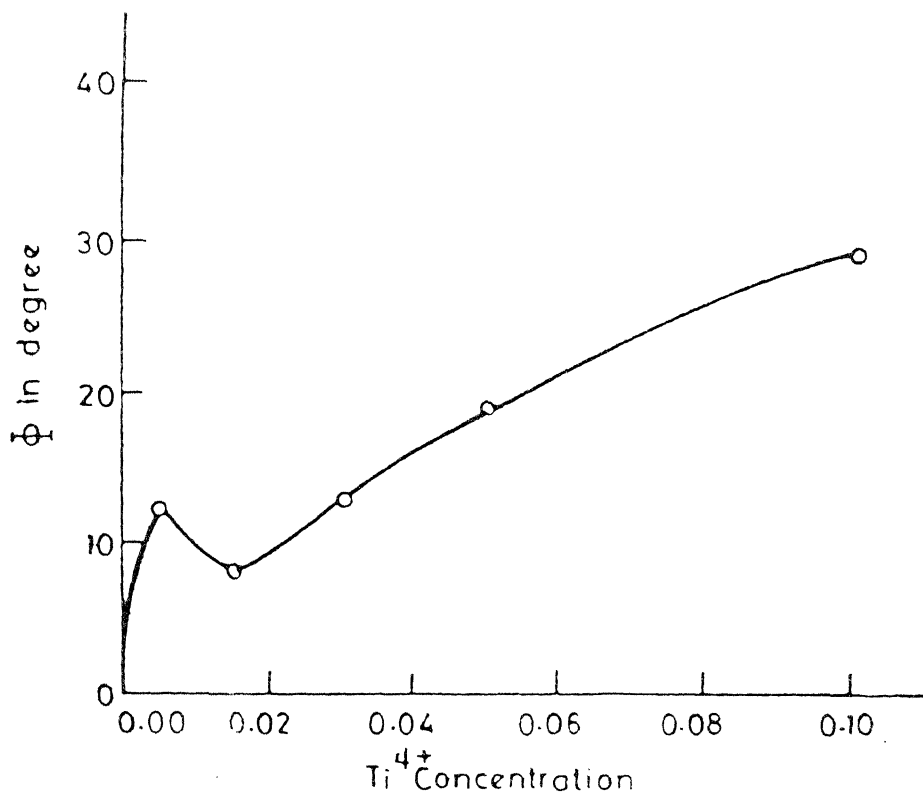


Fig. 4.17 Variation of canting angle with  $Ti^{4+}$  concentration in  $Ni_{1+x} Ti_x Fe_{2-2x} O_4$ .

ions but also due to a more complex process which leads to the development of canted spin structure. The positional readjustment of ions due to electrostatic forces after the entry of  $Ti^{4+}$  ions in the lattice causes readjustment of the values of the exchange constants,  $J_{Fe^{3+}(A)-Ni^{2+}(B)}$ ,  $J_{Fe^{3+}(A)-Fe^{3+}(B)}$ ,  $J_{Ni^{2+}(B)-Ni^{2+}(B)}$ ,  $J_{Fe^{3+}(B)-Ni^{2+}(B)}$ ,  $J_{Fe^{3+}(B)-Fe^{3+}(B)}$  and,  $J_{Fe^{3+}(A)-Fe^{3+}(A)}$ . The most important feature of the new situation is that  $J_{AA}$  now becomes comparable to  $J_{AB}$  and the canting starts at A sublattice. The magnetization results were analysed using the three sublattice Yafet-Kittel type model. If canting takes place at A site then the magnetization is given by

$$M = M_B - M_A \cos\phi \quad (4.2)$$

where  $\phi$  is the canting angle. The variation of canting angle with  $Ti^{4+}$  concentration, as calculated from magnetization data is shown in fig. (4.17).

The analysis of exchange constants in the  $Ti^{4+}$  substituted  $Ni_{1-y}Zn_yFe_2O_4$  system is based on the modified version of Srivastava's three sublattice model. The molecular field acting on various ions are given by

$$\begin{bmatrix} \vec{H}_{A1}(Fe) \\ \vec{H}_{A2}(Fe) \\ \vec{H}_B(Ni) \\ \vec{H}_B(Fe) \end{bmatrix} = \begin{bmatrix} \lambda_{AA} & \lambda_{AA} & \alpha & \beta \\ \lambda_{AA} & \lambda_{AA} & \alpha & \beta \\ \alpha & \alpha & \gamma & \epsilon \\ \beta & \beta & \epsilon & \delta \end{bmatrix} \begin{bmatrix} A_F & \vec{m}_{A1}(Fe) \\ A_F & \vec{m}_{A2}(Fe) \\ B_N & \vec{m}_B(Ni) \\ B_F & \vec{m}_B(Fe) \end{bmatrix}$$

where  $H_{A1}(Fe)$  is the molecular field acting on the  $Fe^{3+}$  ion at A1 site due to all other ions, etc.  $A_F$ .  $B_N$ .  $B_F$  are the concentration of  $Fe^{3+}$  ion,  $Ni^{2+}$  ions and  $Fe^{3+}$  ions at A1 or A2, B and, B sublattices respectively. The interactions  $A1(Fe^{3+}) - A1(Fe^{3+})$ ,  $A1(Fe^{3+}) - A2(Fe^{3+})$ ,  $A1(Fe^{3+}) - B(Ni^{2+})$ ,  $A1(Fe^{3+}) - B(Fe^{3+})$ ,  $A2(Fe^{3+}) - A1(Fe^{3+})$ ,  $A2(Fe^{3+}) - A2(Fe^{3+})$ ,  $A2(Fe^{3+}) - B(Ni^{2+})$ ,  $A2(Fe^{3+}) - B(Fe^{3+})$ ,  $B(Ni^{2+}) - A1(Fe^{3+})$ ,  $B(Ni^{2+}) - A2(Fe^{3+})$ ,  $B(Ni^{2+}) - B(Ni^{2+})$ ,  $B(Fe^{3+}) - A1(Fe^{3+})$ ,  $B(Fe^{3+}) - A2(Fe^{3+})$ ,  $B(Fe^{3+}) - B(Ni^{2+})$ ,  $B(Fe^{3+}) - B(Fe^{3+})$  are represented by the molecular field coefficients  $\lambda_{AA}$ ,  $\lambda_{AA}$ ,  $\alpha$ ,  $\beta$ ,  $\lambda_{AA}$ ,  $\lambda_{AA}$ ,  $\alpha$ ,  $\beta$ ,  $\alpha$ ,  $\alpha$ ,  $\gamma$ ,  $\epsilon$ ,  $\beta$ ,  $\beta$ ,  $\epsilon$  and,  $\delta$  respectively.

And,

$$\begin{aligned}
 \vec{m}_{A1} \cdot \vec{m}_B &= -|\vec{m}_{A1}| |\vec{m}_B| \cos \phi \\
 \vec{m}_{A2} \cdot \vec{m}_B &= -|\vec{m}_{A2}| |\vec{m}_B| \cos \phi \\
 \vec{m}_{A1} \cdot \vec{m}_{A1} &= |\vec{m}_{A1}| |\vec{m}_{A2}| \cos 2\phi \\
 |\vec{m}_i(Fe^{3+})| &= 5\mu_B \quad i = A1, A2, B \\
 |\vec{m}_B(Ni^{2+})| &= 2.3\mu_B
 \end{aligned}$$

Minimizing the magnetic interaction energy

$$E = - \sum_{i,j} 2 J_{ij} \vec{S}_i \cdot \vec{S}_j \quad (4.3)$$

for canting model the Yafet-Kittel angle comes out to be

$$\cos \phi = \frac{23\alpha A_F B_N + 50\beta A_F B_F}{200 \lambda_{AA}^2 A_F^2} \quad (4.4)$$

From the observed variation of the canting angle with concentration it is possible to evaluate the molecular field constants. But as pointed out by Satyamurthy et al.[14] a small error in the value of the Yafet-Kittel angles can lead to large variations in the field constants. This fact is also vindicated by Misra [40]. So we choose to reverse the direction of action. We started with  $J$  values reported by Khan et al. [18] for  $\text{Ni}_{1-y} \text{Zn}_y \text{Fe}_2 \text{O}_4$  and converted them to molecular field constants using the relation

$$\lambda_{A-B} = \frac{2Z_{AB} J_{A-B}}{N_B g_A g_B \mu_B^2} \quad (4.5)$$

where  $Z_{AB}$  is the number of nearest neighbours of 'B' kind surrounding the 'A' kind,  $N_B$  is the number of 'B' type ions per formula unit,  $g_A$  and  $g_B$  are the gyromagnetic ratios for A and B ions respectively. Using the information that (i) octahedral ion has six nearest neighbour tetrahedral ions, (ii) tetrahedral ion has twelve nearest neighbour octahedral ions, (iii) octahedral ion has six nearest neighbour octahedral ions and, (iv) tetrahedral ion has four nearest neighbour tetrahedral ions, we get a set of  $\alpha$ ,  $\beta$  and  $\lambda_{AA}$ . These parameters were adjusted with the help of a computer programme using the Eq. (4.4) unless we get the best fitted value of  $\cos\phi$ . The molecular field constants obtained in this manner yield the  $J$  values which

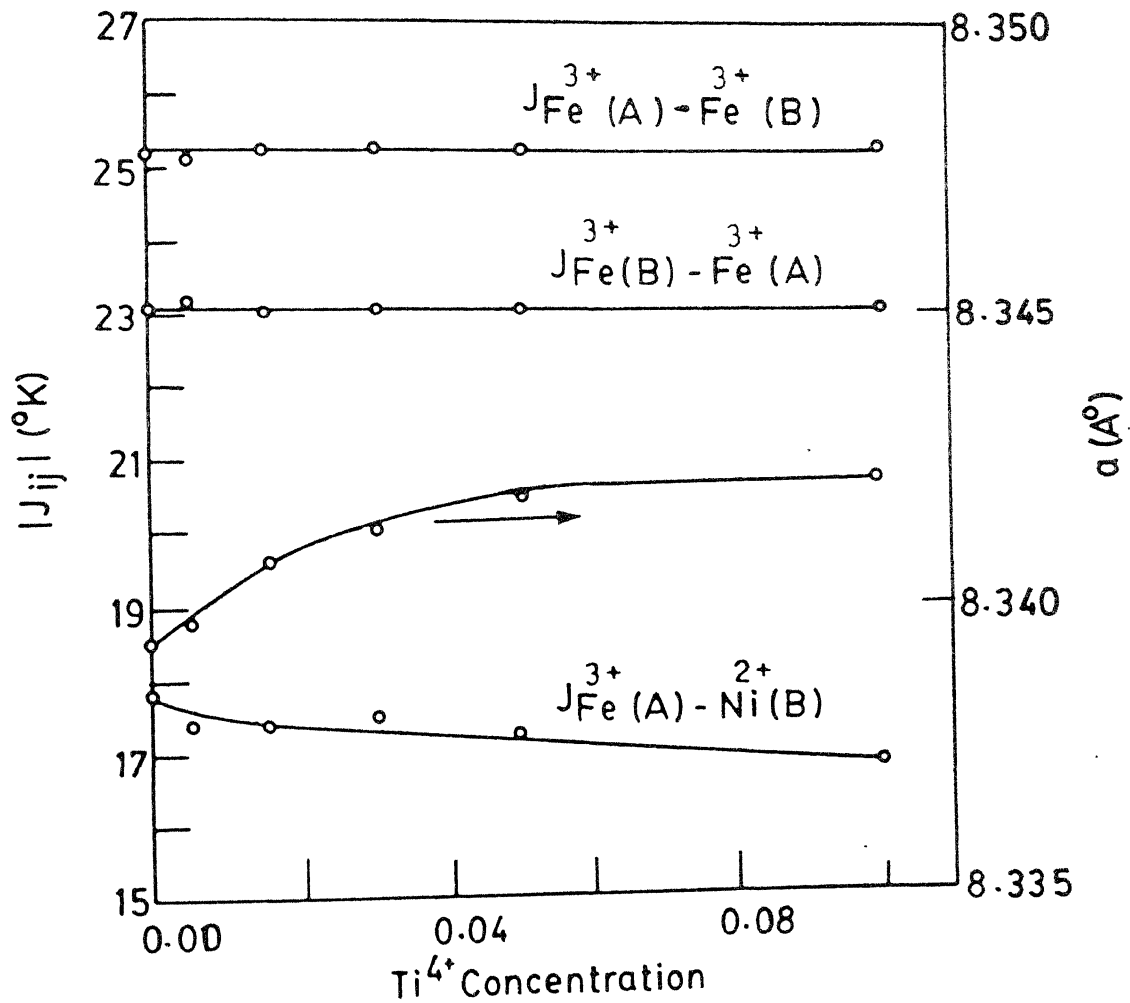


FIG. 4.18 VARIATION OF EXCHANGE CONSTANTS AND LATTICE PARAMETER WITH  $\text{Ti}^{4+}$  CONCENTRATION IN  $\text{Ni}_{1+x} \text{Ti}_x \text{Fe}_{2-2x} \text{O}_4$  FERRITE.

are plotted against  $Ti^{4+}$  concentration in fig (4.18). It is evident from the graph that  $J_{Fe^{3+}(A)-Fe^{3+}(B)}$  and  $J_{Fe^{3+}(A)-Fe^{3+}(A)}$  remain almost constant whereas  $J_{Fe^{3+}(A)-Ni^{2+}(B)}$  decreases with the increase of  $Ti^{4+}$  concentration. In fig. (4.18) we have also shown the change of lattice parameter, obtained from X-ray diffraction data. The change in lattice parameter is reflected by the change in  $J_{Fe^{3+}(A)-Ni^{2+}(B)}$ . As the titanium concentration increases, the lattice parameter also increases. This causes a decrease in the overlap of the atomic orbitals and hence a decrease in the exchange constant.

Based on the hard sphere model, the lattice parameter and oxygen parameter were calculated but there were no significant change in either of the parameters with the increase of titanium concentration. Thus, the experimental curve for lattice parameter could not be reproduced by theoretical calculations. This shows that the hard sphere model is not valid in this case. The Madelung constant was also calculated using the eq. 5 of Krupicka et al. [41] which is based on the generalized Ewald's method used by Thompson and Grimes [42]. Here we find that the Madlung constant remains almost unchanged by the increase of titanium concentration into the lattice. However, using the Born formula relating the lattice parameter with the

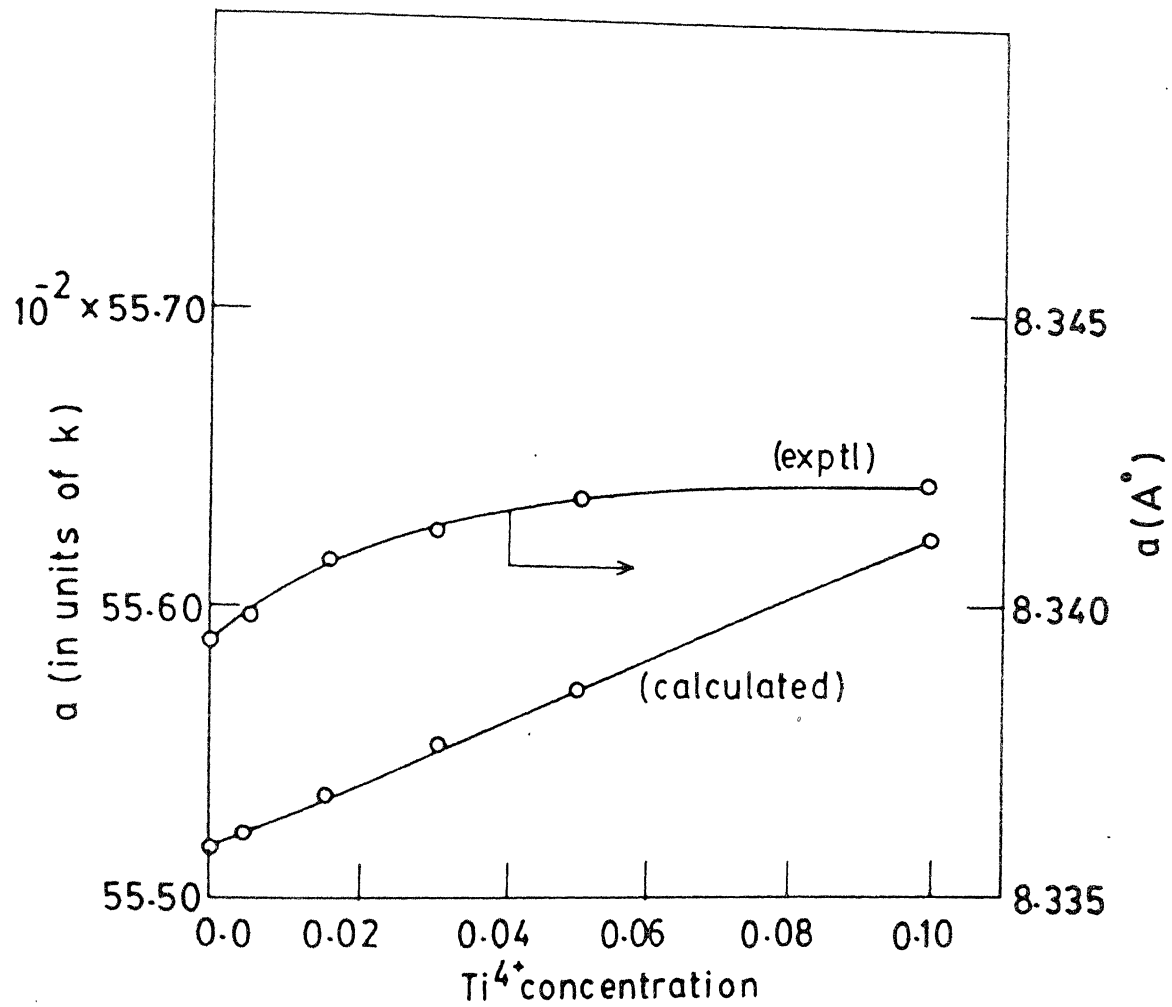


Fig. 4.18a Variation of lattice parameter with  $\text{Ti}^{4+}$  concentration in  $\text{Ni}_{1+x} \text{Fe}_{2-2x} \text{Ti}_x \text{O}_4$  ferrite

Madelung constant [Eq. 4.8], and the root mean square charge deviation at each site gives a variation of  $M$  and correspondingly of  $a$  [fig. 4.18a].

#### 4.4.2 $Ti^{4+}$ Substituted $Ni_{0.7}Zn_{0.3}Fe_2O_4$ Ferrite :

In fig. (4.19) we have shown the variation of magnetization and the net effective magnetic field with  $Ti^{4+}$  concentration on comparable scales. For a better visual aid in comparison between the magnetization and the net effective magnetic field an inverted scale has been chosen for the net effective magnetic field. It is evident from the graph that the variation of net effective magnetic field with  $Ti^{4+}$  concentration follows the same trend as that of the saturation magnetization.

Mössbauer spectroscopy, beyond any doubt, confirms that in  $Ni_{0.7+x}Zn_{0.3}Ti_xFe_{2-2x}O_4$  ( $x = 0.0-0.1$ ) ferrite  $Ti^{4+}$  ions occupy solely B site. If we consider the Néel type of magnetic ordering then a linear fall in the magnetization is expected with the increase of  $Ti^{4+}$  concentration. The magnetization shows a steep fall [fig. (4.19)] from  $2.62 \mu_B$  at zero concentration of  $Ti^{4+}$  to  $2.19 \mu_B$  at the  $Ti^{4+}$  concentration of  $x = 0.016$ . It is then followed by an increase in the magnetization upto the  $Ti^{4+}$  concentration of  $x = 0.032$  and then the magnetization becomes almost constant upto the  $Ti^{4+}$  concentration of  $x = 0.08$ . This

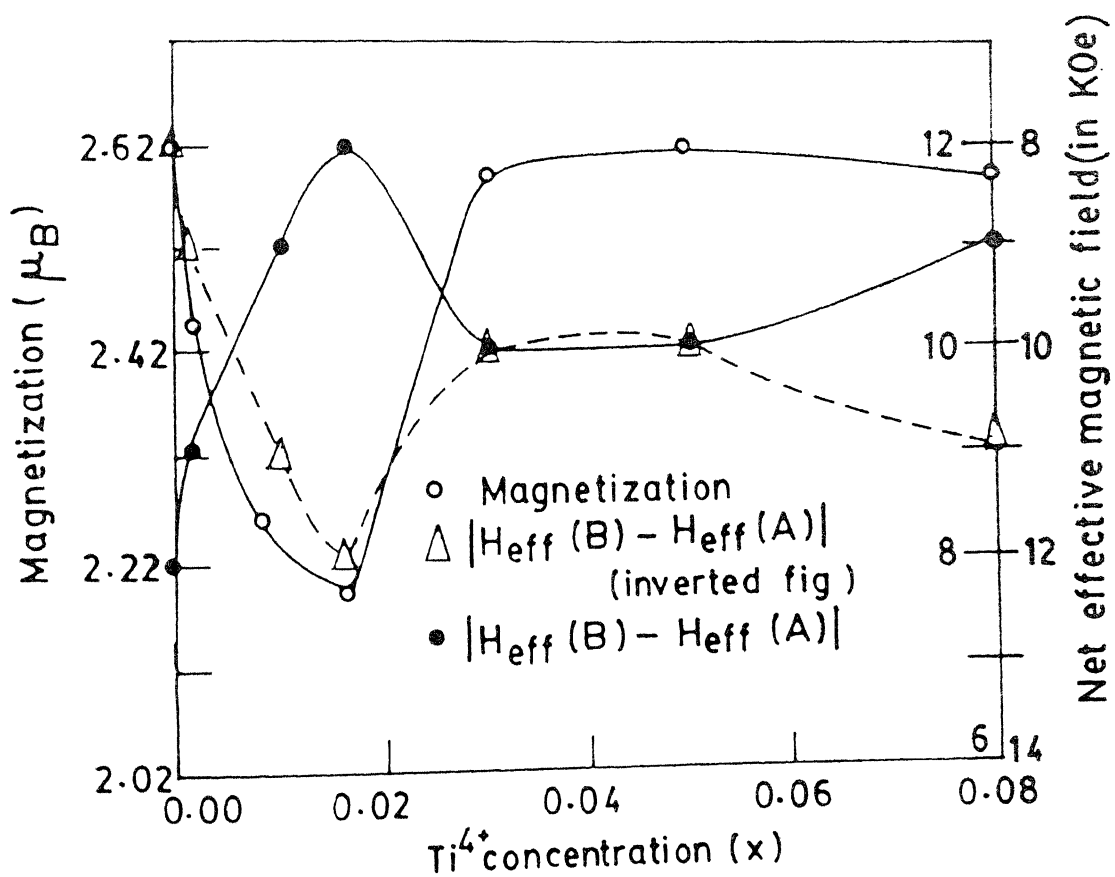


FIG. 4.19 Variation of magnetization and net effective magnetic field with  $Ti^{4+}$  concentration in  $Ni_{0.7+x} Zn_{0.3} Ti_x Fe_{2-2x} O_4$ . The outer scale on the right is for  $\Delta$  and the inner scale is for  $\bullet$ .

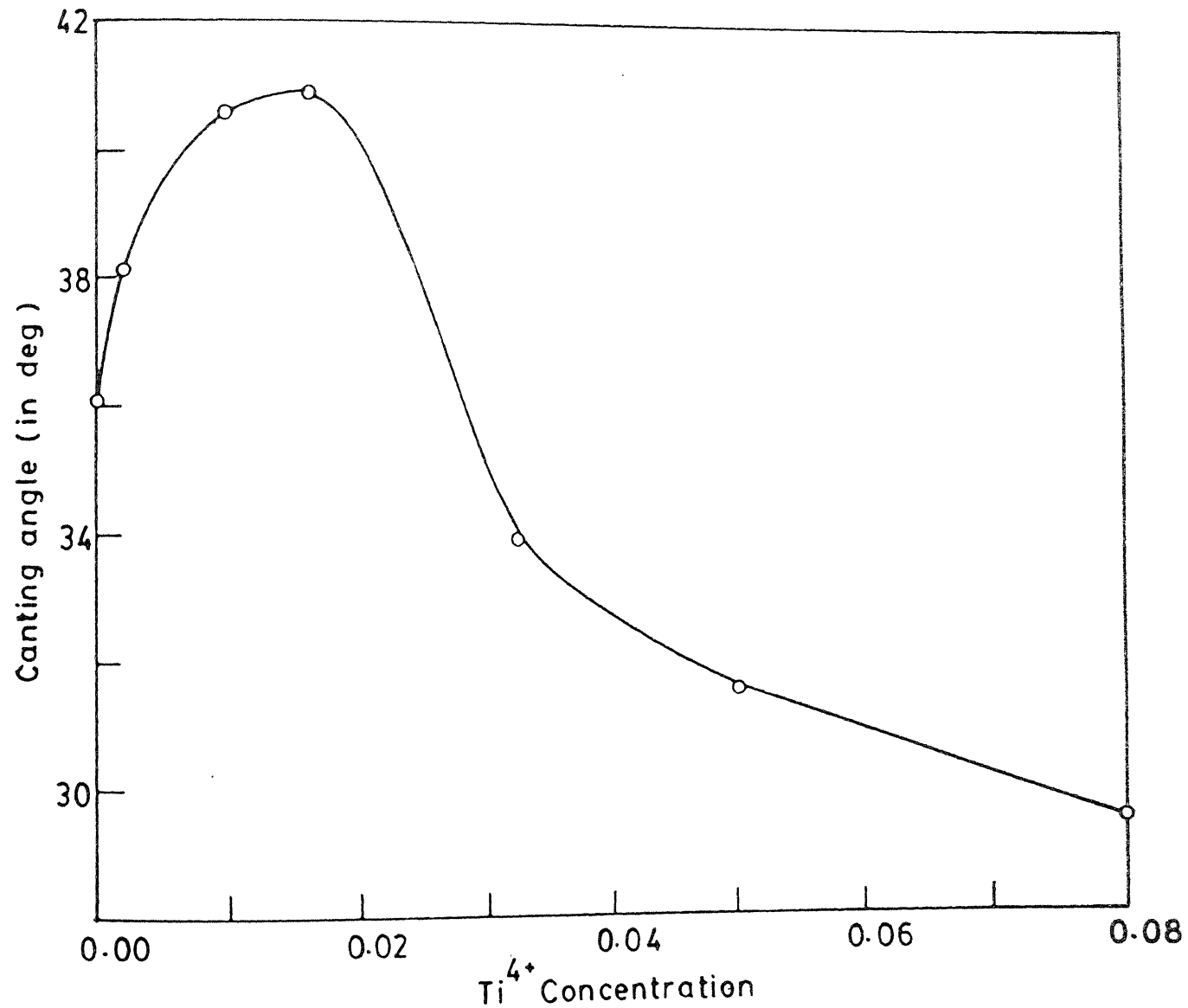


FIG.4.20 VARIATION OF CANTING ANGLE WITH  $Ti^{4+}$  CONCENTRATION  
IN  $Ni_{0.7+x} Zn_{0.3} Ti_x Fe_{2-2x} O_4$  Ferrite.

anomalous behaviour of magnetization suggests the development of canted spin structure. In a spinel structure each ion at A site is surrounded by twelve B site nearest neighbour cations while a cation at B site has six B and six A ions as the nearest neighbours. Since all the nonmagnetic  $Ti^{4+}$  ions occupy the B site it is possible that the A-B superexchange interaction and the B-B superexchange interaction become comparable to each other. This will then lead to the development of canting of spins at B site. The magnetization, in this case, is given by

$$M = M_B \cos\phi - M_A \quad (4.6)$$

where  $\phi$  is the canting angle.

The variation of canting angle with  $Ti^{4+}$  concentration, as calculated from magnetization data, is shown in fig. (4.20). The canting angle increases from  $36.1^\circ$  at zero concentration of  $Ti^{4+}$  to  $40.9^\circ$  at the  $Ti^{4+}$  concentration of  $x = 0.016$  followed by the decrease in the canting angle upto  $29.5^\circ$  for the  $Ti^{4+}$  concentration of  $x = 0.08$ . The interpretation of this result is given along with that of  $Ti^{4+}$  substituted  $Ni_{0.6}Zn_{0.4}Fe_2O_4$  ferrite.

#### 4.4.3 $Ti^{4+}$ Substituted $Ni_{0.6}Zn_{0.4}Fe_2O_4$ Ferrite :

We have shown the variation of magnetization and the net effective magnetic field with  $Ti^{4+}$  concentration on comparable scales in fig. (4.21). It is observed that the

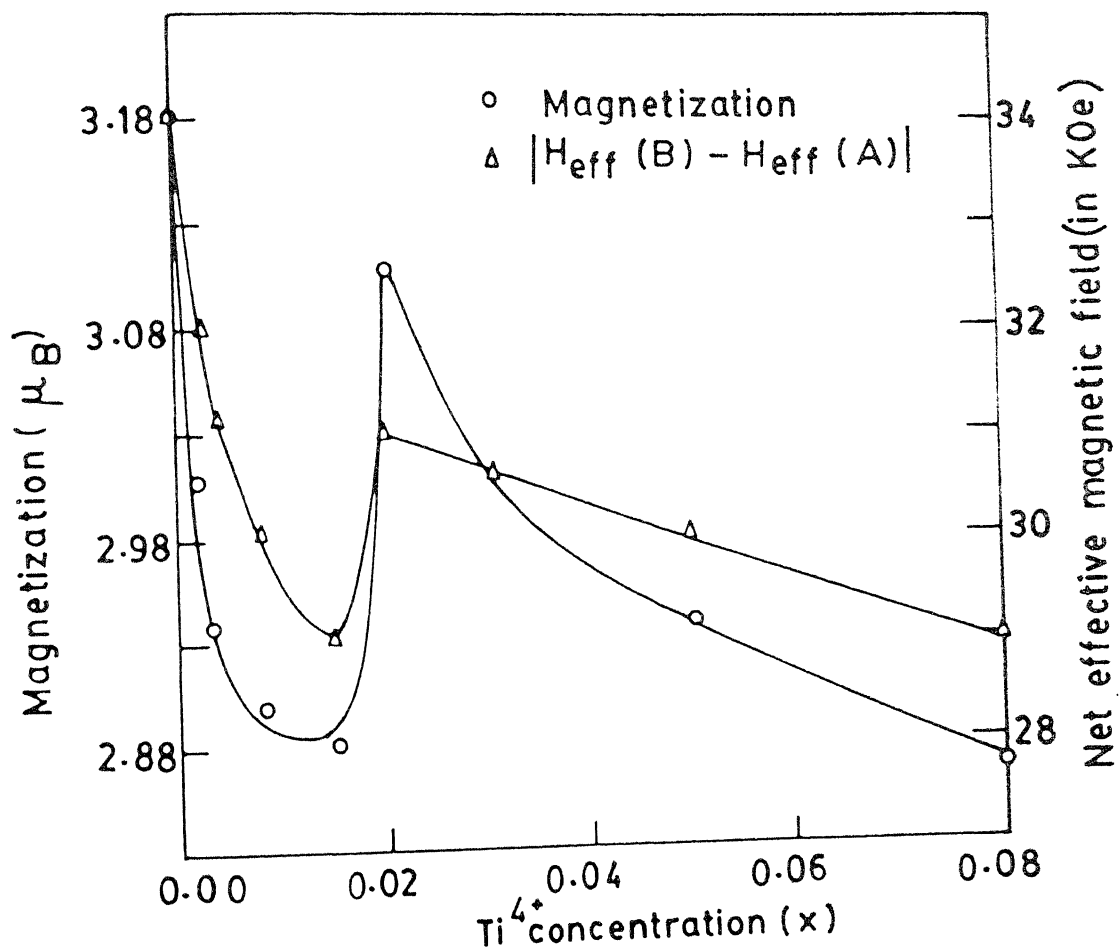


FIG.4.21 Variation of magnetization and net effective magnetic field with  $Ti^{4+}$  concentration in  $Ni_{0.6+x}Zn_{0.4}Ti_xFe_{2-2x}O_4$  ferrite.

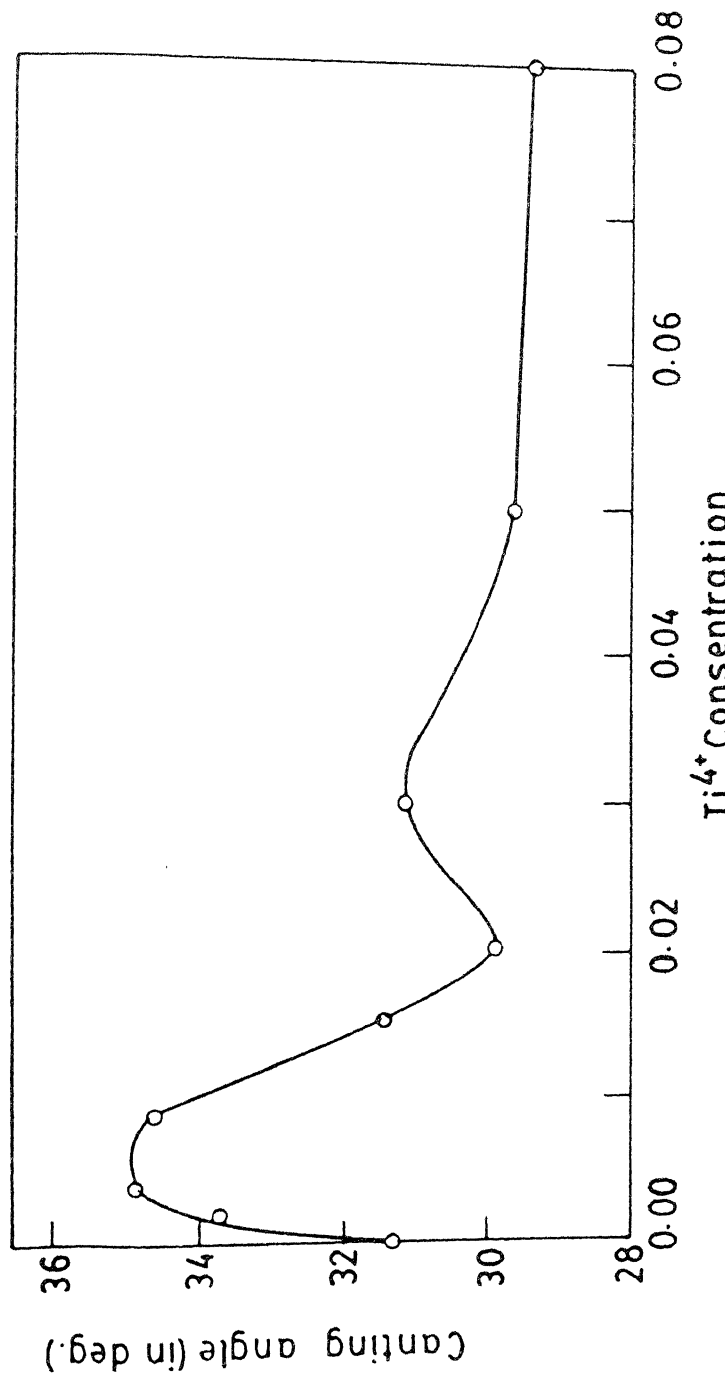


FIG. 4.22 VARIATION OF CANTING ANGLE WITH  $Ti^{4+}$  CONCENTRATION  
IN  $Ni_{0.6+x}Zn_{0.4}Ti_xFe_{2-2x}O_4$  FERRITE.

trend in the variation of magnetization and the net effective magnetic field with  $Ti^{4+}$  concentration is same. The magnetization falls sharply from  $3.18 \mu_B$  at zero concentration of  $Ti^{4+}$  to  $2.88 \mu_B$  at the  $Ti^{4+}$  concentration of  $x = 0.015$  followed by an increase upto  $3.11 \mu_B$  for  $x = 0.02$ . The magnetization again decreases upto  $2.87 \mu_B$  for the  $Ti^{4+}$  concentration of  $x = 0.08$ . As seen in the previous sections (4.4.1) and (4.4.2), the deviation from the linear fall of magnetization cannot be explained on the basis of Néel type of magnetic ordering and hence the Yafet and Kittel type of magnetic ordering is resorted to. Here we find a very peculiar behaviour of canting angle with  $Ti^{4+}$  concentration. The canting angle increases from  $31.3^\circ$  at zero concentration of  $Ti^{4+}$  to  $34.8^\circ$  for  $x = 0.004$  followed by a decrease upto  $29.8^\circ$  for  $x = 0.02$ . This is again followed by a slow increase upto  $31.3^\circ$  for  $x = 0.03$  and then a slow decrease upto  $29.3^\circ$  for  $x = 0.08$ . The variation of canting angle with  $Ti^{4+}$  concentration is shown in fig. (4.22).

Since in these cases the canting of spins take place at B-site, we split B-site into two sublattices B1 and B2. As discussed in Sec. (4.4.1) the molecular field acting on various ions are given by

$$\begin{bmatrix} \vec{H}_A (\text{Fe}) \\ \vec{H}_{B1} (\text{Ni}) \\ \vec{H}_{B1} (\text{Fe}) \\ \vec{H}_{B2} (\text{Ni}) \\ \vec{H}_{B2} (\text{Fe}) \end{bmatrix} = \begin{bmatrix} \lambda_{AA} & \alpha & \beta & \alpha & \beta \\ \alpha & \gamma & \varepsilon & \gamma & \varepsilon \\ \beta & \varepsilon & \delta & \varepsilon & \delta \\ \alpha & \gamma & \varepsilon & \gamma & \varepsilon \\ \beta & \varepsilon & \delta & \varepsilon & \delta \end{bmatrix} \begin{bmatrix} A_F \vec{m}_A (\text{Fe}) \\ B_N \vec{m}_{B1} (\text{Ni}) \\ B_F \vec{m}_{B1} (\text{Fe}) \\ B_N \vec{m}_{B2} (\text{Ni}) \\ B_F \vec{m}_{B2} (\text{Fe}) \end{bmatrix}$$

here  $A_F$ ,  $B_N$  and,  $B_F$  are the concentrations of  $\text{Fe}^{3+}$  ions,  $\text{Ni}^{2+}$  ions,  $\text{Fe}^{3+}$  ions at A, B1 or B2 and B1 or B2 sublattices respectively. The interactions  $A(\text{Fe}^{3+}) - A(\text{Fe}^{3+})$ ,  $A(\text{Fe}^{3+}) - B1(\text{Ni}^{2+})$ ,  $A(\text{Fe}^{3+}) - B1(\text{Fe}^{3+})$ ,  $A(\text{Fe}^{3+}) - B2(\text{Ni}^{2+})$ ,  $A(\text{Fe}^{3+}) - B2(\text{Fe}^{3+})$ ,  $B1(\text{Ni}^{2+}) - B2(\text{Ni}^{2+})$ ,  $B1(\text{Fe}^{3+}) - B2(\text{Fe}^{3+})$ ,  $B1(\text{Ni}^{2+}) - B2(\text{Fe}^{3+})$  and  $B1(\text{Fe}^{3+}) - B2(\text{Ni}^{2+})$  are represented by the molecular field coefficients  $\lambda_{AA}$ ,  $\alpha$ ,  $\beta$ ,  $\alpha$ ,  $\beta$ ,  $\gamma$ ,  $\delta$ ,  $\varepsilon$  and  $\varepsilon$  respectively.

And,

$$\begin{aligned} \vec{m}_{B1} \cdot \vec{m}_A &= -|\vec{m}_{B1}| |\vec{m}_A| \cos\phi \\ \vec{m}_{B2} \cdot \vec{m}_A &= -|\vec{m}_{B2}| |\vec{m}_A| \cos\phi \\ \vec{m}_{B1} \cdot \vec{m}_{B2} &= |\vec{m}_{B1}| |\vec{m}_{B2}| \cos\phi \end{aligned}$$

Minimizing the total magnetic interaction energy for canting model the expression for Yafet-Kittel angle comes out to be

$$\cos\phi = \frac{23\alpha A_F \cdot B_N + 50\beta A_F \cdot B_F}{21.16\gamma B_N^2 + 96\varepsilon B_N \cdot B_F + 100\delta B_F^2} \quad (4.7)$$

As discussed in Sec. (4.4.1) the exchange constants were obtained using the above expression and are plotted in figs. (4.23) and (4.24). We see that all the exchange constants remain almost unchanged except  $J_{Ni^{2+}(B)-Ni^{2+}(B)}$ . In the same figures, we have shown the variation of lattice parameter, obtained from X-ray data, with  $Ti^{4+}$  concentration. We see that the change in the exchange constant  $J_{Ni^{2+}(B)-Ni^{2+}(B)}$  reflects exactly the change in the lattice parameter. It is then evident that the overlap of the wavefunctions of the  $Ni^{2+}$  ions (through  $O^{2-}$  ions) and its change with the ion separation are basically responsible for the change in the canting of the spins and consequently the anomalous magnetization of these ferrites.

A correlation between the lattice parameter and exchange constant can also be evidenced from the work of Shiga [44]. Dionee [45] has also found a change in the exchange constant by the diamagnetic substitutions.

A simple hard sphere model calculation shows that the lattice parameter remains constant with  $Ti^{4+}$  addition. We then used the Born formula relating the lattice parameter with the Madelung constant, i.e.,

$$a = k M^{1/(1-n)} \quad (4.8)$$

where  $n$  is a constant (usually 10). A calculation of  $M$  with the average charge at each lattice site gave no change

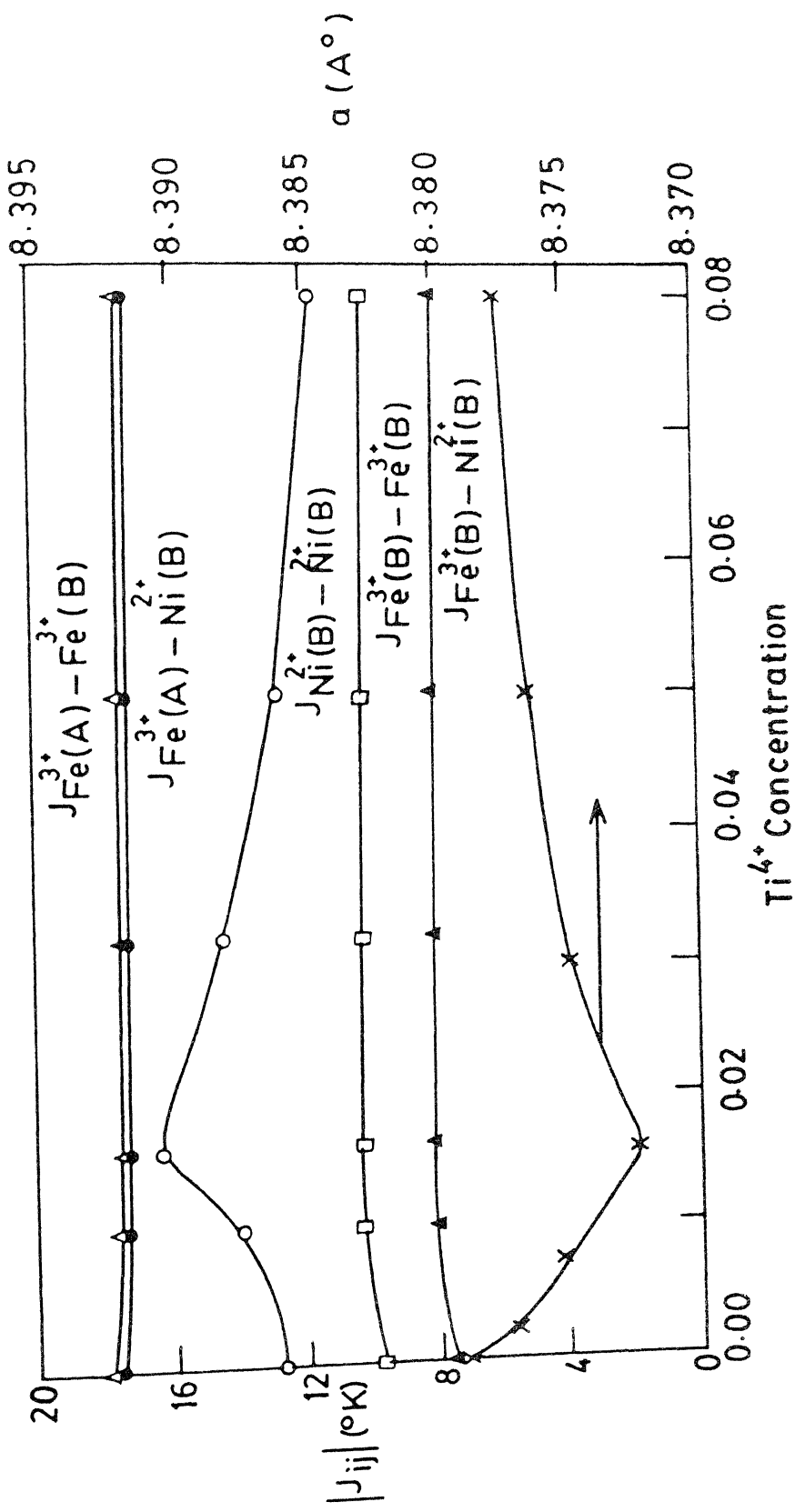


FIG. 4.23 VARIATION OF EXCHANGE CONSTANTS AND LATTICE PARAMETER WITH  $Ti^{4+}$  CONCENTRATION IN  $Ni_{0.7+x}Zn_{0.3}Ti_xFe_{2-2x}O_4$  FERRITE.

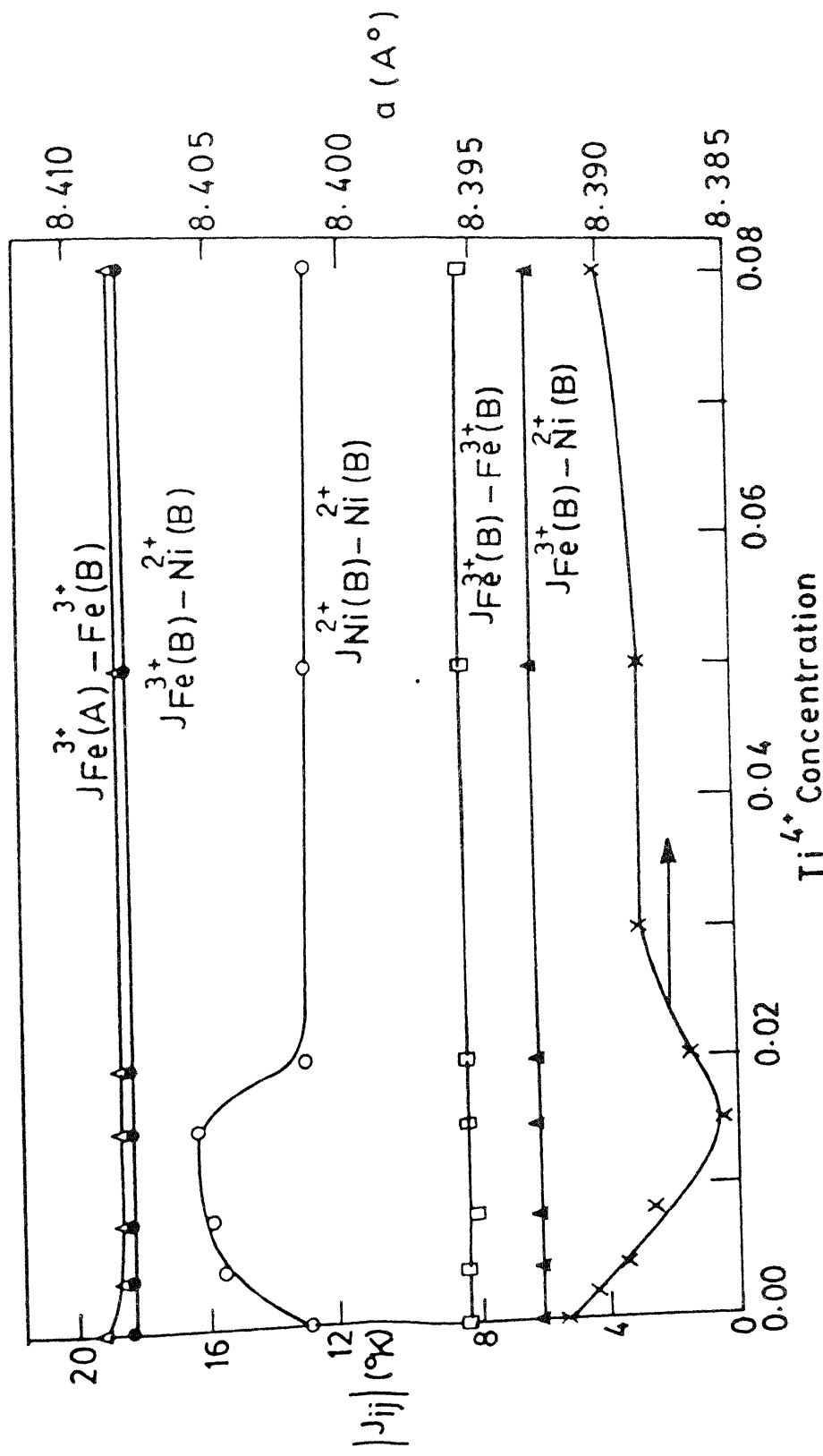


FIG. 4.24 VARIATION OF EXCHANGE CONSTANTS AND LATTICE PARAMETER WITH  $Ti^{4+}$  CONCENTRATION IN  $Ni_{0.6+x}Zn_{0.4}Ti_xFe_{2-2x}O_4$  FERRITE.

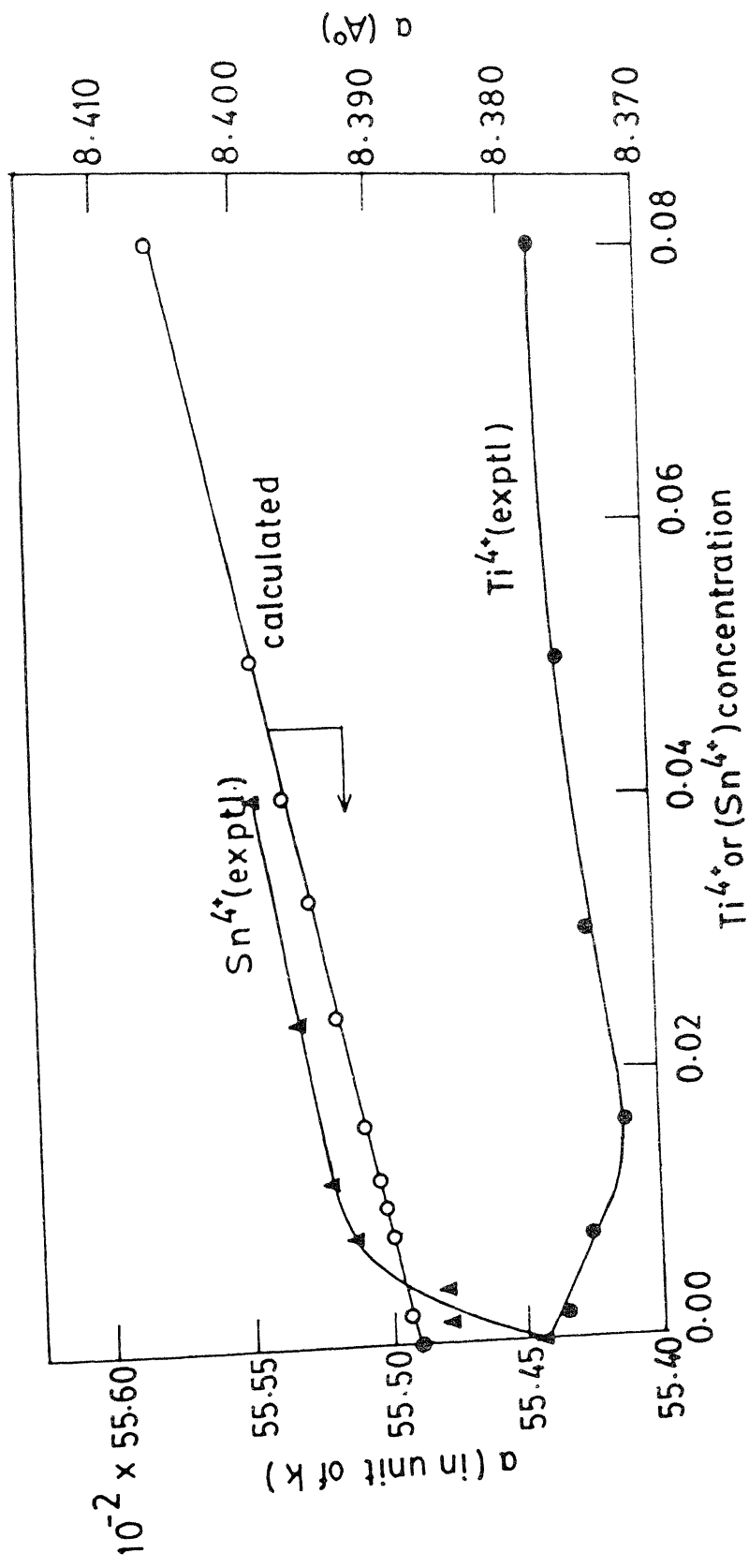


Fig. 4.25 Variation of lattice parameter with  $Ti^{4+}$  or  $(Sn^{4+})$  in substituted  $Ni_{0.7}Zn_{0.3}Fe_2O_4$  Ferrite

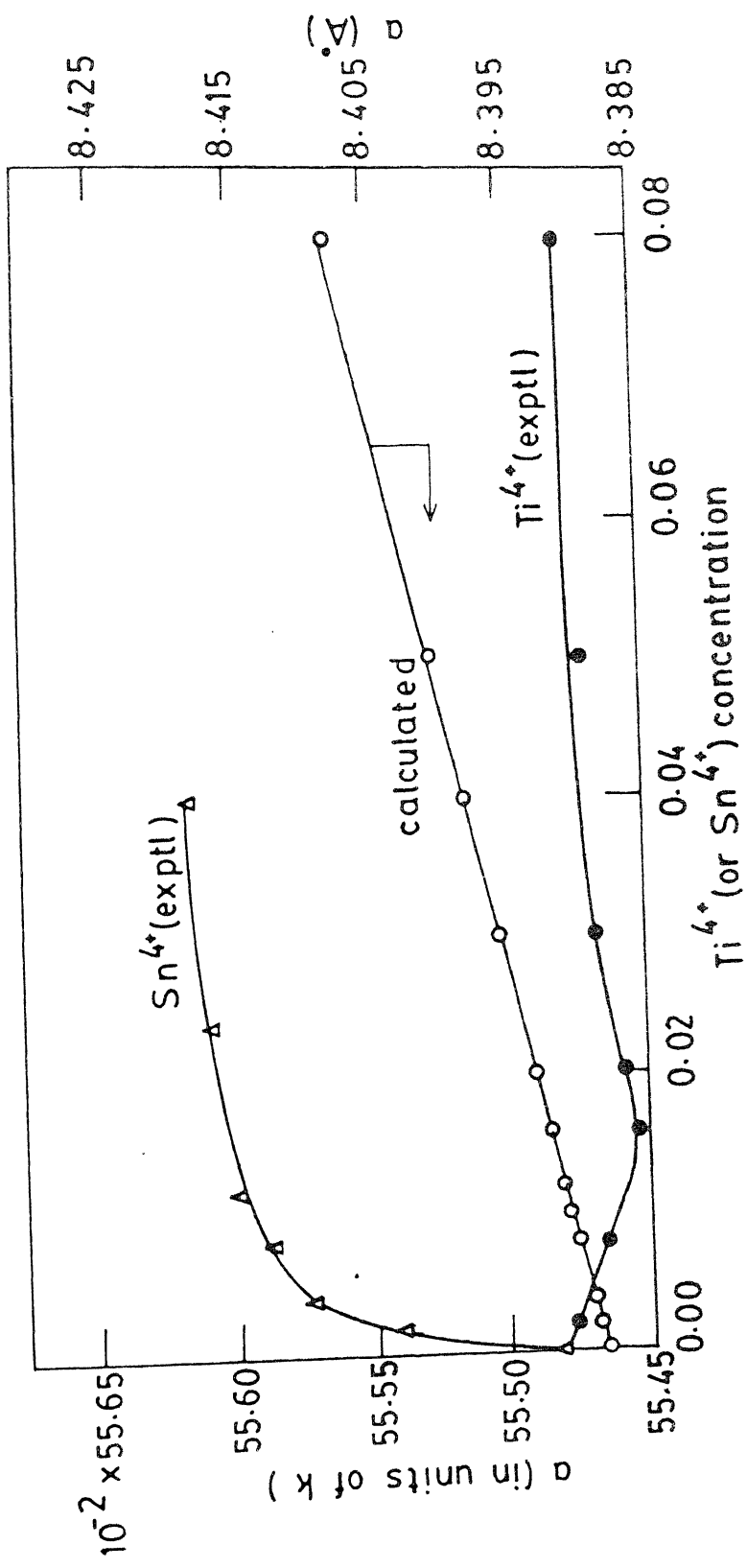


Fig. 4.26 Variation of lattice parameter with  $Ti^{4+}$  or  $(Sn^{4+})$  concentration in substituted  $Ni_{0.6}Zn_{0.4}Fe_2O_4$  ferrite.

of  $M$ , and hence  $a$ , with  $Ti^{4+}$  concentration. However, using the root mean square charge deviation at each site gives a variation of  $M$ , and correspondingly of  $a$ . The two effects added together give a crude representation of the experimental values of lattice parameter as a function of  $Ti^{4+}$  concentration [figs. (4.25) and (4.26)]. However, details such as the dip and the slope, are not in agreement. Hence a more sophisticated calculation of the Madelung constant is in order.

## REFERENCES

1. A.S. Boxer, J.F. Ollom, R.F. Rauchmiller and W.H. Von Aulock, Hand Book of Microwave Ferrite Materials (Academic Press, New York and London, 1965) p-379.
2. V.I. Goldanskii, V.F. Belov et al., Zh Eksp. Teor. Fiz., 49, 1681 (1965) [ Sov. Phys. JETP, 22, 1149 (1966) ].
3. J.M. Daniels and A. Rosencwaig, Can. J. Phys., 48, 381 (1970).
4. P. Raj and S.K. Kulshrestha, Phys. Stat. Solidi A4, 501 (1971).
5. L.K. Leung, B.J. Evans and A.H. Morris, Phys. Rev. B8, 29 (1973).
6. S.C. Bhargava and N. Zeeman, Phys. Rev. B21, 1717 (1980).
7. C. Guillaud, J. Phys Rad. 12, 239 (1951).
8. E.W. Gorter, Philips Res. Rep., 9, 295-320, 321-365, 403-443 (1954).
9. L. Néel, Ann. Phys., 3, 137 (1948).
10. Y. Yafet and C. Kittel, Phys. Rev., 87, 290 (1952).
11. M.A. Gilleo, Phys. Chem. Solids, 13, 33 (1960).
12. V.C. Wilson and J.S. Kasper, Phys. Rev. 95, 1408 (1954).
13. Y. Ishikawa, J. Phys. Soc. Japan, 17, 1877 (1962).
14. N.S. Satya Murthy, M.G. Natera, S.I. Youssef, R.J. Begum and C.M. Srivastava, Phys. Rev., 181, 969 (1969).

15. H. Abe, M. Matsuura, H. Yasuoka, A. Hirai, T. Hasi and T. Fukuyama, *J. Phys. Soc. Japan*, 18, 1400 (1963).
16. C.M. Srivastava and M.J. Patni, *J. Magn. Res.* 15, 359 (1974).
17. D.C. Khan, M. Misra and A. R. Das, *J. Appl. Phys.* 53, 2722 (1982).
18. D.C. Khan and M. Misra, *Bull. Mater. Sci.* 17, 253 (1985).
19. A.R. Das, V.S. Ananthan and, D.C. Khan, *J. Appl. Phys.*, 57, 4189 (1985).
20. C. Prakash and J.S. Baijal, *Solid State Commun.* 50, 557 (1984).
21. J.S. Baijal and Chandra Prakash, *Proc. of the Forth Int. Conf. on Ferrites, Part II* (San Francisco, California, Oct. 31-Nov 2, 1984) p-187.
22. R.K. Puri, L. Atmaram and, K.H. Rao, *Proc. of the Forth Int. Conf. on Ferrites, Part II* (San Francisco, California, Oct. 31 - Nov. 2, 1984) p-199.
23. J. Smit and H.P.J. Wijn, *Ferrites*, Philips Technical Library (1959).
24. J.P. Morel, *Phys. Chem. Solids*, 28, 629 (1967).
25. J. Chaput and R.B. Frankel, *Phys. Rev. Lett.* 19, 570 (1967).
26. V.A. Bokov, A.S. Kamzin, S.I. Yushchuk, and N.N. Parfenova, *Sov. Phys. Solid State*, 16, 2360 (1975).

27. N.E. Erikson in : The Mössbauer Effect and its Application in Chemistry, R.F. Gould (ed.) (Advances in Chem. Series 68, American Chem. Soc., Washington DC 1967), p-86.
28. S. Margulies and J.R. Ehrman, Nucl. Inst. Meth., 12, 131, (1961).
29. R.P. Edward, C.E. Johnson and R.J.P. Williams, J. Chem. Phys. 47, 2074 (1967).
30. E. Simanek and Z. Sroubek, Phys. Rev. 163, 275 (1967).
31. R.V. Pound and G.A. Rebka, Phys. Rev. Lett., 4, 274 (1960).
32. B.D. Josephson, Phys. Rev. Lett. 4, 341 (1960).
33. J.P. Morel, Phys. Chem. Solids, 28, 629 (1967).
34. J. Chaput and R.B. Frankel, Phys. Rev. Lett., 19, 570 (1967).
35. E. Matthias, W. Schneider and, R.M. Steffen, Phys. Rev., 125, 261 (1962).
36. E. Simanek, N.L. Huang and R. Orbach, J. Appl. Phys. 38, 1072 (1967).
37. F. Van der Woude and G.A. Sawatzky, Phys. Rev. B, 4, 3159 (1971).
38. G.A. Sawatzky and F. Van der Woude, J. de Physique 12, C6-47 (1974).
39. S. Geller, H.J. Williams, R.C. Sherwood and, G.P. Espinosa, J. Phys. Chem. Solids, 23, 1525 (1962).
40. M. Mishra, Ph.D. Thesis, Indian Institute of Technology, Kanpur, India (1981).

41. S. Krupicka and P. Novak in 'Ferromagnetic Materials' Vol. 3 [Ed. by E.P. Wohlfarth], North-Holland Pub. Co., (1982).
42. P. Thompson and N.W. Grimes, Philos. Mag. 36, 501 (1977).
43. R.D. Shannon, Acta. Crystallogr., A32, 751 (1976.)
44. M. Shiga, AIP Conf. Proc. no. 18, pt. 1, 463 (1973). (19th Annual Conf. on Magnetism and Magnetic Materials, Pt. I, Boston, Mass. USA, 13-16 Nov, 1973).
45. G.F. Dionne, J. Appl. Phys. 42, 2142 (1971).

## CHAPTER 5

MOSSBAUER AND MAGNETIC STUDIES OF  
 $\text{Sn}^{4+}$  SUBSTITUTED Ni-Zn FERRITE

5.1 *Introduction:*

$\text{Sn}^{4+}$  substituted Ni-Zn ferrites have been studied by many workers [1-8]. Varshney et al [5] found that for the series of  $\text{Ni}_{1+x-y}\text{Zn}_y\text{Sn}_x\text{Fe}_{2-2x}\text{O}_4$  ferrite all the A-site sextets showed pure Zeeman splitting for  $x = 0.1-0.5$  and  $y = 0.1-0.5$ . B site sextets for samples having  $y = 0.1, 0.3$  and  $x = 0.1$  to  $0.5$ ; and  $y = 0.5, x = 0.1$  have been identified as pure Zeeman sextets whereas all other B-site sextets exhibited relaxation effect. It was observed that the  $\text{Sn}^{4+}$  ions enter B-site first (upto  $x = 0.3$ ) and then on both A and B sites. Moreover,  $H_{\text{eff}}(A)$  was found to decrease faster with  $\text{Sn}^{4+}$  concentration than that of  $H_{\text{eff}}(B)$ . It is expected that  $I.S.(A) < I.S.(B)$  in spinel ferrites because of smaller bond separation  $\text{Fe}_A^{3+}-\text{O}^{2-}$  as compared to  $\text{Fe}_B^{3+}-\text{O}^{2-}$ . There was, however, a discrepancy in the isomer shift values of A and B sites [5] for  $x = 0.1, y = 0.3; x = 0.2, y = 0.3; x = 0.1, y = 0.5$  and  $x = 0.5, y = 0.5$  in  $\text{Ni}_{1+x-y}\text{Zn}_y\text{Sn}_x\text{Fe}_{2-2x}\text{O}_4$  ferrite.

Das et al [6] found that the saturation magnetization of  $\text{Sn}^{4+}$  substituted  $\text{Ni}_{0.3}\text{Zn}_{0.7}\text{Fe}_2\text{O}_4$  ferrite falls rapidly from 60 emu/gm at zero concentration of  $\text{Sn}^{4+}$  to a value of 45 emu/gm at 1 wt. percent of  $\text{Sn}^{4+}$ , followed by a very slow decrease upto 43 emu/gm as the concentration of  $\text{Sn}^{4+}$

increases upto 5 wt. percent.

As discussed in Chapter 4, if the Néel type of magnetic ordering is considered then the saturation magnetization should fall linearly with  $\text{Sn}^{4+}$  concentration. Thus the introduction of  $\text{Sn}^{4+}$  cations into the lattice introduces anomalous magnetic behaviour.

As discussed in Chapter 4, the Mössbauer spectra of Ni-Zn ferrite system for high Zn concentration are relaxed and it is difficult to resolve the spectrum for A and B sites. In the present series of samples we have chosen the  $\text{Sn}^{4+}$  substituted  $\text{Ni}_{1-y}\text{Zn}_y\text{Fe}_2\text{O}_4$  ferrite in the non-canting zone ( $y = 0.0 - 0.4$ ). These studies will help us understand the anomalous magnetic properties developed with the introduction of non-magnetic tetravalent cations in the Ni-Zn ferrite.

5.2  $\text{Sn}^{4+}$  Substituted  $\text{Ni}_{1-y}\text{Zn}_y\text{Fe}_2\text{O}_4$  ( $y = 0.3, 0.4$ ) Ferrite :

5.2.1 Mössbauer Study of  $\text{Sn}^{4+}$  Substituted  $\text{Ni}_{0.7}\text{Zn}_{0.3}\text{Fe}_2\text{O}_4$  Ferrite:

Mössbauer spectra of  $\text{Ni}_{0.7+x}\text{Zn}_{0.3}\text{Sn}_x\text{Fe}_{2-2x}\text{O}_4$  ( $x = 0.00 - 0.04$ ) were recorded at room temperature and liquid nitrogen temperature. These spectra are well defined Zeeman patterns consisting of two separate sextets, one being due to  $\text{Fe}^{3+}$  ions at A site and the other due to  $\text{Fe}^{3+}$  ion at B site. The Mössbauer spectra of the samples at 295

COUNTS (Arb. units)

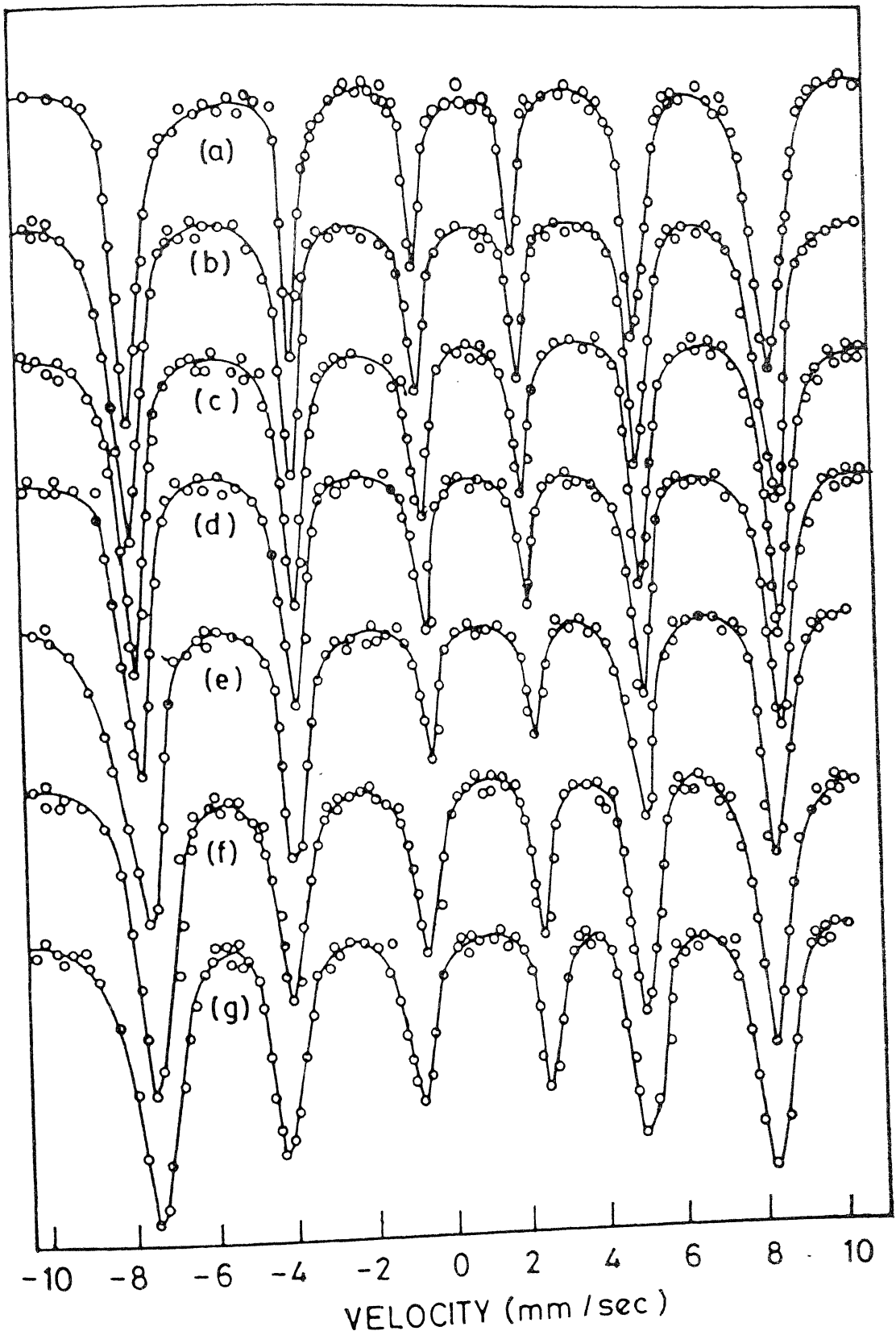


FIG. 5.1 Mössbauer spectra of  $\text{Ni}_{0.7+x} \text{Zn}_{0.3} \text{Sn}_x \text{Fe}_{2-2x} \text{O}_4$  at room temperature (a)  $x = 0.0$ , (b)  $x = 0.002$ , (c)  $x = 0.004$ , (d)  $x = 0.008$ , (e)  $x = 0.012$ , (f)  $x = 0.024$ , (g)  $x = 0.04$ .

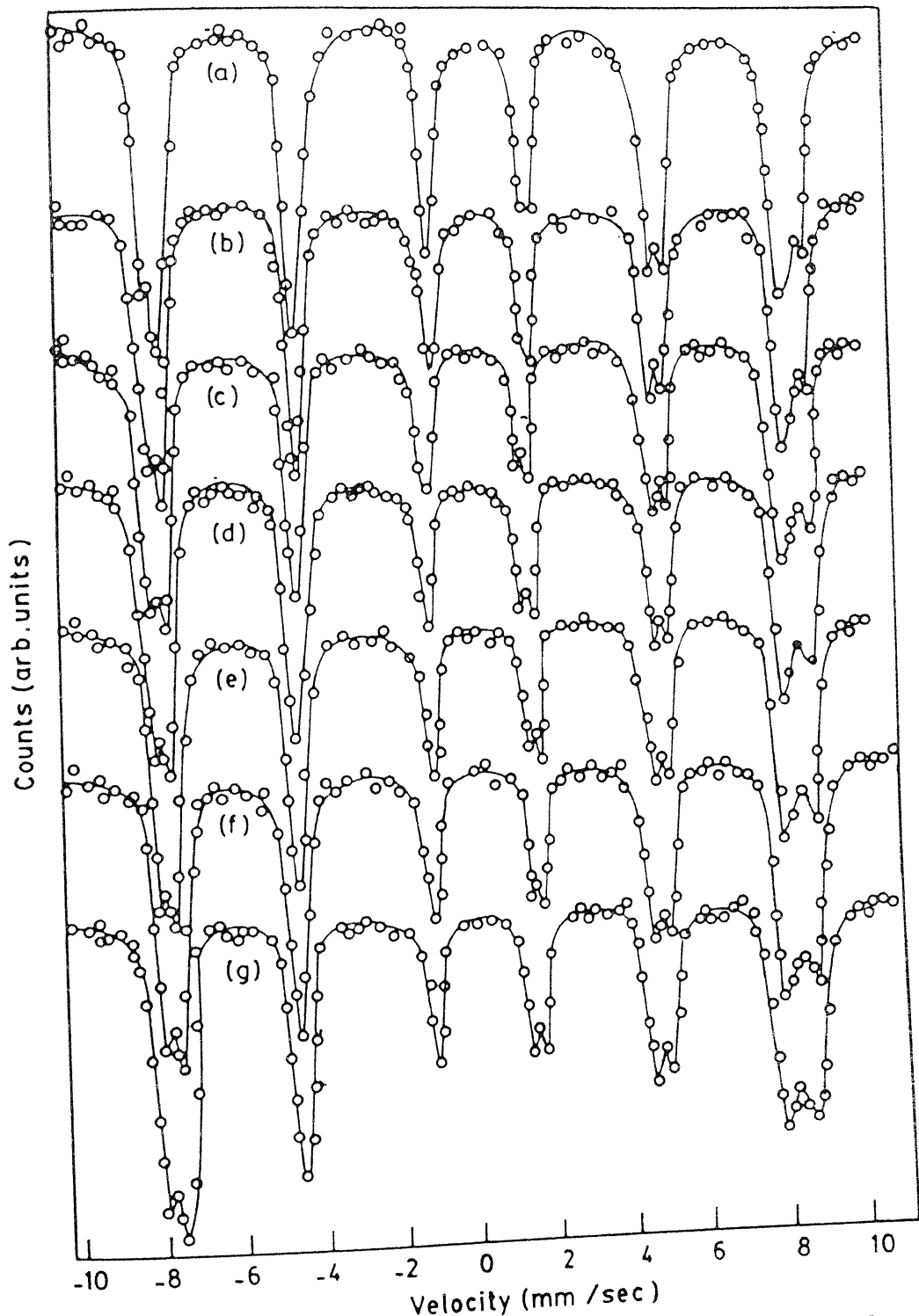


Fig. 5.2 Mössbauer spectra of  $\text{Ni}_{0.7+x} \text{Zn}_{0.3} \text{Sn}_x \text{Fe}_{2-2x} \text{O}_4$  at  $77^\circ\text{K}$  (a)  $x = 0.00$ , (b)  $x = 0.002$ , (c)  $x = 0.004$ , (d)  $x = 0.008$ , (e)  $x = 0.012$ , (f)  $x = 0.024$ , (g)  $x = 0.04$ .

and 77°K are shown in figs (5.1) and (5.2) respectively.

It is observed that the isomer shift of  $\text{Fe}^{3+}$  ions (with respect to SNP) at tetrahedral site, I.S.(A), and octahedral site, I.S.(B), show no significant change with  $\text{Sn}^{4+}$  concentration. The variation of isomer shift with  $\text{Sn}^{4+}$  concentration at 295 and 77°K are shown in fig. (5.3). The weighted average value of isomer shift at A and B sites at 295°K are  $0.509 \pm 0.002$  and  $0.633 \pm 0.002$  mm/sec respectively. At 77°K, the weighted average value of isomer shift at A and B sites are  $0.690 \pm 0.002$  and  $0.857 \pm 0.002$  mm/sec respectively.

In all the samples exhibiting Zeeman hyperfine pattern, no quadrupole splitting was observed within the experimental error for both A and B sites.

At room temperature and at liquid nitrogen temperature the variation of effective magnetic field at the two sub-lattices with  $\text{Sn}^{4+}$  concentration are shown in fig. (5.4). It is evident from the graph that  $H_{\text{eff}}^{(B)}$  remains almost constant at the value of  $495 \pm 1$  Koe whereas  $H_{\text{eff}}^{(A)}$  decreases from  $487 \pm 1$  Koe to  $480 \pm 1$  Koe. A similar behaviour of  $H_{\text{eff}}^{(A)}$  and  $H_{\text{eff}}^{(B)}$  with  $\text{Sn}^{4+}$  concentration is observed at 77°K also. In this case,  $H_{\text{eff}}^{(B)}$  remains almost constant at the value of  $518 \pm 1$  KOe. and  $H_{\text{eff}}^{(A)}$  decreases from  $492 \pm 1$  KOe to  $485 \pm 1$  KOe. For the zero concentration of  $\text{Sn}^{4+}$  ions, the values of  $H_{\text{eff}}$

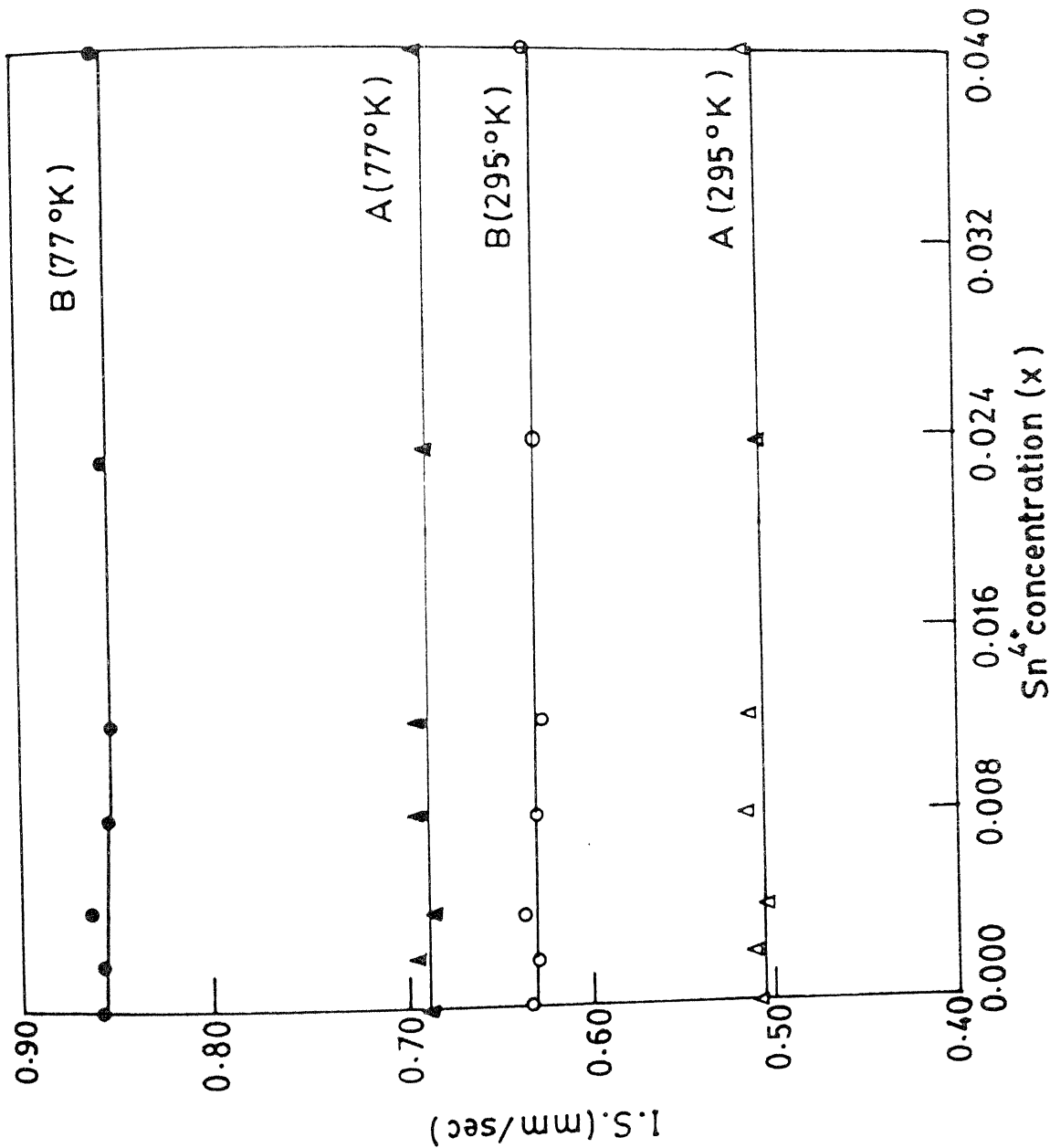


FIG. 5.3 Variation of isomer shift with  $\text{Sn}^{4+}$  concentration in  $\text{Ni}_{0.7-x}\text{Zn}_{0.3}\text{Sn}_x\text{Fe}_{2-2x}\text{O}_4$  ferrite.

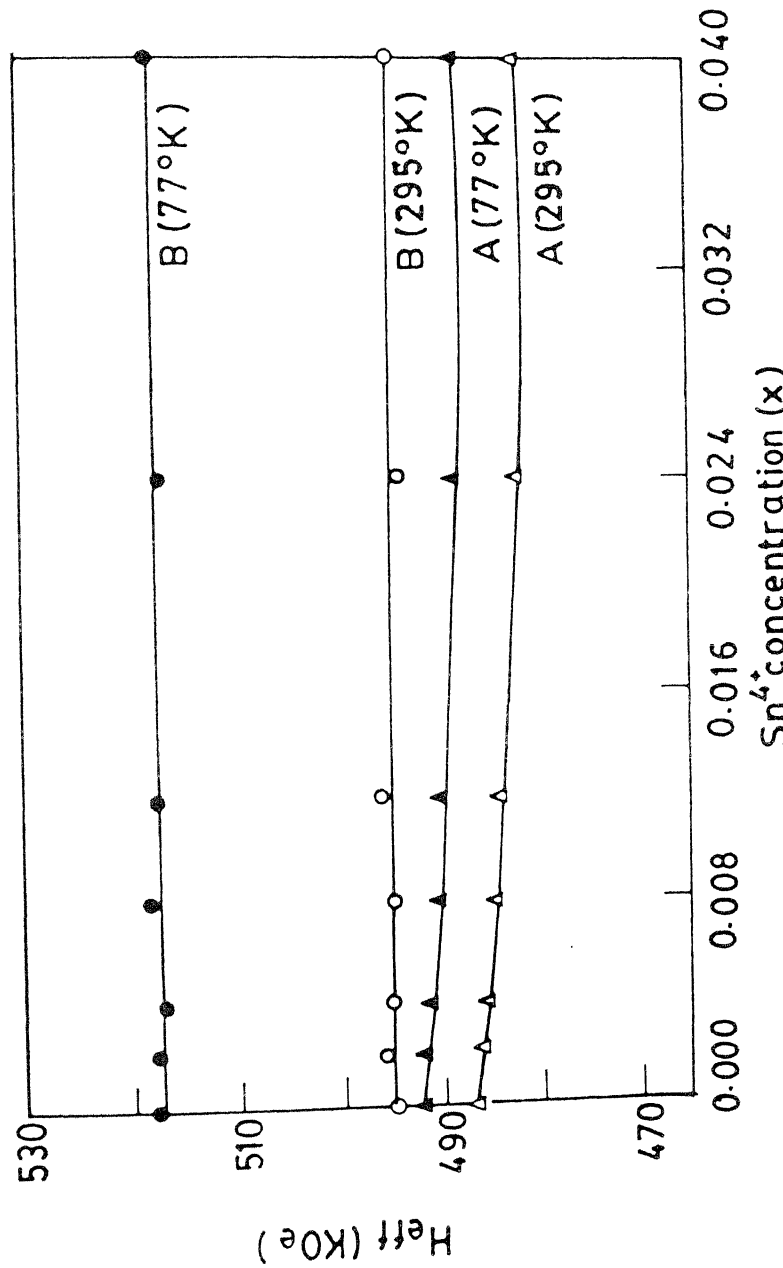


FIG. 5.4 Variation of effective magnetic field with  $\text{Sn}^{4+}$  concentration in  $\text{Ni}_{0.7-x}\text{Zn}_{0.3}\text{Sn}_x\text{Fe}_{2-2x}\text{O}_4$  ferrite.

at the two sublattices at 295 and 77°K are in excellent agreement with the values reported in the literature [8].

In fig. (5.5) we have shown the variation of full width at half maximum with  $\text{Sn}^{4+}$  concentration in  $\text{Ni}_{0.7+x}\text{Zn}_{0.3}\text{Sn}_x\text{Fe}_{2-2x}\text{O}_4$  ferrite. We see that there is no significant change in the values of  $\Gamma_B$  at 295 and 77°K with  $\text{Sn}^{4+}$  concentration. At 295°K,  $\Gamma_B$  is almost constant at the value of  $0.775 \pm 0.003$  mm/sec and at 77°K it drops to  $0.610 \pm 0.004$  mm/sec and remains almost constant at that value as the concentration of  $\text{Sn}^{4+}$  increases from  $x = 0.00$  to  $x = 0.04$ . The tetrahedral line width,  $\Gamma_A$ , at 295°K, increases from  $0.561 \pm 0.004$  mm/sec to  $0.641 \pm 0.003$  mm/sec as the concentration of  $\text{Sn}^{4+}$  increases from  $x = 0.00$  to  $x = 0.04$ . At 77°K,  $\Gamma_A$  increases from  $0.501 \pm 0.003$  mm/sec to  $0.561 \pm 0.003$  mm/sec for the same range of increase in the concentration of  $\text{Sn}^{4+}$ . The values of  $\Gamma_A$  and  $\Gamma_B$  at 295 and 77°K for the zero concentration of  $\text{Sn}^{4+}$  are in good agreement with the values reported in [9].

### 5.2.2 Mössbauer Study of $\text{Sn}^{4+}$ Substituted $\text{Ni}_{0.6+x}\text{Zn}_{0.4}\text{Sn}_x\text{Fe}_{2-2x}\text{O}_4$ Ferrite :

The Mössbauer spectra of  $\text{Ni}_{0.6+x}\text{Zn}_{0.4}\text{Sn}_x\text{Fe}_{2-2x}\text{O}_4$  ( $x = 0.0-0.04$ ) ferrite system at room temperature show a well defined Zeeman pattern consisting of two separate sextets; one due to  $\text{Fe}^{3+}$  ions at A site and the other due to  $\text{Fe}^{3+}$  ions at B site. The Mössbauer spectra of the samples at

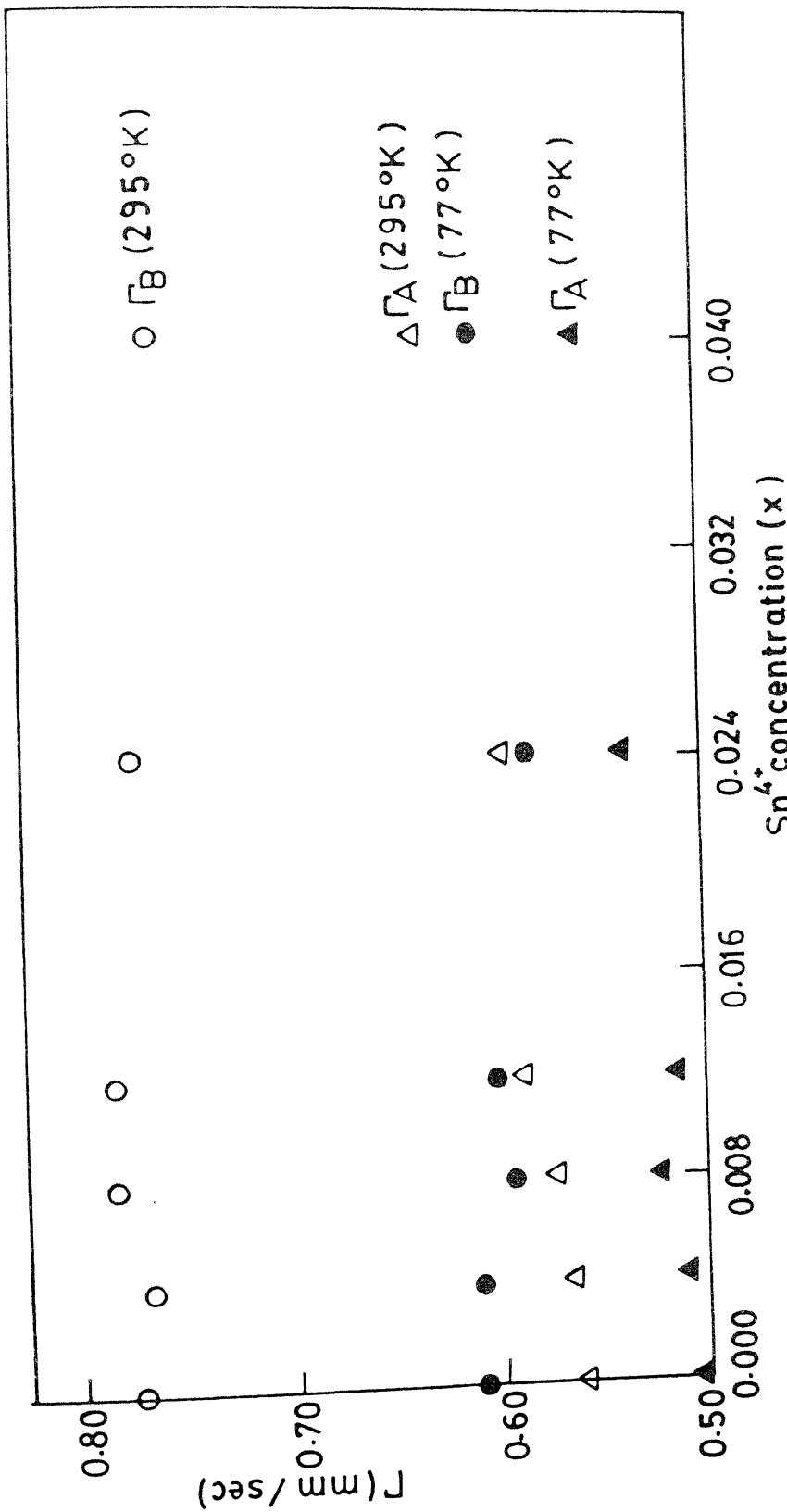


FIG. 5.5 Variation of FWHM with  $\text{Sn}^{4+}$  concentration in  $\text{Ni}_{0.7+x} \text{Zn}_{0.3} \text{Sn}_x \text{Fe}_{2-2x} \text{O}_4$  ferrite.

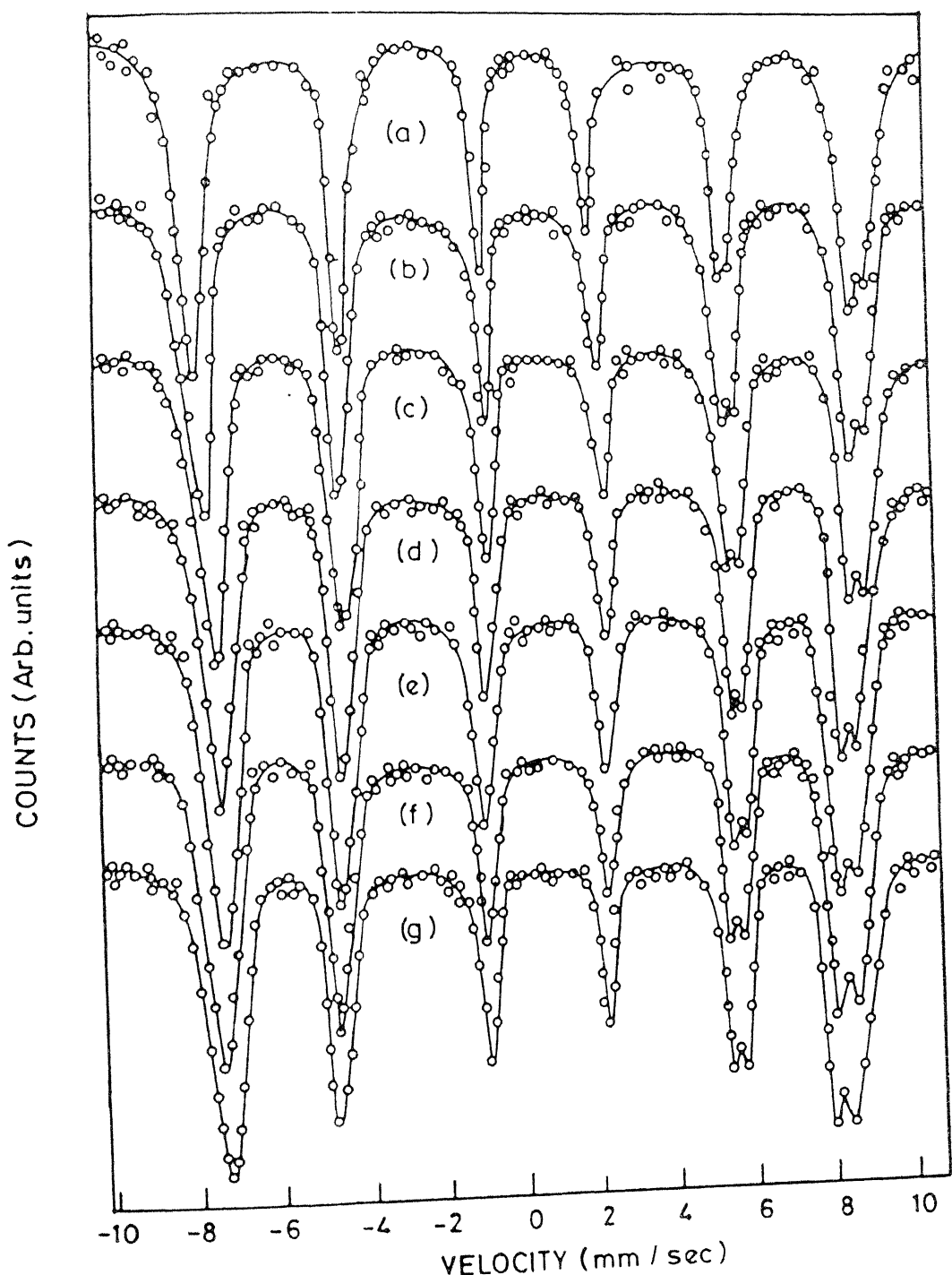


FIG. 5.6 Mössbauer spectra of  $\text{Ni}_{0.6+x}\text{Zn}_{0.4}\text{Sn}_x\text{Fe}_{2-2x}\text{O}_4$  at  $295^\circ\text{K}$  (a)  $x = 0.0$ , (b)  $x = 0.002$ , (c)  $x = 0.004$ , (d)  $x = 0.008$ , (e)  $x = 0.012$ , (f)  $x = 0.024$ , (g)  $x = 0.04$ .

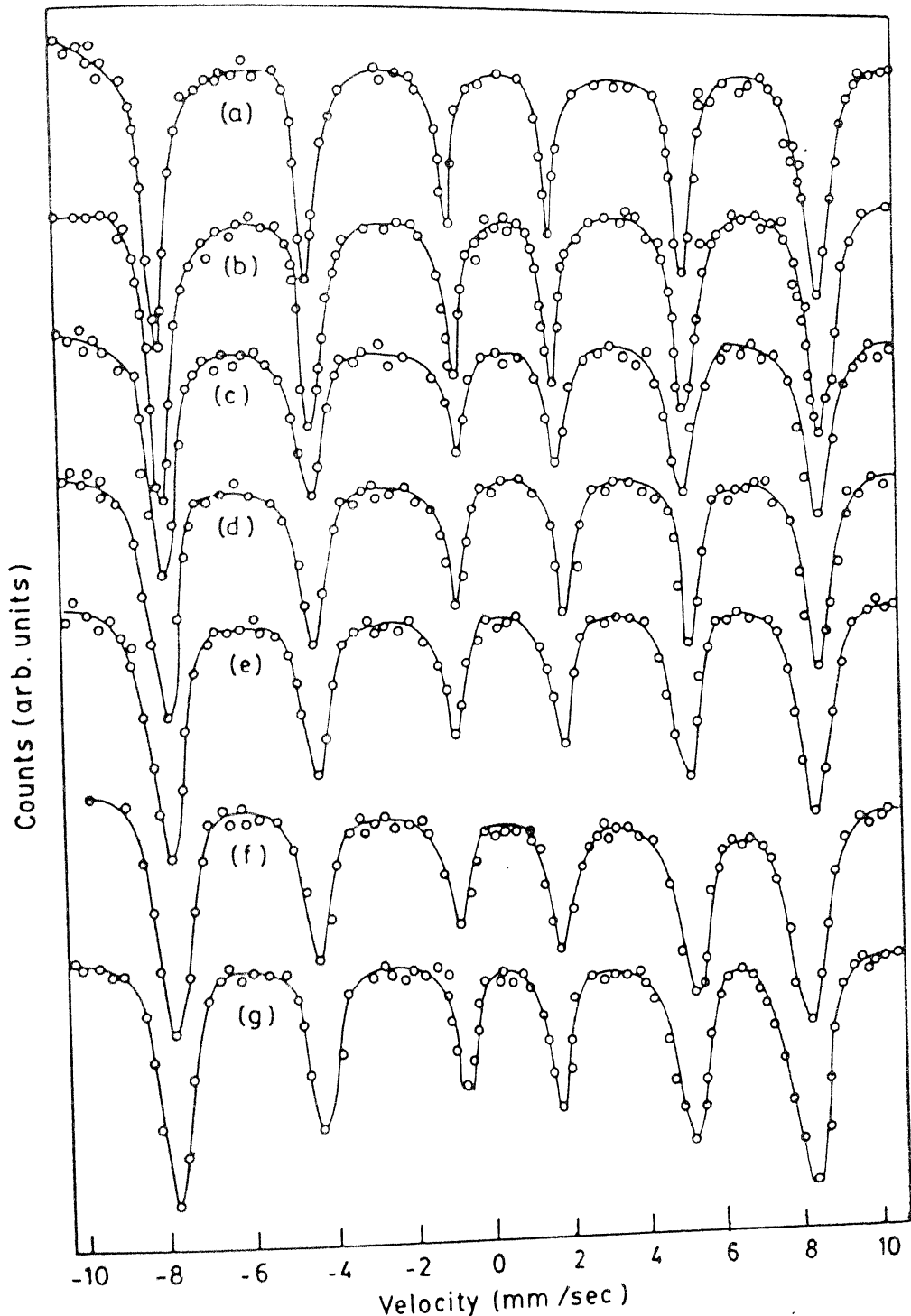


Fig. 5.7 Mössbauer spectra of  $\text{Ni}_{0.6+x} \text{Zn}_{0.4} \text{Sn}_x \text{Fe}_{2-2x} \text{O}_4$  at  $77^\circ \text{K}$  (a)  $x = 0.00$ , (b)  $x = 0.002$ , (c)  $x = 0.004$ , (d)  $x = 0.008$ , (e)  $x = 0.012$ , (f)  $x = 0.024$ , (g)  $x = 0.04$ .

295 and  $77^{\circ}\text{K}$  are shown in figs. (5.6) and (5.7) respectively.

It is observed that the isomer shift of  $\text{Fe}^{3+}$  ions (with respect to SNP) at tetrahedral site, I.S.(A), and at octahedral site, I.S.(B), remain almost constant with  $\text{Sn}^{4+}$  concentration [fig. (5.8)]. The weighted average value of the isomer shift at A and B sites at  $295^{\circ}\text{K}$  are  $0.541 \pm 0.002$  and  $0.660 \pm 0.002$  mm/sec. respectively and the respective values at  $77^{\circ}\text{K}$  are  $0.726 \pm 0.002$  and  $0.888 \pm 0.002$  mm/sec.

In  $\text{Ni}_{0.6+x}\text{Zn}_{0.4}\text{Sn}_x\text{Fe}_{2-2x}\text{O}_4$  ferrite system we did not find any observable quadrupole splitting for both A and B sites within the experimental error limit.

At room temperature the variation of effective magnetic field at the two sublattices with  $\text{Sn}^{4+}$  concentration is shown in fig.(5.9). It is observed that at  $295^{\circ}\text{K}$ ,  $H_{\text{eff}}(\text{B})$  remains almost constant at the value of  $446 \pm 1$  KOe. and  $H_{\text{eff}}(\text{A})$  decreases from  $480 \pm 1$  KOe. to  $475 \pm 1$  KOe. as the concentration of  $\text{Sn}^{4+}$  increases from  $x = 0.00$  to  $x = 0.04$ . Similar variation of  $H_{\text{eff}}$  at A and B sites is obtained at  $77^{\circ}\text{K}$  and its variation with  $\text{Sn}^{4+}$  concentration is shown in fig. (5.10). At  $77^{\circ}\text{K}$ ,  $H_{\text{eff}}(\text{B})$  remains almost constant at  $518 \pm 1$  KOe. whereas  $H_{\text{eff}}(\text{A})$  decreases from  $506 \pm 1$  KOe. to  $500 \pm 1$  KOe. as the concentration of  $\text{Sn}^{4+}$  increases from  $x = 0.00$  to  $x = 0.04$ .

In fig. (5.11) we have shown the variation of FWHM

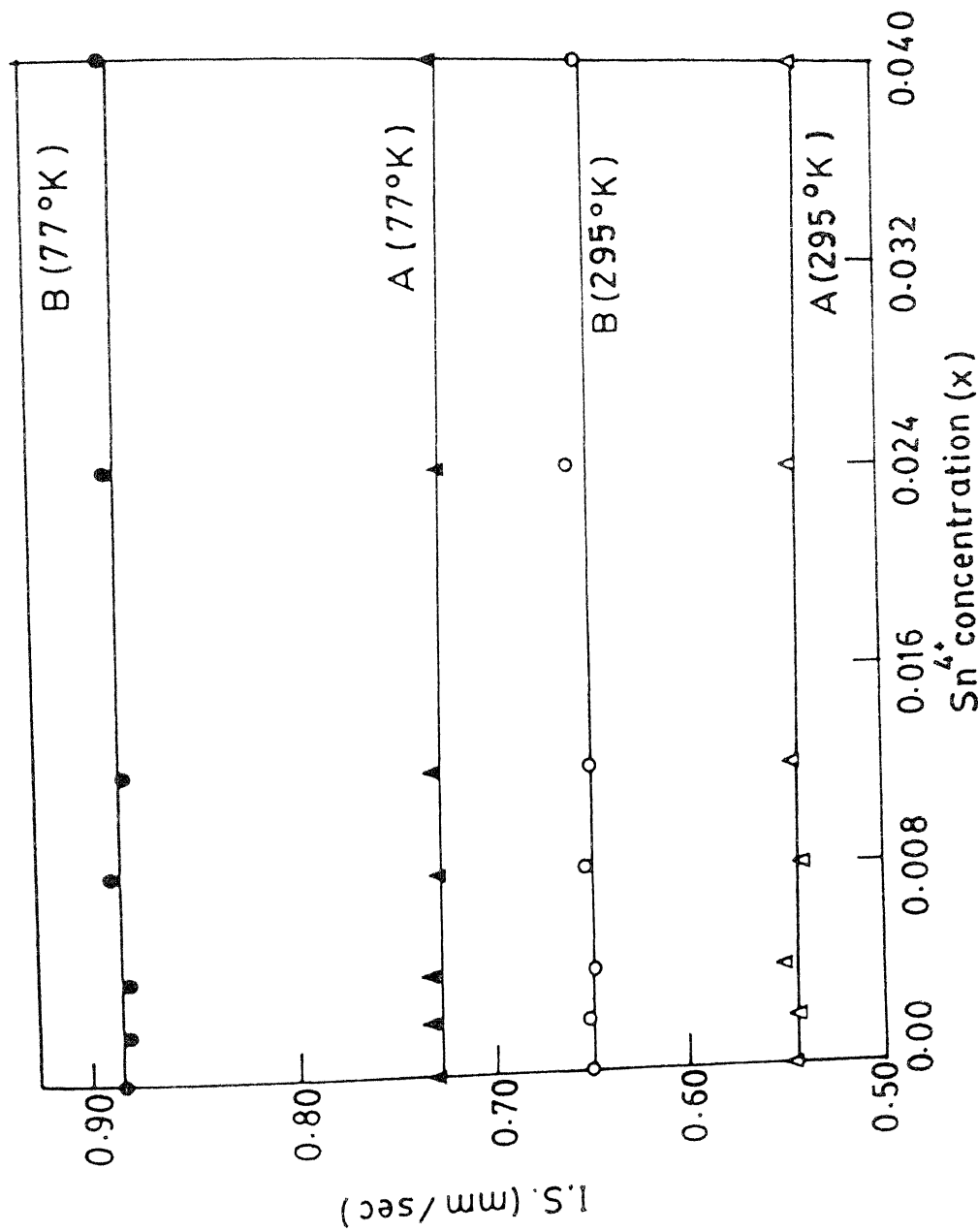


FIG. 5.8 Variation of isomer shift with  $\text{Sn}^{4+}$  concentration in  $\text{Ni}_{0.6+x}\text{Zn}_{0.4}\text{Sn}_x\text{Fe}_{2-2x}\text{O}_4$  ferrite.

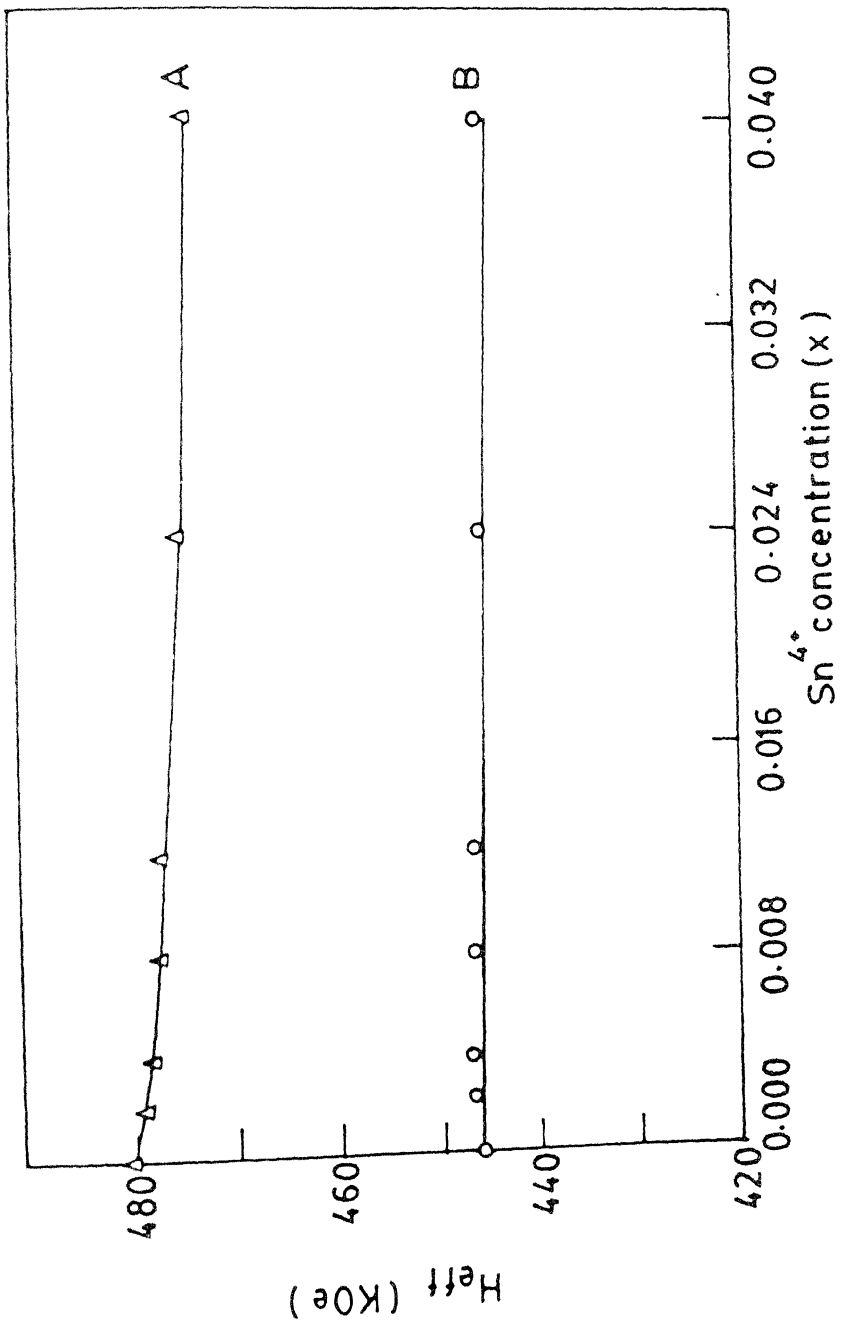


FIG.5.9 Variation of effective magnetic field with  $Sn^{4+}$  concentration at room temperature in  $Ni_{0.6+x} Zn_{0.4} Sn_x Fe_{2-2x} O_4$  ferrite.

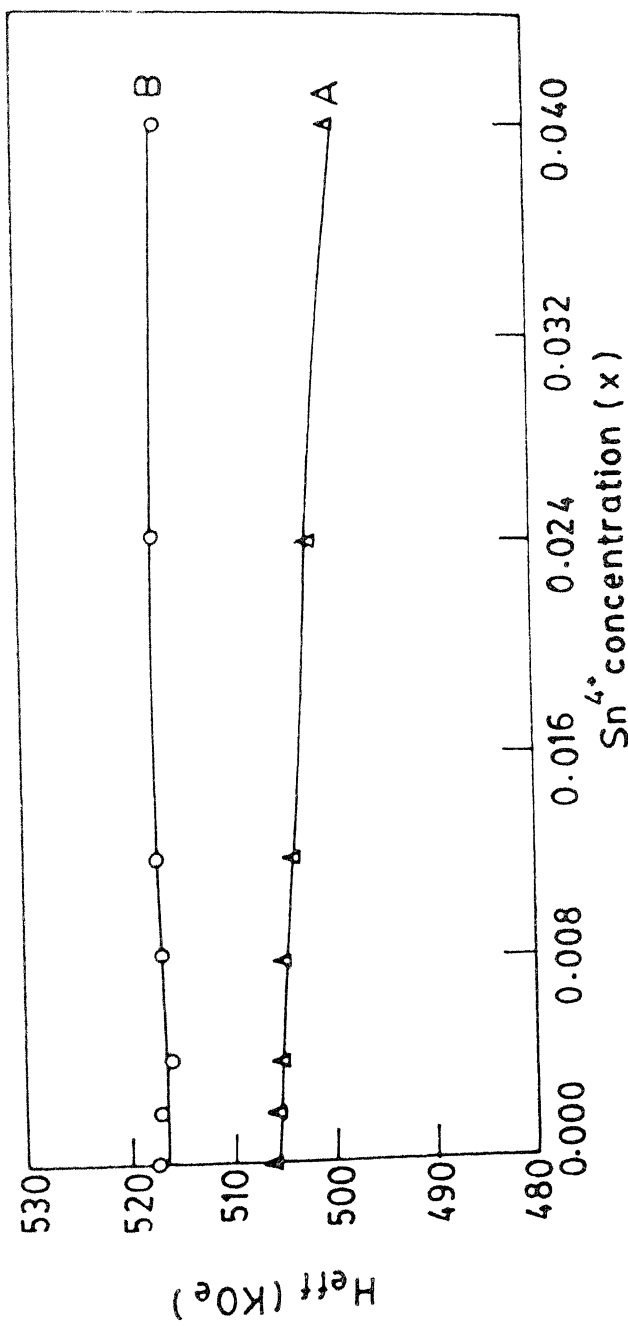


FIG. 5.10 Variation of  $H_{eff}$  with  $Sn^{4+}$  concentration at  $77^{\circ}K$  in  $Ni_{0.6+x}Zn_{0.4}Sn_xFe_{2-2x}O_4$  ferrite.

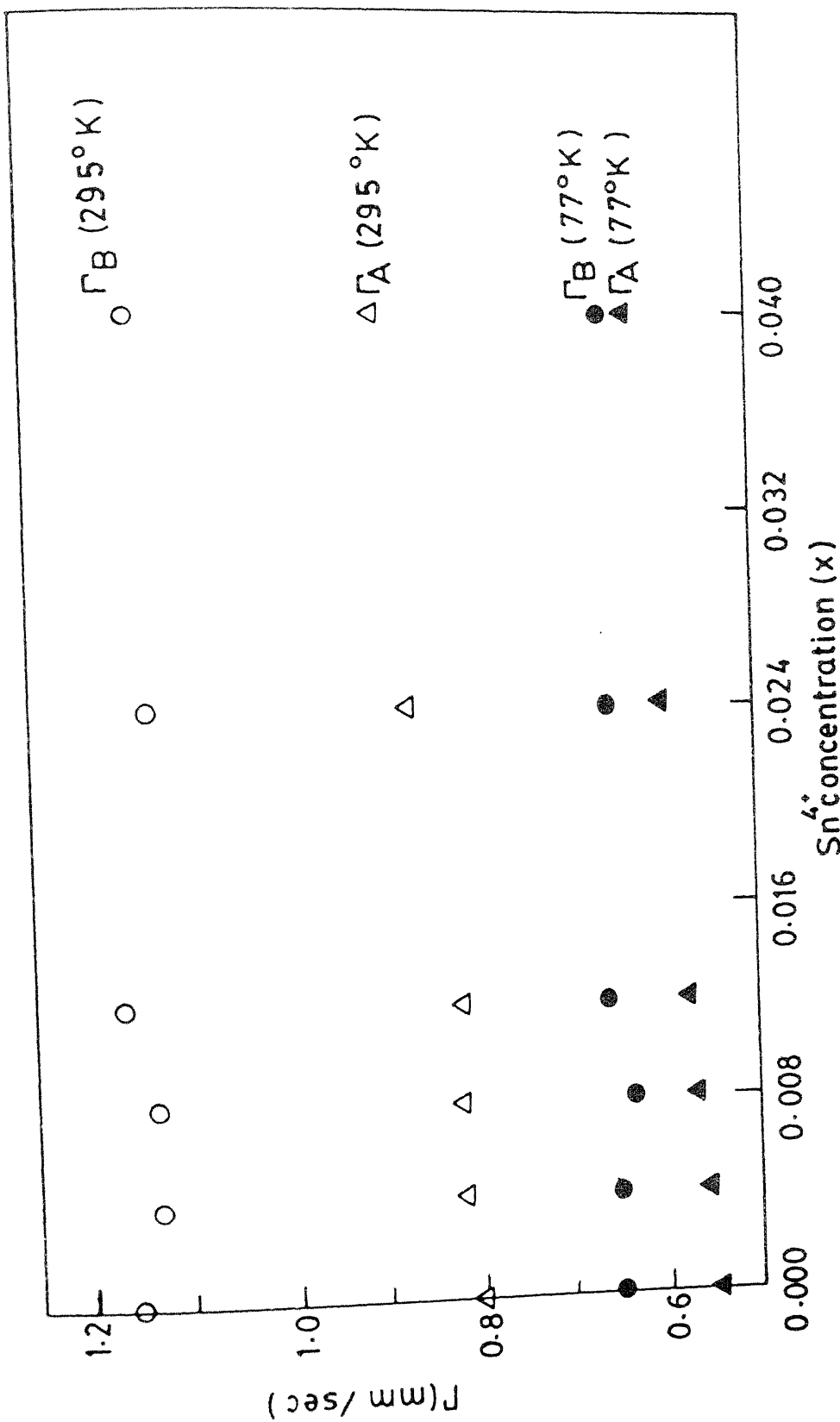


FIG. 5.11 Variation of FWHM with Sn concentration in  $\text{Ni}_{0.6+x} \text{Zn}_{0.4} \text{Sn}_x \text{Fe}_{2-2x} \text{O}_4$  Ferrite.

with  $\text{Sn}^{4+}$  concentration in  $\text{Ni}_{0.6+x}\text{Zn}_{0.4}\text{Sn}_x\text{Fe}_{2-2x}\text{O}_4$  ferrite. It is observed that at  $295^\circ\text{K}$ ,  $\Gamma_B$  remains almost constant at  $1.151 \pm 0.004$  mm/sec as the concentration of  $\text{Sn}^{4+}$  increases from  $x = 0.00$  to  $x = 0.04$ . This value of  $\Gamma_B$  is a little less than the value ( $\Gamma_B = 1.2$  mm/sec) reported by Daniels et al. [9] of  $\text{Ni}_{0.6}\text{Zn}_{0.4}\text{Fe}_2\text{O}_4$  ferrite. At  $77^\circ\text{K}$ ,  $\Gamma_B$  remains almost constant at  $0.650 \pm 0.003$  mm/sec. as the concentration of  $\text{Sn}^{4+}$  increases from  $x = 0.00$  to  $x = 0.04$ . At  $295^\circ\text{K}$ ,  $\Gamma_A$  increases from  $0.801 \pm 0.004$  to  $0.902 \pm 0.004$  mm/sec. Whereas at  $77^\circ\text{K}$ , it increases from  $0.500 \pm 0.003$  to  $0.621 \pm 0.003$  mm/sec as the concentration of  $\text{Sn}^{4+}$  increases from  $x = 0.00$  to  $x = 0.04$ . A similar behaviour of  $\Gamma_A$  and  $\Gamma_B$  at  $295$  and  $77^\circ\text{K}$  was found in case of  $\text{Ti}^{4+}$  substituted  $\text{Ni}_{0.6}\text{Zn}_{0.4}\text{Fe}_2\text{O}_4$  ferrite.

### 5.3 Discussion of Results :

#### 5.3.1 Isomer Shift :

In both the systems i.e.,  $\text{Sn}^{4+}$  substituted  $\text{Ni}_{0.7}\text{Zn}_{0.3}\text{Fe}_2\text{O}_4$  and  $\text{Ni}_{0.6}\text{Zn}_{0.4}\text{Fe}_2\text{O}_4$  ferrite, the isomer shift remain unchanged at A and B sites with the increase of  $\text{Sn}^{4+}$  concentration. Since for a particular type of Mössbauer probe the isomer shift depends only on the s-electron density at the nucleus hence we infer that  $\text{Sn}^{4+}$  substitution in  $\text{Ni}_{0.7}\text{Zn}_{0.3}\text{Fe}_2\text{O}_4$  and  $\text{Ni}_{0.6}\text{Zn}_{0.4}\text{Fe}_2\text{O}_4$  ferrite does not affect the s-electron density at the nucleus of  $\text{Fe}^{3+}$  ions at A and B sites. The larger value of isomer shift for octahedral site is interpreted as due to larger

bond separation  $Fe^{3+}-O^{2-}$  for the octahedral ions as compared to that of tetrahedral ions. Due to the smaller overlapping of orbitals of  $Fe^{3+}$  ions and  $O^{2-}$  ions, the covalency effect is small, and hence the isomer shift is large at the octahedral site. The large value of isomer shift at  $77^{\circ}K$  is due to the thermal red shift between the source at  $295^{\circ}K$  and the absorber at  $77^{\circ}K$  [10, 11].

### 5.3.2 Quadrupole Splitting :

$Ni_{0.7+x}Zn_{0.3}Sn_xFe_{2-2x}O_4$  and  $Ni_{0.6+x}Zn_{0.3}Sn_xFe_{2-2x}O_4$  ferrite systems do not exhibit observable quadrupole splitting. The explanation is the same as given in Sec. (4.3.2).

### 5.3.3 Magnetic Hyperfine Splitting :

The variation of effective magnetic field at the two sublattices could be understood, as discussed in Chapter 4, on the basis of Néel's molecular field theory [12] and the super-transferred hyperfine field  $H_{STHF}$  [13-15]. The decrease of  $H_{eff}(A)$  has been attributed to the fact that all the  $Sn^{4+}$  ions occupy the B site and thereby reducing the magnetization  $M_B$ . In the present system i.e.,  $Ni_{1-y+x}Zn_ySn_xFe_{2-2x}O_4$  ferrite, let  $x$   $Sn^{4+}$  ions are distributed over A and B sites such that  $z$   $Sn^{4+}$  ions replace  $zFe^{3+}$  ions at A site;  $(x-z)Sn^{4+}$  ions and  $x$   $Ni^{2+}$  ions replace  $(2x-z)Fe^{3+}$  ions at B site. According to this, the structural formula of the present series of

ferrites will be  $(Zn_y^{2+} Fe_{1-y-z}^{3+} Sn_z^{4+})[Ni_{1-y+x}^{2+} Fe_{1+y+z-2x}^{3+} Sn_{x-z}^{4+}]_2^{(2-)}_4$ . According to the assumptions of Néel's molecular field theory, A-B superexchange interactions are stronger than A-A or B-B superexchange interaction.  $Sn^{4+}$  and  $Zn^{2+}$  ions being diamagnetic do not contribute to the magnetic exchange interaction. Moreover,  $Fe_A^{3+} - O^{2-} - Fe_B^{3+}$  superexchange interaction is stronger than  $Fe_A^{3+} - O^{2-} - Ni_B^{2+}$  superexchange interaction [16], the effective magnetic field is mainly due to average  $Fe_A^{3+} - O^{2-} - Fe_B^{3+}$  magnetic bonds per  $Fe^{3+}$  ion. According to the above ionic distribution, the tetrahedral  $Fe_A^{3+}$  ions have, on the average,  $(1+y+z-2x)/2$  of their intersublattice magnetic bonds with  $Fe_B^{3+}$  ions and  $(1-y+x)/2$  of their intersublattice magnetic bonds with  $Ni_B^{2+}$  ions. On the other hand, the octahedral  $Fe_B^{3+}$  ions have, on the average,  $(1-y-z)$  of their intersublattice magnetic bonds with  $Fe_A^{3+}$  ions. Since there is no appreciable change in  $H_{eff}(B)$  with  $Sn^{4+}$  concentration, we conclude that  $Sn^{4+}$  does not enter A site, that is  $z$  is zero, i.e. all the  $Sn^{4+}$  ions occupy B site, thus reducing the number of intersublattice magnetic bond which the  $Fe_A^{3+}$  ions experience. The decrease of  $H_{eff}(A)$  can be explained in the same way as it is done in section (4.3.3).

#### 5.3.4 Full Width at Half Maximum (FWHM) :

It is observed that in all the two systems the FWHM at A site increases with  $Sn^{4+}$  concentration whereas  $\Gamma_B$ , the

FWHM at B site is almost constant. The explanation for these is same as given in section (4.3.4).

#### 5.4 Study of Magnetization :

##### 5.4.1 $\text{Sn}^{4+}$ Substituted $\text{Ni}_{0.7}\text{Zn}_{0.3}\text{Fe}_2\text{O}_4$ Ferrite :

In fig. (5.12) we have shown the variation of magnetization and the net effective magnetic field with  $\text{Sn}^{4+}$  concentration on comparable scales. In this case  $H_{\text{eff}}(B)$  is greater than  $H_{\text{eff}}(A)$  and  $H_{\text{eff}}(A)$  decreases with the increase of  $\text{Sn}^{4+}$  ions. Therefore  $|H_{\text{eff}}(B) - H_{\text{eff}}(A)|$  increases whereas  $|M(B) - M(A)|$  decreases with  $\text{Sn}^{4+}$  concentration. For a better visual aid for comparison of the magnetization and the net effective magnetic field, an inverted scale has been chosen for the net effective magnetic field. From the graph it is evident that variation of net effective magnetic field with  $\text{Sn}^{4+}$  concentration follows the same trend as that of the magnetization. In fig (5.12) we see that the magnetization falls sharply from  $2.62\mu_B$  at zero concentration of  $\text{Sn}^{4+}$  ions to  $2.38\mu_B$  at the  $\text{Sn}^{4+}$  concentration of  $x = 0.004$  followed by a very slow decrease in the magnetization upto  $x = 0.04$ . The Neel type of magnetic ordering which gives an account of linear decrease of magnetization, if all the  $\text{Sn}^{4+}$  ions enter at B site, is unable to explain the variation of magnetization with  $\text{Sn}^{4+}$  concentrations. We, therefore, concluded that there is development of canted

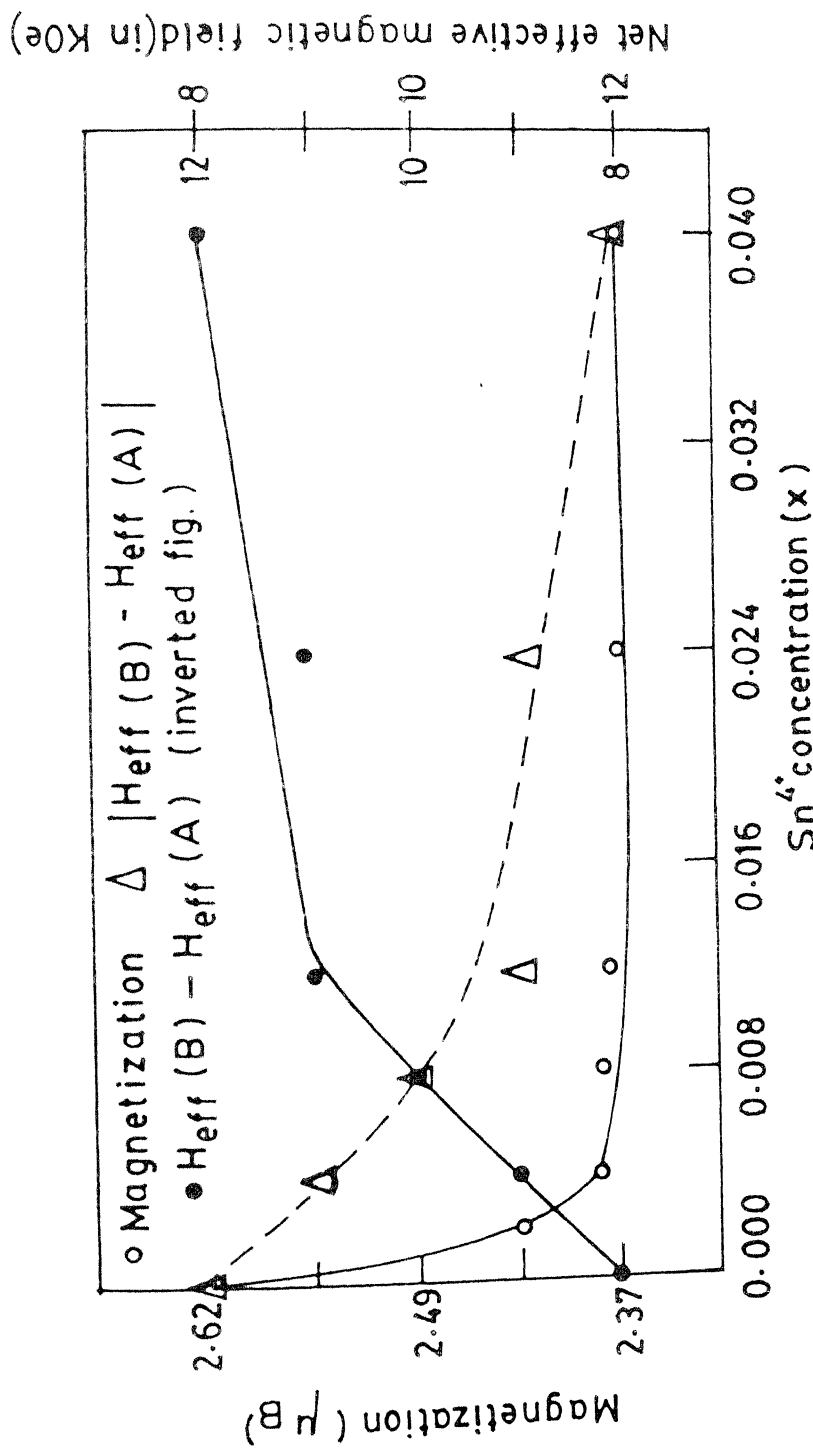


FIG. 5.12 Variation of magnetization and net effective magnetic field with  $\text{Sn}^{4+}$  concentration in  $\text{Ni}_{0.7+x} \text{Zn}_{0.3} \text{Sn}_x \text{Fe}_{2-2x} \text{O}_4$ . The outer scale on the right is for  $\Delta$  (inverted fig.) and the inner scale is for  $\bullet$ .

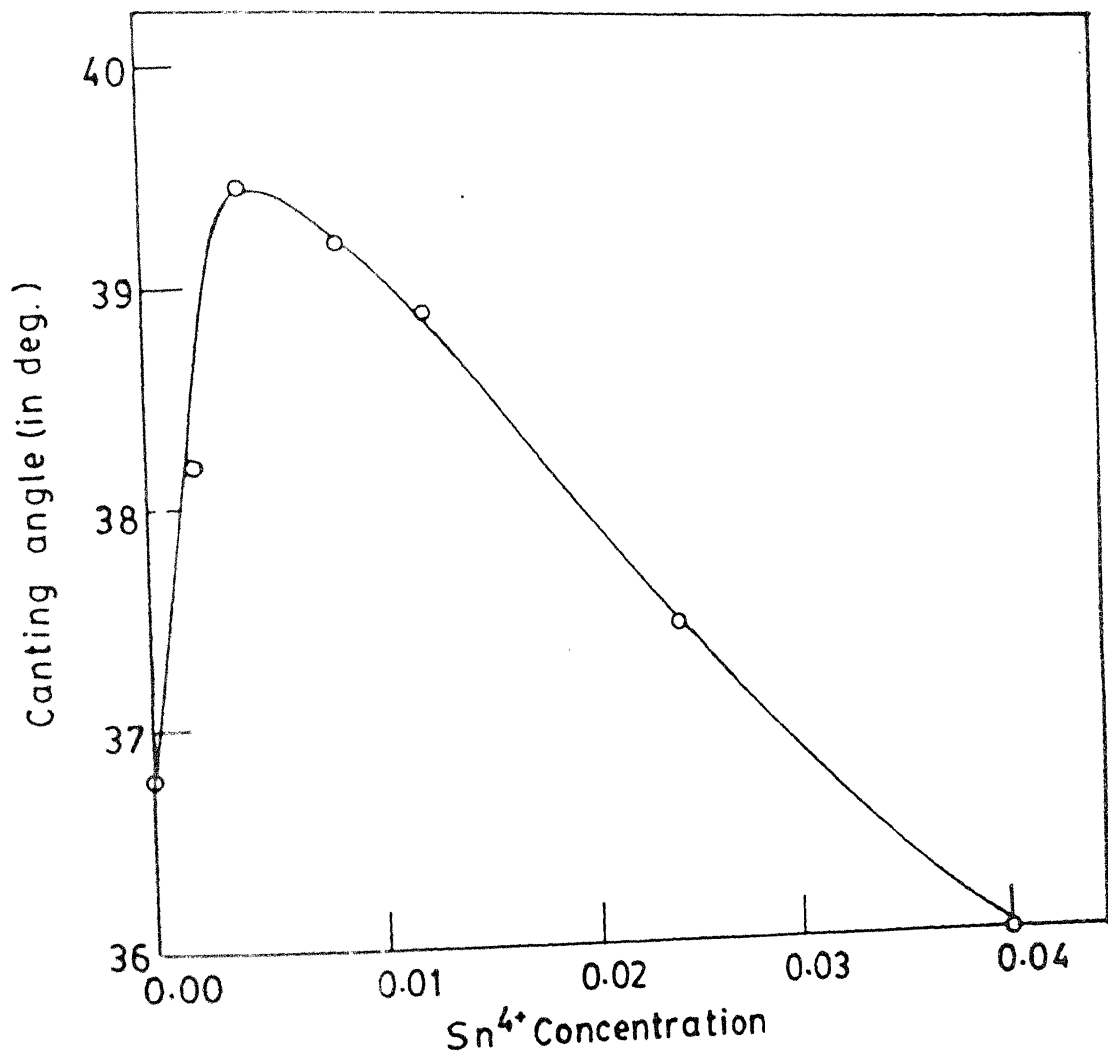


FIG. 5.13 VARIATION OF CANTING ANGLE WITH  $\text{Sn}^{4+}$  CONCENTRATION IN  $\text{Ni}_{0.7+x} \text{Zn}_{0.3} \text{Sn}_x \text{Fe}_{2-2x} \text{O}_4$  FERRITE.

spin structure. Normally, it is found that if the non-magnetic ion is entering at B site then the canting of spins take place at A site. But in our case  $\text{Sn}^{4+}$  ions occupy B site and canting of spins also take place at B site. In fig (5.13) we have shown the variation of canting angle, as calculated from the magnetization data, with  $\text{Sn}^{4+}$  concentration. The canting angle increases from  $36.8^\circ$  at zero concentration of  $\text{Sn}^{4+}$  to  $39.4^\circ$  for the  $\text{Sn}^{4+}$  concentration of  $x = 0.004$  followed by a decrease in the canting angle upto  $32.4^\circ$  for the  $\text{Sn}^{4+}$  concentration of  $x = 0.04$ . The interpretation of this result is given along with that of  $\text{Sn}^{4+}$  substituted  $\text{Ni}_{0.6}\text{Zn}_{0.4}\text{Fe}_2\text{O}_4$  ferrite.

#### 5.4.2 $\text{Sn}^{4+}$ Substituted $\text{Ni}_{0.6}\text{Zn}_{0.4}\text{Fe}_2\text{O}_4$ Ferrite :

In fig. (5.14) we have plotted the variation of magnetization and the net effective magnetic field with  $\text{Sn}^{4+}$  concentration on comparable scales. From the graph we see that the trend of variation of magnetization and the net effective magnetic field is same. The magnetization falls sharply from  $3.18 \mu_B$  at zero concentration of  $\text{Sn}^{4+}$  to  $2.94 \mu_B$  at the  $\text{Sn}^{4+}$  concentration of  $x = 0.004$  followed by a slow decrease upto  $2.88 \mu_B$  at the  $\text{Sn}^{4+}$  concentration of  $x = 0.04$ . The net effective magnetic field, on the other hand, falls from 34 KOe. at zero concentration of  $\text{Sn}^{4+}$  to 30 KOe. at  $\text{Sn}^{4+}$  concentration of  $x = 0.04$ . Again the deviation from linear decrease of magnetization suggests the development of canted spin structure. In fig (5.15) we

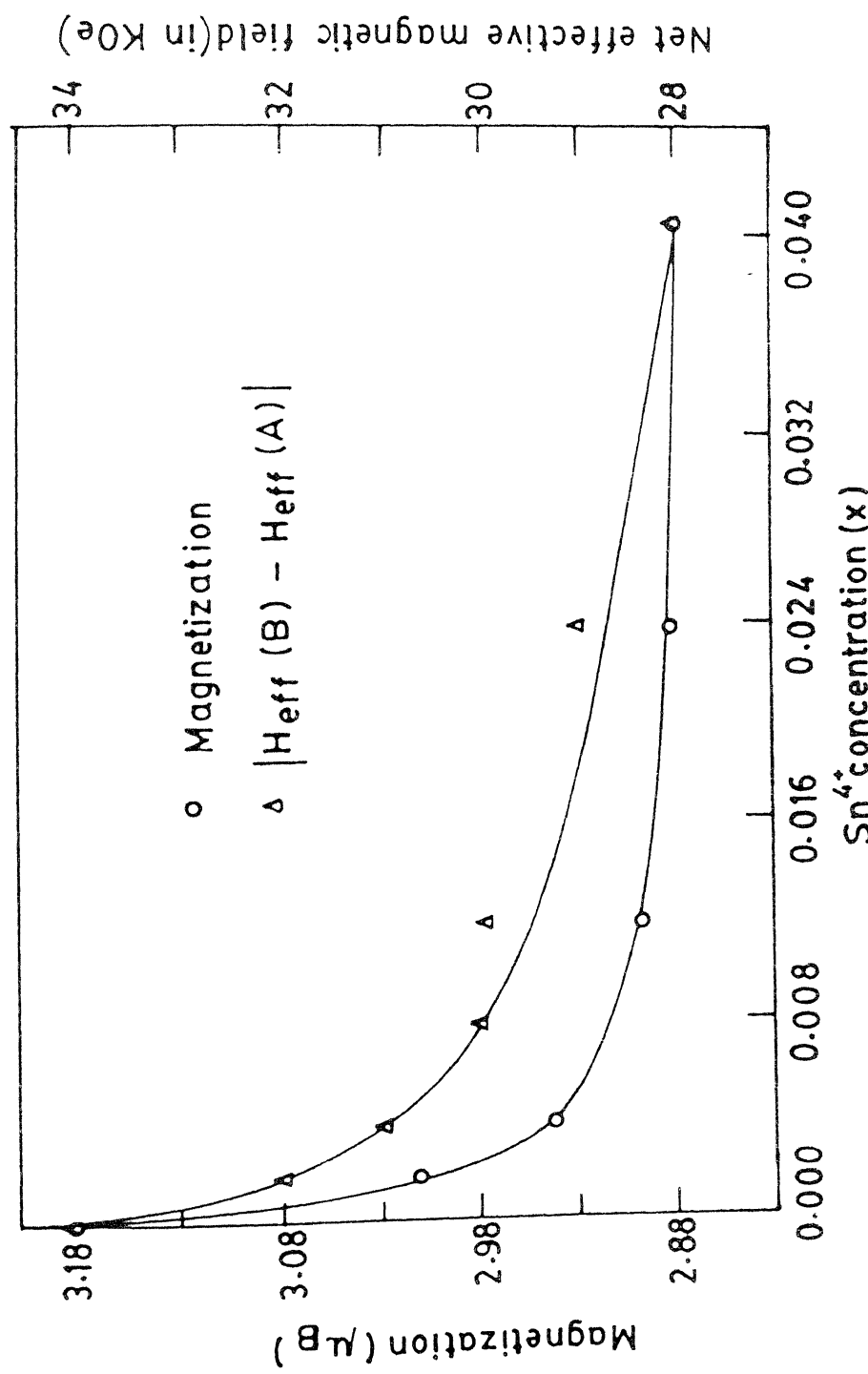


FIG. 5.14 Variation of magnetization and net effective magnetic field with  $\text{Sn}^{4+}$  concentration in  $\text{Ni}_{0.6+x} \text{Zn}_{0.4} \text{Sn}_x \text{Fe}_{2-2x} \text{O}_4$  ferrite.

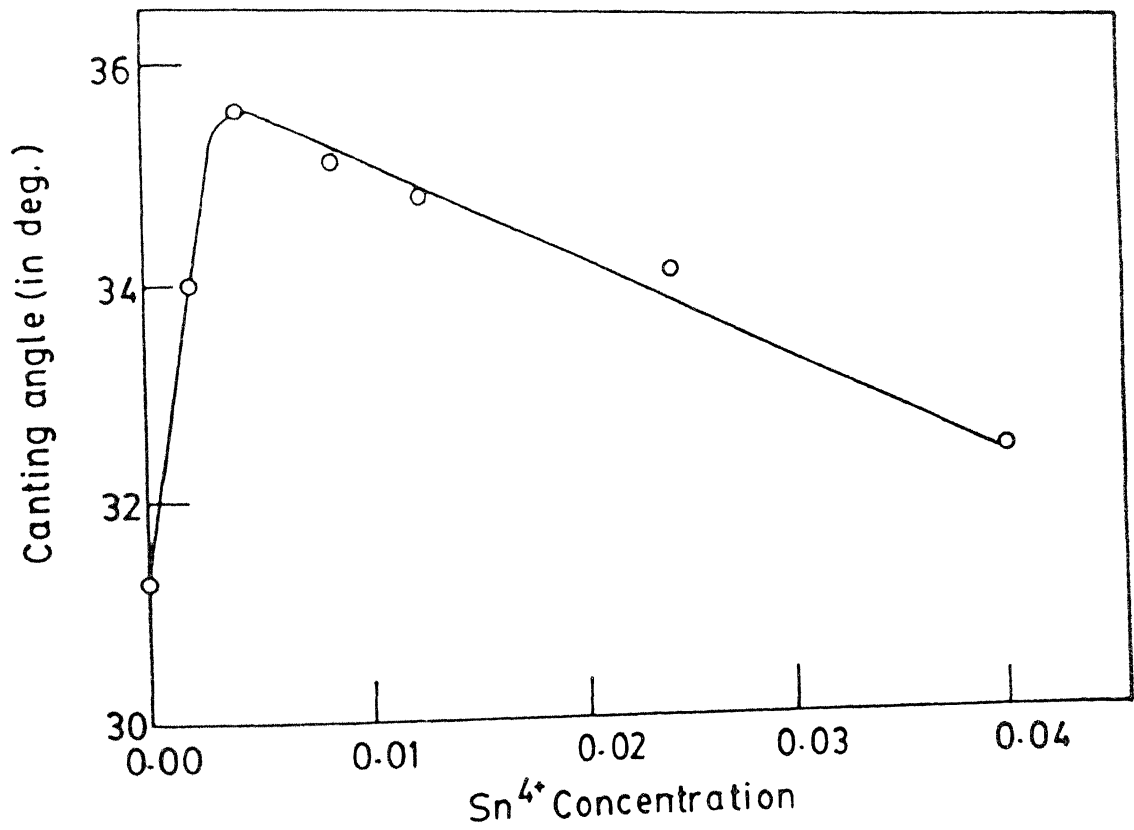


FIG.5.15 VARIATION OF CANTING ANGLE WITH  $\text{Sn}^{4+}$  CONCENTRATION IN  $\text{Ni}_{0.6+x} \text{Zn}_{0.4} \text{Sn}_x \text{Fe}_{2-2x} \text{O}_4$  FERRITE.

have shown the variation of canting angle at B site with  $\text{Sn}^{4+}$  concentration. We found that the canting angle increases from  $31.3^\circ$  at zero concentration of  $\text{Sn}^{4+}$  to  $35.6^\circ$  at the  $\text{Sn}^{4+}$  concentration of  $x = 0.004$  followed by a decrease upto  $32.4^\circ$  at the  $\text{Sn}^{4+}$  concentration of  $x = 0.04$ .

In figs (5.16) and (5.17) we have shown the variation of exchange constants with  $\text{Sn}^{4+}$  concentration. These constants were calculated using eq. (4.7) and as discussed in Sec. (4.4.1). In the same figures we have also shown the variation of lattice parameter with  $\text{Sn}^{4+}$  concentration. The lattice parameter increases monotonically with the increase of  $\text{Sn}^{4+}$  concentration. For the  $\text{Sn}^{4+}$  concentration of more than  $x = 0.004$ , the change of exchange constant,  $J_{\text{Ni}^{2+}(\text{B})-\text{Ni}^{2+}(\text{B})}$ , reflects the change in lattice parameter. However, for the concentration of  $\text{Sn}^{4+}$  less than  $x = 0.004$ , the change of ionic separation and exchange constant  $\{J_{\text{Ni}^{2+}(\text{B})-\text{Ni}^{2+}(\text{B})}\}$  show contradictory trend. One would suspect that the outermost 4d-electrons of  $\text{Sn}^{4+}$  contribute to this trend. However, a satisfactory elucidation of this problem can be achieved by  $^{119}\text{Sn}$  Mössbauer spectroscopy of the system. In these systems too the calculation of lattice parameter by hard sphere model does not yield the experimentally observed curve. The calculation of lattice parameter using eq. (4.8) and the root mean square charge deviation at each site gives a variation of M and hence of  $\alpha$  [figs. (4.25) and (4.26)]. It is evident that the nature

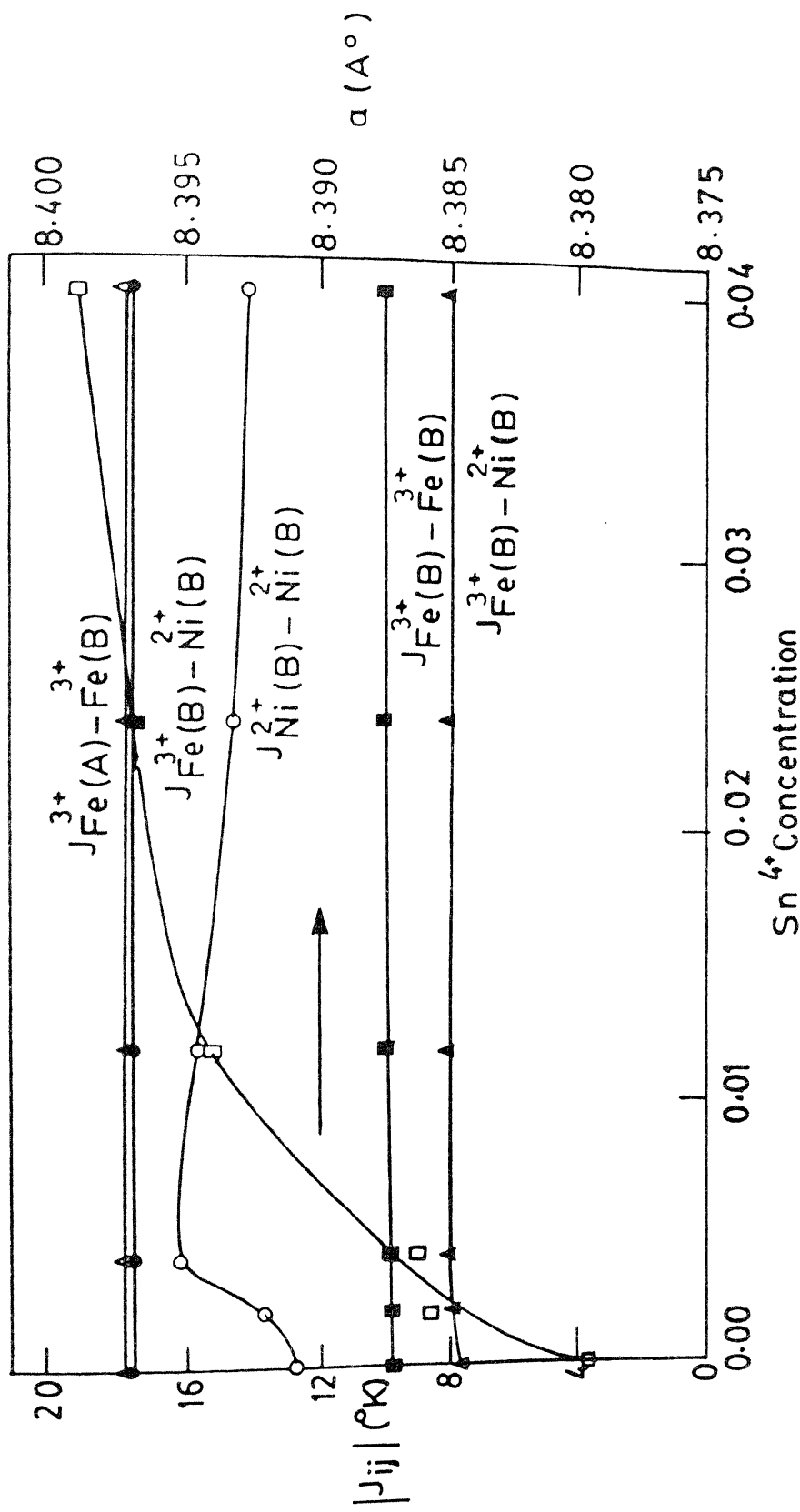


FIG. 5.16 VARIATION OF EXCHANGE CONSTANTS AND LATTICE PARAMETER WITH  $\text{Sn}^{4+}$  CONCENTRATION IN  $\text{Ni}_{0.7+x} \text{Zn}_{0.3} \text{Sn}_x \text{Fe}_{2-2x} \text{O}_4$  FERRITE.

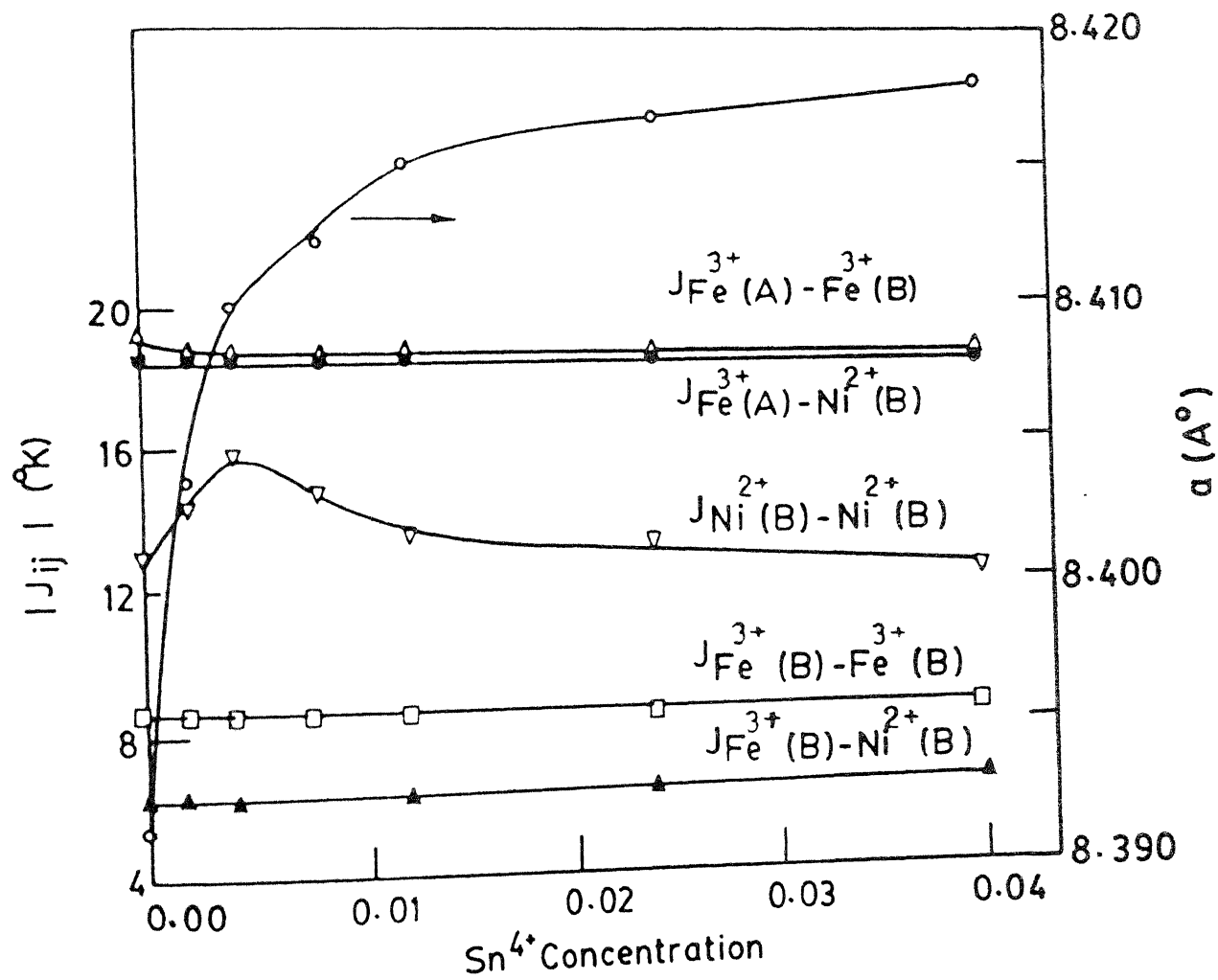


FIG. 5.17 VARIATION OF EXCHANGE CONSTANTS AND LATTICE PARAMETER WITH  $\text{Sn}^{4+}$  CONCENTRATION IN  $\text{Ni}_{0.6+x} \text{Zn}_{0.4} \text{Sn}_x \text{Fe}_{2-2x} \text{O}_4$  FERRITE.

of variation of lattice parameter with  $\text{Sn}^{4+}$  concentration is similar for  $x > 0.008$  in case of both calculated and experimentally observed lattice parameters. However, for a more accurate variation of lattice parameter with  $\text{Sn}^{4+}$  concentration a more sophisticated theory is called for.

## REFERENCES

1. V.A. Bokov, G.V. Novikov, Yu. G. Saksonov, V.A. Trukhtanov and S.I. Yushchuk, Sov. Phys. Solid State 16, 2364 (1975).
2. Usha Varshney, R.K. Puri, K.H. Rao, and R.G. Mendiratta, Proc. of the third International Conference on Ferrites, Kyoto, Japan (29 Sept. - 2 Oct, 1980) p-207.
3. Usha Varshney, R.K. Puri, and M.G. Mendiratta, Proc. of the International Conference on the Application of the Mössbauer Effect, Jaipur, India (14-18 Dec. 1981) p-190.
4. M.K. Fayek, Proc. of the Int. Conf. on the Application of the Mossbauer Effect, Jaipur, India (14-18 Dec. 1981) p-253.
5. R.K. Puri and Usha Varshney, J. Phys. Chem. Solids, 44, 655 (1983).
6. A.R. Das, V.S. Ananthan and, D.C. Khan, J. Appl. Phys. 57, 4189 (1985).
7. J.S. Baijal, D. Kothari and, S. Phanjoubam, Solid State Commun. 69, 277 (1989).
8. Usha Varshney and R. K. Puri, Proc. of the Forth Int. Conf. on Ferrites (San Francisco, California, Oct. 31-Nov 2, 1984) p-291.
9. J.M. Daniels and A. Rosencwaig, Can. J. Phys. 48, 381 (1970).

10. R.V. Pound, G.A. Rebka, Phys. Rev. Lett. 4, 274 (1960).
11. B.D. Josephson, Phys. Rev. Lett. 4, 341 (1960).
12. L. Néel, Ann. Phys. 3, 137 (1948).
13. E. Simanek, N.L. Huang and R. Orbach, J. Appl. Phys. 38, 1072 (1967).
14. F. Van der Woude and G.A. Sawatzky, Phys. Rev. B, 4, 3159 (1971).
15. G.A. Sawatzky and F. Van der Woude, J. de Physique 12, C6-47 (1974).
16. S. Geller, H.J. Williams, R.C. Sherwood and G.P. Espinosa, J. Phys. Chem. Solids, 23, 1525 (1962).

## CHAPTER 6

MÖSSBAUER STUDY OF SOME IRON COMPLEXES  
IN EXTERNAL ELECTRIC FIELD6.1 *Introduction* :

Previous studies of the influence of an external electric field on the hyperfine structure of Mössbauer spectra were primarily performed on ferroelectrics. Thus the changes in the parameters and shape of Mössbauer spectra with a phase transition in ferroelectrics or reorientation of domains in an electric field were studied [1-4]. Even though the internal crystal field was expected to be several orders of magnitude more than the applied field, the detection of the effect of external field by a high resolution spectrometer was not ruled out.

In this chapter we present some new findings in the well known systems such as ferrous sulphate heptahydrate, ferrous ammonium sulphate hexahydrate, sodium nitroprusside, potassium ferricyanide, red and black Roussin salts. As reported below, the induced start effect is clearly identifiable in all the complexes.

6.2 *Experimental* :

Mössbauer spectra of the samples were recorded by keeping the powdered sample between two capacitor plates made of thin aluminium foil and using a highly stable constant-acceleration spectrometer. The stability of the

spectrometer was confirmed by taking the spectra of standard absorbers (natural iron foil and sodium nitroprusside) before and after each run of the sample. The data were stored in the ND-62 multichannel analyser obtained from Nuclear Data Corporation, USA. A 25 MCi  $^{57}\text{CO}$ -in-Rh source obtained from M/s E.I.du Pont, U.S.A. was used. The spectra were recorded for various applied fields along the direction of  $\gamma$ -ray propagation.

Commercially available high purity  $\text{FeSO}_4 \cdot 7\text{H}_2\text{O}$ ,  $\text{Fe}(\text{NH}_4\text{SO}_4)_2 \cdot 6\text{H}_2\text{O}$ ,  $\text{Na}_2[\text{Fe}(\text{CN})_5\text{NO}] \cdot 2\text{H}_2\text{O}$ , and  $\text{K}_3[\text{Fe}(\text{CN})_6]$  were used for samples. Red Roussin salt,  $\text{Na}[(\text{NO})_2\text{FeS}]$ , was prepared by the action of Roussin's black ammonium salt with sodium hydroxide. Black Roussin salt,  $\text{Na}[(\text{NO})_7\text{Fe}_4\text{S}_3]$ , was prepared from the red salt by the action of iron nitrosyl sulphate. The isomer shift of all the systems except sodium nitroprusside was reported with respect to sodium nitroprosside. For sodium nitroprusside it was referred to natural iron foil.

### 6.3 Results :

The Mössbauer absorption spectrum of  $\text{FeSO}_4 \cdot 7\text{H}_2\text{O}$  at zero external field was a quadrupole doublet with  $\Delta E_Q = 3.203 \pm 0.002$  mm/sec and isomer shift  $1.559 \pm 0.002$  mm/sec. These values are in excellent agreement with the standard values quoted in the literature [5-9]. When the external electric field was applied in the direction of  $\gamma$ -ray, it

was found that the quadrupole splitting,  $\Delta E_Q$ , increases upto  $3.248 \pm 0.002$  mm/sec for a maximum field of 50 KV/Sec. Two typical Mössbauer spectra of  $\text{FeSO}_4 \cdot 7\text{H}_2\text{O}$ , one at zero external field and the other at 50 KV/Cm is shown in fig. (6.1). The variation  $\delta(\Delta E_Q)$  with the applied field is shown in fig. (6.2). This is in good agreement with the values reported by Nair et al. [10]. The isomer shift of the system changes from  $1.559 \pm 0.002$  mm/sec to  $1.586 \pm 0.002$  mm/sec for the same range of applied electric field. The variation of isomer shift with the externally applied electric field is shown in fig. (6.3).

The intensity ratio of the two peaks  $I_1/I_2$  (i.e., for  $\left| \frac{3}{2}, \pm \frac{1}{2} \right\rangle \longrightarrow \left| \frac{1}{2}, \pm \frac{1}{2} \right\rangle$  and  $\left| \frac{3}{2}, \pm \frac{3}{2} \right\rangle \longrightarrow \left| \frac{1}{2}, \pm \frac{1}{2} \right\rangle$  transitions) at room temperature and without the field was found to be unity. This, however, decreased upto 0.86 at 50 KV/CM. [fig. (6.4)].

In  $\text{Fe}(\text{NH}_4\text{SO}_4)_2 \cdot 6\text{H}_2\text{O}$  the experimental value of quadrupole splitting and isomer shift without the external field was found to be  $1.760 \pm 0.002$  and  $1.574 \pm 0.002$  mm/sec respectively. These values are in excellent agreement with the values reported by other authors [10]. Two typical spectra of the system is shown in fig.(6.5). With the application of external field the quadrupole splitting increases upto  $1.786 \pm 0.002$  mm/sec for a maximum field of 30 KV/cm [fig. (6.2)]. For the same range of field, there was no observable change in the isomer shift

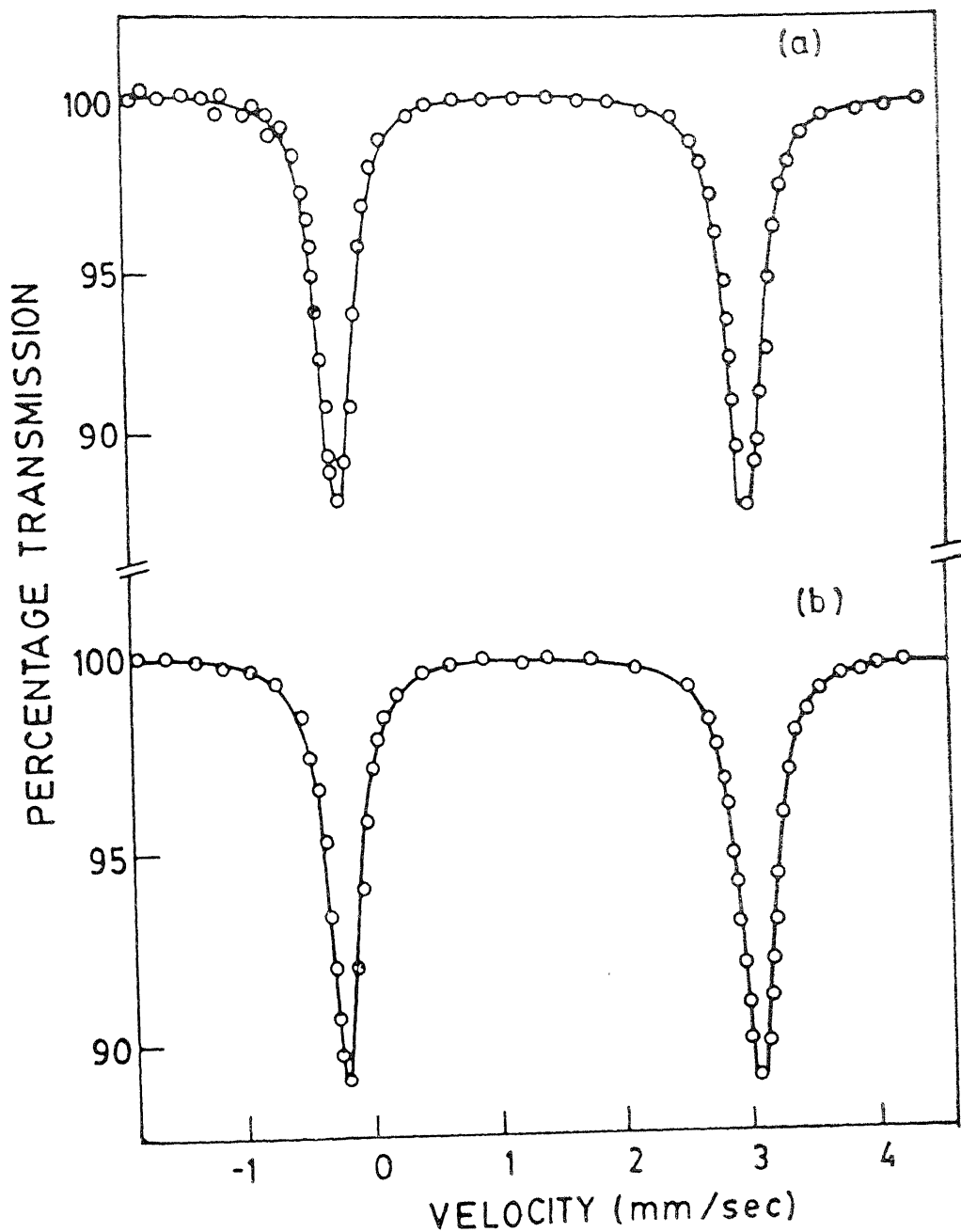
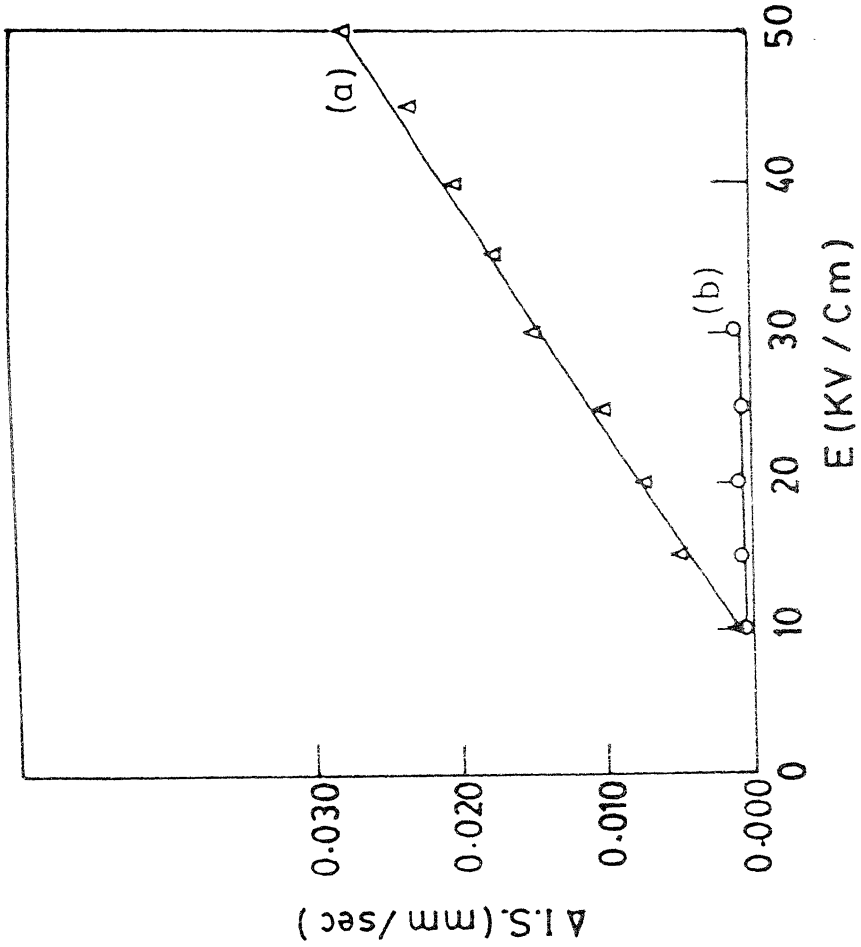
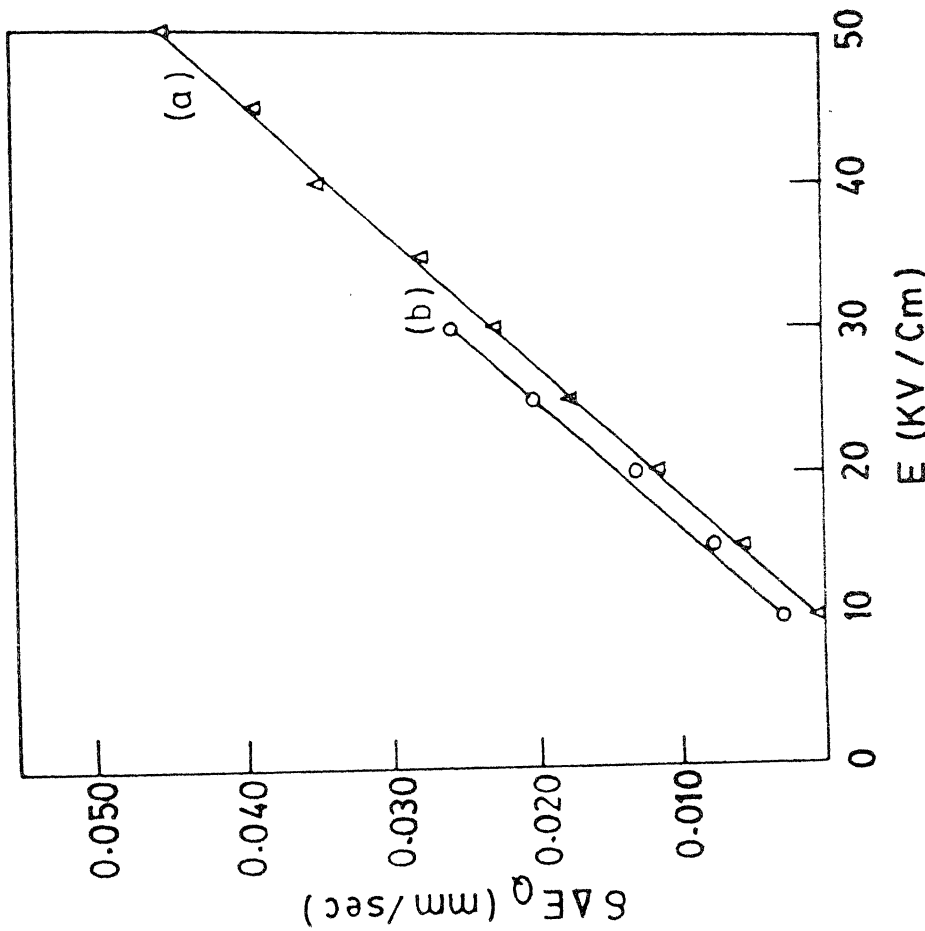


FIG. 6.1 Mössbauer spectra of  $\text{FeSO}_4 \cdot 7\text{H}_2\text{O}$  at  
(a) Zero field, (b) 50 KV/Cm.



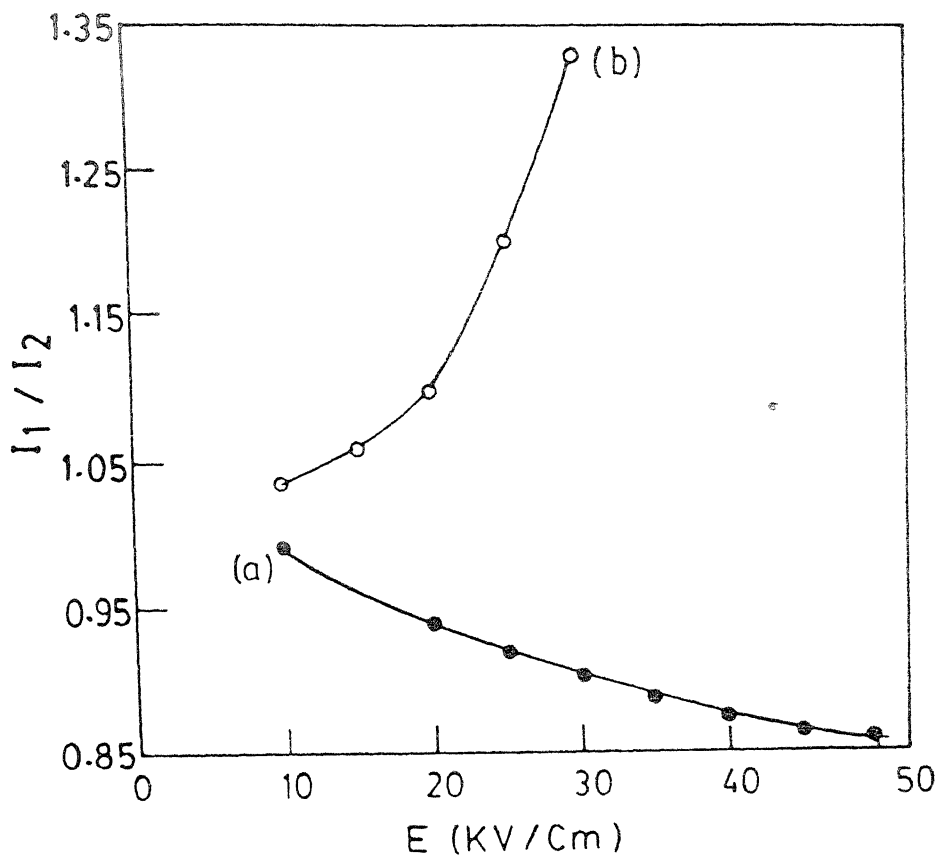


FIG. 6.4 Variation of the intensity ratio of the two peaks with applied field in  $\text{FeSO}_4 \cdot 7\text{H}_2\text{O}$  [curve (a)] and in  $\text{Fe}(\text{SO}_4)_2(\text{NH}_4)_2 \cdot 6\text{H}_2\text{O}$  [curve (b)].

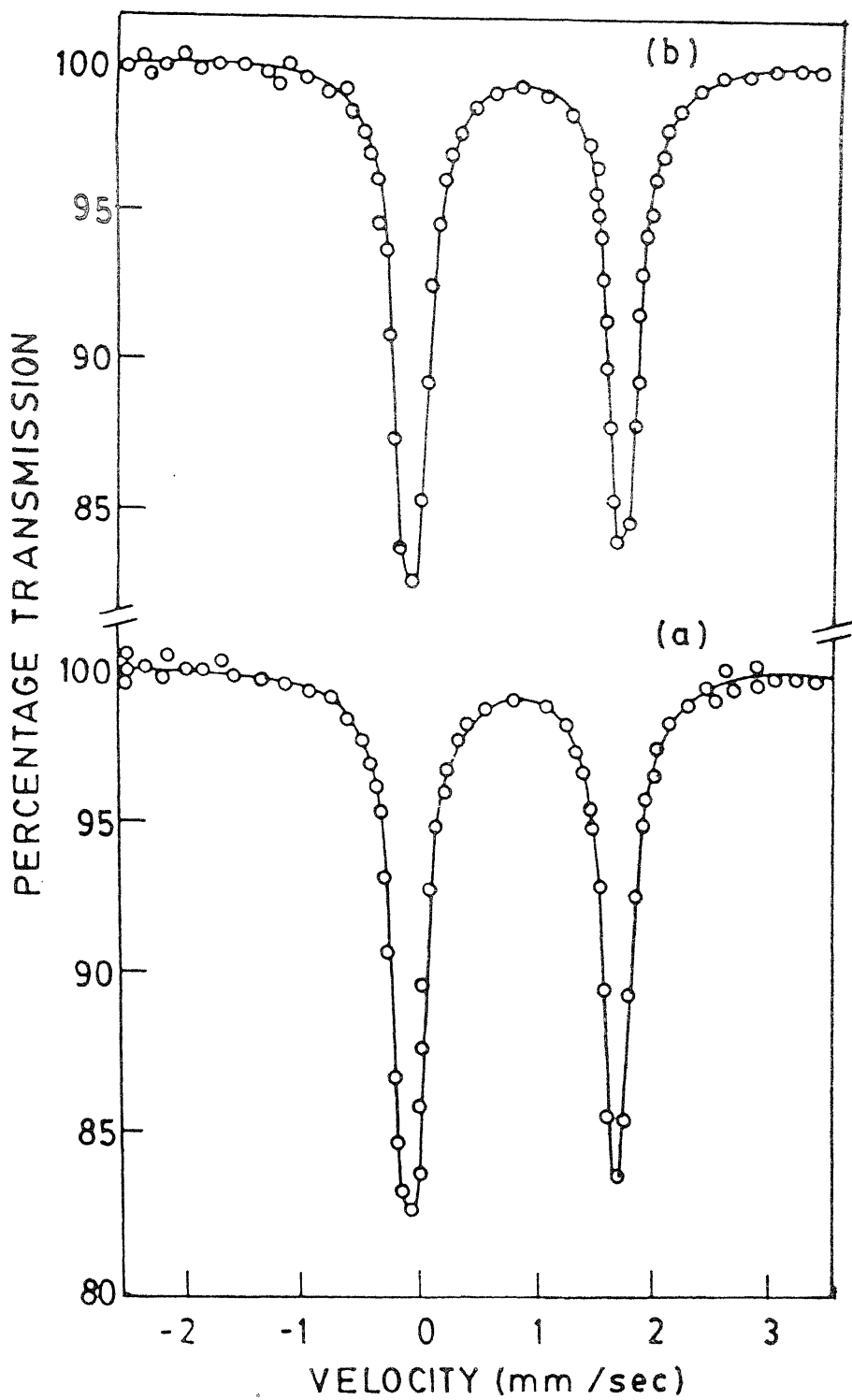


FIG. 6.5 Mössbauer spectra of  $\text{Fe}(\text{SO}_4)_2(\text{NH}_4)_2\cdot 6\text{H}_2\text{O}$  at (a) Zero field, (b) 30 KV /Cm.

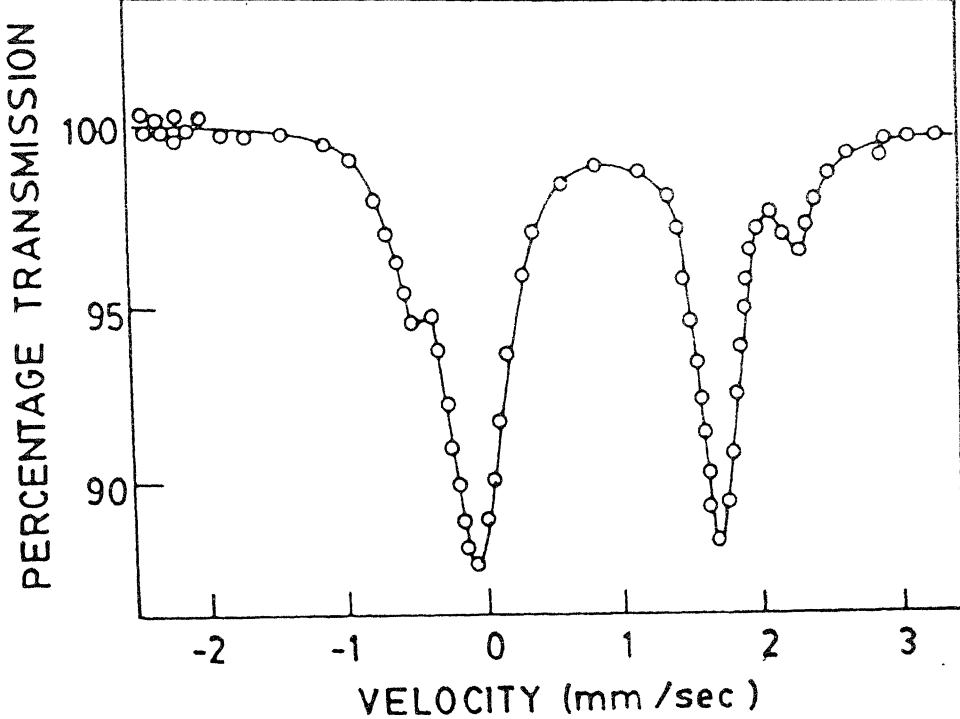


FIG. 6.6 Mössbauer spectrum of  $\text{Fe}(\text{SO}_4)_2(\text{NH}_4)_2 \cdot 6\text{H}_2\text{O}$  at 35 KV / Cm .

of the system [fig. (6.3)]. In this system, an increase in the intensity ratio of the two peaks was found. The variation of the intensity ratio of the peaks with applied field is shown in fig. (6.4).

In this system no change in quadrupole splitting was observed by Nair et al. [10] probably because of high value of full width at half maximum [FWHM],  $0.278 \pm 0.004$  mm/sec of their peaks. But in our case we took special care to improve the resolution of the spectrometer by arresting all sorts of unwanted vibrations of the experimental arrangements, and, reduce the FWHM to  $0.224 \pm 0.002$  mm/sec. As in the experiments of Nair et al., we also observed two new peaks at 35 KV/cm. [fig. (6.6)]. These new peaks may possibly be attributed to the change of hydration state [11] or the implantation of electrode (Al) atoms in the system.

In sodium nitroprusside, at zero external field, the quadrupole splitting and isomer shift was found to be  $1.705 \pm 0.002$  mm/sec and  $-0.260 \pm 0.002$  mm/sec respectively. These values are in very good agreement with the values reported by other workers [12-15]. Two typical spectra of sodium nitroprusside is shown in fig. (6.7). The effect of external electric field on quadrupole splitting of sodium nitroprusside is shown in fig. (6.8). It was observed that as the external electric field increases the quadrupole splitting decreases upto  $1.655 \pm 0.002$  mm/sec for a maximum

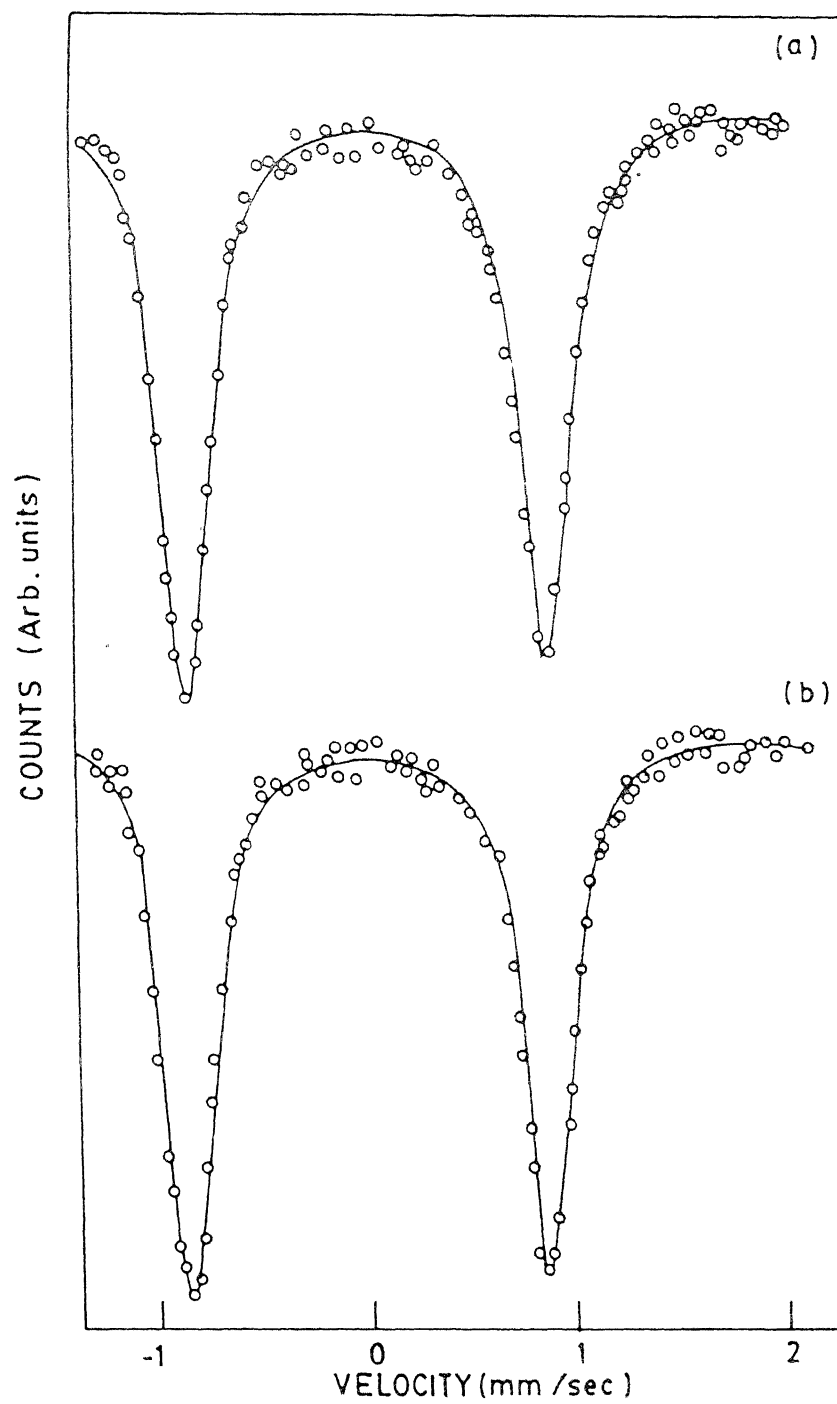


FIG. 6.7 Mössbauer spectra of SNP at (a) Zero field ,  
(b) 40 KV /Cm .

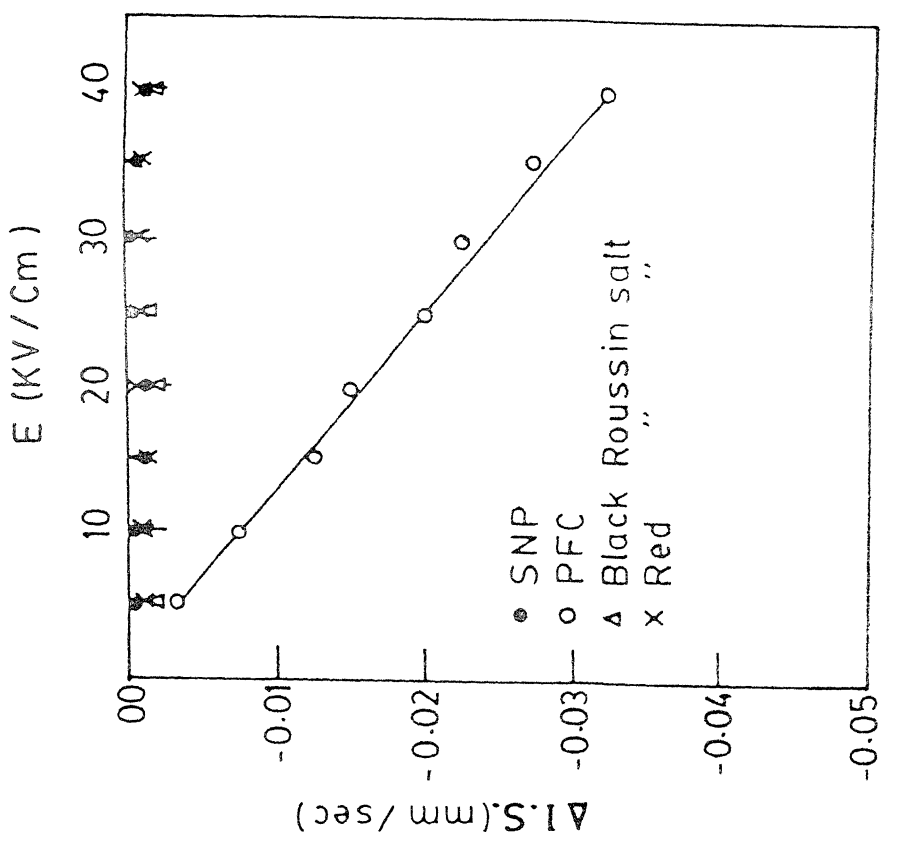


FIG. 6.8 Change in quadrupole splitting with applied electric field.

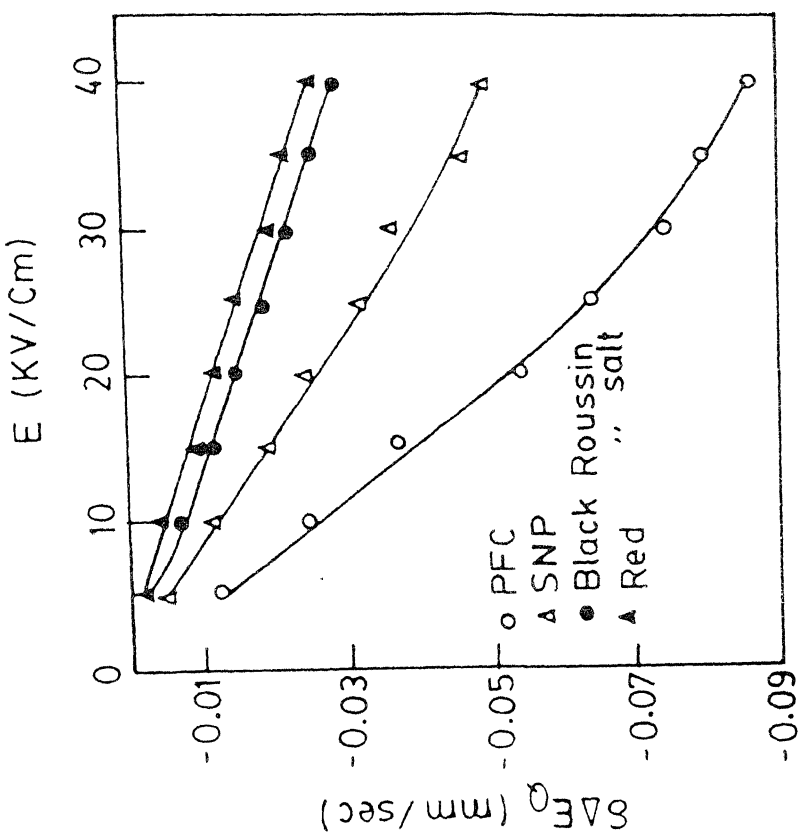


FIG. 6.9 Change in isomer shift with applied electric field.

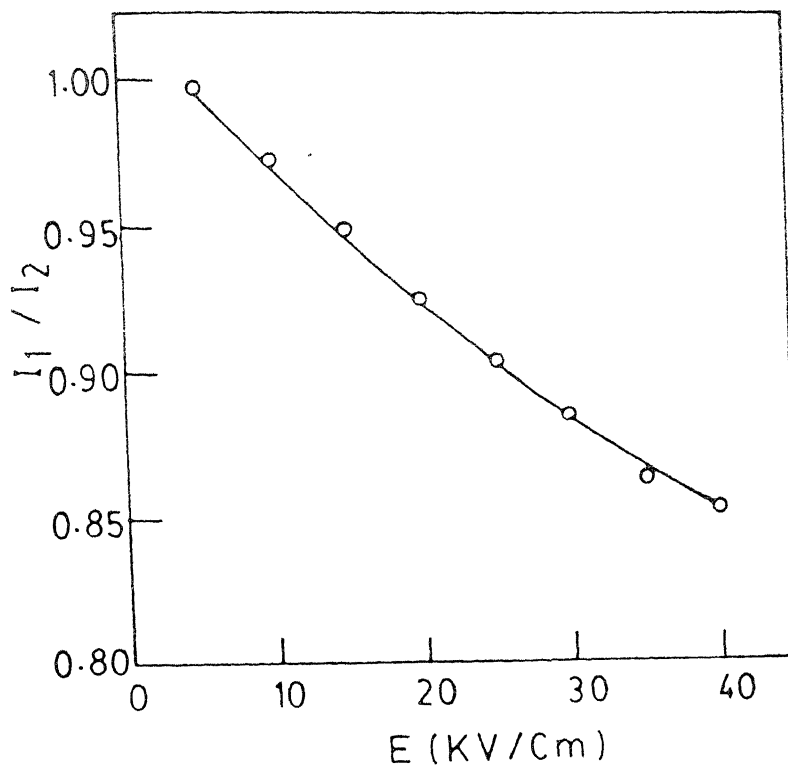


FIG. 6.10 Variation of the intensity ratio of the two peaks with applied electric field in sodium nitroprusside.

field of 40 KV/cm. There was, however, no significant change in the isomer shift of the system [fig.(6.9)]. An asymmetry of line shpaes was observed under applied electric field and this asymmetry increases with the increase of field. The variation of intensity ratio of the two lines,  $I_1/I_2$ , with external electric field is shown in fig. (6.10).

In  $K_3[Fe(CN)_6]$  the quadrupole splitting and isomer shift without the external field was found to be  $0.282 \pm 0.003$  and  $-0.217 \pm 0.003$  mm/sec respectively, which are in quite good agreement with the values in the literature [16]. Two typical Mössbauer absorption spectra of the system at zero and 40 KV/Cm. external field are shown in figs. (6.11) and (6.12) respectively. When an external electric field is applied across the sample the quadrupole splitting decreases upto  $0.195 \pm 0.003$  mm/sec for a maximum field of 40 KV/cm. The change in quadrupole splitting with the applied electric field is shown in fig.(6.8). The isomer shift of the system also decreases upto  $-0.249 \pm 0.004$  mm/sec for the same maximum field of 40 KV/cm. The decrease of isomer shift with the applied electric field is shown in fig.(6.9). The asymmetry of line shpaes in  $K_3[Fe(CN)_6]$  increases with the increase of applied electric field. The variation of intensity ratio of the peaks with applied field is shown in fig. (6.13).

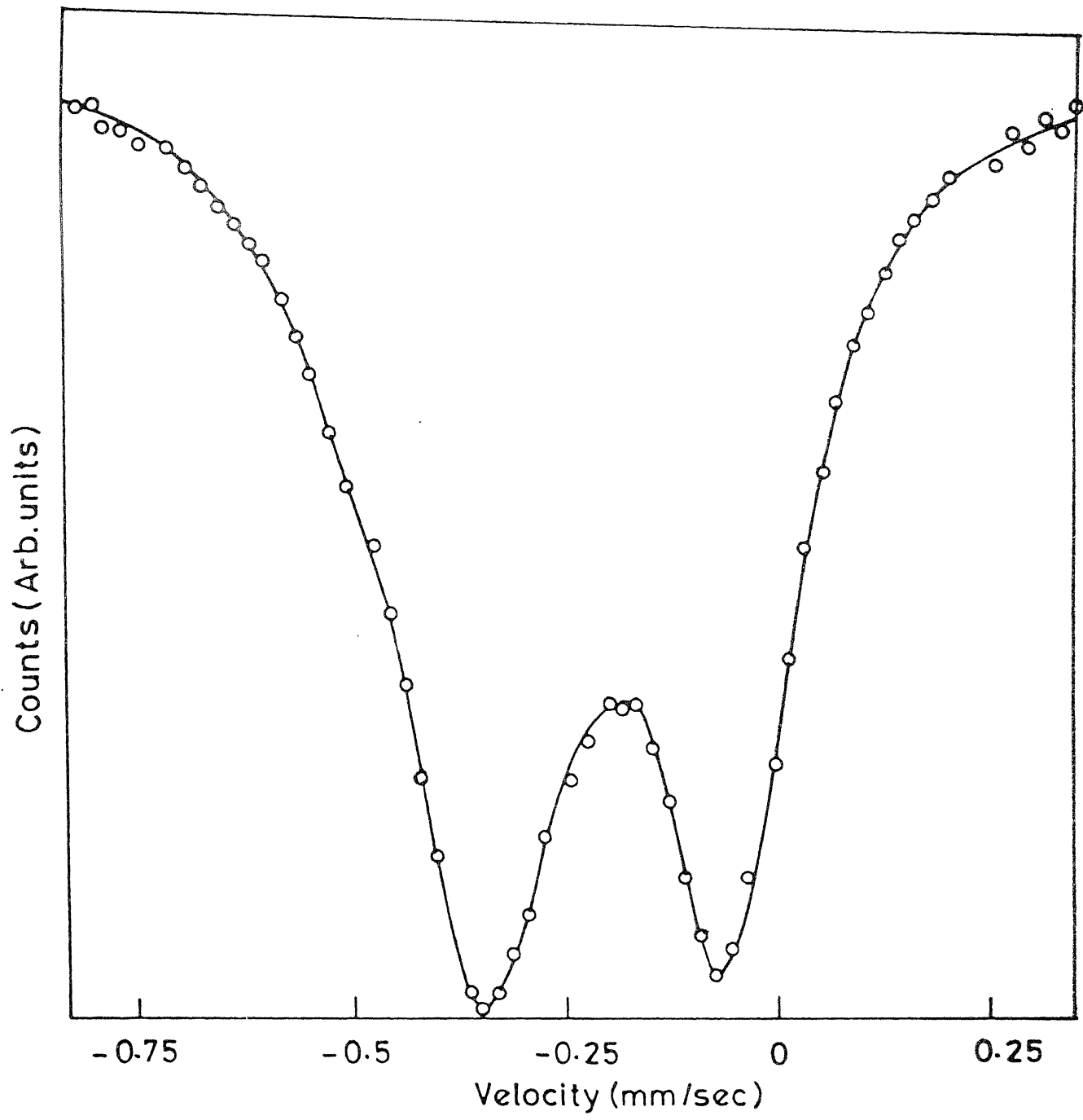


FIG. 6.11 Mössbauer spectrum of Potassium Ferricyanide at zero field.

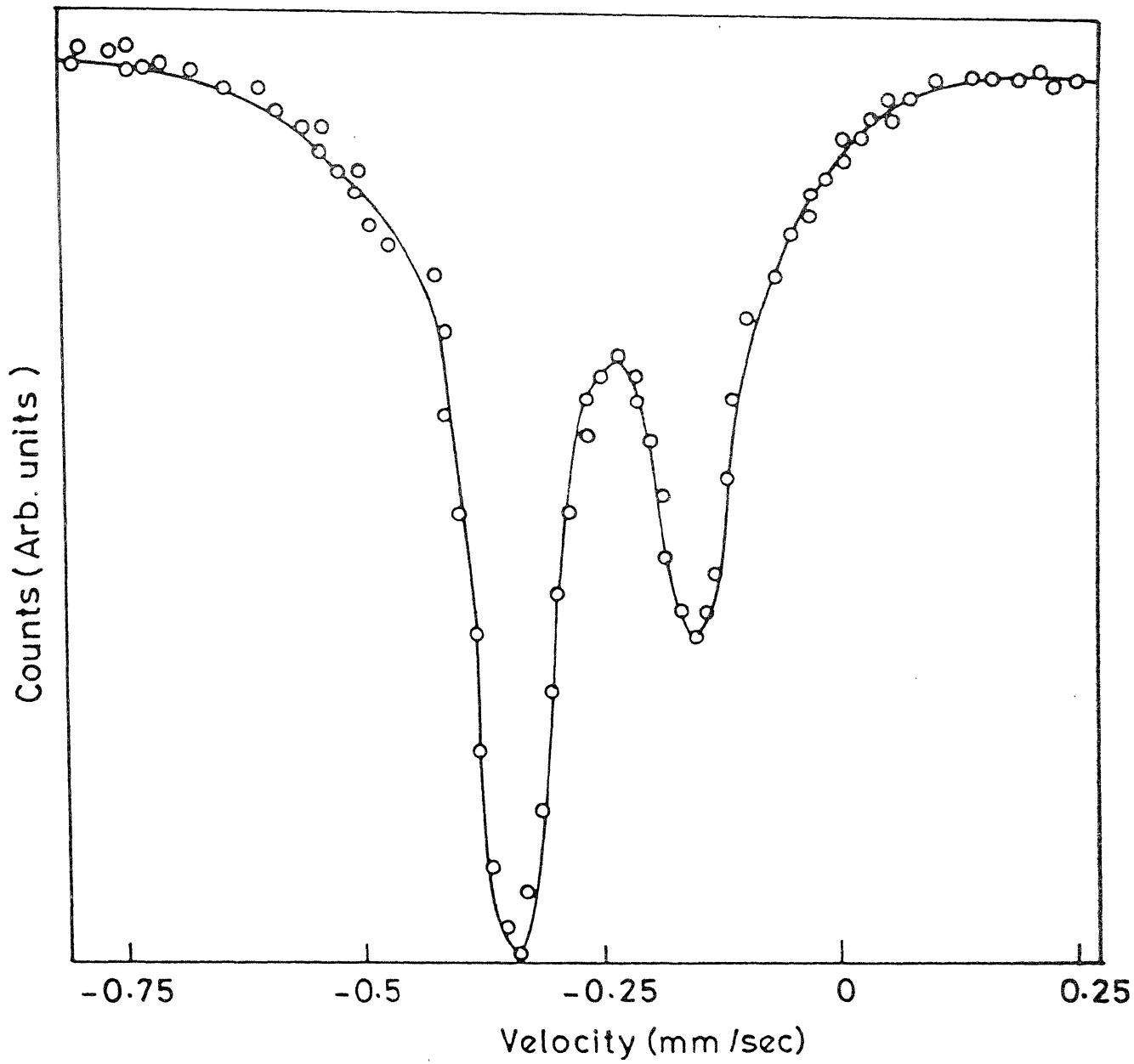


FIG. 6.12 Mössbauer spectrum of Potassium Ferricyanide at 40 KV/Cm.

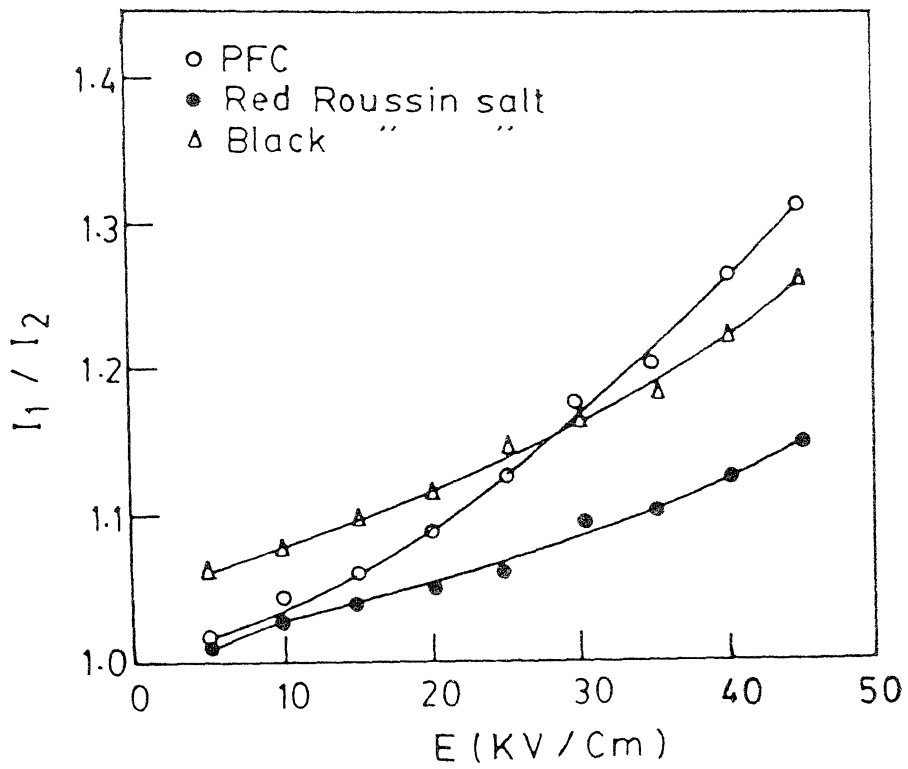


FIG.6.13 Variation of intensity ratio of the two peaks with applied electric field.

Mössbauer absorption spectrum of red Roussin salt,  $\text{Na}[(\text{NO})_2\text{FeS}]$ , shows a quadrupole doublet [fig. 6.14]. The value of quadrupole splitting without the application of external electric field was found to be  $0.625 \pm 0.004$  mm/sec. With the application of external electric field the quadrupole splitting decreases upto  $0.599 \pm 0.004$  mm/sec for a maximum field of 40 KV/cm. The variation in quadrupole splitting with the electric field is shown in fig. (6.8). The isomer shift of the system without the field was found to be  $0.267 \pm 0.004$  mm/sec. However, there was no significant change in isomer shift of the system for the same range of maximum field [fig. (6.9)]. The values of quadrupole splitting and isomer shift without the field are in good agreement with the values of other authors [17]. In this system too the asymmetry of line shape increases with the application of external electric field [fig. (6.13)].

In black Roussin salt,  $\text{Na}[(\text{NO})_7\text{F}_4\text{S}_3]$ , the Mössbauer absorption spectrum at zero external field was found to be a quadrupole doublet with  $\Delta E_Q = 0.870 \pm 0.004$  mm/sec and isomer shift  $0.321 \pm 0.004$  mm/sec. These values are in good agreement with the values reported by other workers [17]. Some typical spectra of black Roussin salt are shown in fig. (6.15). When an external electric field is applied the quadrupole splitting of the system decreases upto 0.840

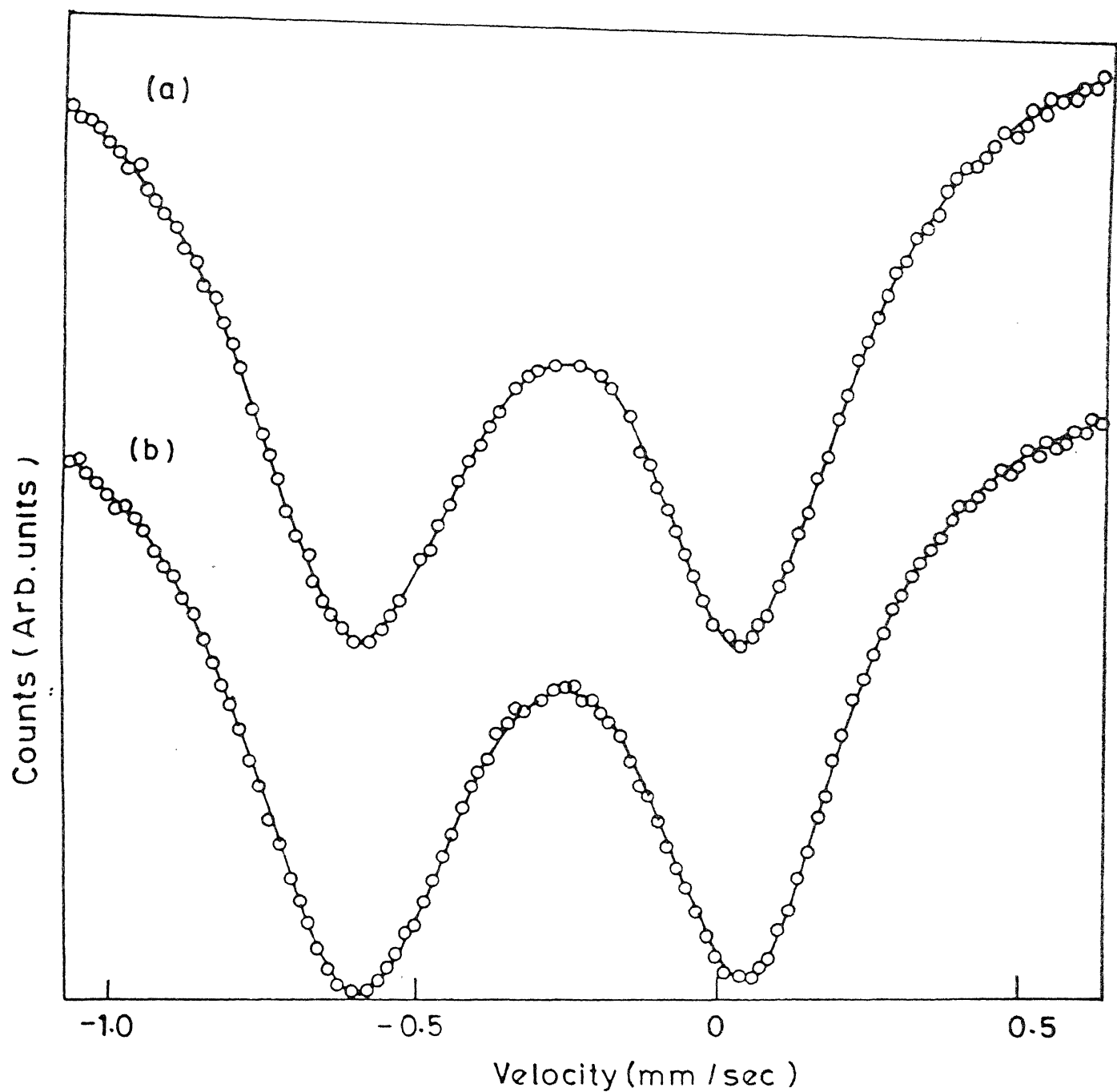


FIG. 6.14 Mössbauer spectra of Red Roussin Salt at  
(a) Zero field, (b) 40 KV / Cm.

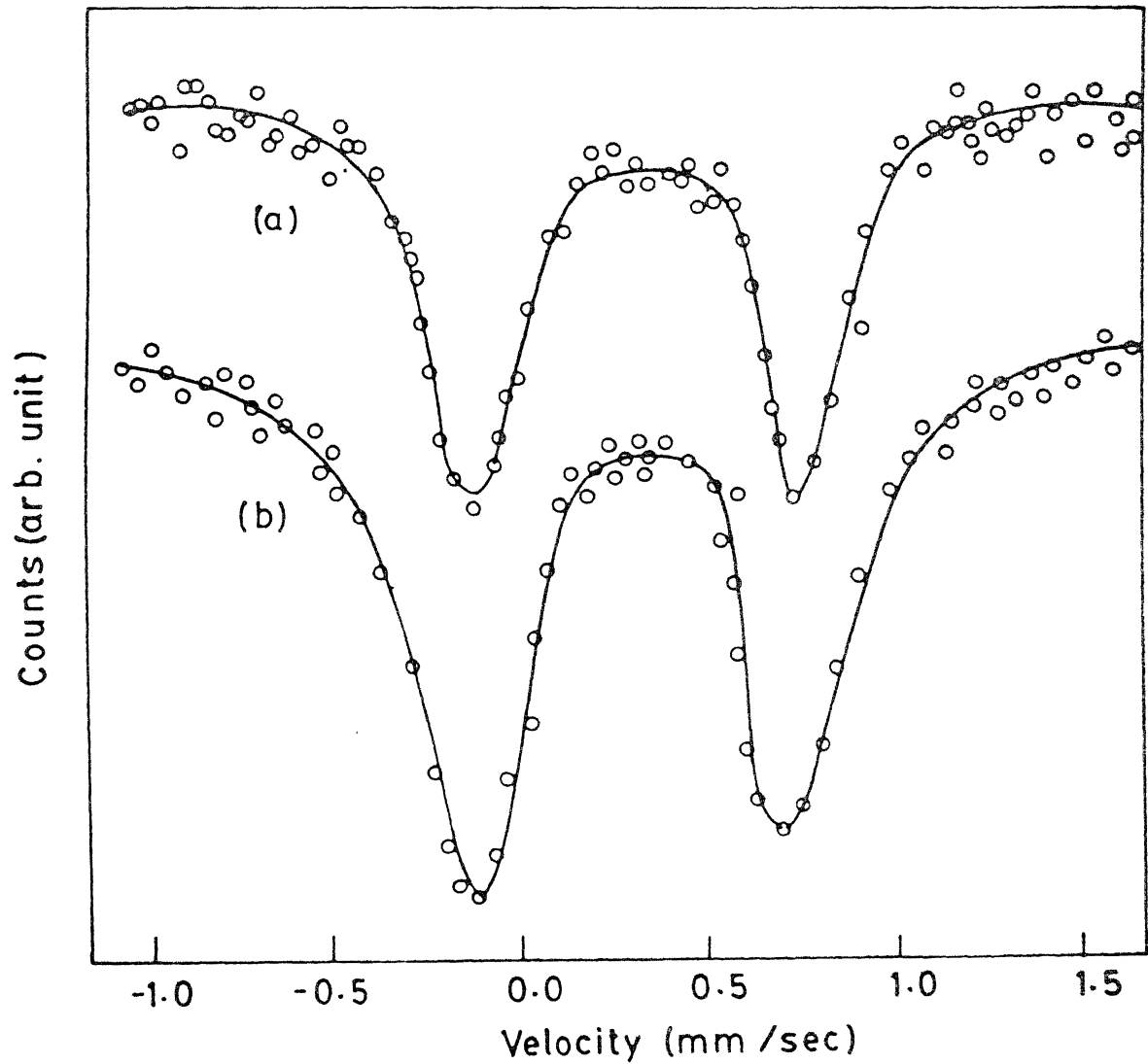


Fig 6.15 Mössbauer spectra of black roussin salt at (a) Zero field  
(b) 40 KV /Cm.

$\pm 0.004$  mm/sec for a maximum field of 40 KV/cm. But the isomer shift of the system does not show any significant change [fig. (6.9)]. The variation of quadrupole splitting of the black Roussin salt is shown in fig. (6.8). The variation of intensity ratio of the two peaks is shown in fig. (6.13).

#### 6.4 Discussion :

Thus we see that the effect of an external electric field on the Mössbauer hyperfine parameters is clearly identifiable in all the systems. Bashkirov and Lebedev [1] had made a perturbation calculation of the polarization of the  $\text{Fe}^{3+}$  ion 4s-shell by an electric field and its contribution to the hyperfine parameters. For a field  $E = 45 \times 10^3$  V/cm, using their equations (2) and (3), the 4s-shell polarization effect tends to zero. Hence, the contribution could be due to the 3d-shell polarization and/or the effect of the induced dipoles at the lattice sites. To our knowledge, the problem of the effect of a perturbation on the 3d-shell has not been worked out yet. A detailed theoretical work on this is in order.

## REFERENCES

1. Sh. Sh. Boshkirov and V.N. Debedev, *Fiz Tverd. Tela* 21, 262 (1979) [*Sov. Phys. Solid Stat* 21, 156 (1979)].
2. Sh. Sh. Bashkirov and V.N. Lebadev in : *Paramagnitnyi razonans* (Paraamagnetic resonance) Kazan 1979, No. 15, p 100.
3. N. Bloembergen, *Phys. Rev. Lett.* 7, 90 (1961).
4. A.S. Jvanov, A.V. Kilpakov and R.N. Kuzmin, *Zh. Eksp. Teor. Fiz.* 66, 697 (1974) [*Sov. Phys. JETP*, 39, 336 (1974)].
5. R. Ingalls, *Phys. Rev.* 113, A781 (1964).
6. R. Ingalls, K. Ono and Louis Chandler, *Phys. Rev.* 172, 295 (1968).
7. K. Chandra and S.P. Puri, *Phys. Rev.* 169, 272 (1968).
8. W. Kerler, *Z. Phys.* 167, 194 (1962).
9. V.I. Goldanskii and R.H. Herber, *Chemical Applications of Mössbauer Spectroscopy* (Academic Press, New Yor, 1968).
10. N.V. Nair and D.C. Khan, *Phys. Rev. B*, 24, 5417 (1981).
11. D.P. Johnson and J.G. Dash, *Phys. Rev.* 172, 983 (1968).
12. E.A. Paez, W.T. Oosterhuis and D.L. Weaver, *Chem. Comm.* 506 (1970).
13. N.N. Greenwood and T.C. Gibb, *Mössbauer Spectroscopy* (Chapman and Hall Ltd., London, 1971).

14. R.W. Grant, R.N. Housley and U. Gonser, Phys. Rev. 178, 523 (1969).
15. Mössbauer Effect Data Index, Edited by J.G. Stevens and V.E. Stevens (North American Aviation Science Centre, Thousand Oak, Calif., 1975).
16. W. Kerler and W. Neuwirth, Z. Physik, 167, 176 (1962).
17. W. Kerler, W. Neuwirth, E. Huck, P. Kuhn and B. Zimmerman, Z. Physik 173, 321 (1963).

## CONCLUSION

The present work is aimed at the understanding of anomalous behaviour of saturation magnetization of high valent, diamagnetically substituted Ni-Zn ferrites. The problem is investigated by Mössbauer spectroscopy, Magnetic measurements and X-ray diffraction pattern. For better homogeneity the samples were prepared by solution route technique. The X-ray diffraction pattern confirmed the presence of single spinel phase.

$^{57}\text{Fe}$  Mössbauer spectra of all the samples were recorded at 295 and  $77^{\circ}\text{K}$ . The hyperfine parameters were obtained by least square curve fitting of the experimental data on DEC-1090. The isomer shift values at A and B sites confirmed that iron is in  $\text{Fe}^{3+}$  high spin state. The analysis of hyperfine magnetic field yields that in  $\text{Ni}_{1-y+x} \text{Zn}_y \text{Ti}_x \text{Fe}_{2-2x} \text{O}_4$  and  $\text{Ni}_{1-y+x} \text{Zn}_y \text{Sn}_x \text{Fe}_{2-2x} \text{O}_4$  ( $0 \leq x \leq 0.1$ ;  $y = 0.0, 0.3$  and  $0.4$ ) all the tetravalent non-magnetic cations occupy the B site only.

If Néel's type of magnetic ordering is considered in the present series of ferrites then a linear decrease of magnetization is expected with the increase of non-magnetic cations as they enter at B site only. But in all the cases a deviation from this behaviour was observed. Hence we conclude that the change of magnetization is not only due to the simple replacement of magnetic ions at B site by the

non-magnetic  $Ti^{4+}$  or  $Sn^{4+}$  ions but also due to a more complex process which leads to the development of canted spin structure. The canting angle, which depends on the relative strength of various exchange constants  $[J_{Fe^{3+}(A)-Fe^{3+}(A)}, J_{Fe^{3+}(A)-Fe^{3+}(B)}, J_{Fe^{3+}(A)-Ni^{2+}(B)}, J_{Fe^{3+}(B)-Fe^{3+}(B)}, J_{Fe^{3+}(B)-Ni^{2+}(B)}, J_{Ni^{2+}(B)-Ni^{2+}(B)}]$ , changes with the change of  $Ti^{4+}$  or  $Sn^{4+}$  concentration in the lattice. The calculation of exchange constants show that almost all the exchange constants remain unchanged except  $J_{Ni^{2+}(B)-Ni^{2+}(B)}$  [in case of  $y = 0.3, 0.4$ ] and  $J_{Fe^{3+}(A)-Ni^{2+}(B)}$  [in case of  $y = 0.0$ ]. We proposed that the change of exchange constants is basically due to the change in lattice parameter. The simple Born expression for the lattice parameter shows that this is proportional to the  $M^{1/(1-n)}$  where  $M$  is the Madelung constant and  $n$  is a constant (usually equal to 10). The calculation with the average charge on the lattice site shows that  $M$  does not change with  $Ti^{4+}$  or  $Sn^{4+}$  addition. However, the calculation with the root mean square charge at the lattice sites show the correct variation of the Madelung constant and lattice parameter for the  $Sn^{4+}$ -substitution case for concentration of  $Sn^{4+} > 0.008$  per formula unit. However, this explains only part of the lattice parameter variation with  $Ti^{4+}$  substitution and calls for a more sophisticated calculation of the Madelung constant.

Now we propose some problems for the further study.

It is well known that the Mössbauer spectrum of iron ( $^{57}\text{Fe}$ ) consists of six absorption peaks when the magnetic hyperfine splitting is present. These peaks correspond to  $\Delta m = \pm 1, 0$  transitions between the excited state ( $I = 3/2$ ) and the ground state ( $I = 1/2$ ) of the  $^{57}\text{Fe}$  nucleus. For an ideal thin absorber with a negligible quadrupole interaction the line areas in a Mössbauer spectrum are proportional to

$$\begin{aligned} A_{1,6} &\propto 3(1+\cos^2\theta) \\ A_{2,5} &\propto 4\sin^2\theta \\ \text{and} \quad A_{3,4} &\propto 1+\cos^2\theta \end{aligned}$$

where  $A_{i,j}$  is the area of the  $i$ th ( $i = 1, 2, 3$ ) or  $j$ th ( $j = 4, 5, 6$ ) lines and  $\theta$  is the angle between the direction of propagation of the  $\gamma$ -ray and the direction of magnetization. The ratio  $A_{1,6} : A_{3,4}$  is equal to 3 : 1 regardless of the angle  $\theta$ . If the magnetization directions in the absorber are oriented randomly, the relative intensities of the six absorption lines are in the ratio 3:2:1:1:2:3. For a direct test of the canted spin structure, the absorber is placed in an external magnetic field, applied parallel to the direction of propagation of the gamma ray. If the field is strong enough to orient the magnetization in the direction of the field and the spin structure is collinear, then  $\Delta m = 0$  transitions vanish and consequently the lines 2 and 5 disappear from the Mössbauer

absorption spectrum. On the other hand, if canted spin structure does exist, the intensity of these transitions will not be zero. The intensity of these lines depend on the degree of canting and the canting angle can be obtained from the ratio  $A_{2,5} : A_{1,6}$

$$\frac{A_{2,5}}{A_{1,6}} = \frac{4 \sin^2 \theta}{3(1 + \cos^2 \theta)}$$

$$\text{or } \theta = \sin^{-1} \left[ \frac{\frac{3}{2} \left( A_{2,5}/A_{1,6} \right)}{1 + \frac{3}{4} \left( A_{2,5}/A_{1,6} \right)} \right]^{1/2}$$

In our present work we could not take the Mössbauer spectra of samples in an external magnetic field. We propose to take up this problem in our later work.

The study of these systems by neutron diffraction also offers the valuable information regarding the magnetic structure of these ferrites. From the presence of certain peaks in the neutron diffraction pattern the presence of canted spin structure at A or B sites can be tested.

In  $\text{Sn}^{4+}$  substituted Ni-Zn ferrite systems it was observed by  $^{57}\text{Fe}$  Mössbauer spectroscopy that  $\text{Sn}^{4+}$  ions occupy the B site. This can be further corroborated by  $^{119}\text{Sn}$  Mössbauer spectroscopy. As seen in Chapter 5, a contradictory change was found between the lattice parameter and  $J_{\text{Ni}^{2+}(\text{B})-\text{Ni}^{2+}(\text{B})}$  for the concentration of  $\text{Sn}^{4+}$  less than 0.004 per formula unit. It was suspected

that the outermost 4d electrons of  $\text{Sn}^{4+}$  contribute to this trend. For a satisfactory explanation of this problem we propose to study the system by  $^{119}\text{Sn}$  Mössbauer spectroscopy.

It is hoped that the present work has contributed to our knowledge of the hyperfine interaction of substituted Ni-Zn ferrites leading to a knowledge of their microscopic structure.

108472

TH 537.5352 Date Slip A108477  
S-28-2

Sy 38p  
This book is to be returned on the  
date last stamped.

PHY-1989-0-SRI-MOS